NEUTRON CROSS SECTION MEASUREMENT USING THE ASSOCIATED PARTICLE TECHNIQUE

- by -

P. B. JOHNSON

A Thesis submitted for the
Degree of Doctor of Philosophy

Victoria University of Wellington
New Zealand
June, 1966

ABSTRACT

The associated particle technique is applied to the $D(d,n)\,He^3$ reaction, in order to produce a tagged neutron beam of accurately known energy, flux, and direction. The incident deuteron beam is obtained from a 400 kv positive ion Van de Graaff accelerator. A description is given of the design of a uniform field sector magnet and other equipment associated with the stabilization and calibration of the energy of the incident deuteron beam. A versatile n-He^3 coincidence system is described. The use of a silicon surface barrier detector with a thin nickel foil window enables complete resolution of the He^3 peak with consequent improved neutron flux determination. The tagged neutron beam is used to measure the absolute neutron cross sections of the $K^{39}\,(n,p)\,A^{39}$ and $K^{39}\,(n,\alpha)\,Cl^{36}$ reactions at a neutron energy of 2.46 Mev. The results obtained, (95 ± 4) mb and (6.2 ± 1) mb respectively, are compared with values obtained by other workers, and with theoretical predictions.

CONTENTS

C H A P T E R 3:

THE PERFORMANCE AND CALIBRATION OF THE STABILIZING SYSTEM

C H A P T E R 4:

THE ABSOLUTE CROSS SECTIONS OF THE K^{39} (n,p) A^{39} and K^{39} (n, α)Cl^{36} REACTIONS FOR 2.46 - MEV NEUTRONS

LIST OF PLATES:

CHAPTER I: INTRODUCTION

1.1. Neutron Cross section measurement:

The probability that a neutron incident on an atomic nucleus will undergo a nuclear interaction with that nucleus is an important parameter in the elucidation of nuclear structure. The total neutron cross section σ, provides a measure of this probability and is defined to be the number of neutron induced events occurring per nucleus per unit time per unit incident neutron flux. A knowledge of the incident neutron flux is usually needed if the cross section of a nuclide is to be measured. Direct measurements of neutron flux are difficult and the flux is usually deduced from known or measured properties of the source from which the neutrons are emitted. A suitable neutron flux may be obtained from nuclear reactions occuring in a target bombarded with a charged particle beam from a nuclear accelerator. Such a neutron source has advantages in both intensity and in variable neutron energy over photoneutron and other radioactive neutron sources.[1] In this case the effective neutron flux taking part in the cross section measurement may be estimated from a knowledge of the integrated beam current and the cross section and angular distribution of the neutron producing reaction.

An improved method of flux determination has resulted from detecting the charged recoil nucleus associated with any neutron produced in the reaction. The total number of such recoil nuclei is then equal to the total number of neutrons generated in the target. Since application of this method requires that the recoil nuclei possess sufficient energy to be detected, it is most suited to reactions having a positive Q value.

This associated particle technique has been extended to the identification or "tagging" of individual neutrons by the detection of their associated recoil nucleus. For a particular incident charged particle beam energy and associated recoil particle

direction relative to the incident beam, the energy and direction of the neutron associated with a given recoil particle are determined uniquely. In this way restrictions placed on the detected particles enable the production of a beam of individually "tagged" neutrons of known flux, energy, angular divergence, and spatial direction. A "tagged" neutron beam has two further advantages:

(1) The energy of the "tagged" neutrons may be varied by altering the energy of the incident charged particle beam or by altering the direction of the tagged neutron beam selected by the recoil particle detector and,

(2) A considerable reduction in the number of background events induced in the nuclide sample by unwanted scattered neutrons and gamma rays, may be effected by requiring that the neutron induced events are in time coincidence with events in the associated recoil particle detector.

The associated particle coincidence technique has been mainly developed using the T(d,n) He^4 and D(d,n) He^3 reactions. [2-8]

$$T + d \rightarrow n + He^4 + 17.59 \text{ Mev.}$$
$$D + d \rightarrow n + He^3 + 3.27 \text{ Mev.}$$

For low incident deuteron energies the α-particle and neutron from the T(d,n) He^4 reaction have energies of about 3.5 Mev and 14 Mev respectively while the Helium-3 particle and neutron from the D(d,n) He^3 reaction have approximately 800 Kev. and 2.5 Mev respectively.

Neutron cross section measurements and neutron time flight studies using the 'tagged' neutron beam from the D(d,n) He^3 reaction is the main interest of this laboratory. The deuteron beam is produced in the Physics Departments Model PN-400 Van de Graaff accelerator* Although rated at 400 kv. this accelerator

* Manufactured by the High Voltage Engineering Corporation, Burlington, Massachusetts.

will deliver onto a target, 150 μA of positive ion beam current at voltages in excess of 500 kv. This model accelerator has no form of beam energy stabilization and as a consequence the beam energy has, in the past, had to be controlled manually for the duration of any experiment. The effect that changes in the incident deuteron beam energy have on the direction and energy of the tagged neutron beam may be assessed from consideration of the kinematics of the D(d,n) He^3 reaction (Appendix 1). Figure (1) shows the dependence of the neutron and Helium-3 energy on the incident deuteron energy Ed, drawn as a family of curves with the laboratory angle of emission of the neutron θ_n as parameter. The dependence of θ_n on E_d, with the laboratory angle of emission of the associated Helium -3 particle ϕ, as parameter is also shown in figure (1). Figure (2) shows the dependence of the neutron energy E_n and ϕ, on θ_n drawn as a family of curves with E_d as parameter.

It can be seen (figure 2) that the neutron energy varies appreciably with changes in the energy of the incident deuteron except for values of θ_n close to 100°. For values of θ_n in this region, the direction of emission of the neutron varies rapidly with E_d. In general, it is not possible to choose a value of θ_n that simultaneously minimizes the dependence of both the energy and direction of the neutron on the incident deuteron energy. If the energy and direction of the tagged neutron beam are both to be determined precisely over as wide a range of neutron energy as possible, then stabilization and accurate energy calibration of the incident deuteron beam is essential. This is especially important in view of the rapid variations in neutron cross section with energy[2], for neutron energies around 2.5 Mev.

In general, the study and utilization of reaction products from nuclear reactions induced in a target by a charged particle beam requires accurate calibration and stabilization of the

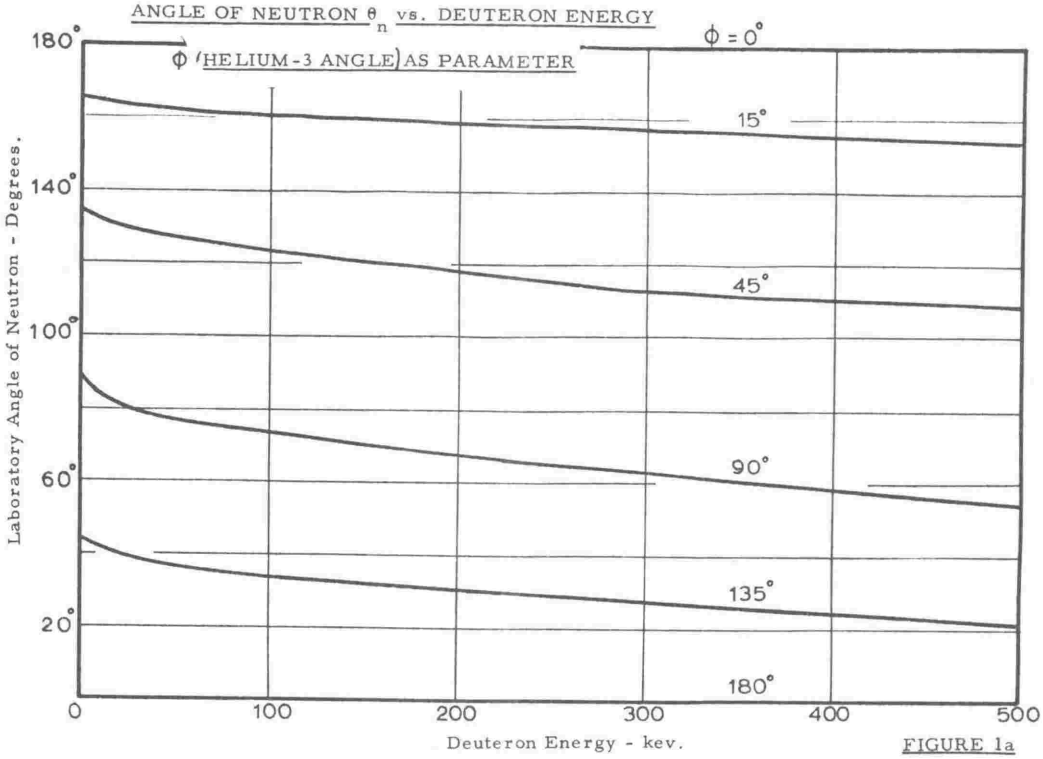

FIGURE 1a

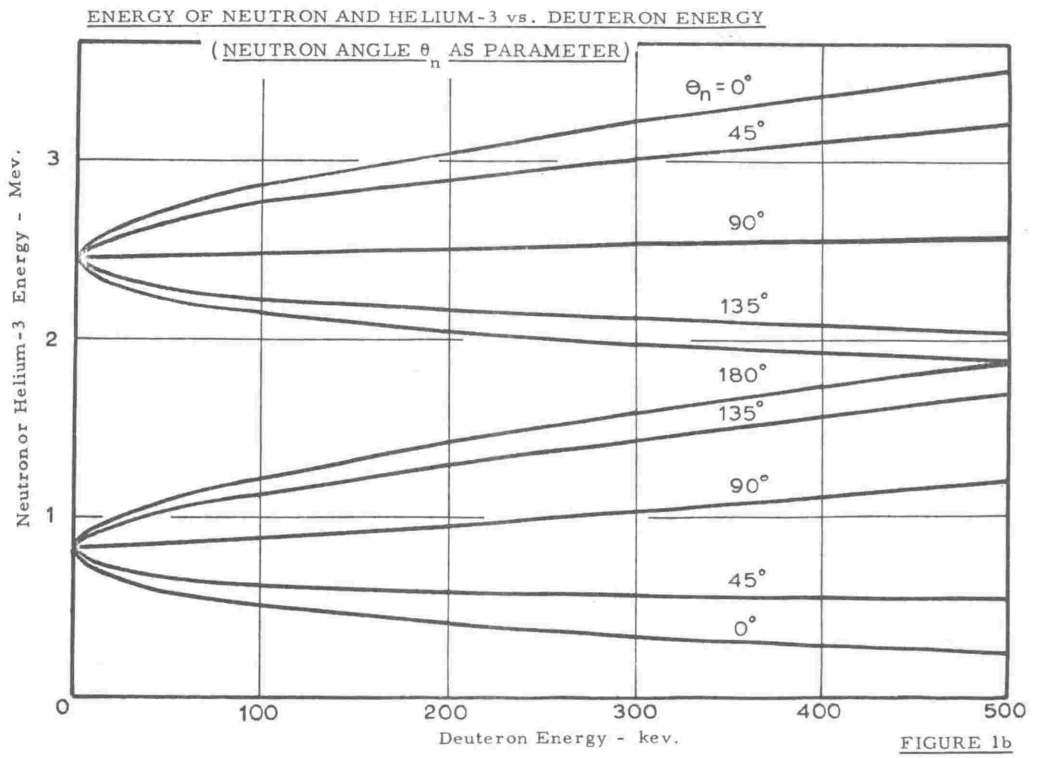

FIGURE 1b

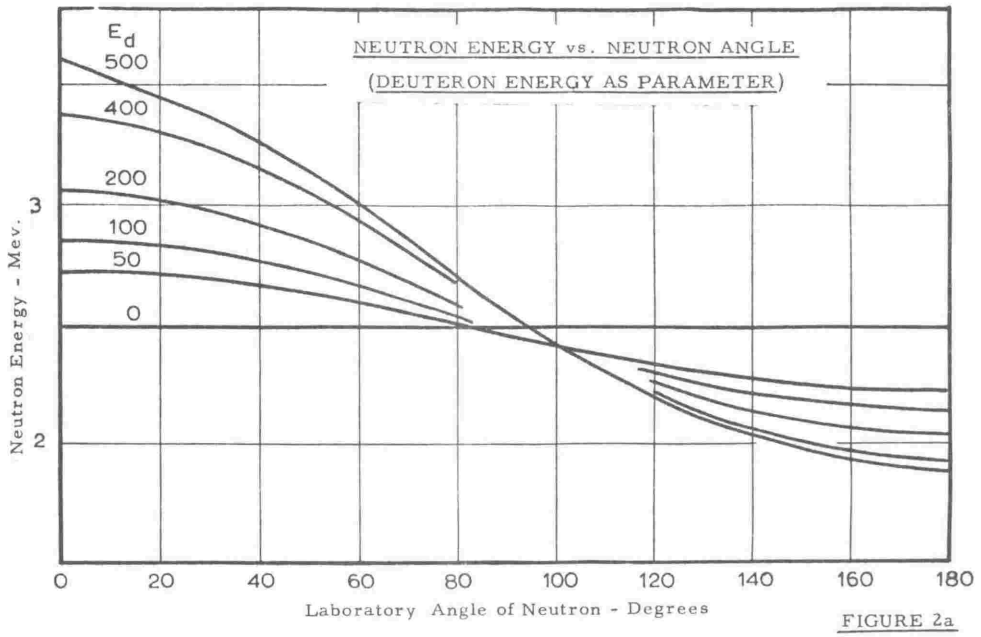

FIGURE 2a

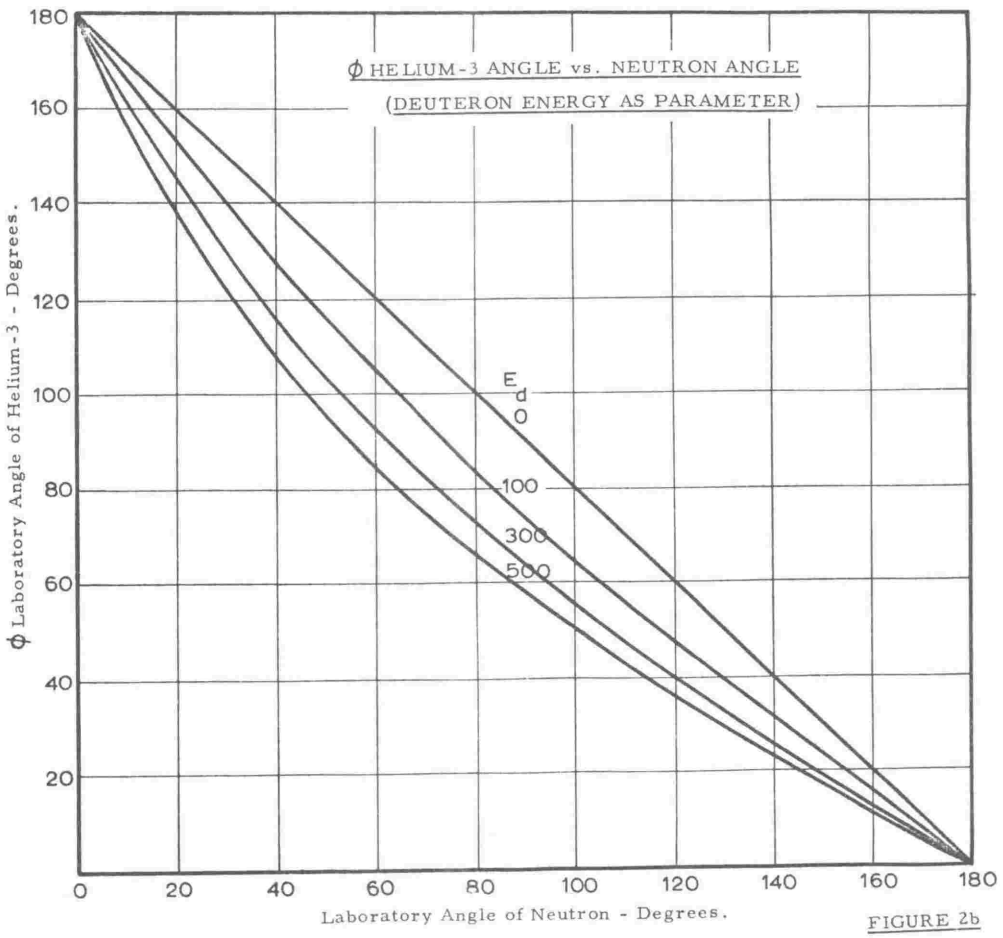

FIGURE 2b

incident beam energy. Considerations similar to those illustrated above with reference to the D(d,n) He^3 reaction show that any instability in the incident beam energy results in an uncertainty in both the energy and relative direction of the reaction products. As the Q value of the reaction under study decreases, the stability and accuracy required of the incident beam energy increase. Uncertainties from this source can introduce large errors into threshold measurements and experiments performed using reaction products from negative Q value reactions.

1.2. Recoil He^3 Particle Detection:

The cross sections of the D(d,n) He^3 and D(d,p)T reactions are approximately equal for low deuteron bombarding energies. In addition therefore to He^3 particles, there will also be incident on the recoil particle detector protons and tritons with energies of 3 Mev. and 1 Mev respectively, together with deuterons elastically scattered from the primary beam, light emitted from the target, and neutron capture gamma rays from surrounding material. For this reason unambiguous identification of the 800 kev He^3 particles is difficult.

Dixon and Aitken[2] have described an associated particle detector for use with the D(d,n)He^3 reaction in which a thin (0.51 mm) crystal of CsI(Tl) was used in conjunction with a photomultiplier. An aluminium coating of 225 ug/cm^2 was evaporated onto the front face of the crystal to prevent light emission from the target reaching the photomultiplier.

It was originally intended using a scintillation counter of this type as the recoil particle detector but a number of serious disadvantages were found:-

(1) The thickness of the foil covering the scintillator was found to be very critical. The foil thickness should be sufficient to prevent light and scattered deuterons from reaching the scintillator, but must not be thick enough to degrade the He^3 pulse height to a level comparable with the noise level of the system.

(2) The inherently poor resolution of a scintillation detector results in a broad He^3 peak. Consequently, if only genuine He^3 particles are to be selected for neutron tagging, a narrow pulse height window must be used. Such a restriction results in a relatively low He^3 counting rate with consequent poor efficiency.

(3) The poor energy spectrum shape (Chapter 4) does not allow the immediate recognition of the penetration of the aluminium foil by scattered deuterons. In a strong deuteron flux the possibility of the light output from a number of low energy deuterons summing within the crystal to give a resultant pulse entering the He^3 pulse height window is not negligible.

(4) The sensitivity of the crystal to neutron capture gamma radiation was not entirely eliminated despite the use of a thin crystal.

A considerable improvement over previously described systems has been realised by using a solid state detector as the associated particle detector. Semiconductor detectors combine a low sensitivity to light and gamma rays with an intrinsically high energy resolution. The best energy spectrum of the He^3 particles is obtained when the thickness of the foil covering the detector is only just sufficient to absorb the full energy of the scattered deuterons (Chapter 4). It has been found that a foil selected for optimum thickness for a particular deuteron energy will not be effective if the incident beam energy is allowed to rise by even quite small amounts. As semiconductor detectors are destroyed by even short exposure to a strong deuteron flux, energy stabilization of the primary deuteron beam is essential for optimum results with this technique.

This thesis describes the production of a tagged neutron beam of precisely known energy and direction. Chapter 2 decribes the design of an analyzing sector magnet and associated equipment necessary for the stabilization of the ion beam energy of the Van de Graaff accelerator. Chapter 3 is concerned with the calibration of the ion beam energy in terms of the magnetic field strength in the pole gap of the analyzing magnet, and with the performance and stability of the energy stabilization system.

The n - He^3 coincidence system, comprising the recoil particle detector, neutron detector, and associated electronics is described in Chapter 4. Included in this chapter is a description of the utilization of the tagged neutron beam for the measurement of the absolute cross sections of the K^{39} (n, α) Cl^{36} and $K^{39}(n,p)A^{39}$

reactions. The observed cross sections are interpreted in terms of current nuclear theory (Chapter 4). The conclusions drawn from this work may be found in Chapter 5.

CHAPTER II

THE ENERGY STABILIZATION OF THE VAN DE GRAAFF ACCELERATOR

2.1. INTRODUCTION:

2.1.1 The Positive Ion Accelerator

A Van de Graaff positive ion accelerator consists of a high voltage generator together with components used for the production of the ion beam. Although many developments and modifications[12-16] have been made to the belt charged type, electrostatic high voltage generator since R.J. Van de Graaff first demonstrated its practical value for nuclear physics research,[17] the basic principles of operation remain unchanged. For this reason only a brief description of features having particular relevance to the voltage stabilization of such a generator will be given.

A high voltage ($\sim$ 20 kv.) power supply sprays charge from a row of corona points (the charging screen) onto an endless, moving, rubberized fabric belt. The charge is carried by the belt into the field free region, inside a hollow hemispherical metal terminal which is electrically connected to a second row of corona points (the collector screen) that are in close contact with the belt. As the charge on the belt approaches the collector screen, it induces on it a charge of opposite polarity. This leaves a charge, of equal magnitude and polarity as the charge on the belt, residing on the outside of the metal terminal. The charge on the belt comes into contact with and neutralises the opposite polarity induced charge on the collector screen. The final result is as if the charge on the belt flows onto the outside of the terminal.

The potential V of the high voltage terminal is related to the charge Q on the terminal and the capacitance C of the terminal with respect to ground, by the relation $V = Q/C$. If the charging process were to continue the voltage would rise, either until electrical breakdown occurred from the terminal to the surroundings, or until the breakdown of the insulating properties of the belt caused the charging process to cease. In the model PN-400 Van de Graaff the cylindrical insulating column supporting the high voltage terminal, is made up of an off centre cylindrical column (containing the evacuated accelerator tube) fitted with circular metal planes placed at regular intervals down the column at right angles to the axis. Mechanical rigidity of the column as a whole is ensured by porcelain cylindrical spacing blocks located between the column planes. The belt runs parallel to the axis of the column and passes through apertures in the column planes. The development of excessive voltage on the top terminal is prevented by the onset of a corona discharge in the gap between hemispherical corona domes located between pairs of adjacent column planes. High resistances ($\sim 10^9$ ohms) placed between successive column planes ensure a uniform potential gradient down the belt and column, and a small steady stabilizing current drain from the top terminal.

The entire high voltage generator is encased in a pressure vessel filled with an insulating gas mixture of nitrogen, carbon dioxide, and sulphur hexafluoride at a pressure of six atmospheres. This allows good electrical insulation of the generator without the need for the large overall physical dimensions required for machines insulated by air at atmospheric pressure. A set of corona points facing into the high voltage terminal are mounted on a port in the wall of the pressure vessel.

In the original model the current drawn from the terminal by the corona discharge in the insulating gas is controlled by manual adjustment of the distance of the points from the high voltage terminal.

The positive ion source and focus power supply are located inside the high voltage terminal. Control of these components is effected by insulated control rods passing down through the column planes to coupling shafts which pass out through the base plate of the pressure vessel to small servomotors mounted on the outside. The outer cylindrical case of the belt drivemotor serves both as the rotor of the motor and as the bottom pulley for the belt. The terminal pulley is the rotor of an alternator driven by the belt and provides the electrical power for the components located inside the high voltage terminal. Hydrogen or deuterium gas supplied from small gas cylinders located within the terminal is allowed to flow slowly through a controlled (the 'gas' control) thermo-mechanical leak into an evacuated glass envelope where ionization of the gas takes place in an rf discharge. The positive ions formed are extracted from the plasma through a narrow aluminium canal and into the entrance of the accelerator tube by the application of a small dc extraction potential, (o to $\sim$2 kv. determined by the setting of the 'beam' control). Here, acceleration of the ions down the evacuated accelerator beam tube takes place under the action of the electric field existing between the high voltage terminal and ground. Coarse focussing of the positive ion beam is accomplished by the shape of the electric field within the accelerator tube. The field distribution within the beam tube is determined by shaped metal planes[14] which pass out through the insulating wall of the accelerator tube and are electrically

connected to the column planes. These metal planes serve also to equalise the potential gradient down the length of the accelerator tube and to prevent high voltage discharge within the vacuum. Precise focussing of the ion beam is achieved by adjusting the potential applied to the focus electrode by means of the 'focus' control. This electrode is electrically connected to both the first column plane and the focus power supply and is situated at the high voltage end of the beam tube (where the ion velocities are least) immediately following the extraction canal from the ion source. The vacuum pump used for evacuating the ion source glass envelope and beam tube is located outside the generator pressure vessel and is coupled into the beam tube where it emerges through the pressure vessel base plate.

2.1.2 Voltage Stabilization of the Generator:

Although usually regarded as a constant voltage device, the Van de Graaff is in fact a constant current generator. The high voltage terminal can be regarded as the 'point' in the application of Kirchoff's first law; the algebraic sum of the currents at the terminal being zero for a steady state potential. At equilibrium the belt charge current is exactly balanced by the current drain from the top terminal consisting of the potential divider, beam and corona load currents together with some small contribution from leakage corona currents.

Fluctuations occurring in any one of these currents will cause the potential on the high voltage terminal to fluctuate. The main source of terminal potential variations, in practice, are caused by fluctuations occurring in the belt charge current. There is little possibility of achieving substantial reduction in these fluctuations through improved belt technology[18], and so their effects must be cancelled in the stabilization process.

Stabilization systems differ in both the method used to sense the potential on the high voltage terminal and in the mechanism used to correct any changes in the potential. Common sensing methods include "sampling" the potential by means of a high resistance potential divider placed between the high voltage terminal and ground[19], detecting high frequency excursions in the terminal potential with diametrically opposed capacitive pickups[18], using the output voltage from an electrostatic generating voltmeter viewing the high voltage terminal from a port through the wall of the pressure vessel,[20-24] and the generally preferred method of deriving an energy 'error' signal from the deviation of the ion beam from the centre of the vertical slit between two insulated metal electrodes placed in the image plane of either a magnetic,[25-28] or electrostatic[22,23,29-31] analyzer used to deflect the positive ion beam. This last method has the advantage of enabling absolute calibration of the energy of the ion beam in terms of the magnetic or electric field strength in the beam deflecting analyzer. A magnetic analyzer has the further advantage of enabling the separation of ions having the same energy but differing charge to mass ratios; an essential feature when the ion beam from the accelerator contains a high proportion of singly charged, double and treble mass ions. Any advantages that may be gained by the use of an electrostatic analyzer for the beam deflection (for example the increased accuracy of energy calibration, simpler construction and power supply requirements, and smaller physical size) together with a small subsidary magnetic analyzer for the removal of the heavier mass ions - were felt to be outweighed by the technical difficulties and inconvenience associated with the need for precise, independent adjustment of two fields to select the ion energy.

Variation of the corona current drawn from the high voltage terminal is the most attractive mechanism for correcting changes in the terminal potential of a Van de Graaf generator.

Here, the amount of negative charge sprayed onto the positive high voltage terminal is controlled by altering the grid-cathode bias of a triode valve placed in series with the corona points. Advantages included in this method of control are

(1) The corona points are substantially at earth potential and are readily accessible being mounted on the internal wall of the pressure vessel.

(2) Rapid corrections to the terminal potential are possible because of the short transit times of the negative charges in a corona discharge in an insulating gas. The latest experimental evidence [32] indicates that the transit time of ionization through an insulating gas is governed by photo-ionization processes and is therefore much shorter than originally thought.[18]

The rest of this chapter describes the design and construction of a stabilizing system for a Van de Graaff accelerator using magnetic momentum analysis of the ion beam to sense fluctuations in the high voltage terminal potential. The error signal is derived by passing the ion beam emerging from the analyzing magnet through a slit defined by a pair of electrically insulated metal sensing electrodes placed in the image plane of the magnetic analyzer. If the terminal potential of the Van de Graaff generator becomes higher or lower than the potential corresponding to the particle momentum selected by the magnetic field, the ion current striking the outer or inner metal electrode respectively, will be increased. The difference signal developed between the sensing electrodes is amplified by a dc differential amplifier and applied as a correction signal to the grid of the corona triode, in such a way as to offset the potential change of the high voltage terminal.

2. 2. THE DESIGN OF THE ANALYZING MAGNET

2. 2. 1. THE DEFLECTION AND FOCUSSING OF CHARGED PARTICLES IN A UNIFORM MAGNETIC FIELD

2. 2. 1. 1. HORIZONTAL AND VERTICAL FOCUSSING

An essential requirement of an analyzing magnet is that the cross-sectional area of the ion beam after deflection in the magnetic field, is sufficiently small to permit a high ion current to be delivered onto a small target area. The possible defocussing of the ion beam during deflection in the magnetic field region must therefore be considered in the magnet design.

The focussing of charged particles in a plane at right angles to the direction of a uniform magnetic field (termed the horizontal plane) was orignally discussed by Barber[33] for the case where the particles entered and left the magnetic field along normals to the magnetic field boundaries (i.e. for angles E_o and E of figure 3(a) equal to zero). The conditions necessary to achieve such horizontal focussing were subsequently studied in greater detail by Stephens[34,35], Brueche and Scherzer[36], Herzog[37], and Cartan[38] and the treatment was extended to cover the case of oblique entry and exit of the particles at the magnetic field boundaries, (i.e. angles E_o and E not zero). For this latter case, Cotte[39] showed that the non-uniform fringing field, extending in practice beyond the pole boundaries of a magnet had a vertical focussing effect on those particles not entering the field in the median plane (i.e. the horizontal plane, through the middle of the magnet pole piece gap, considered in earlier treatments). The equations derived for focussing in the vertical plane, together with those already developed for horizontal focussing in the median plane, showed that it was possible with certain geometrical configurations to achieve simultaneous focussing in both the horizontal and vertical directions. Cotte, however, made no investigation of these configurations.

PARTICLE TRAJECTORIES IN THE HORIZONTAL PLANE
OF A SECTOR-SHAPED UNIFORM MAGNETIC FIELD

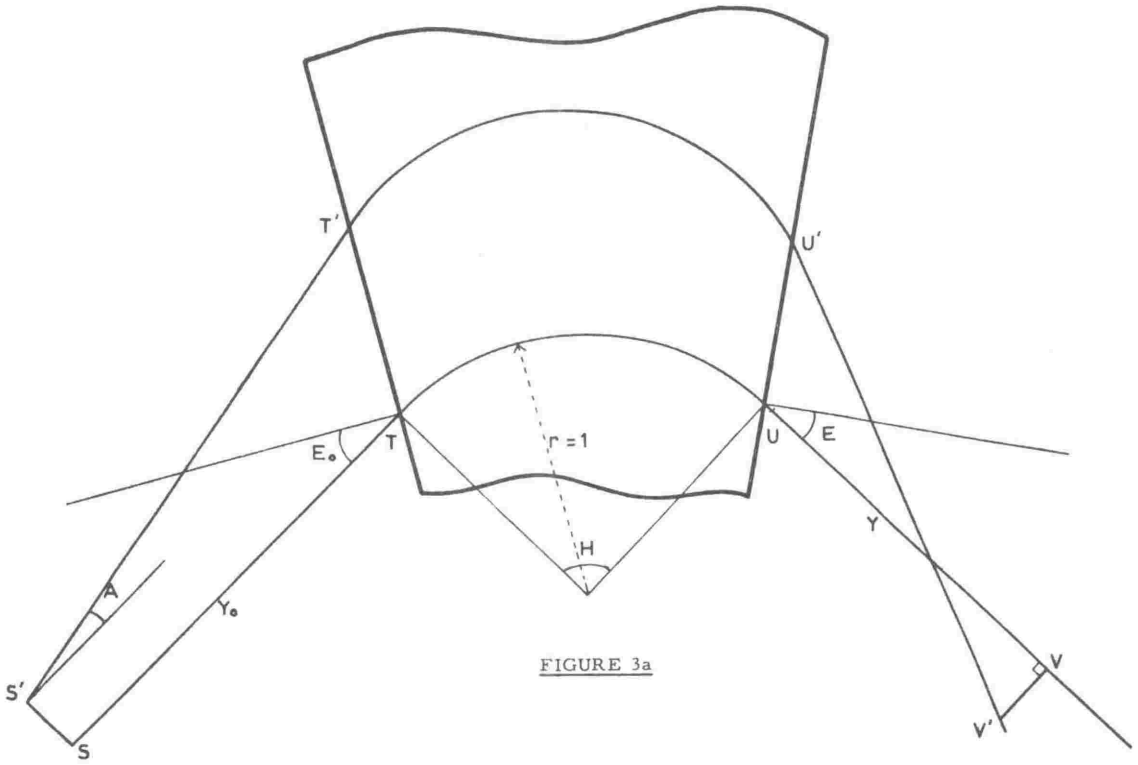

FIGURE 3a

PARTICLE TRAJECTORIES IN THE VERTICAL PLANE
OF A SECTOR-SHAPED UNIFORM MAGNETIC FIELD

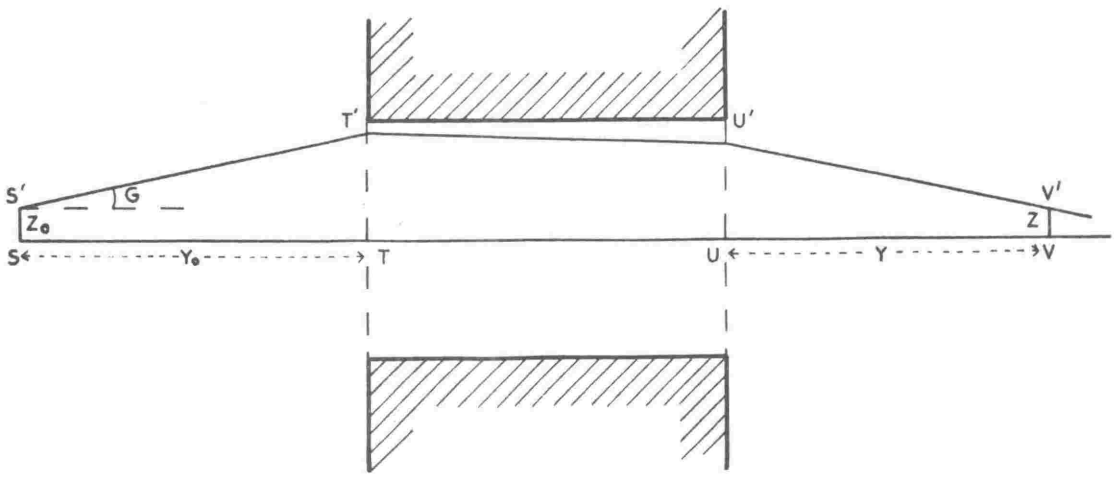

FIGURE 3b

The use of a non-uniform field to achieve focussing in two perpendicular directions was employed by Svartholm and Seigbahn[40], and by Shull and Dennison[41], in magnetic sector spectrometers in which the magnetic field strength within the sector was a function of position. Judd[42], Svartholm[43], and Rosenblum[44], extended the theory of two directional focussing in non-uniform fields to include the case where both source and image lay outside the effective magnetic field boundaries.

Camac[45], and in a more comprehensive form, Cross[46], investigated the use of the non-uniform fringing field associated with a uniform field, sector magnet for obtaining vertical focussing at the same point as the image produced by horizontal focussing occurring in the uniform sector field as a whole. It is this type of two directional or double focussing that will now be discussed.

Focussing in the horizontal plane occurs when the angles E_o and E of figure 3(a) are such that the path S'T'U'V' of a particle having a slightly different initial position, direction and momentum to a particle following the mean path STUV, has a longer trajectory in the magnetic field and is thereby caused to converge on the mean path after leaving the magnetic field. The relation between object and image distances for focussing in the horizontal plane follows from purely geometrical considerations (appendix 2). The effect of the fringing field on ion trajectories in the horizontal (xy) plane is to cause a slight lateral displacement and change in magnification of the image, and is discussed further in appendix (6).

The reason for the vertical focussing action of the fringing field is not as immediately apparent. The charged particles under consideration (figure 4) enter the magnetic field region in the $z = z_o$ plane and make an angle, in the xy plane, of E_o with the normal to the pole boundary. The initial velocity of the particles in the Z direction is zero,

$$\text{i.e. } V_z = 0 \text{ when } t = 0$$

CO-ORDINATE SYSTEM FOR VERTICAL OR Z FOCUSSING
OF IONS IN FRINGING FIELD

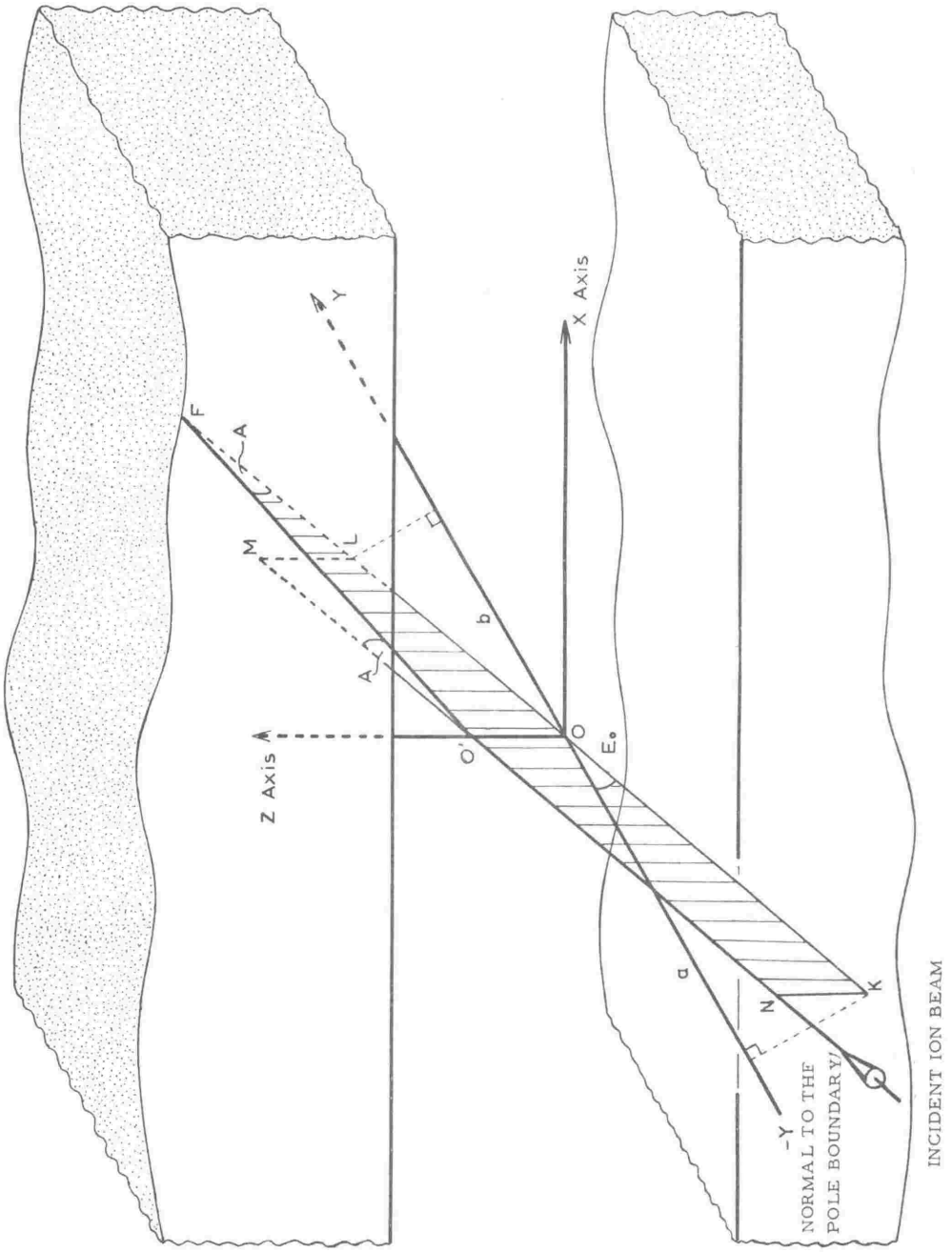

FIGURE 4

The magnetic force $\underline{F}$, acting on such a moving charged particle is given in mks units by

$$\underline{F} = e(\underline{V}_o \times \underline{B}) \qquad \text{---------- (1)}$$

where $\underline{V}_o$ is the velocity vector of a charged particle, $\underline{B}$ is the magnetic flux density vector and e is the charge in coulombs carried by the particle. The Z component of this force is

$$m \frac{d^2Z}{dt^2} = e \ (V_x B_y - V_y B_x) \qquad \text{---------- (2)}$$

where V_x is the component of the velocity V_o, in the X direction, and the same notation holds for the other symbols. As the X axis runs parallel with the pole boundary the component of the fringing field in the X direction is zero and $B_x = 0$. Furthermore

$$V_x = V_o \sin E_o$$

$$V_y = V_o \cos E_o$$

and $$V_x = V_y \tan E_o = \frac{dy}{dt} \tan E_o$$

Substituting this value for V_x in equation (2) gives

$$\frac{d^2Z}{dt^2} = e \frac{dy}{dt} B_y \tan E_o$$

and $$\frac{dZ}{dt} = \frac{e}{m} \tan E_o \int_{a}^{b} B_y \cdot dy \qquad \text{---------- (3)}$$

$z = z_o$

where the integration is carried out between the limits a and b in the $z = z_o$ plane. The point $y = a$ is chosen sufficiently far outside the pole gap for B_z to equal zero. The point $y = b$ is chosen in the uniform field region inside the pole gap where $B_y = 0$. The integral in equation (3) may be evaluated by applying the Ampère Circuital Law for B/μ_o, to the closed path KLMNK, (where μ_o is the permeability of the medium).

Then $\oint \frac{B}{\mu_o} \cdot \underline{dl} = 0$ as no current is enclosed by the loop.

and

$$0 = \int_{a\ z=0}^{b} \frac{B_y}{\mu_o} \cdot dy + \int_{0\ y=b}^{z_o} \frac{B_z}{\mu_o} \cdot dz + \int_{b\ z=z_o}^{a} \frac{B_y}{\mu_o} \cdot dy + \int_{z_o\ y=a}^{0} \frac{B_z}{\mu_o} \cdot dz$$

As $B_z = B_o$ when $y = b$ (B_o is the uniform field in the gap)
$B_z = 0$ when $y = a$,
and $B_y = 0$ when $z = 0$. (i.e. the magnetic flux is everywhere normal to the median plane), one obtains from the above

$$\int_{a\ z=z_o}^{b} B_y \cdot dy = B_o Z_o$$

and equation (3) becomes

$$V_z = \frac{dz}{dt} = Z_o \frac{e}{m} B_o \tan E_o$$

where V_z is the Z component of the velocity of the charged particle after passing through the fringing field.

The focal length of a thin lens in the optical case, is defined as the distance from the lens to the point on the axis where an incident parallel beam of light is brought to a focus. In a similar manner a focal length f_o, can be ascribed to the fringing field of a magnet for focussing in the Z direction, where

$$f_o = \frac{O\,O'}{\tan A_o} = \frac{Z_o}{\tan A_o} \qquad \text{(from triangle OFO').}$$

But $\tan A_o = \frac{V_z}{V_o}$

$$\therefore \quad f_o = \frac{m V_o}{e B_o \tan E_o} \qquad \text{----------(4)}$$

For horizontal deflection in the uniform magnetic field of strength B_o, the charged particle trajectory has a radius of curvature r in the horizontal plane, where from equation (1)

$$B_o e V_o = \frac{m V_o^2}{r}$$

$$\text{giving} \quad r = \frac{m V_o}{B_o e}$$

and

$$f_o = \frac{r}{\tan E_o} = \frac{r}{a_o} \qquad \text{----------(5)}$$

where

$$a_o = \tan E_o$$

In a similar way the focal length f ascribed to the fringing field at the second magnetic field boundary may be found.

Here

$$f = \frac{r}{\tan E} = \frac{r}{a} \qquad \text{----------(6)}$$

Equations (5) and (6) show that a positive focussing action takes place in the Z direction at both field boundaries, provided that E_o and E are greater than zero and positive. Angles E_o and E are defined as positive when the path of a particle outside the field region lies on the same side of the normal to the pole boundary as the centre of curvature of the trajectory in the horizontal plane, (E_o and E are shown positive in figures (3) and (4). In the derivation of equations (5) and (6) no special assumption is made about the precise shape of the fringing field, except that its extent in the Y direction is small compared with the radius of curvature of the particle trajectory in the uniform field. This requirement is met by most practical analyzing magnets in which the air gap between the poles is small compared with the width of the pole faces.

The relationship between the object and image distances for vertical focussing in the magnet as a whole may now be found, either from purely geometrical considerations similar to those of appendix (2)[45], or by solving the equivalent optical problem, as in appendix (3). (These two appendices illustrate the two principal methods of solving problems in ion optics). Although these equations are suitable for locating image and object distances, more comprehensive equations are needed for predicting the magnification, beam profile, and momentum dispersion produced by an analyzing magnet, for an object of finite cross-section.

2.2.1.2. GENERAL FOCUSSING EQUATIONS:

More general forms of the focussing equations [38, 39, 46] follow an exactly similar treatment to that given in appendices (2) and (3). Figure 3 (a) shows the paths of particles in the median plane of a sector magnetic field. The magnetic field is in the "vertical" direction perpendicular to the plane of the paper (the diagram has been exaggerated in the longitudinal direction of the page, for the sake of clarity). The path STUV shows the mean trajectory of a particle of momentum, p_o . S'T'U'V' is the path of a particle having an initial direction and position differing slightly from those of the mean trajectory, and a momentum given by $p_o (1 + B)$ where $B \ll 1$. The displacement x of this trajectory from the mean path, at a point outside the magnetic field boundary will depend in general on A, B, and x_o. From the work of Cartan[38]

$$x = uA + vB - wx_o + \text{second-order terms in } A, B, \text{ and } x_o \quad \text{---------} \quad (7)$$

where the coefficients u, v, and w are given by

$$u = \frac{(1 - pq) \cos E_o \cos E}{\sin N} \quad \text{---------} \quad (8)$$

$$v = \frac{2 \cos E \sin (\frac{1}{2} H)}{\sin N} \left[\cos (E_o - \tfrac{1}{2}H) + q \cos (E - \tfrac{1}{2}H)\right] \quad (9)$$

$$w = q \frac{\cos E}{\cos E_o} \quad \text{---------} \quad (10)$$

where

$$p \equiv \frac{y_o \sin N - \cos E_o \cos (H-E)}{\cos^2 E_o} \quad \text{---------} \quad (11)$$

$$q \equiv \frac{y \sin N - \cos E \cos (H-E_o)}{\cos^2 E} \quad \text{---------} \quad (12)$$

$$n \equiv H - (E_o + E) \quad \text{---------} \quad (13)$$

and all remaining angles and distances are shown in figure 3 (a). All distances are measured in units of the radius of curvature in

the uniform field and hence r does not enter into the above equations. For relativistic velocities B must be multiplied by the factor $(1 - V_o^2/c^2)$ which does not appear in the non-relativistic equation. The lateral and longitudinal displacement of the image caused by deflection in the fringing field outside the pole boundaries is small provided the path of the particle within the uniform field region is long compared with the pole gap width. Methods of compensating for the image displacement (appendix 6) caused by the fringing field have been discussed by Coggeshall[50], BainBridge[48], and Ploch and Walcher[49]. These methods have been more recently reviewed by Bainbridge[51].

Figure 3(b) shows the trajectories of particles in the vertical plane of the uniform magnetic field of figure 3(a). In this case STUV is the mean trajectory, while a particle having a path differing from the mean in both initial position and direction will follow a trajectory such as S'T'U'V'. Unlike the horizontal case, small fractional changes in the particles momentum can not effect a first-order change in the trajectory followed by the particle in the vertical plane, because a particle travelling initially in the median plane is not deflected regardless of what momentum it possesses. The vertical displacement z of the trajectory S'T'U'V' from the mean path outside the magnetic field boundary, will depend then in the first order, only upon z_o and G (figure 3(b)) and z may be represented by[46]:

$$z = mz_o + nG \qquad \text{---------- (14)}$$

where $m = 1 - H\tan E_o - y_v\left[\tan E_o + \tan E\,(1 - H\tan E_o)\right]$ ---- (15)

and $n = H + y_o(1 - H\tan E_o) - y_o y_v\left[\tan E_o + \tan E\,(1 - H\tan E_o)\right] + y_v\,(1 - H\tan E)$ ---------- (16)

The derivation of this formula requires that the path length within the fringing field is small compared with the path length within the uniform field region; but requires no special assumptions as to the shape and distribution of the fringing field (appendix 3).

2.2.1.3. CONDITIONS FOR STIGMATIC FOCUSSING:

Angular focussing in the horizontal plane occurs when the displacement x of the general trajectory S'T'U'V' is independent of the angle A. From equations (7) and (8) the coefficient of A vanishes when u equals o, that is when

$$pq = 1$$

On substituting for p and q, the condition for angular focussing in the horizontal plane becomes (note 1, appendix 4)

$$y = (\cos E)\ \frac{\sin H \cos E_o + y_o \cos (H - E_o)}{y_o \sin N - \cos E_o \cos (H - E)} \qquad \text{(17)}$$

Angular focussing in the vertical plane occurs when the displacement z of the general trajectory S'T'U'V' is independent of the angle G. The coefficient of G vanishes when n equals zero and from equation (16)

$$y_v = \frac{H + y_o\ (1 - H \tan E_o)}{y_o \left[\tan E_o + \tan E\ (1 - H \tan E_o)\right] - (1 - H \tan E)} \qquad \text{(18)}$$

Equations (17) and (18) can be written in a more suitable form for computation (note 2; appendix 4) by defining quantities P and Q by the equations

$$\tan P = \tan E_o + \frac{1}{y_o} \qquad \text{(19)}$$

$$\tan Q = \tan E_o - \frac{1}{y_o} \qquad \text{(20)}$$

Equation (17) then becomes simply,

$$\frac{1}{y} = \tan (H - P) - \tan E \qquad \text{(21)}$$

and (18)

$$\frac{1}{y_v} = \tan E - \frac{1}{H - \cot Q} \qquad \text{(22)}$$

The condition that horizontal and vertical focussing takes place at the same point y_d is that

$$y = y_v = y_d$$

This condition is best expressed as an equation determining E:

$$\tan E = \frac{1}{2}\left[\tan(H - P) + \frac{1}{H - \cot Q}\right] \text{---------} \quad (23)$$

while the distance from the pole boundary to the point of double focussing may be found by eliminating E from equations (23) and (22)

$$\frac{1}{y_d} = \frac{1}{2}\left[\tan(H - P) - \frac{1}{H - \cot Q}\right] \text{----------} \quad (24)$$

For any given pair of y_o and E_o, P and Q may be calculated using equations (19) and (20). Substitution of these values into equations (23) and (24) enable the values of E and y_d required for a stigmatic focus, to be calculated for a particular value of the angle of deflection H. For the formation of a real image the value of y_d so obtained must be positive.

A general analytical discussion of all possible double focussing configurations producing real images is extremely difficult. However, a large number of theoretically acceptable real image arrangements, prove to be experimentally unsuitable. The useful range of values that may be assumed by E_o and E, is restricted by the following experimental considerations.

(1) A positive focussing action in the vertical plane at the first magnetic field boundary is essential if the beam is to be prevented from diverging and striking the magnet pole pieces within the pole gap. From equation (6), it may be seen that E_o is restricted to positive values by this requirement.

(2) It is desirable to wind the coils of any electromagnet directly onto the pole pieces. The irregular shaped pole pieces resulting from the use of large negative values of E make this difficult, and increase the demands on yoke design

and construction if local saturation effects, and the consequent introduction of inhomogeneities into the uniform field region, are to be avoided.

(3) The long path lengths in the fringing field, concomitant with large positive values of E_o and E, invalidate the assumptions on which equations (19) to (24) are based. The uncertainties in particle trajectories, introduced by the small local inhomogeneities in the fringing field caused by local saturation effects in the magnet yoke and pole pieces, are also increased. These effects result in the calculated focussing properties not being realised in practice,

Experimentally desirable double focussing configurations will therefore have E_o in the range 0^o to $+ 60^o$, and E in the range -40^o to $+60^o$. Except for specialised applications (e.g. high resolution studies) the dictates of economy and convenience limit H to values of 90^o or less. Figure (5) shows the relation between y_d, E_o, and E for real image double focussing for particular values of H and y_o. The data from which these graphs were drawn was compiled by substituting given values of E_o and y_o in equations (19) and (20). The values of P and Q so obtained, together with the particular value of H, were substituted into equations (23) and (24), and the values of E and y_d necessary for double focussing were found.

2.2.1.4. THE CHOICE OF H, THE ANGLE OF DEFLECTION:

Three possibilities arise when focussing the charged particle beam from an accelerator.

(1) A substantially parallel beam ($y_o = \infty$) from the accelerator, is brought to a focus by the analyzing magnet at a finite value of y_d.

(2) The machine focussing of the accelerator is used to focus the beam in the plane of an entrance slit placed some distance y_o in front of the first magnetic field boundary. The analyzing

RELATIONS AMONG OBJECT DISTANCE (Y_o) IMAGE DISTANCE (Y_d) AND ENTRANCE AND EXIT ANGLES (E_o and E) FOR DOUBLE FOCUSSING

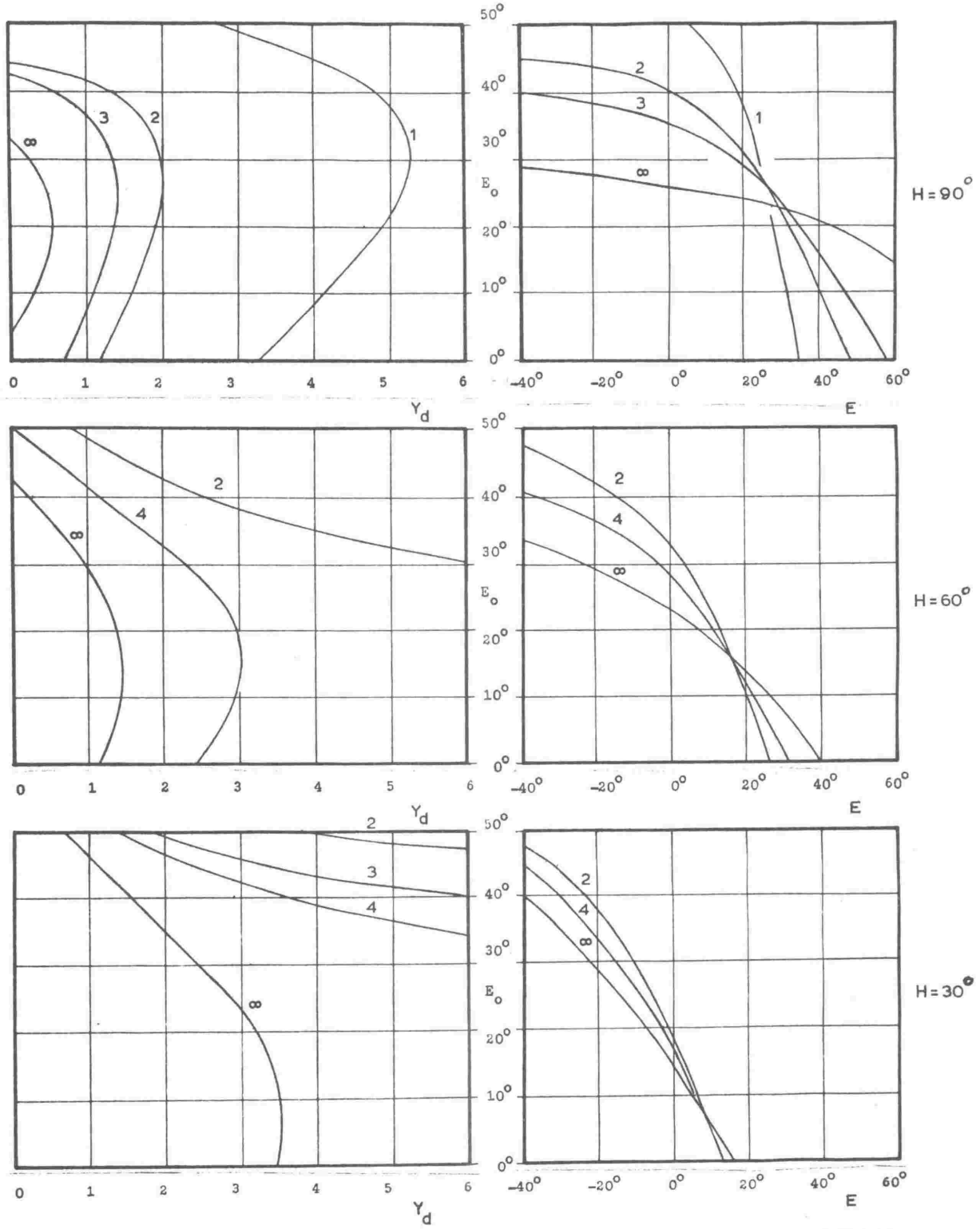

FIGURE 5

magnet is then used to form a stigmatic image of this 'object' slit at some finite distance y_d.

(3) The analyzing magnet forms a stigmatic image at infinity, of the object described above (i.e. the beam emerges parallel from the analyzing magnet).

This last possibility is not generally suitable because, in order to utilize the full energy resolution and dispersion (see, for example, section 2.2.1.5) capabilities of this arrangement, the slits from which the energy correction signal is derived must be placed at prohibitively large distances from the analyzing magnet.

The first possibility, while having several attractive features, has a serious drawback that is not immediately apparent. The cross-sectional area of a beam from an accelerator is greatest just after leaving the ion source and before the particle trajectories start to converge under the focussing action of the focus electrode[52]. If, in order to obtain a parallel beam, the effective focal length associated with this focussing action is increased, the cross sectional area of the beam at the entrance to the magnet is increased. In practice this means relatively large values of both the gap between the magnet pole faces, and of E_o must be used in order to prevent any slight deviations of the incident beam from the parallel, resulting in a loss of an appreciable part of the ion beam through collision with the magnet pole faces. For these reasons the second method is chosen in this work and a design having relatively short object and image distances is sought.

The variation of the stigmatic object and image distances, with the value of H may be found from figure (5). The following conclusions are drawn.

(1) For values of H less than 90° and relatively small values of y_o and y_d double focussing occurs mainly for large positive and negative values of E_o and E, respectively. For the smaller values of E_o and $H < 90^\circ$, y_d is a rapidly varying function of y_o. Double focussing arrangements having relatively small and nearly equal positive values of E_o

and E can be found, and many of the practical difficulties associated with acutely angled pole boundaries can be avoided by choosing $H = 90^{\circ}$.

(2) For particular values of r, y_o and y_d, the energy resolution and dispersion of the analyzing magnet (section 2.2.1.5) increase with H.

(3) If adjustable mechanical elements such as rotating inserts (see, for example, figures (12) and (13)) are provided at the points of entrance and exit of the beam to the field region, the angle the beam makes with the pole boundaries at these points, can be altered by small amounts about a mean value. In this way the values of E_o and E can be changed and the focussing conditions altered to suit the experimental requirements. For values of H much less than 90°, the range over which E_o and E must be varied in order to provide a range of appreciably different focussing configurations, is prohibitively large. In the region of H around 90° however, small variations in E_o and E can be used to effect relatively large changes in the double focussing object and image distances.

Although magnets which deviate the beam through lesser angles offer some advantages in economy and size, a magnet giving 90° deflection has been chosen for the reasons given above. The emergent beam direction following a deflection of 90°, is also the direction most suited to the physical layout of the target room.

2.2.1.5 ENERGY RESOLUTION, DISPERSION AND IMAGE MAGNIFICATION

The x displacement of the general trajectory from the mean path usually depends (equation (7), section 2.2.1.2.) on three parameters A, B, and x_o. At the image position x is independent of A (from the definition of angular focussing) and here x is a function of the two variables B and x_0, where B is the fractional difference of the particle momentum, from the mean momentum p_o.

i.e. $$B = \frac{(p - p_o)}{p_o}$$

and from Equation (7)

$$x = \frac{v\,(p - p_o)}{p_o} - wx_o \qquad \text{----------} \qquad (25)$$

i.e. $$x = F(x_o, p)$$

where x_o and p are independent. The total differential of x may therefore be written as

$$dx = \left[\frac{d}{dx_o} F(x_o,p)\right]_{p\ \text{const.}} \cdot dx_o + \left[\frac{d}{dp} F(x_o,p)\right]_{x_o\ \text{const.}} \cdot dp \qquad (26)$$

i.e. $$dx = \frac{v}{p_o} \cdot dp - w\,dx_o \qquad \text{----------} \qquad (27)$$

This equation shows the effect on x of small changes in the particle momentum, and position in the plane of the object. The total relative momentum spread $\Delta p/p_o$ in the analyzed ion beam passing through slits of width s_o and s placed in the object and image planes respectively (figure 6), can be found by integration of equation (27). The limits for this integration are from

$$x_o = -(\tfrac{1}{2} s_o) \quad \text{to} \quad +(\tfrac{1}{2} s_o)$$

$$x = -(\tfrac{1}{2} s) \quad \text{to} \quad +(\tfrac{1}{2} s)$$

and $$p = p_o - (\tfrac{1}{2}\Delta p) \quad \text{to} \quad p_o + (\tfrac{1}{2}\Delta p)$$

The integral equation is

$$\int_{-\frac{1}{2}s_o}^{+\frac{1}{2}s_o} dx = \int_{p_o - \frac{1}{2}\Delta p}^{p_o + \frac{1}{2}\Delta p} \frac{v}{p_o} \cdot dp - \int_{-\frac{1}{2}s_o}^{+\frac{1}{2}s_o} w.dx_o \qquad (28)$$

which gives

$$s = \frac{v}{p_o} \cdot \Delta p - ws_o$$

Solving for $(\Delta p/p_o)$ gives

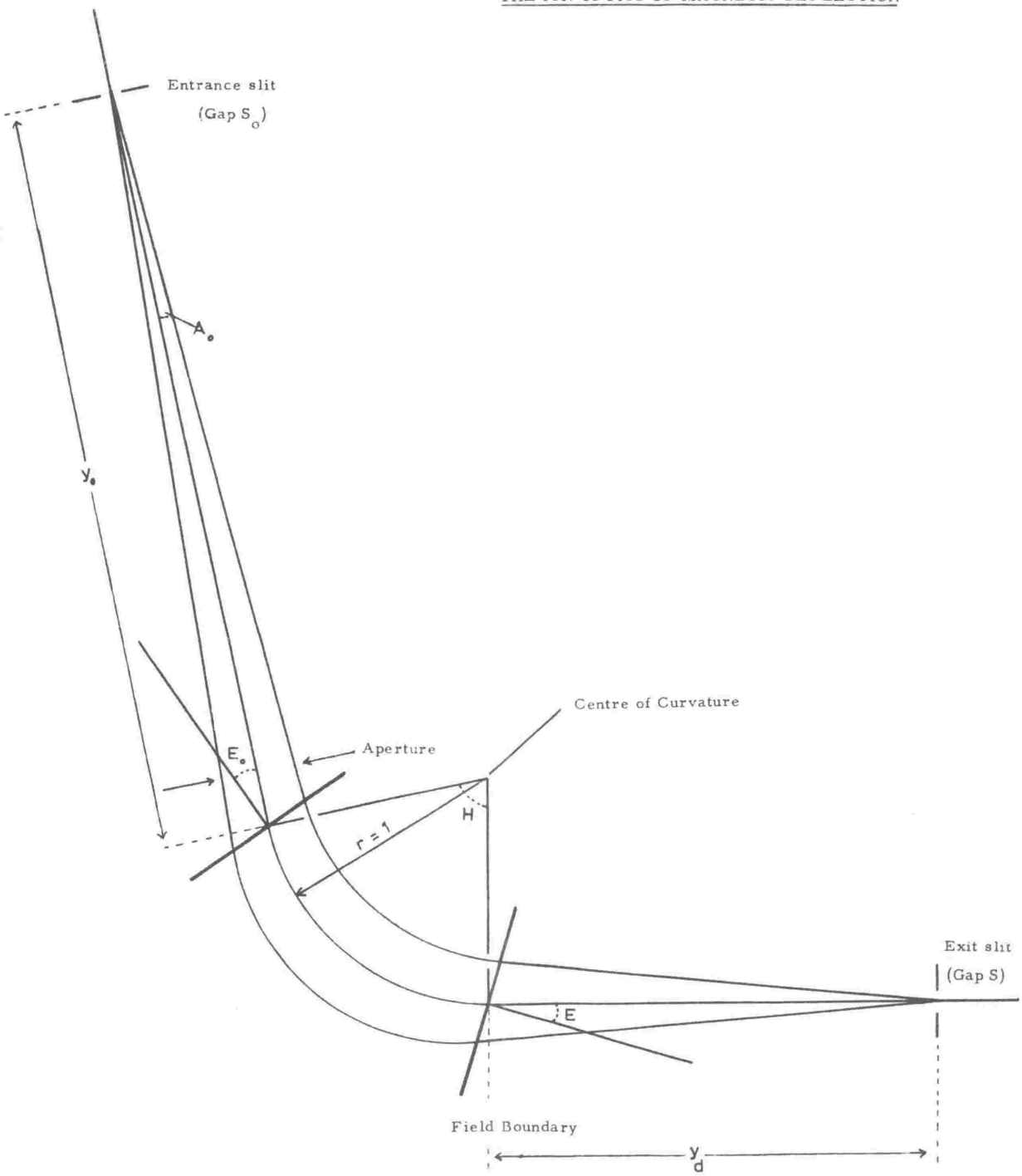
Entrance slit
(Gap S_o)
A_o
y_o
E_o
Aperture
Centre of Curvature
H
r = 1
Exit slit
(Gap S)
E
Field Boundary
y_d

FIGURE 6

$$\frac{\Delta p}{p_o} = \frac{ws_o + s}{v} = \frac{s_o}{(v/w)} + \frac{s}{v} \qquad \text{---------- (29)}$$

where s and s_o are the slit widths measured in units of the radius of curvature r of the mean path in the horizontal plane. The total fractional energy spread $\Delta W / W_o$ of the ion beam passing through the slits is obtained from the relation between energy and momentum, for a particle of mass m, viz.,

$$(p^2 / 2m) = W \qquad \text{---------- (30)}$$

from which

$$\frac{\Delta W}{W_o} = 2.\frac{\Delta p}{p_o} \qquad \text{---------- (31)}$$

Equation (29) may be written in the form

$$\frac{\Delta p}{p_o} = \frac{s_o}{D_o} + \frac{s}{D} \qquad \text{---------- (32)}$$

where D_o (= v/w) is termed the resolution factor and D (= v) is termed the dispersion of the analyzing magnet. On putting dx_o = o, in equation (27) and expressing the particle momentum in terms of the radius of curvature in median plane, it can be seen that D may be defined as the distance, measured in the image plane, between the focus for particles having the mean radius r_o and the path of a particle having a radius of $r_o + \Delta r$, divided by Δr, the difference in radii of curvature in the median plane. The dispersion therefore provides a measure of the lateral displacement of the ion beam in the image plane, caused by a fractional change in the beam energy. In applications where an energy correction signal is derived from electrodes placed in the image plane, the dispersion should be as high as practicable so as the largest possible 'error' signal is obtained.

The image magnification M can be found from equation (27) whence

$$M = \left(\frac{dx}{dx_o}\right)p \text{ constant} = w = \frac{D}{D_o} \qquad \text{---------- (33)}$$

Equation (32) then becomes

$$\frac{\Delta p}{p_o} = \frac{M s_o + s}{D} \qquad \text{----------} \qquad (34)$$

and it can be seen that increasing the width of the slit placed in the object plane by an amount s_o, has the same effect on the total momentum spread in the analyzed ion beam, as increasing the image slit width by $M s_o$.

The physical significance of the resolution factor can be found in the following way. When the momentum spread in the ion beam is zero (i.e. $\Delta p = o$), equation (27) shows that the geometrical image width is $M s_o$, and a particle of momentum p_o passing through the middle of the object slit will pass through the centre of the image. If the particle momentum is increased by an amount $\Delta p'$ so that the particle trajectory is displaced by half the geometrical image width, then from equation (27)

$$\frac{M s_o}{2} = v \frac{\Delta p'}{p_o} - \frac{M s_o}{2}$$

and $$D_o = \frac{v}{M} = \left(\frac{p_o}{\Delta p'}\right) s_o$$

The resolution factor D_o, is then, the reciprocal of the fractional momentum change required to displace the particle trajectory by half the geometrical image width in the image plane, multiplied by the source width s_o in units of r .

The dispersion, resolution factor, and image magnification can be expressed directly in terms of the geometrical parameters associated with the analyzing magnet (appendix 4, Note 3).

$$D_o = y_o (\sin H + \tan E_o (1 - \cos H)) + 1 - \cos H \qquad (35)$$

$$D = y (\sin H + \tan E (1 - \cos H)) + 1 - \cos H \qquad (36)$$

and the image magnification M is given by (D/D_o).

The only assumption made in the derivation of the above equations (appendix 4, note 3) is that the condition for angular focussing in the horizontal plane (i.e. $pq = 1$) is satisfied. The values obtained for D_o, D and M are measured in the horizontal image plane of the analyzer

and apply, not only to the case of double focussing, but to any median plane focussing in a uniform sector-magnetic field.

Both D_o and D increase with H. For particular values of S_o and S, the total energy spread in the analyzed ion beam therefore decreases for increasing values of H. This result is used in the discussion on the choice of H (section 2.2.1.4).

For the particular value of H = 90^o, equations (35) and (36) become respectively

$$D_o = y_o (1 + a_o) + 1 \qquad \text{----------} \qquad (37)$$

and $$D = y (1 + a) + 1 \qquad \text{----------} \qquad (38)$$

2.2.1.6. THE CHOICE OF THE FOCUSSING PARAMETERS:

The design of an analyzer is governed by many, often conflicting considerations and no general conclusions can be reached which are valid under all conditions and for all experimental requirements. For this reason it is considered advantageous to use adjustable semicircular blocks (see section 2.2.2.1) at the points of exit and entrance of the beam at the pole boundaries, so that E_o and E can be altered to suit a particular experiment without involving major reconstruction of the magnet. Adjustable elements also enable fine adjustments to be made to the focussing should they prove necessary. The range over which E_o and E can be varied in this way, without causing appreciable distortion of the magnetic field, is limited. The values of E_o and E corresponding to the mean position of the adjustable elements, should be the values giving the most suitable analyzer performance characteristics for general use.

The following considerations are regarded as especially important in the design of the present analyzer.

(1) If the object slit is fully illuminated by the incoming ion beam it can be shown using equation (27) that the intensity in the analysed beam is proportional to the object and image slit widths and inversely proportional to the dispersion D. For a given total allowable energy spread in the analyzed ion beam, the maximum intensity occurs when s_o and s are chosen such that $(s_o/D_o) = (s / D) = (\frac{1}{2}\Delta r)$. (This criteria follows from equation (32); Δr is measured in units of r). At this maximum $(s_o\ s/D) = \frac{1}{4} D_o (\Delta r)^2$, showing that for high intensity both D_o and r (because for a given momentum spread Δr increases with r), should be made as large as possible.

(2) The image magnification M should be unity or less in order that sufficient ion current density can be delivered onto a target placed after the image slit.

(3) An analyzer having a high dispersion D is advantageous, for then any change in the beam energy produces a large lateral displacement of the ion beam and consequently a large energy 'error' signal to operate the stabilization system.

(4) The energy spread in the analyzed ion beam should be small, and hence D_o and D large.

(5) The profile of the emergent ion beam at a point following the analyzer image slit, should not be appreciably distorted by slight departures from the correct object distance caused by incorrect focussing of the accelerator.

From equation (37) and (38) it can be seen that D_o and D increase with increasing values of y_o and y respectively. As the object distance y_o increases the double focussing image distance y_d decreases (figure 5). For most applications it is equally important, from the point of view of analyzer performance, that both D_o and D (and hence y_o and y_d) are large, and for this reason a configuration in which y_o and y_d are equal is chosen. This occurs for the double focussing parameters

$$y_o = y_d = 2$$

$$E_o = E = 26^o34' \quad (\text{i.e. } \tan E_o = \tfrac{1}{2})$$

For this configuration,

$$D_o = D = 4,$$

$$M = 1,$$

and the total energy spread in the analyzed beam is given by,

$$\frac{\Delta W}{W_o} = \frac{s_o + s}{2} \qquad \text{----------} \qquad (39)$$

where s_o and s are measured in units of r. This configuration gives the highest energy resolution (lowest fractional spread in energy) for a double focussing arrangement satisfying the above requirements.

The dependence of the emergent ion beam profile (see point (5) above) on the object distance can be deduced from figure (7). Here the vertical focussing image distance y_v, and the horizontal focussing image distance y have been plotted separately as a function of the object distance y_o. In addition to the chosen configuration ($\tan E_o = \tan E = \frac{1}{2}$), a second double focussing configuration ($\tan E_o = \frac{1}{4}$; $\tan E = 0.6$; which gives double focussing for $y_o = 1$) is shown for comparison. The difference $(y - y_v)$ provides a measure of the image distortion that will occur if y_o deviates from the double focussing value. It can be seen that, for the chosen configuration the curves, y vs y_o, and y_v vs y_o run close together over a wide range of y_o, while for the second configuration appreciable distortion of the beam profile will occur if y_o departs significantly from the double focussing value. (Braams and Smith[26] have utilized the closeness of the horizontal and vertical focussing curves given by the first configuration in an analyzer constructed without rotating elements. These workers tolerate the astigmatism produced for values of y_o differing from the double focussing value, and use a range of values of y_o and y.) A more detailed analysis confirms that the chosen configuration is the only practical double focussing configuration having this advantage.

VERTICAL (y_v) AND HORIZONTAL (y) FOCUSSING AS A FUNCTION OF THE OBJECT DISTANCE (y_o)[r]

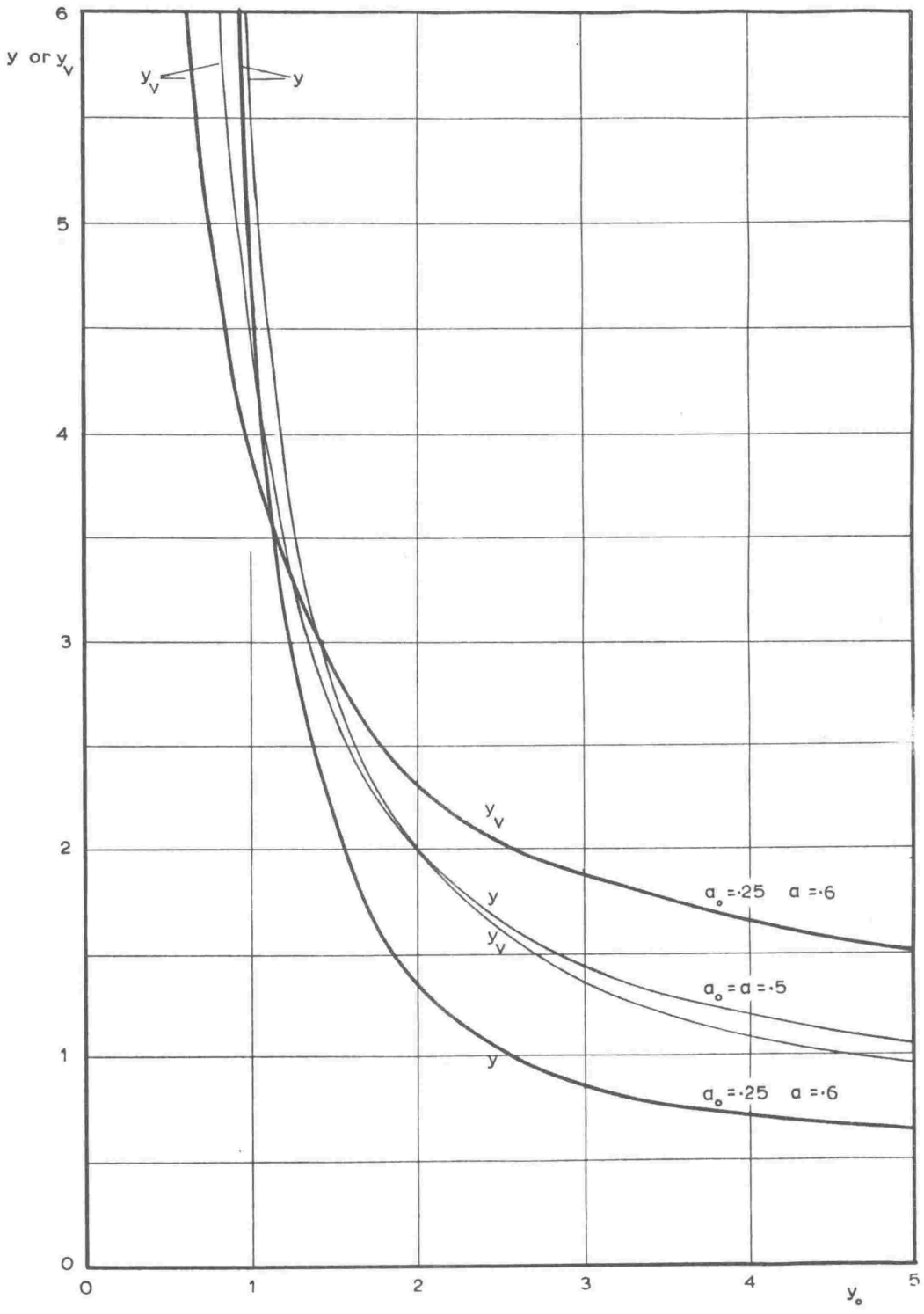

FIGURE 7

An additional attractive feature of using values of E_o and E in this range is that only small changes in E_o and E are required to give double focussing configurations (figure 5) having a markedly increased dispersion. These higher magnification focussing configurations are of special interest when an energy stabilized ion beam of low ion current density is required.

2.2.1.7. THE CHOICE OF r, THE RADIUS OF CURVATURE

A particle of mass m and charge e, accelerated through a potential difference W, has a kinetic energy given by,

$$\tfrac{1}{2} m v_o^2 = e W$$

where v_o is the particle velocity (restricted in this discussion to non-relativistic velocities). The trajectory of such a charged particle, moving in a uniform magnetic field, has a radius of curvature r, such that the centrifugal force mv_o^2/r is just balanced by the centripetal force $e(\underline{v}_o \times \underline{B})$ (equation 1, section 2.2.1.1) due to its motion in the magnetic field. For particle deflection in a uniform magnetic field of flux density B (normal to r) one obtains

$$B r = \frac{m v_o}{e} = \left(\frac{2m W}{e}\right)^{\frac{1}{2}} \qquad \text{----------} \qquad (40)$$

In this work the analyzer is required to bend a beam of ions having an energy of 500 kev, and having a charge to mass ratio of $\frac{1}{2}$ electronic charges per nucleon, (e.g. D^+ or $^4_2He^{++}$ ions). Such ions have a momentum of approximately,

$$B r = 145 \text{ kilogauss - cm.} \qquad \text{----------} \qquad (41)$$

Mechanical considerations such as economy of magnet iron and coil wire, compactness, the provision of adequate mechanical support, and ease of aligning the beam tube components, all require that r should be small. However, the intensity of the analyzed ion beam (see section 2.2.1.6), and the energy resolution capabilities of the analyzer increase for higher values of r. Furthermore as the actual object and image distances are $y_o r$ and $y_d r$ respectively, larger values

of r allow more room in which to place measuring and vacuum equipment between the image and object slit boxes and the magnet.

In this work a compromise is reached by making r only just sufficiently large to obtain the desired energy resolution with object and image slit widths of approximately 1 mm. Tentative magnet designs showed that a value of r = 200 mm was acceptable from all points of view and enabled advantage to be taken of the maximum permeability of the iron in the magnet yoke (see section 2.2.2.1). The total fractional energy spread in the analysed ion beam for this value of r is 5 parts per 1000 per mm slit width (assuming $s_o = s$).

2.2.2. THE MECHANICAL AND ELECTRICAL DESIGN OF THE ANALYZING MAGNET AND ASSOCIATED EQUIPMENT

2.2.2.1 THE ANALYZING MAGNET:

A magnetic field strength of 7,500 gauss* gives a value of 200 mm for the radius of curvature of a 500 kev D^+ ion (equation 41). There is some advantage however in being able to attain a field strength of 9,000 gauss, as this then allows 90° deflection of D_2^+ ions, over the nominal energy range of the accelerator (0 to 400 kev). The magnet specifications are, then,

(1) An angle of deflection of 90° in the horizontal plane.

(2) A radius of curvature of 200 mm in the uniform field region

(3) A distance of 40 cm between the magnetic field boundaries and the object and image slits.

(4) An angle of 26° 34' between the normals to the pole boundaries, and the ion beam direction at the point of entrance and exit to the magnetic field region, together with the provision of adjustable mechanical elements at these points to enable small changes in these angles to be made.

(5) A maximum field, in the uniform field region of 9,000 gauss (0.9 webers/metre^2), and

(6) A mechanical support that allows the heavy magnet to be positioned with sufficient accuracy to enable the calculated focussing properties to be fully realised in practice.

* Footnote Although rationalised mks units are employed in this work, the cgs[54] (or more properly emu) units of magnetic flux density (gauss) and magnetising force (oersted) are used here for consistency with the established literature on this subject.

MAGNETIC YOKE AND POLE PIECE SHAPE

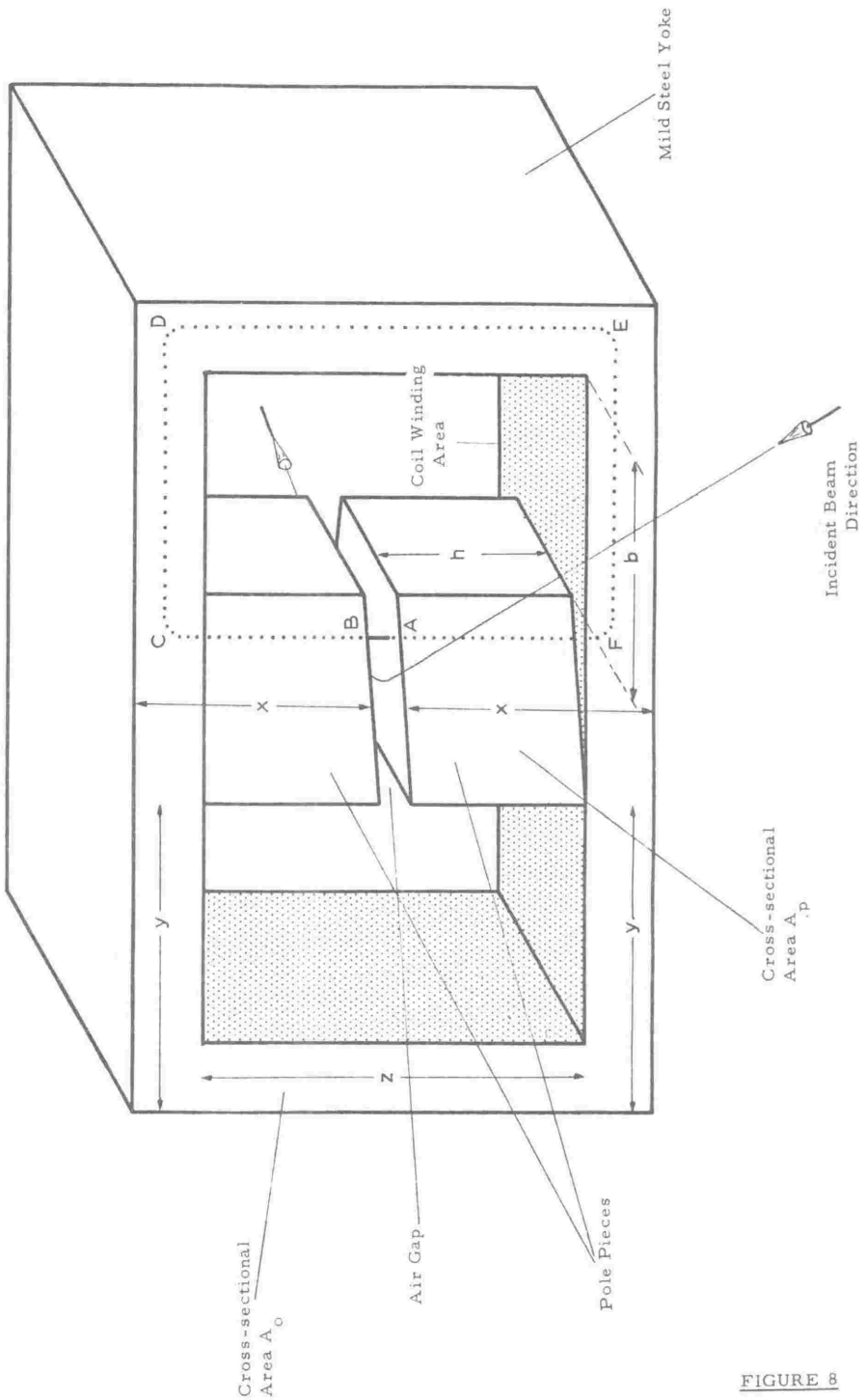

FIGURE 8

The shape of the yoke and pole pieces of the magnet are shown in figure (8). The two coils used to excite the magnetic field in the magnet pole gap, are would directly onto the magnet pole pieces. This results in considerably less magnetic flux 'leakage', than if the coils are wound onto the yoke.

In view of the unavailability of high grade magnet iron (such as Armco or Swedish iron) the magnetic properties of a locally available low carbon, bright mild steel plate, were investigated. A ballistic method, described for example by Bates[53], was used. Approximately 600 turns of cotton insulated copper wire were wound onto a toroidal steel sample having a cross-sectional area of approximately 222 mm^2. The magnetic flux induced in the sample for a given current in this primary winding, was found by using a ballistic galvanometer to measure the charge flowing in a secondary winding when the current in the primary circuit was suddenly interrupted[53]. The magnetic field intensityH, was calculated from the known primary current, and the magnetic flux density B, from the observed galvanometer deflection.

The virgin B - H curve, drawn from data found in this way, is shown in figure (9). The insert in this figure shows the dependence of the magnetic permeability of the steel, on the magnetic flux density, B. Although the high magnetic permeability and saturation flux density ($\sim$21,000 gauss) of this steel make it suitable for use in the construction of the magnet yoke and pole pieces, the high retentivity is a disadvantage.

This steel is commercially available in the form of two inch thick plate. A second advantage then, of the yoke shape shown in figure (8) over the alternative horseshoe yoke, is that it enables a sufficient cross-sectional area of steel to be obtained in the yoke without the need for facing two plates together to form a double thickness. The need for large area precision grinding is then obviated.

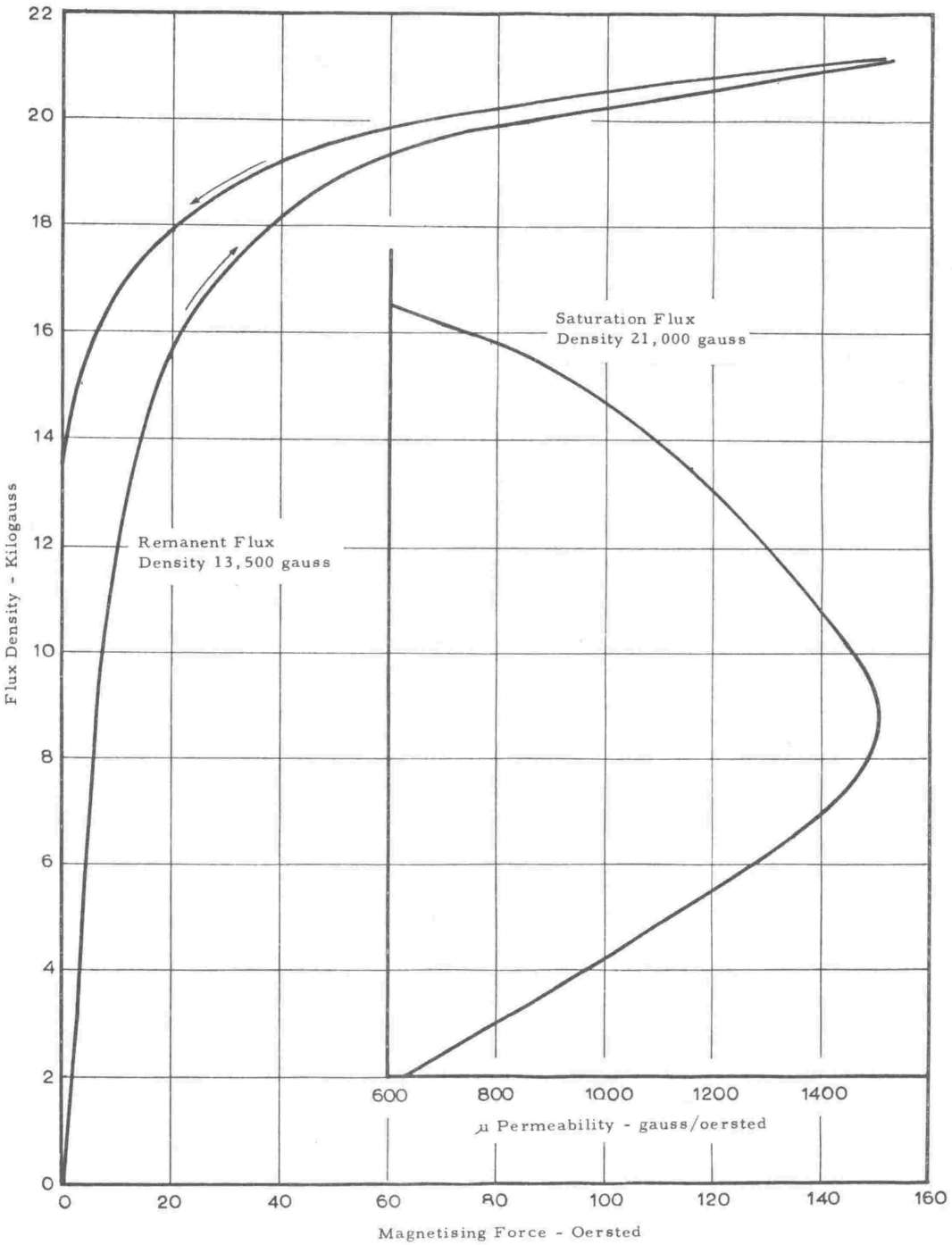
Saturation Flux
Density 21,000 gauss
Remanent Flux
Density 13,500 gauss
Flux Density - Kilogauss
Magnetising Force - Oersted
μ Permeability - gauss/oersted
0
2
4
6
8
10
12
14
16
18
20
22
0
20
40
60
80
100
120
140
160
600
800
1000
1200
1400

FIGURE 9

The number of ampere - turns required in the magnet coils in order to achieve a given flux density in the pole gap, can be calculated by regarding the closed path ABCDEFA as a magnetic circuit[54,58]. In this method complicated considerations of self-demagnetisation in the iron yoke are avoided by accounting for the magnetic 'leakage' flux through the use of empirical rules.

The analogy between a magnetic and a dc electrical circuit may be established by considering a cylindrical magnetic sample of cross-sectional area A, length l, and magnetic permeability μ. The magnetic flux density B, within such a magnetic 'conductor' is related to the magnetic field intensity H, by the equation $\underline{B} = \mu \underline{H}$. This equation has the same form as the equation linking the current density J and the electrical field strength E, within an electrical conductor of conductivity g, namely $\underline{J} = g \underline{E}$. In the dc electrical case the current is confined to the high conductivity components forming the electrical citcuit; in the magnetic case the flux is confined to the magnetic circuit provided the magnetic permeability within the circuit is high compared with that of the surrounding media. Kirchoffs law of currents at a point in an electrical circuit is based on the conservation of electrical charge. The similar law for magnetic flux ϕ, is based on the conservation of magnetic flux lines. By analogy, the following magnetic quantities may be defined.

The magnetomotive force (mmf) acting along the length of a magnetic conductor is the line integral $\int \underline{H}.\ \underline{dl}$ evaluated for a path taken along the conductor length (just as the emf is the line integral of E). The reluctance of a magnetic conductor can be written in terms of μ, l, and A by analogy with the expression giving the dc electrical resistance in terms of g, l, and A, namely

$$R_m = \frac{l}{\mu A} \qquad \text{----------} \qquad (41)$$

The magnetic flux ϕ flowing through a magnetic conductor is the magnetomotive force across the length of the conductor divided by the reluctance, (cf. Ohms Law)

Magnetic circuits can then be analyzed in a similar way to electrical circuits. Two important differences arise, however. Firstly the magnetic permeability is, in general, dependent on H, and secondly the ratio of the permeabilities in iron and air is considerably less than the ratio of the electrical conductivities in copper and air. In practice this means that the magnetic flux is not confined entirely to the iron parts of the magnetic circuit and allowances must be made for flux 'leakage' from the magnetic circuit.

The reluctance of the magnetic circuit ABCDEFA (figure 8) can be calculated using equation (41). The section of the yoke labelled CDEF is in parallel with the similar section of yoke in the other arm. The total reluctance of this parallel combination is given by

$$R \text{ (yoke)} = \tfrac{1}{2}\left(\frac{2y}{A_o \mu} + \frac{z}{A_o \mu}\right) \qquad \text{---------} \qquad (42)$$

where y, z, and A_o are shown in figure (8), and μ is the average permeability of the iron in the yoke (the value of μ depends on the magnetic flux density in the yoke and therefore differs from the value of the permeability of the iron in the magnet pole pieces.) The reluctance of the pole pieces is given approximately by

$$R_p = \frac{2x}{A_p \mu'} \qquad \text{---------} \qquad (43)$$

where μ' is the mean permeability of the iron in the pole pieces. The reluctance of the air gap is

$$R_g = \frac{d}{A_p \mu_o} \qquad \text{---------} \qquad (44)$$

where μ_o is the permeability associated with empty space. The total reluctance in the magnetic circuit is then

$$R = R(\text{yoke}) + R_p + R_g \qquad \text{---------} \qquad (45)$$

The contribution to the total reluctance, of the iron parts of the magnetic circuit, depends on the permeability of the iron and therefore on the magnetic flux density in the iron. On substituting typical values of the permeability into equations (42) - (44) it can

be seen that the total reluctance of the magnetic circuit is due, almost entirely, to the reluctance of the air gap (approximately 95%). The number of ampere-turns required to produce a field of 0.9 webers/m^2, in the magnet pole gap can therefore be calculated with sufficient accuracy for preliminary design work, if the contribution made by the pole pieces and yoke to the total magnetic reluctance, is neglected.

The magnetomotive force around the path ABCDEA is by Ampères Circuital Law equal to the number of ampere-turns in the coils. From the analogy established above, the magneto-motive force also equals the magnetic flux within the magnetic circuit, multiplied by the total reluctance of the circuit. If A_p is the area of the pole gap then the flux required to produce a field of 0.9 (wb/m^2) in the gap is 0.9 A_p (where A_p is in square metres).

To this flux must be added the magnetic flux that bypasses the air gap and any magnetic flux that has not kept to the iron circuit (for example that in the coils). These additional magnetic fluxes are proportional in the first order, to the field in the pole gap and can be allowed for empirically by multiplying the known flux in the gap by the factor k. The total flux is then 0.9 A_p k and the number of ampere-turns (NI) required is

$$NI = 0.9\ A_p.k\ x\ \frac{d}{A_p \mu_o}$$

$$= 0.9\ kd/\mu_o$$ (where μ_o is 4π x 10^{-7} henrys/metre

where k depends on the details of the geometrical configuration of the magnet, d is the gap width between the pole pieces in metres, and N is the total number of turns in the coils. The number of ampere-turns is in the first order independent of the pole face area A_p. A second order dependence does arise however due to the variation of k with the value of the ratio A_p/d.

Consideration of the trajectories of particles in the vertical plane of the magnet (2.2.1.6.), together with an assessment of the maximum likely cross-sectional area of the beam from the accelerator, indicates that the vertical aperture at the entrance to the magnetic field

should be at least 10 mm. In practice this is determined by the vertical internal dimension of the evacuated beam tube, at the point of entrance to the magnetic field. On allowing a further 5 mm for the thickness of the walls of this beam tube, and requiring 0.5 mm clearance between the beam tube and each pole face, a total magnet pole gap height d, of at least 16 mm is required and the number of ampere-turns needed is

$$NI = 11{,}450\ k \qquad (46)$$

Before the number of turns N, in the magnet coils can be calculated values must be arrived at for the magnet coil current I, and for the magnetic flux leakage factor k.

Magnet coil current:

From the point of view of coil construction it is in general easier to achieve a given number of ampere-turns by winding a small number of turns of a heavy gauge conductor, than a large number of turns of a light gauge conductor, especially if the coil former is large. Trial calculations using the empirical winding demensions given in copper wire tables[55,57], show that for a given number of ampere turns, coils containing a small number of turns of a heavy gauge wire are more compact. The difficulty of design and construction (and hence price) of highly regulated current supplies increases with the current supplied. A current of 10 amps was decided on as the best compromise between coil size on the one hand and difficulties in power supply requirements on the other.

The magnet pole piece profile:

An estimate of k may be made only when A_p (and hence the pole piece profile) is known. To ensure correct focussing in agreement with calculations, the magnetic field in the region of the path of the ion beam must be uniform. The area of the pole faces should therefore/be very much greater than the gap width squared (i.e. $A_p >> d^2$)[54]. An alternative, and more useful criteria in

practice, is that the perpendicular distance between the path of the ion beam and the edge of the pole face should be larger than the pole gap width by a ratio of at least three times[55].

A pole profile consistent with this criteria is shown in figure (10) and was obtained in the following way. The radius of curvature of the ion paths in the uniform field region is 200 mm and the angle of deflection is $\pi/2$ radians. The path of the mean particle in the uniform field region can therefore be drawn (see for example figure 3(a)). As E_o and E (and hence the inclinations of the magnetic field boundaries to the mean particle path) are known, the lines corresponding to the magnetic field boundaries can be constructed at V and W, where the arc VW subtends an angle of $\pi/2$ at the centre of curvature of the ion path.

In practice the magnetic field does not drop immediately to zero at the pole boundary but extends some distance beyond it. The integrated effect of this non-uniform fringing field on the particle trajectories, can be accounted for in the magnet design by regarding the uniform field region as dropping suddenly to zero at an 'effective' magnetic field boundary located some distance beyond the real pole boundary. It has become usual to assume that the separation between the real pole boundary and the effective magnetic boundary is one pole gap width[26,50] although theoretical curves[51] based on the assumption of pole pieces of infinite permeability, suggest that the separation may in fact be somewhat larger than this. This question is discussed further in Chapter (3). The precise value taken for the separation does not have a critical effect on the magnet design. The small lateral displacement and change in magnification of the image that result from any discrepancy between the real and design values of the separation, may be compensated for by moving the magnet through a small distance along the line bisecting the angle between the real pole boundaries, (the line a - e, in figure 10). For this reason the real pole gap boundary is simply taken for the purposes of calculation, as one pole gap width inside and parallel to, the effective magnetic field boundary.

MAGNET POLE PIECE PROFILE

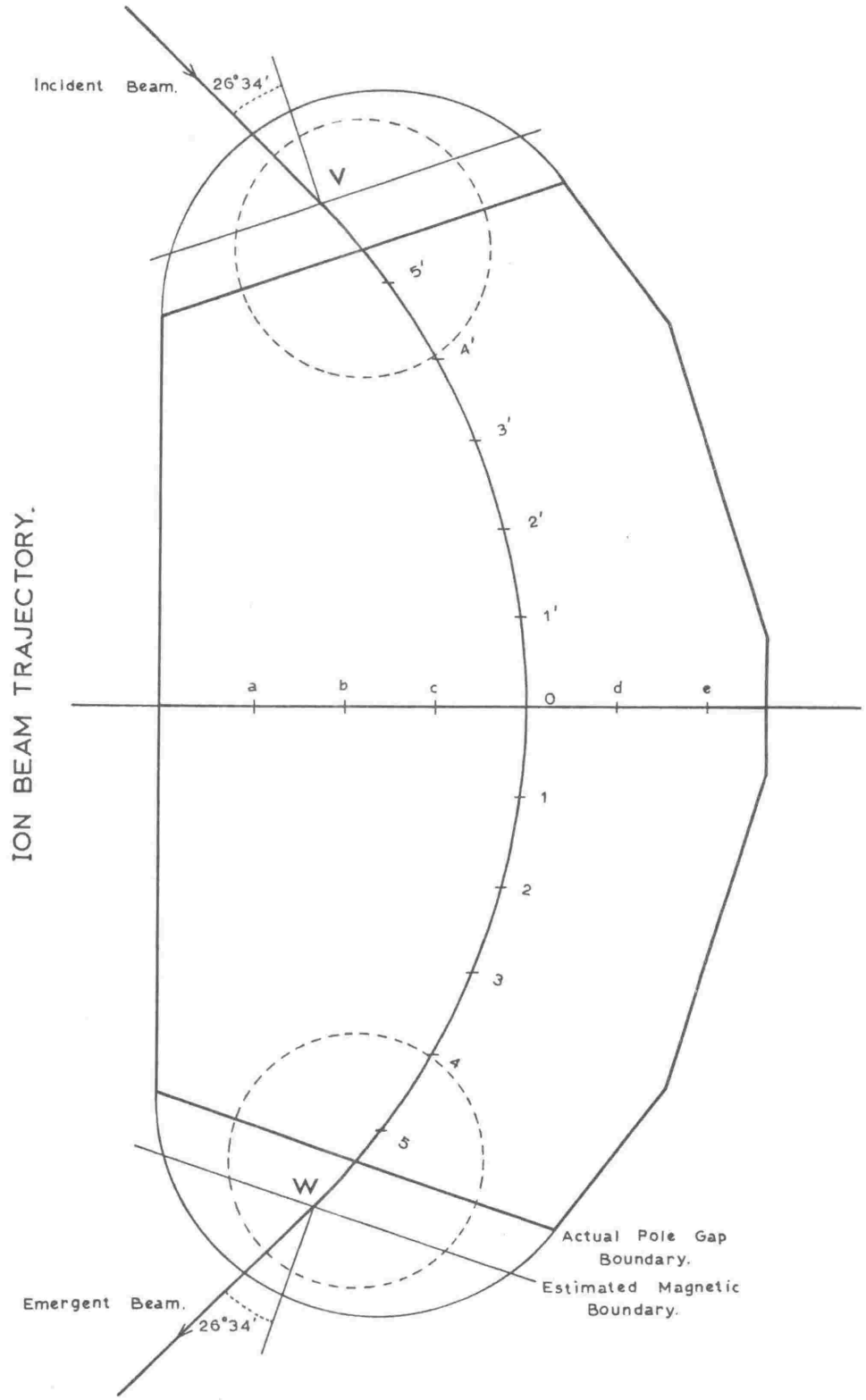

FIGURE 10

The longitudinal pole boundaries may be any convenient shape, the only requirement being that the boundary nowhere approaches closer than three gap widths to the mean path trajectory. Pole boundaries made up of straight line sections are used for ease of machining with the workshop facilities available. As the pole piece profile also determines the shape of the coil former, acute angles in the pole profile are removed by the addition of non-magnetic cylindrical sections which serve both as bushes for the rotating cylinders placed at the points of exit and entrance, and as mechanical supports for the coil formers. The resulting profile then gives a suitable shape on which to wind heavy gauge copper wire.

The value of k obtained using a value of A_p found from a scale drawing of the pole profile, and empirical formulae given by Frisch[55] and Newlands[56], is 1.35. This corresponds to a figure of 20% for the magnetic flux bypassing the pole gap and 15% for the flux lost in the coil windings. A comparison made between the observed magnetic field strength in the gap of a 4" electromagnet in this laboratory, and the field strength calculated from the known ampere-turns, indicates that the safety factor incorporated in the above leakage flux allowances is probably excessive.

The magnet coils:

On putting $k = 1.35$, $I = 10$ amps, and making allowance for the finite reluctance of the magnet iron, equation (46) shows that a total number of 1,800 turns will be required in the coils. A total coil resistance of 10 ohms or less offers some advantages, as the price of 10 amp regulated power supplies increases rapidly as the voltage required rises above 100 volts. Also, in the event of the regular magnet power supply failing, the current requirements of the magnet could be met using a 100 volt, 10 amp power supply already in this laboratory.

In practice a wide range of wire diameters and winding techniques can be used to construct a coil meeting a given set of specifications. For example the problem of Joule ($I^2 R$) heating produced in the coils can be overcome in two alternative ways.

A heavy gauge conductor having a high current rating (i.e. a low resistance per unit length) can be used. Such a conductor has, in relation to the heat produced by the current per unit length, a high thermal capacity and high heat conductivity per unit length. Heat generated with in the coils is, in this case, rapidly conducted to the large area, exterior surface of the coil and given up to the surroundings. Alternatively, a light gauge conductor of lower current rating can be used and the rate of heat loss from the interior of the coil increased by cooling the outside surface of the coil. This second method is chosen for two reasons. Firstly, for a given number of turns, smaller diameter wire is easier to wind and, secondly, the resulting coil is more compact.

In this case the coil former serves as a mechanical support on which to wind the coil, as a water cooled heat sink, and as a thermal shield placed between the coils and the magnet yoke and pole pieces. This latter function is important from the point of view of the stability of the magnetic field in the pole gap (see for example section 2.2.2.2.).

The coil winding window (of cross-sectional area bh) shown in figure 8 must be large enough to contain both the coil and the coil former. The coil formers, shown in figure 11, are made of 1/8 inch copper plate folded into a U section. Partially flattened 1/4 inch copper pipes, soft soldered to the outside faces provide water cooling of the whole former. The sides of the coil former and cooling tubes occupy 3/4 of an inch of the available winding window height h. It is convenient to make the pole pieces from two thicknesses of 2 inch steel plate. The dimension h is then 4 inches and the interior width of the coil former $3\frac{1}{4}$ inches.

For a coil wound in this way, the heat produced in the coil windings ($\sim$1 kilowatt) at the maximum current of 10 amps is estimated to cause a maximum temperature rise in the coil interior of not more than 100°C. (see for example ref. 55 and 57). The coefficient of increase of resistance with temperature for copper is 0.0028 and hence the resistance of the coils at room temperature ($\sim 16^{\circ}$C) should not

exceed 7.8 ohms, if the coil resistance at the maximum current is not to exceed 10 ohms. A trial and correction method of calculation using coil winding data given in ref. 57 indicates that the smallest diameter wire that can be used without exceeding 7.8 ohms total resistance, is 12 gauge, (British S.W.G number) double cotton covered copper conductor.

This wire can be wound at 80 turns per square inch of coil cross-section. A coil of 900 turns will then have a total cross section of 11.25 square inches and the depth of a coil of width 3.25 inches will be 3.46 inches. The average turn is a distance of 1.855 inches (this figure includes the thickness of the coil former plus half the winding depth of the coil) out from the pole piece. A scale drawing based on the pole profile of figure (10) gives the length of the mean turn as 3.835 feet. A total of 1800 turns of 12 gauge wire (1.018 ohms per 1000 feet) would therefore have a total resistance of 7.05 ohms.

The distance between the pole pieces and the yoke of the magnet (the distance b in figure (8)) has been made slightly greater than that necessary to just accommodate the coil and coil former. This will allow the current carrying capabilities of the coils to be increased to about 16 amps (should this prove necessary in some future application) by simply inserting 0.1 mm shim copper foil between successive layers of the windings (see figure 11).

The magnet yoke and pole pieces:

The constructional details of the final magnet design are shown in figures (11) and (12). For the sake of clarity only the main features and important dimensions are shown. (The brass spacers shown in the magnet pole gap are to prevent any flexing movements of the magnet yoke under the magnetic force of attraction between the magnet pole pieces).

Figures (10), (12) and (13) show details of the rotating pole sections located at the points of entrance and exit of the ion beam to the pole gap. These cylinders, made of half steel and

MAGNET SECTION
(Schematic Assembly Diagram.)

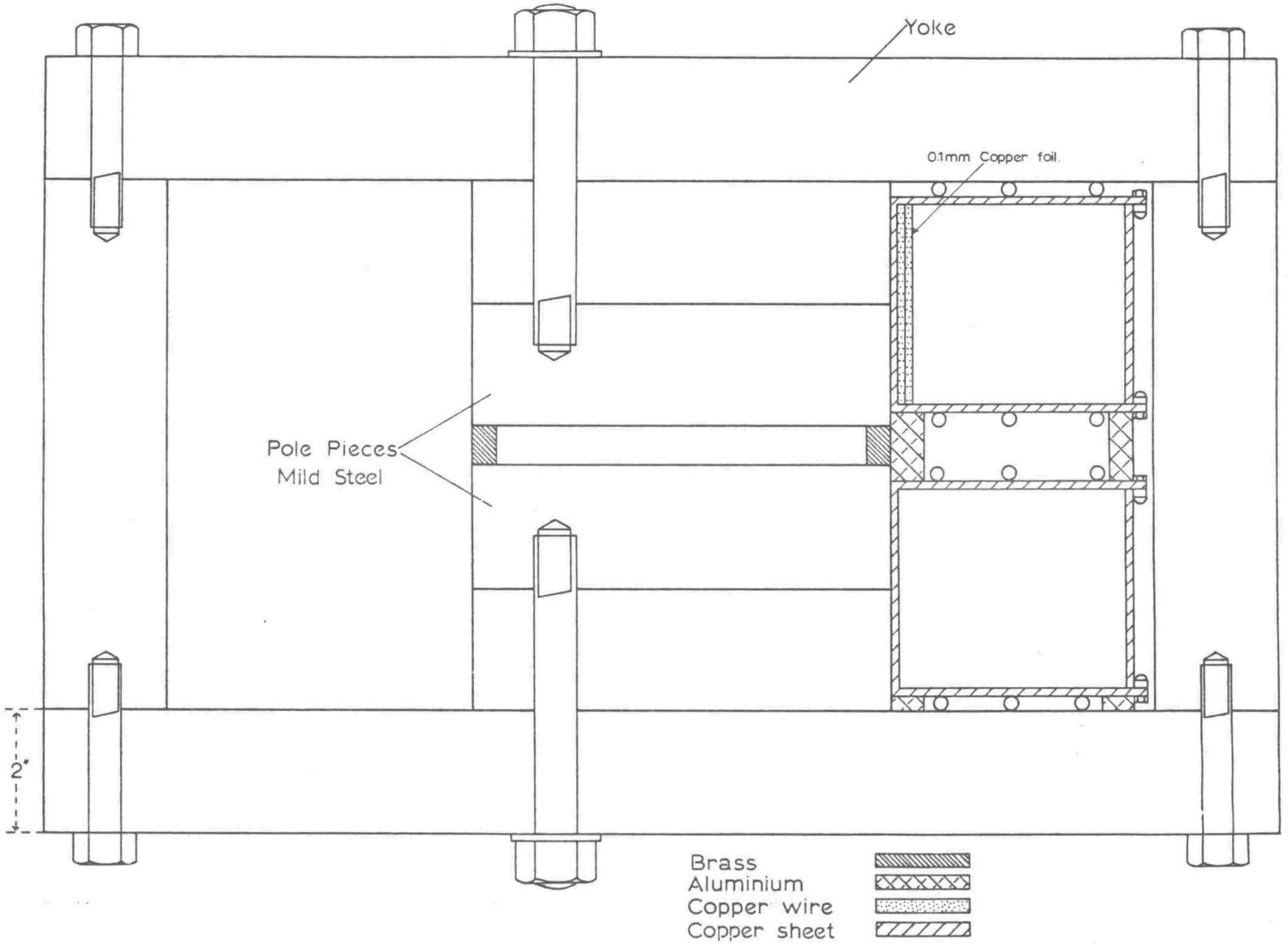

FIGURE 11

PLAN: MAGNET POLE PIECES.

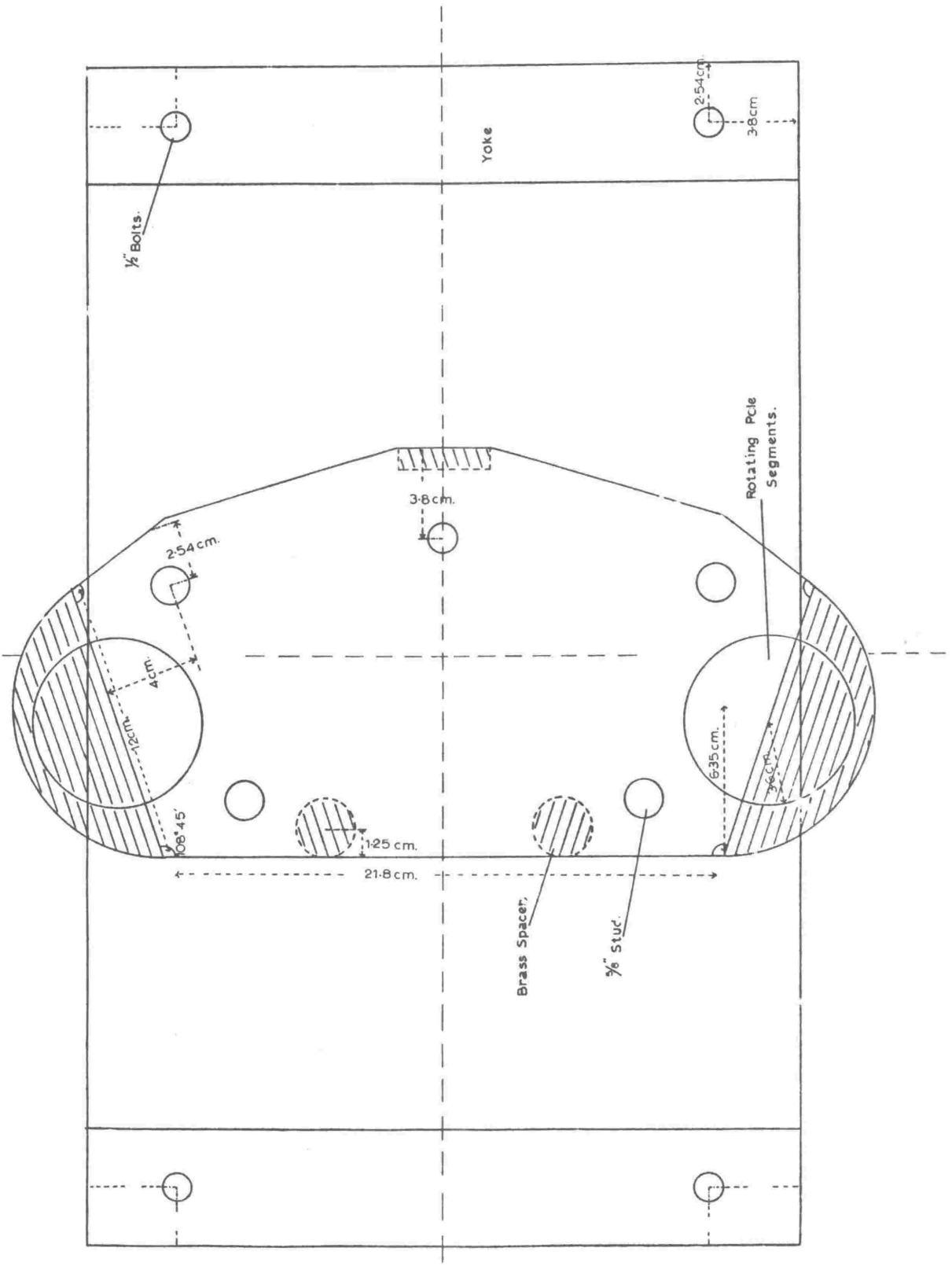

FIGURE 12

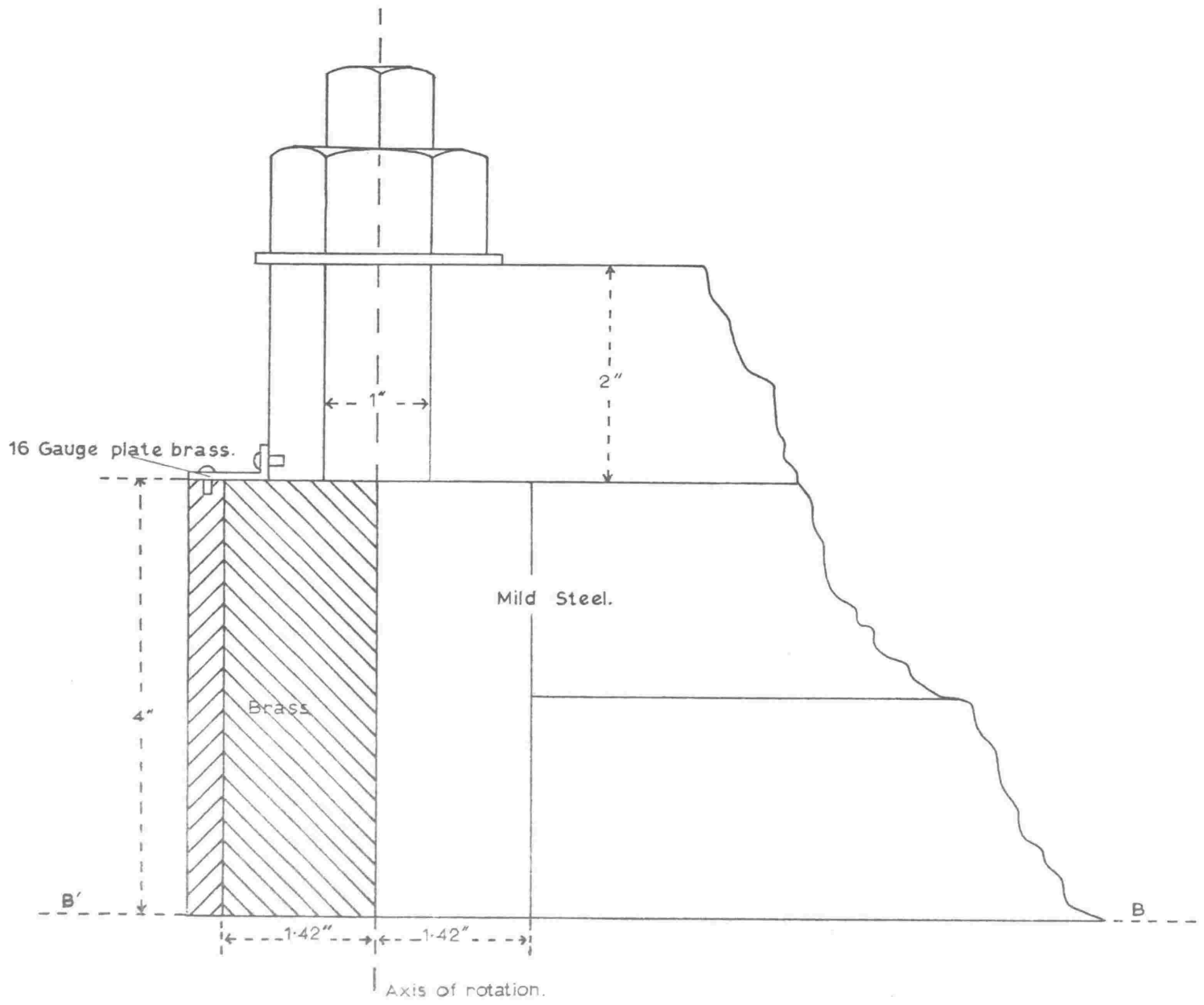

Section Through B'B (see top view).

FIGURE 13

half brass figure (13), are machined as a close fit in cylindrical holes in the pole pieces, and can be rotated by means of the steel shaft passing up through the magnet yoke. The angles (E_o and E) at which the rotating pole sections are set can be directly read on scales mounted on the outer surfaces of the magnet yoke. A setting of 26° 34' corresponds to the steel-brass interface of the rotating cylinders lying along the pole boundary (the position shown in figure 12) with the brass section facing outermost. This is the setting usually used.

The flux density in the yoke is equal to the total flux in the magnetic circuit divided by the cross-sectional area of the yoke (308 cm^2). For the highest normal flux density in the magnet gap (7,500 gauss), the flux density in the pole pieces (A_p = 413 cm^2) will therefore be 10,100 gauss and the flux density in the yoke, 13,500 gauss. The permeability of the iron at these flux densities is from figure (9), 1450 gauss/oersted and 1150 gauss/oersted respectively. Equations (43), (44) and (45) show that the iron parts of the magnetic circuit contribute only 5.2% to the total magnetic reluctance of the circuit for the highest field normally required in the gap. The maximum permeability (least reluctance) of the magnet iron is thus utilized when most needed; in attaining the highest flux densities in the gap.

The percentage contribution of the magnet iron to the total magnetic reluctance, increases as the flux density in the gap (and hence the permeability of the magnet iron) decreases. This causes a slight deviation from a linear relation between the flux density in the gap and the exciting current through the magnet coils.

The magnet support:

Figures (14) and (15) show the main features of the mechanical support for the 850 lb. wt. magnet. This support enables translational movement of the magnet in two horizontal directions at right angles, together with a rotational movement about a vertical axis. Adjustment of the four screwjacks at the

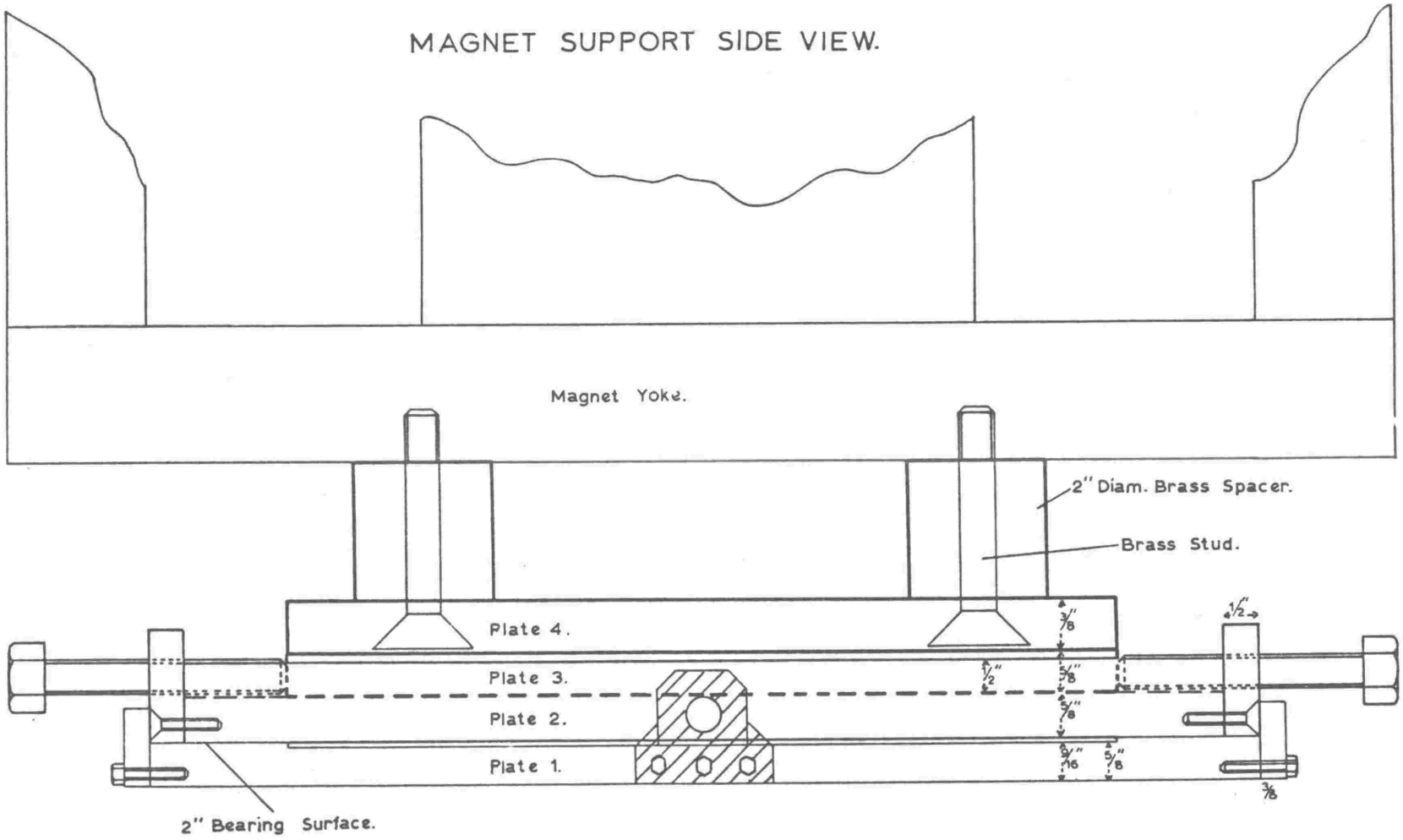
MAGNET SUPPORT SIDE VIEW.
Magnet Yoke.
2" Diam. Brass Spacer.
Brass Stud.
Plate 4.
Plate 3.
Plate 2.
Plate 1.
2" Bearing Surface.
3/8
1/2"
5/8
1/2"
5/8
9/16
5/8
1/2"
3/8

FIGURE 14

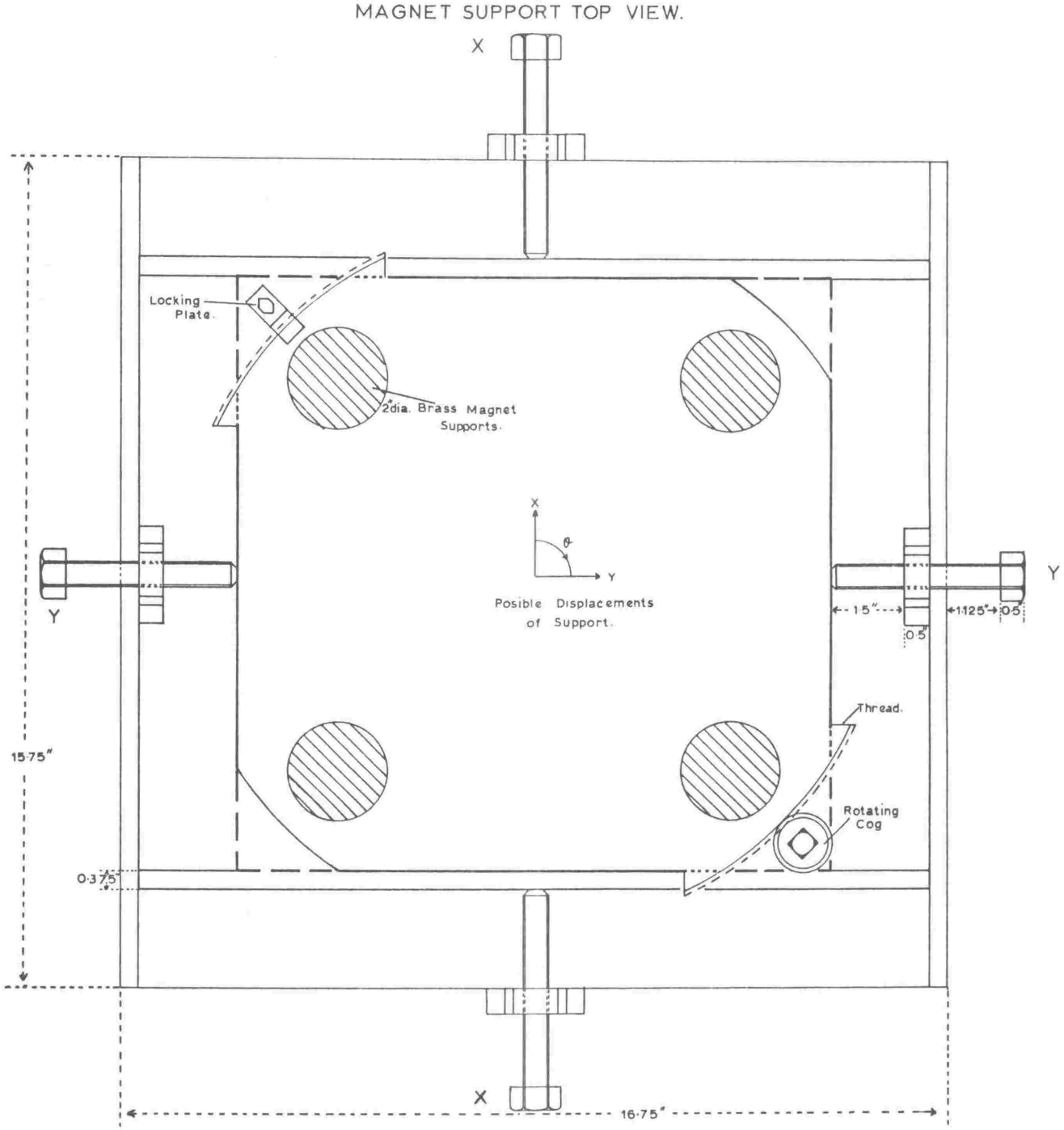
MAGNET SUPPORT TOP VIEW.
X
Locking Plate.
2dia. Brass Magnet Supports.
X
θ
Y
Posible Displacements of Support.
Y
Y
1·5"
1·125"
0·5"
0·5
Thread.
Rotating Cog
15·75"
0·375
X
16·75"

FIGURE 15

four corners of the stand on which the magnet support sits (see plate 1) allows translational movement of the magnet in the vertical direction and some rotational adjustment about the two remaining horizontal axes.

The sliding interfaces between the plates of the magnet support are precision machined and are provided with machined oil grooves along the two inch wide bearing surfaces at each edge of the plates. Oil can be forced under pressure into these grooves through oil nipples mounted on the upper side of each plate.

Horizontal translational movements of the magnet, as small as one thousandth of an inch, can be made while rotational adjustments of a few minutes of arc are possible. Rotations of the magnet of up to 360° are possible about a vertical axis. (For the sake of clarity the full 360° of thread on the rotational plate is not shown in figure 15). This allows the magnet support stand to be conveniently oriented with respect to the magnet.

2.2.2.2. FACTORS AFFECTING THE STABILITY OF THE MAGNETIC FIELD

Any instability in the current supplied to the magnet results in an instability in the energy of the particle beam passing through the magnetic analyzer. Differentiation of equation (40) shows that the fractional change in the selected particle energy is twice the fractional change in the magnetic flux density in the magnet gap. The magnetic flux density in the magnet gap bears an almost (2.2.2.1) linear relation to the current in the exciting coils. To achieve an energy stability of 1 part in 10^3, the magnet power supply must therefore have a current stability of better than 5 parts in 10^4.

A fully transistorised, commercially available* current supply meeting this requirement has been purchased using monetary assistance from the New Zealand University Grants Committee.

The stability in the range

* Alpha Scientific Supplies inc., Berkeley, California
Model Al 100 - 10A.

THE MAGNET AND SUPPORT

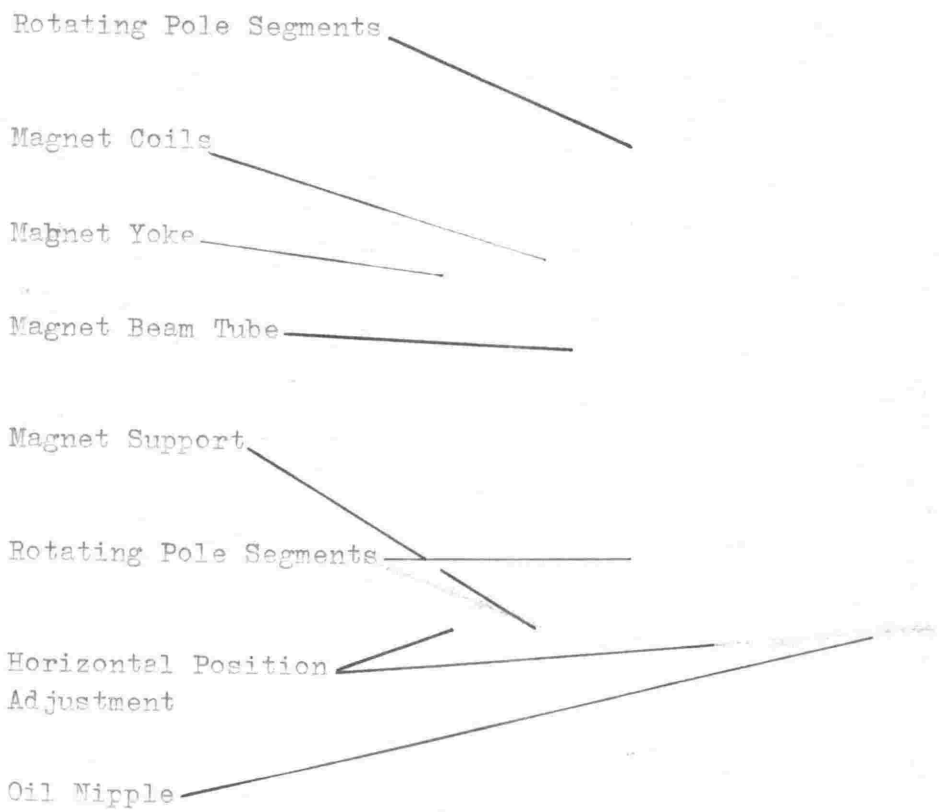

Magnet Support and Stand

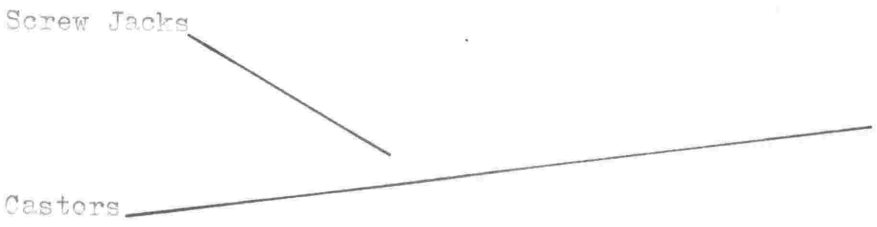

PLATE 1

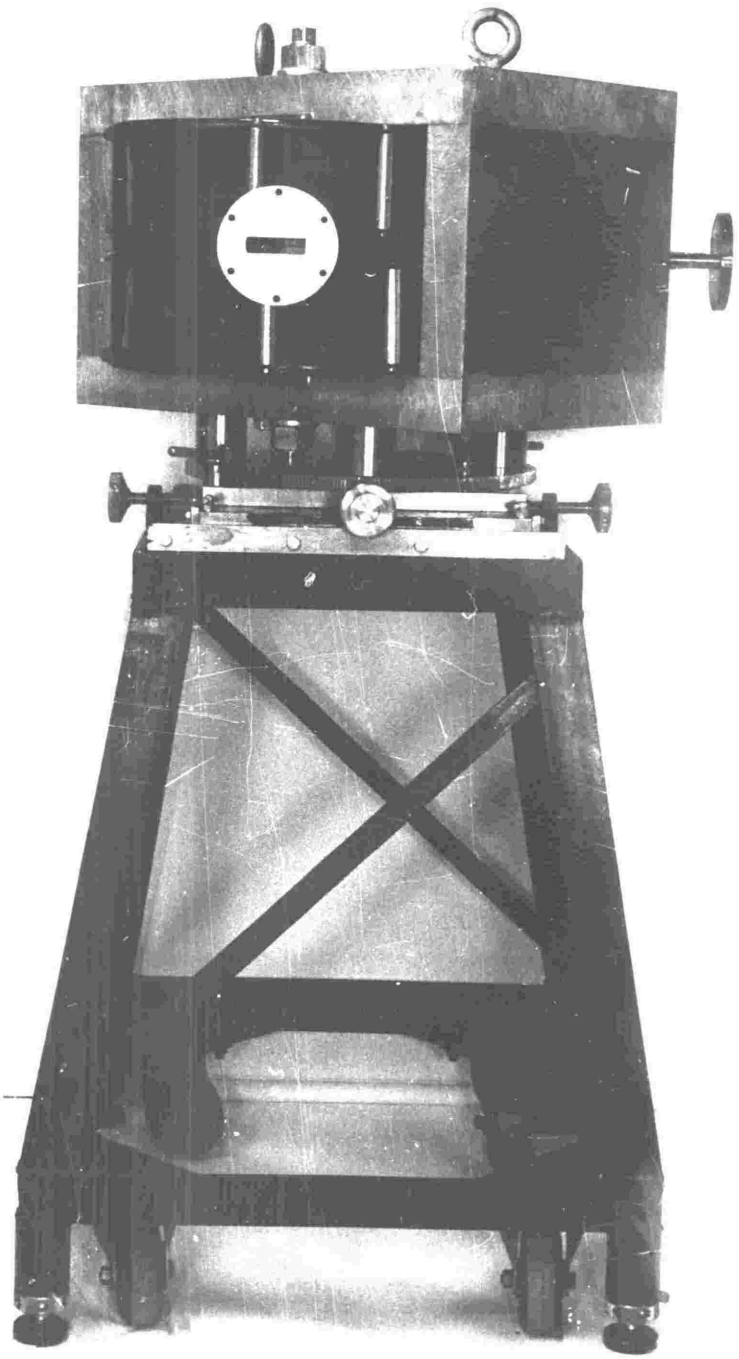

2 to 8 amps. is nominally 1 part in 10^5 and better than 1 part in 10^4 over the entire current range (continuously variable from 0 to 10 amps in the current mode, and from 0 to 100 volts in the voltage mode) for 10% changes in either load resistance or mains supply voltage. To achieve the quoted stabilities at currents above 8 amps it is necessary to allow the coils to warm up for a short time so that subsequent changes in coil resistance caused by increasing coil temperature do not exceed 10%.

Any change in the temperature of the magnet steel results in a change of approximately 10 gauss per oersted per degree centigrade in the magnetic permeability of the magnet steel.[58] The resulting change in the reluctance of the magnetic circuit can be calculated using equations (43) (44) and (45). This calculation shows that the magnetic field strength in the pole gap increases by approximately 3 parts in 10^4 per degree centigrade rise in the temperature of the magnet steel. (Calculated for a magnetic flux density of 7,500 gauss in the magnet pole gap). In order to achieve the required energy stability of the analyzed ion beam, the temperature of the magnet yoke should be kept constant to within $\pm$ 1°C.

2.2.2.3 APPARATUS ASSOCIATED WITH THE MAGNET:

The dimensions, and position of the magnet beam tube and object slit box relative to the magnet pole pieces are shown in figure (16). The image and object slit boxes are symmetrically placed with respect to the vertical plane of symmetry of the magnet. The main constructional features of the image and object slit boxes are shown in figure (17).

The magnet beam tube:

The beam tube, in addition to a 90° part, has an undeviated (or "straight through") position (see plate 2) for high beam current experiments. In order to centralise the primary ion beam from the accelerator on the 'straight through' part, it is first necessary to remove the remanent magnetization of the magnet iron. The method used to demagnetise the magnet yoke is described in section 3.1.3.

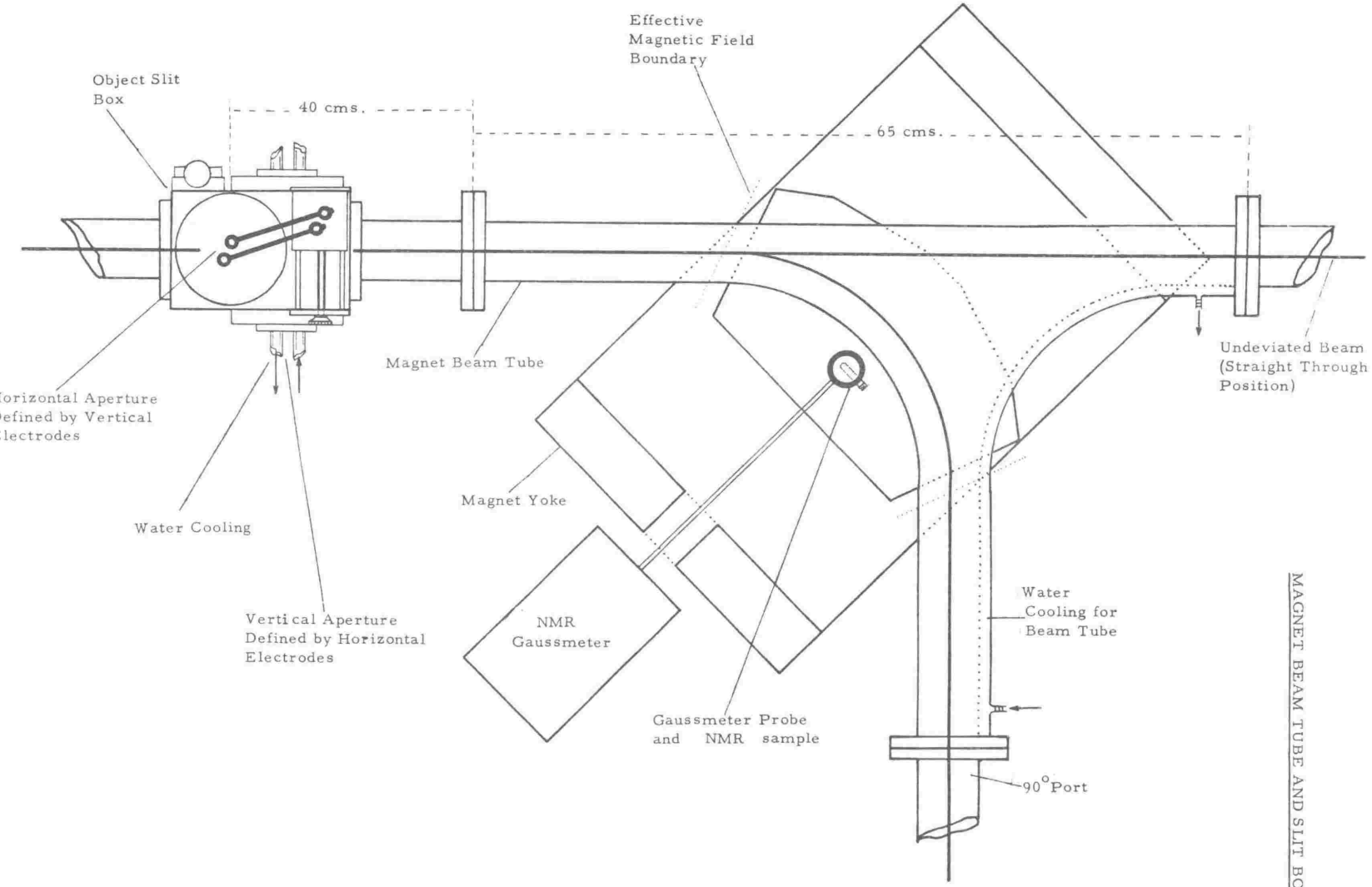

FIGURE 16

MAGNET BEAM TUBE AND SLIT BOX

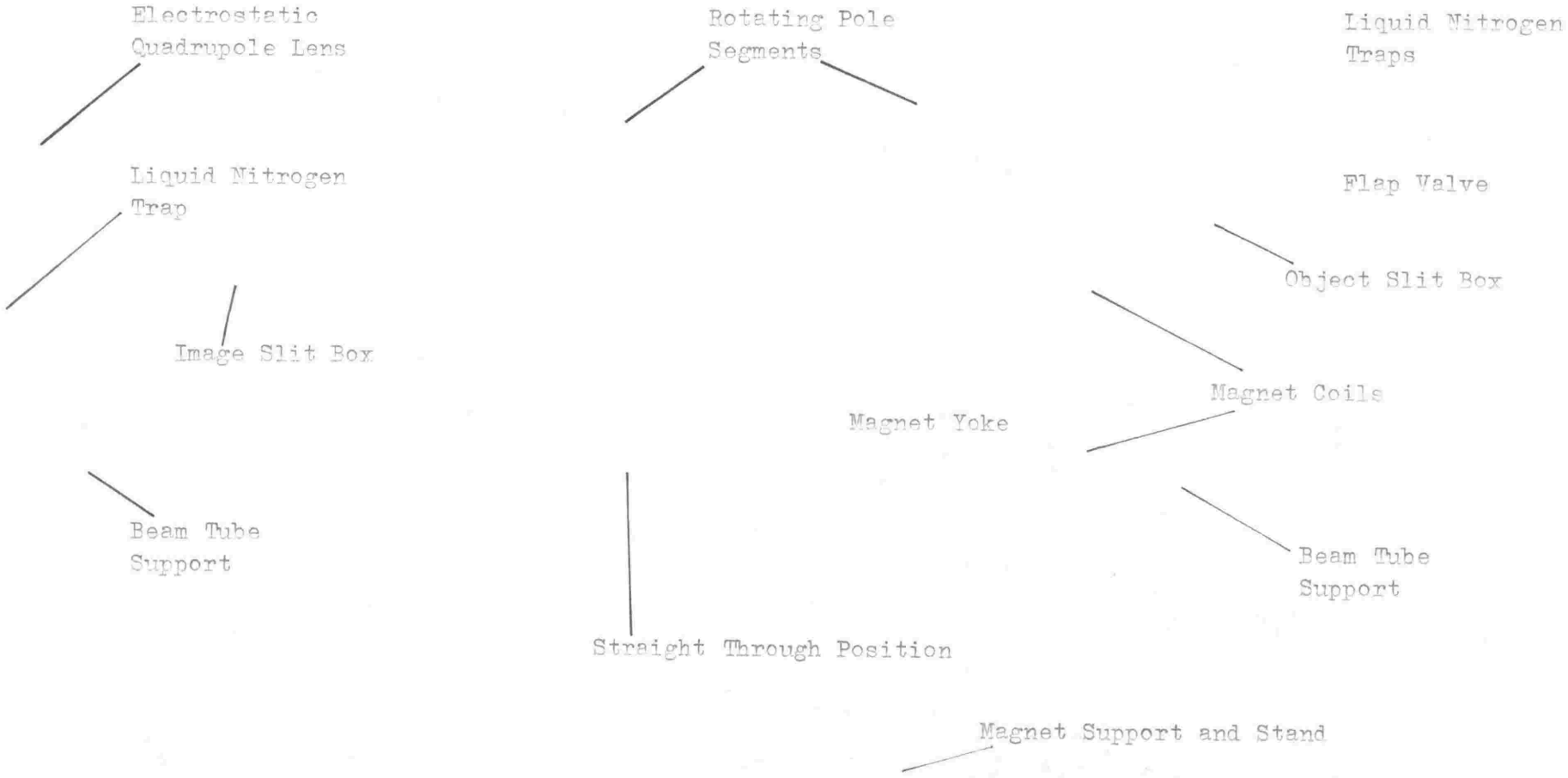

PLATE 2 BEAM TUBE COMPONENTS

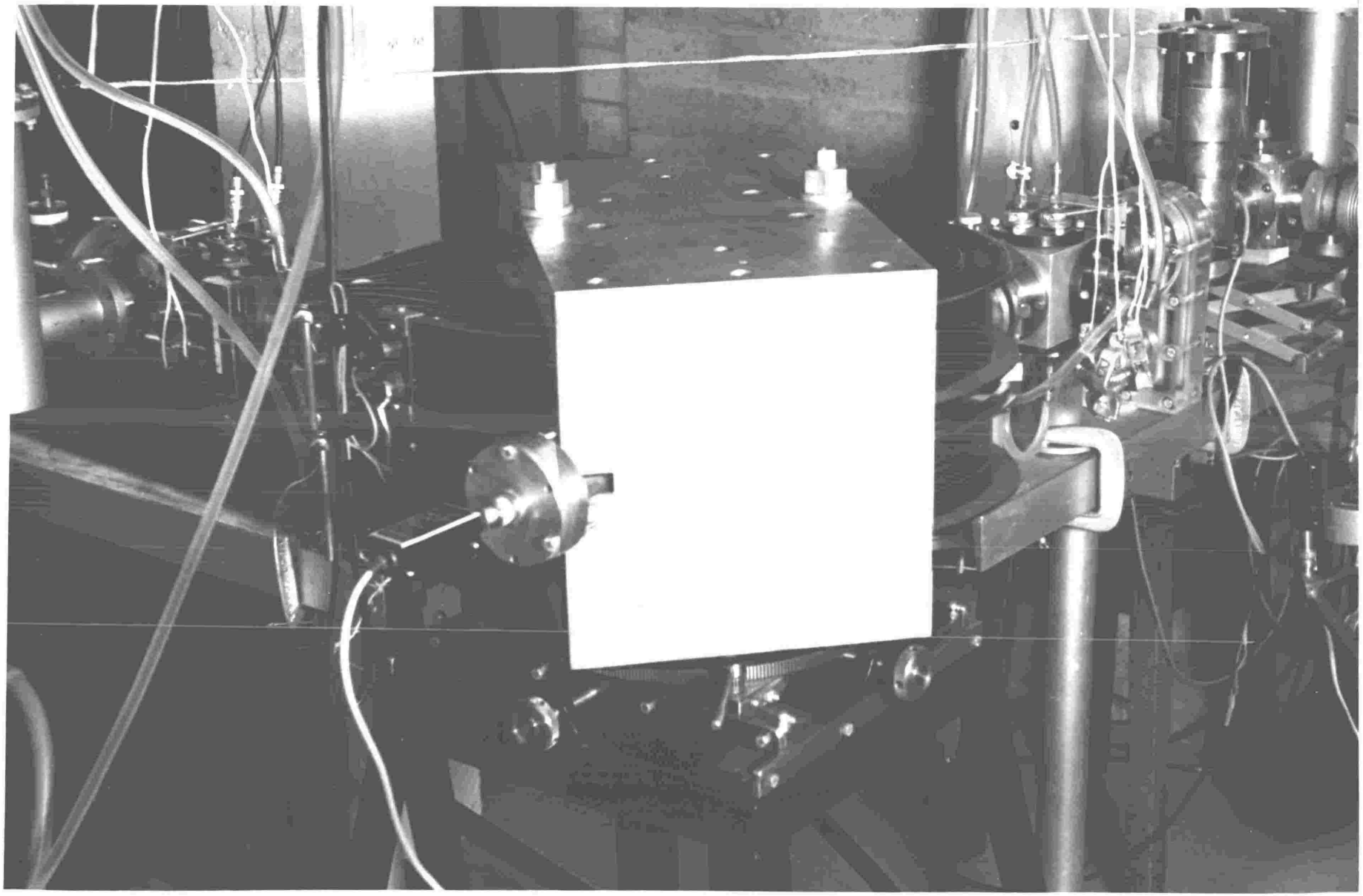

The beam tube is constructed from folded 3/32 inch copper plate and is electrically insulated from the magnet pole pieces, by a 15/1000 inch coating of air dry varnish. This enables the ion current striking the magnet beam tube to be measured. The internal dimensions have been made as large as practicable so that the conductance of the beam tube for gas flow at low pressures is as high as possible. The conductance of the magnet beam tube for gas pressures less than about one micron (i.e. the molecular flow region of gas pressures) is equivalent to approximately 6 feet of the 5 cm. internal diameter cylindrical tubing used in the construction of the rest of the accelerator beam tube. Heating effects (and the consequent vacuum deterioration caused by the beam tube outgassing) have been reduced by water cooling the region of the beam tube struck by the heavier mass components in the ion beam. The beam tube has been curved to allow the magnetic field measuring probe access to the uniform field region of the polegap.

The slit boxes:

The object and image slit boxes are identical. The horizontal slit width (i.e. the width of the aperature in the horizontal plane measured at right angles to the beam direction) is defined by the distance between two cylinders (figure 17). The vertical axis of the shaft supporting the cylinder is parallel to, but laterally displaced from the axis of the cylinder. A rotation of this shaft results in a horizontal displacement of the eccentric cylinder. This provides a convenient method of transmitting a translational displacement through an O - ring vacuum seal[26].

The lateral movement of the carriage is transformed under the action of radial arms (shown in figure 17) into a rotational motion of the cylinder bearing shafts. This method of rotating the shafts ensures that the slit opens symmetrically about a centre line and enables the slit opening to be measured accurately in terms of the almost linearly related distance travelled by the carriage. The total travel of the carriage (5 cm) results in a lateral displacement of 5 mm of each cylinder from the centre line

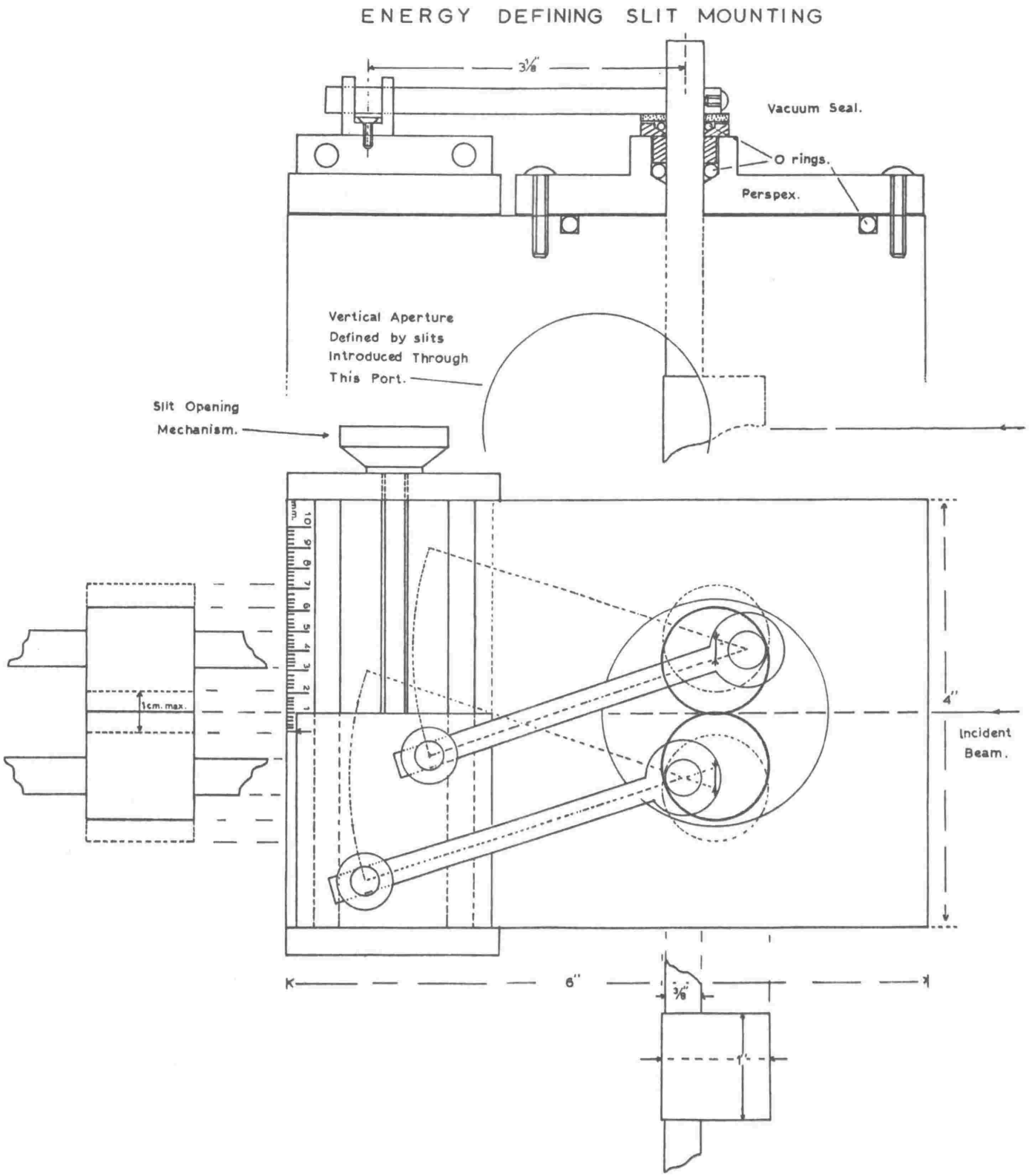
ENERGY DEFINING SLIT MOUNTING
3⅛"
Vacuum Seal.
O rings.
Perspex.
Vertical Aperture
Defined by slits
Introduced Through
This Port.
Slit Opening
Mechanism.
1cm. max.
4"
Incident
Beam.
6"
⅜"

FIGURE 17

and a maximum horizontal aperture of 1 cm. The accuracy with which the travel of the carriage can be read is better than $\pm$ 1 mm and hence the slit width can be determined to an accuracy of $\pm$ 0.02 mm.

The object slit system must be capable of dissipating the heat produced by the ion beam striking the slit defining cylinders (approximately 100 watts maximum). This is ensured by cooling the inside surface of the eccentric cylinders with water (or compressed air in the case of the image slits) flowing down through the inside of the rotating shafts. The eccentric cylinders and rotating shafts are made from heavy gauge copper tubing to ensure adequate heat conduction from the exterior to interior surfaces. Each pair of eccentric cylinders are electrically insulated both from the body of the slit box and from each other by the use of perspex mounting flanges. This enables ion current striking each individual slit to be measured.

The vacuum seals onto the rotating shafts have proved satisfactory without the need for the upper O -ring. The other vacuum seals do not involve moving parts and employ conventional rectangular O-ring grooves and rubber O-rings.

The horizontal cylinders defining the vertical aperture of the slit box, are located to one side of the port containing the vertical cylinders (see plate 3). This arrangement gives a high conductance for low pressure gas flow through the slit box at the expense of a slight deviation from the correct vertical focussing object distance. The image astigmatism resulting from this cause can be seen to be negligible from figure (7).

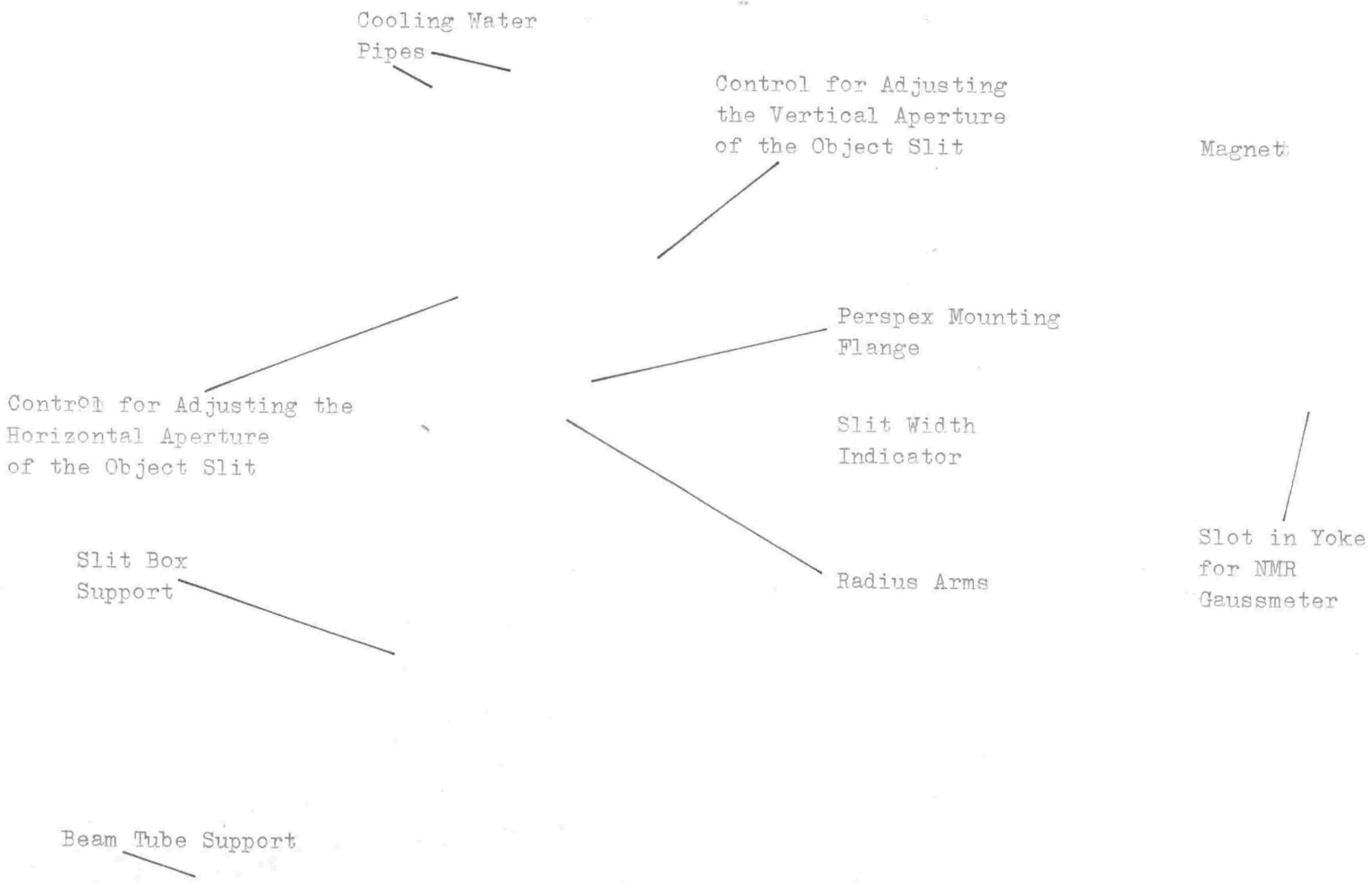

PLATE 3 OBJECT SLIT BOX

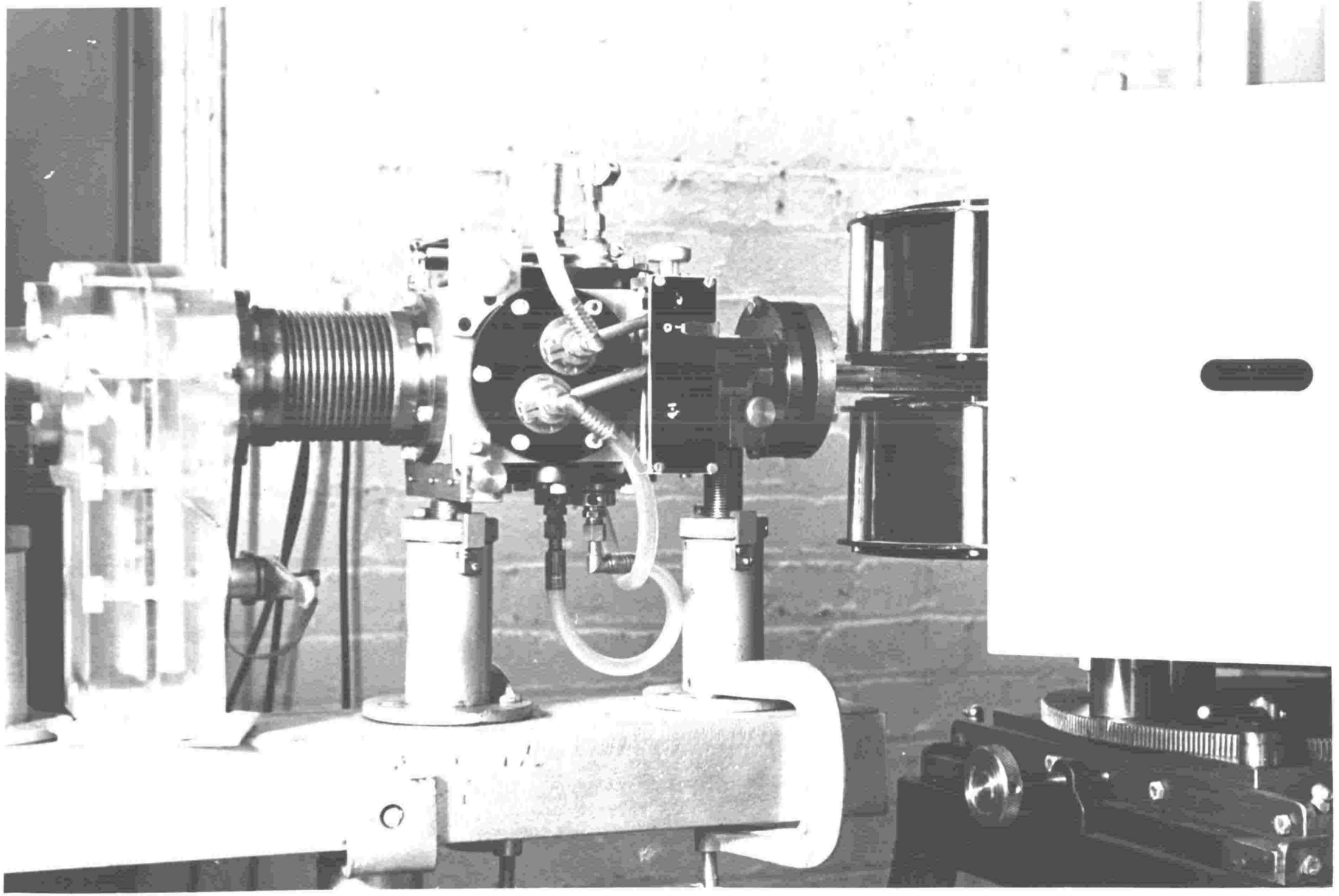

2.3. THE STABILIZING SYSTEM

2.3.1. I N T R O D U C T I O N

2.3.1.1. GENERAL:

Rapid fluctuations in the potential of the high voltage terminal of the Van de Graaff generator arise through inhomogeneities in the surface properties of the charging belt and local corona discharges* around the terminal and down the column. The magnitude of the charge removed from the terminal by these effects is however, small, and the resulting voltage changes are typically less than 0.1% of the high voltage terminal potential[22]. Relatively slow changes of much larger magnitude (of up to 10% of the terminal potential) occur as the result of slow drifts in the charging conditions of the belt, and as the result of the integrated effect of the rapid fluctuations mentioned above. Adjustments made to the accelerator gas and beam controls also result in slow, large amplitude changes in potential. It is the purpose of the stabilization system to reduce changes in the terminal potential resulting from these causes.

Figure (18) is a schematic diagram of the energy stabilization system. The energy error voltage derived from the high and low energy electrodes defining the image slit, is amplified in a d c differential amplifier (the stabilizing amplifier) and applied as a correction voltage between the grid and cathode of the corona triode in series with the corona points. The following sections describe the details of the stabilization mechanism, and for continuity of presentation, the constructional details and performance of the main components forming the stabilization feedback loop. It has also been found convenient to include at this point

* Electrons accelerated back up the accelerator tube give rise to copious X-ray production on striking the terminal hardware. These X-rays can initiate small local corona discharges by ionization of the insulating gas surrounding the high voltage terminal.[18]

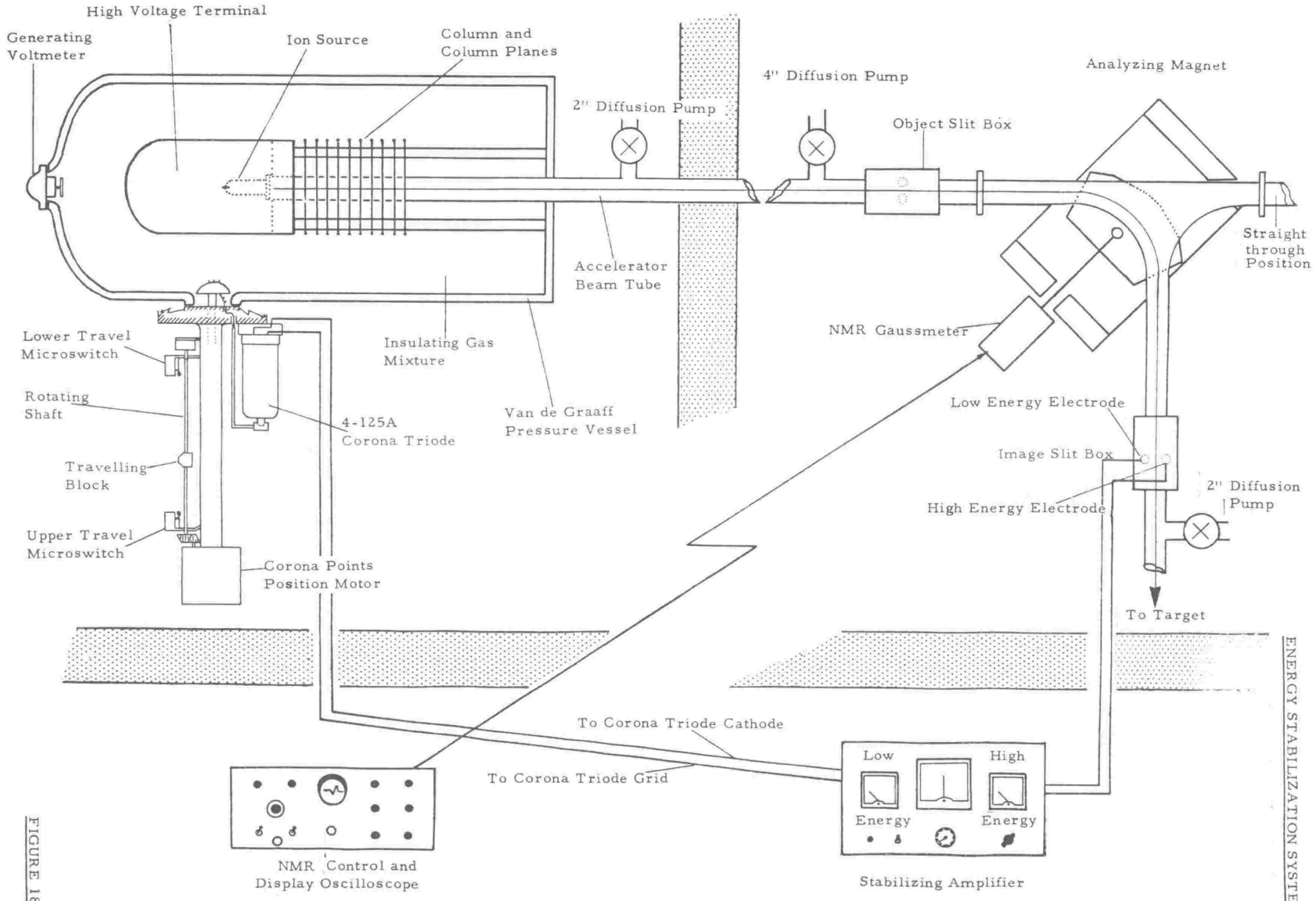

FIGURE 18

ENERGY STABILIZATION SYSTEM

a description of the instrumentation used in the operation of the energy stabilized accelerator.

2.3.1.2. The Energy Error Signal:

Suppose the magnetic field strength in the analyzing magnet pole gap is such that a particle of energy W_o passing through the centre of the object slit is deflected through the centre of the image slit. For zero energy spread in the incident beam and the ion current distributed uniformly over the object slit (i.e. uniform illumination of the object slit) it follows from equation (27) section (2.2.1.5.) that the distribution of ion current in the image plane of the analyzer is also uniform. A plot of the ion current density versus distance from the centre of the image slit would in this case take the form of a rectangle of width s_o centred symmetrically about the middle of the image slit.

If however the ion energies are distributed uniformly within a range of $\pm \Delta W_{max.}$ of the mean energy W_o, a plot of dx versus dx_o (using equation 27) shows that the distribution of the ion current in the image plane of the analyzer takes the form of a truncated triangle centred symmetrically about the middle of the image slit. In the special case when $\Delta W_{max.} / W_o = (s_o / D_o)$ the distribution takes the form of an isosceles triangle. The action of the stabilizing amplifier is to 'hold' this isosceles triangle centred on the image slit.

For the present analyzer, the greatest intensity for a given total energy spread in the analyzed ion beam, occurs for equal settings of the object and image slit widths. Figure 19(a) shows the variation of the total energy spread in the analyzed beam as a function of the slit width for the case $s = s_o$. Also shown on this graph is the variation of the intensity of the analyzed ion beam with s_o, expressed as a percentage of the intensity occurring for the case $s_o = s = 5$ mm, assuming uniform illumination of the object slit. In practice the ion

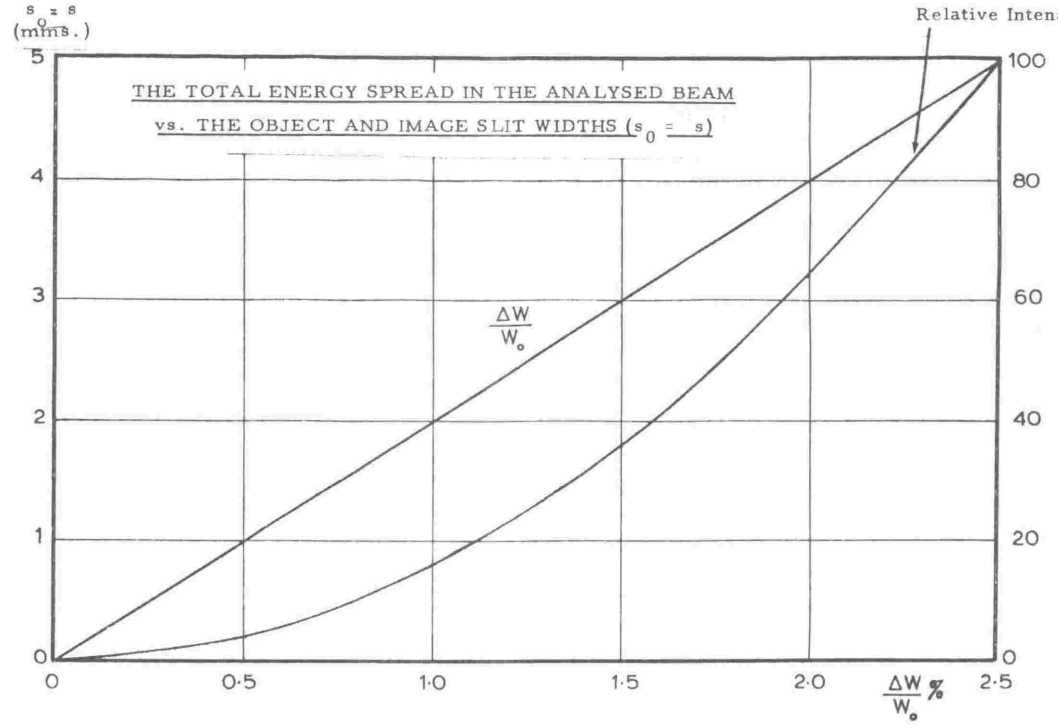

FIGURE 19a

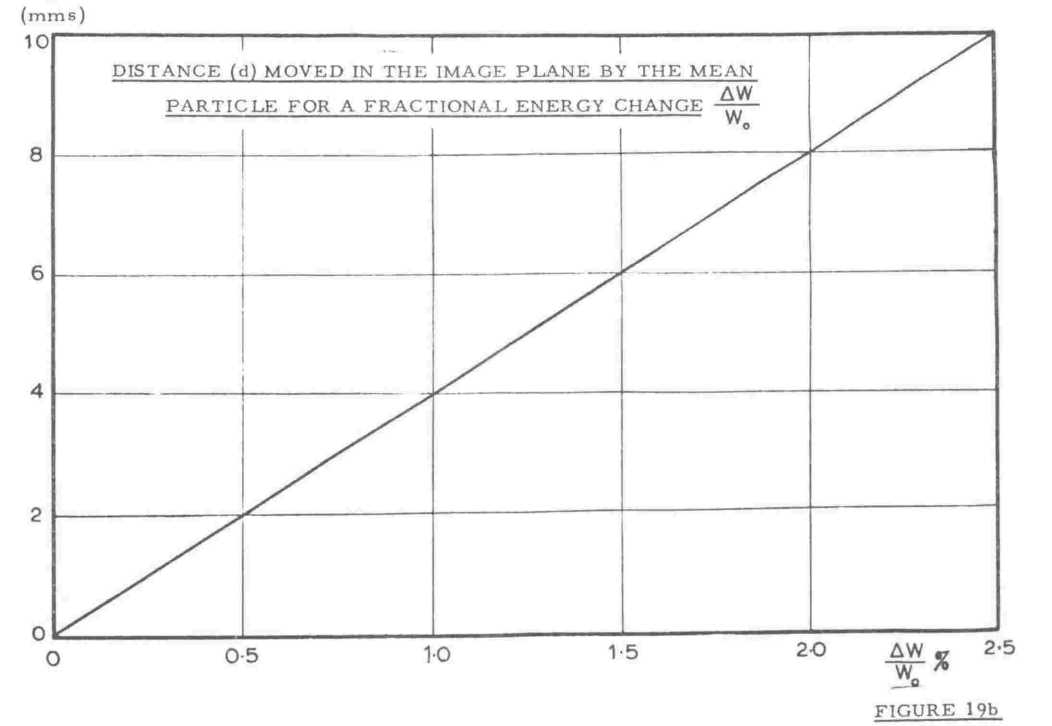

FIGURE 19b

beam can normally be focussed into a smaller diameter cross-section than 5 mm and the relative intensities shown in figure (19) are conservative. The distance moved in the image plane by the mean particle path, for a fractional change in energy $\Delta W/W_o$, can be calculated using equation (38) and the deinition of dispersion. This distance is shown as a function of $\Delta W/W_o$, in figure 19(b).

An estimate of the order of magnitude of the error signal resulting from a given change in the generator terminal potential can be made in the following way. The slit width setting that must be used in order to obtain a given total energy spread in the analyzed ion beam is found from figure 19 (a). An estimate of the analyzed beam current for this slit width setting can be made from the value of the relative intensity found from figure 19 (a). If this beam current is assumed to have a triangular distribution in the image plane, the ion current striking the slit edges for a given displacement of the analyzed ion beam from the centre of the image slit (found, for a given fractional change in terminal potential, from figure 19 (b)) can be calculated.

For example, an analyzed beam having a total fractional energy spread of 2.5 parts per thousand can be achieved with a slit width of s_o = 0.5 mm. At this slit setting the analyzed beam is 1% of the intensity occurring for s_o = 5 mm. An analyzed beam of approximately 50 μA. of H^+ or D^+ ions can be obtained for s_o = 5 mm. (This figure is estimated from the known beam cross section at the object slit, and the fraction of H^+ ions in the incident beam). The analyzed beam current for s_o = 0.5 mm is then 0.5 μA. If the mean energy of the ions increases (or decreases) by 1 part in 1000 the lateral displacement of the ion beam is + (or -) 0.4 mm. Assuming that the beam profile within the image slit is triangular, the current striking the high (or low) energy electrode is slightly less than 0.5 μA. The stabilizing amplifier must be capable of providing a suitable energy correction signal from a smaller error current than this, if major excursions of the analyzed ion beam from the centre of the image slit are to be prevented.

2.3.2. THE CORONA CONTROL ASSEMBLY

2.3.2.1. DESCRIPTION

The corona points assembly * shown diagramatically in figure (18) is the standard corona points assembly for the 3 Mev Van de Graaff accelerator manufactured by the High Voltage Engineering Corporation (Burlington, Mass. U.S.A.) modified in this Laboratory for use on the smaller machine. The corona points assembly is mounted on a port in the pressure vessel wall, in the position originally occupied by the small manually adjusted corona points supplied with the basic accelerator. (See Plate 7.)

The corona points are mounted on the end of a stainless steel shaft passing through a pressure gland (capable of withstanding the 6 atmospheres pressure differential between the insulating tank gas and the atmosphere) located in the mounting flange. The position of the corona points is altered by means of a motor, activated by a switch on the exterior of the corona assembly. This facility provides coarse control of the corona current drawn from the high voltage terminal. The corona points are electrically insulated from the stainless steel supporting shaft by a P.T.F.E. spacer, and are connected by means of a feedthrough electrode in the mounting flange, to the anode of the corona triode (type 4 - 125A). The grid and cathode of this valve are connected to earth through small resistances. Fine control of the corona current drawn from the high voltage terminal is made by altering the grid to cathode bias of this corona triode.

The following modifications and additions have been made to the corona points assembly. An additional shaft driven by the corona points position motor is used to turn, through a gear reduction, a potentiometer at its lower end. The regulated corona triode d c heater voltage is applied across the ends of the potentiometer and the variable voltage on the potentiometer tap is used to provide an indication of the position of the corona points,

* Purchased with a monetary grant from the New Zealand University Grants Committee.

on a meter in the accelerator control console. Rotation of this shaft also causes a metal block to travel lengthwise down the shaft. A microswitch tripped by the travel of the block interrupts a circuit supplying power to the corona points position motor thereby preventing the corona points from being accidently positioned too close to the high voltage terminal.

2.3.2.2. Performance

The corona discharge between the points and the high voltage terminal is maintained by electrons produced mainly from field emission and thermionic emission from the corona points [59]. The corona current therefore depends on, and can be controlled by, the electric field distribution in the immediate vicinity of the points. The field distribution in the neighbourhood of the points is dependent on the potential of the corona points which in turn depends both on the effective resistance between the corona points and ground, and on the corona current. The effective series resistance of the corona triode (the resistance between corona points and ground) is controlled by the bias voltage V_g, applied between the triode grid and cathode. If d is the distance of the corona points from the high voltage terminal and V_t is the generator terminal potential then for a given value of d the corona current I_c depends on both V_t and V_g.

$$\text{i.e.} \quad I_c = F(V_g, V_t)_{\,d \text{ constant}} \qquad \text{---------} \qquad (47)$$

The variation of corona current I_c, with grid bias V_g is shown in figure 20 (a) as a family of curves, with V_t as parameter. The variation of corona current with terminal potential V_t is shown in figure 20 (b) with V_g as parameter. (For a given value of V_g, pairs of I_c and V_t can be found, by varying the generator belt charge current).

In practice, the corona current is maintained within the operating range of the corona triode, by adjustments made to the distance of the corona points from the high voltage terminal.

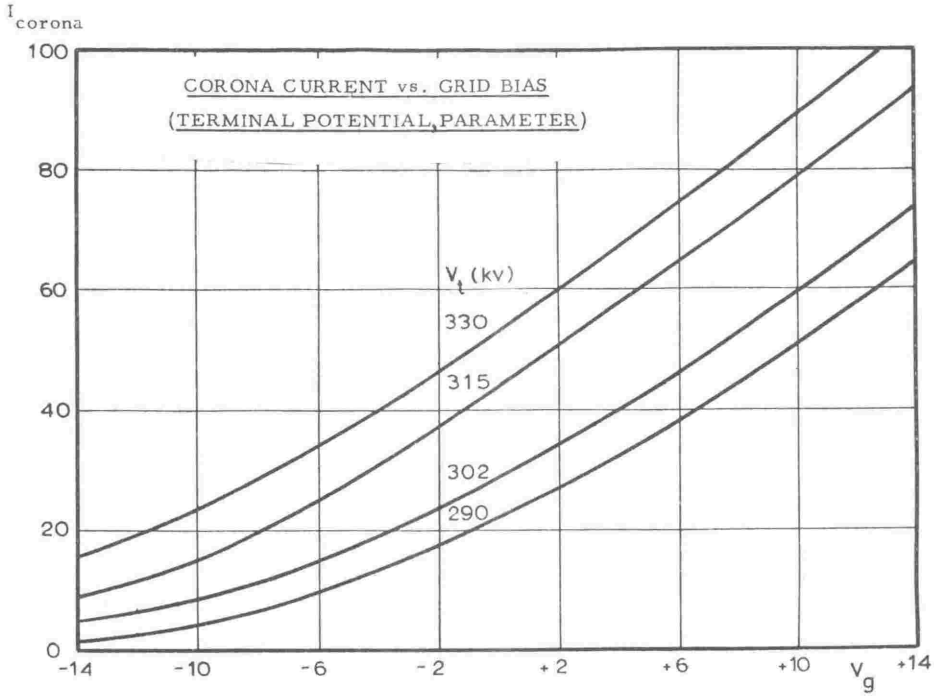

FIGURE 20a

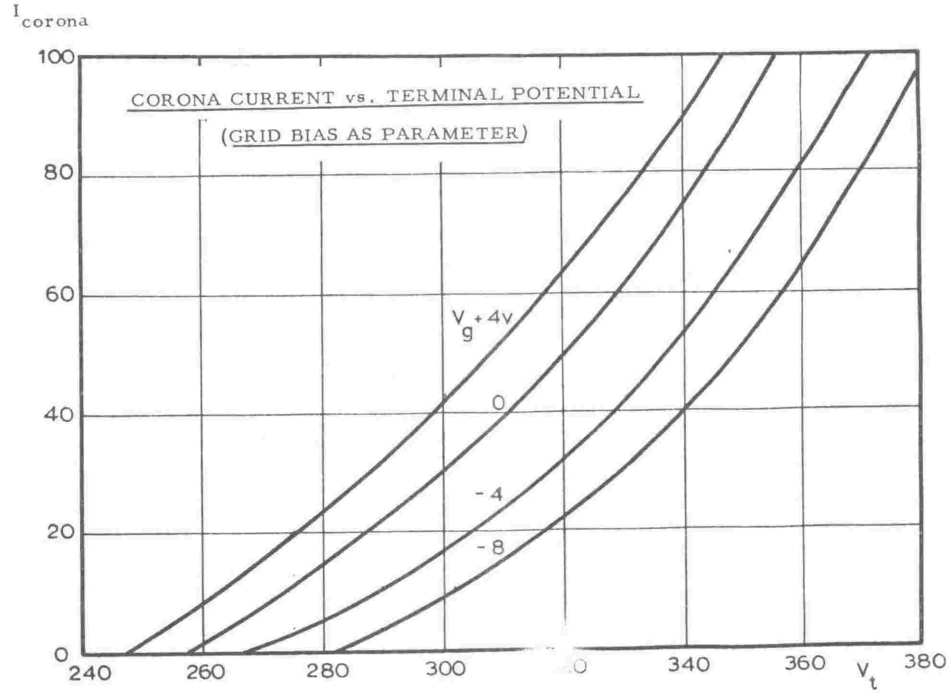

FIGURE 20b

In figure 21 (b) the distance from the pressure vessel wall that the corona points must be positioned, in order to give a corona current of 50 μA is shown as a function of the terminal potential V_t. The data shown in figure (20), corresponds to a constant value of d chosen so as to centralise the graphs about this value of the corona current.

For a steady state potential V_t on the generator high voltage terminal, the algebraic sum of the currents entering and leaving the terminal is zero, and the current balance of the terminal can be represented by the scheme

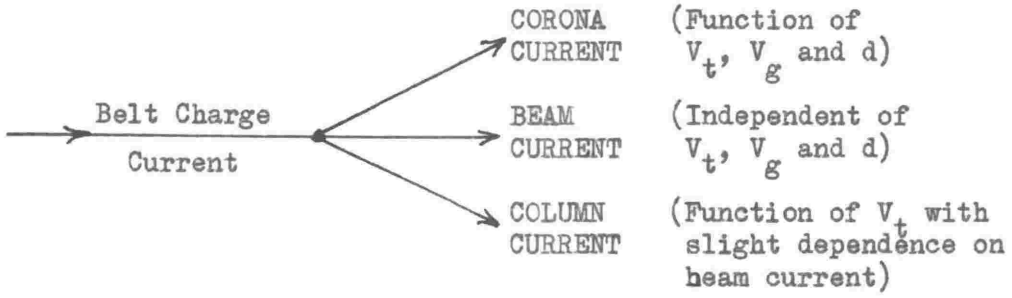

The change in terminal potential resulting from a small change in the corona triode grid bias, can be written in the differential form,

$$\frac{d V_t}{d V_g} = \left(\frac{\partial I_c}{\partial V_g}\right)_{V_t} \cdot \left(\frac{\partial V_t}{\partial I_c}\right)_{V_g} \qquad \text{----------} \qquad (48)$$

(this follows from differentiation of the implicit function of equation (47). The terms on the right hand side can be found from the slope of the curves shown in figure (20). The variation of terminal potential with grid bias is shown in figure 21(a) with corona current as parameter.

The dependence of the column current on high voltage terminal potential is shown for completeness in figure 21(b). The non-linearity is due to the dependence of the column resistance on applied voltage. It should be noted that the column current does not provide a precise measure of the terminal potential because the total resistance of the column can drift with time and the

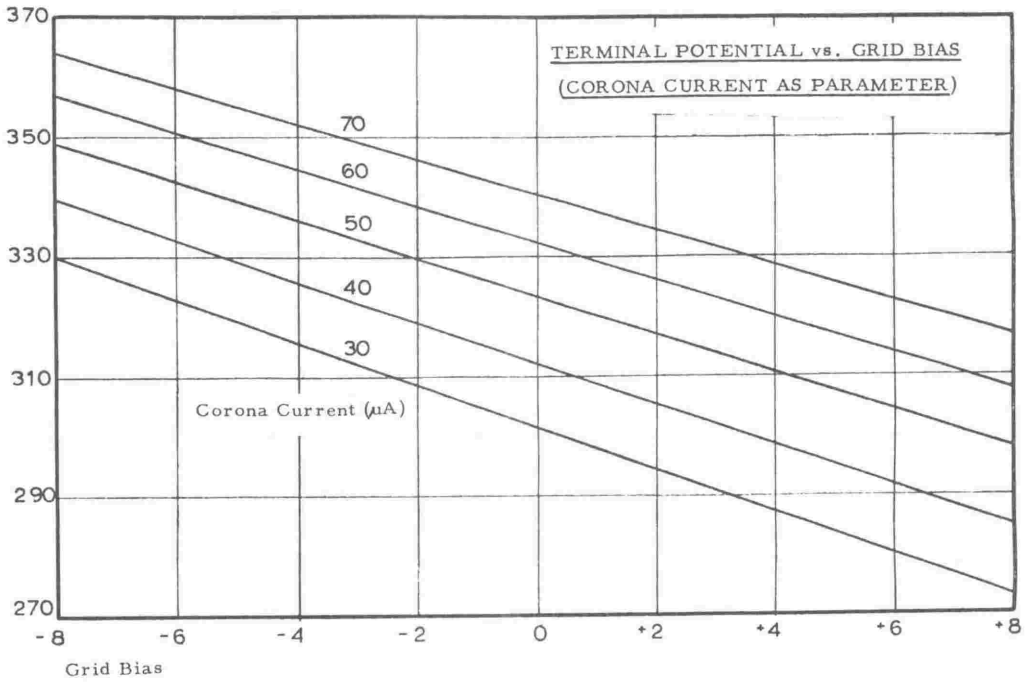
Terminal Potential (Kv)
TERMINAL POTENTIAL vs. GRID BIAS
(CORONA CURRENT AS PARAMETER)
370
350
330
310
290
270
70
60
50
40
30
Corona Current (μA)
-8
-6
-4
-2
0
+2
+4
+6
+8
Grid Bias

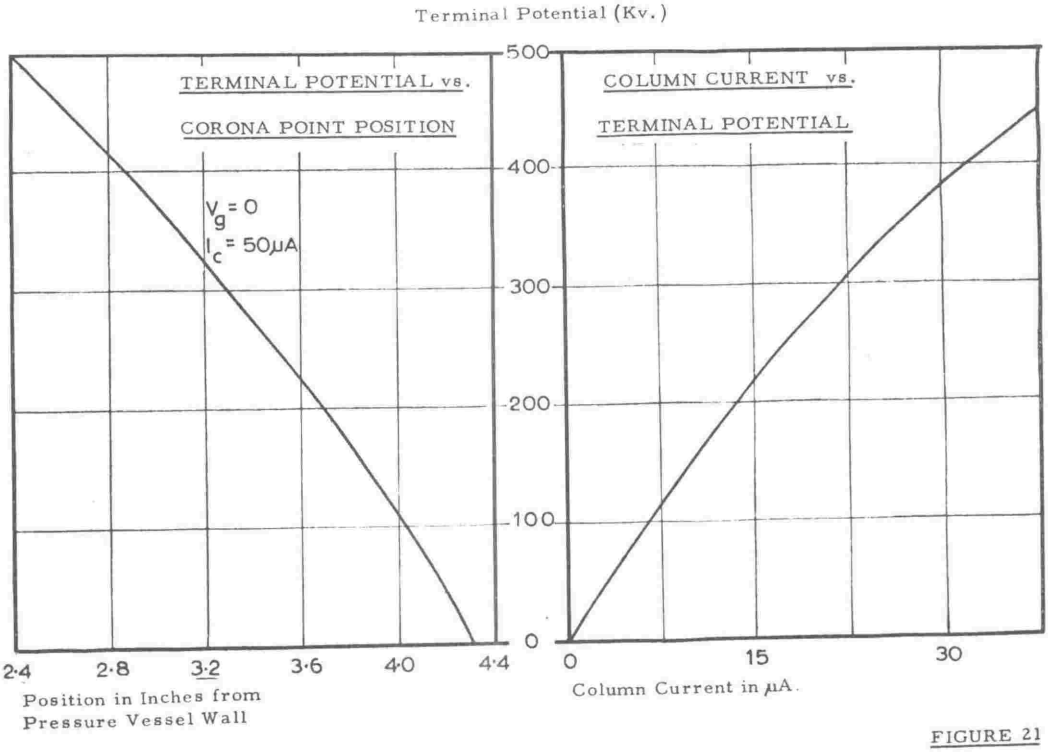
Terminal Potential (Kv.)
TERMINAL POTENTIAL vs.
CORONA POINT POSITION
$V_g = 0$
$I_c = 50\mu A$
500
400
300
200
100
0
2·4
2·8
3·2
3·6
4·0
4·4
Position in Inches from
Pressure Vessel Wall
COLUMN CURRENT vs.
TERMINAL POTENTIAL
0
15
30
Column Current in μA.

FIGURE 21

column current depends on the properties of the ion beam in the accelerator tube. (Ions and electrons produced by ionization in the beam tube strike the column planes at points down the column and in this way contribute to the effective column current)

2.3.3. THE STABILIZING AMPLIFIER

2.3.3.1. DESCRIPTION

The circuit of the stabilizing amplifier is shown in figure (22). The circuit of the power supply used to furnish the power requirements of the amplifier is shown in figure (23).

The stabilizing amplifier consists of two identical dc amplifiers based on a High Voltage Engineering Corporation design. The high energy electrode is connected to the input of the first; the low energy electrode to the input of the second.

In each amplifying channel the potential developed across the ganged sensitivity potentiometer is proportional to the ion current striking the appropriate energy defining electrode. This ion current is monitored on a 50 μA full scale meter. The voltage across the potentiometer is amplified in two amplifying stages. Coupling between stages is accomplished with zener diodes for the low frequency ac and dc components of the signal, while the high frequency components are coupled capacitively. The amplified signal is fed to the appropriate corona triode electrode, by an output cathode follower.

The balance control is common to both channels, and enables the standing grid-cathode bias on the corona triode to be adjusted to zero in the event of any unbalance in the gain of the two channels. The balance meter provides a visual indication of the grid-cathode bias. The degree of fluctuation in this meter reading also provides an indication of the stability of operation of the stabilization feedback system. The sensitivity control alters the feedback loop gain and is adjusted for optimum stability as indicated by the balance meter.

STABILIZING AMPLIFIER CIRCUIT

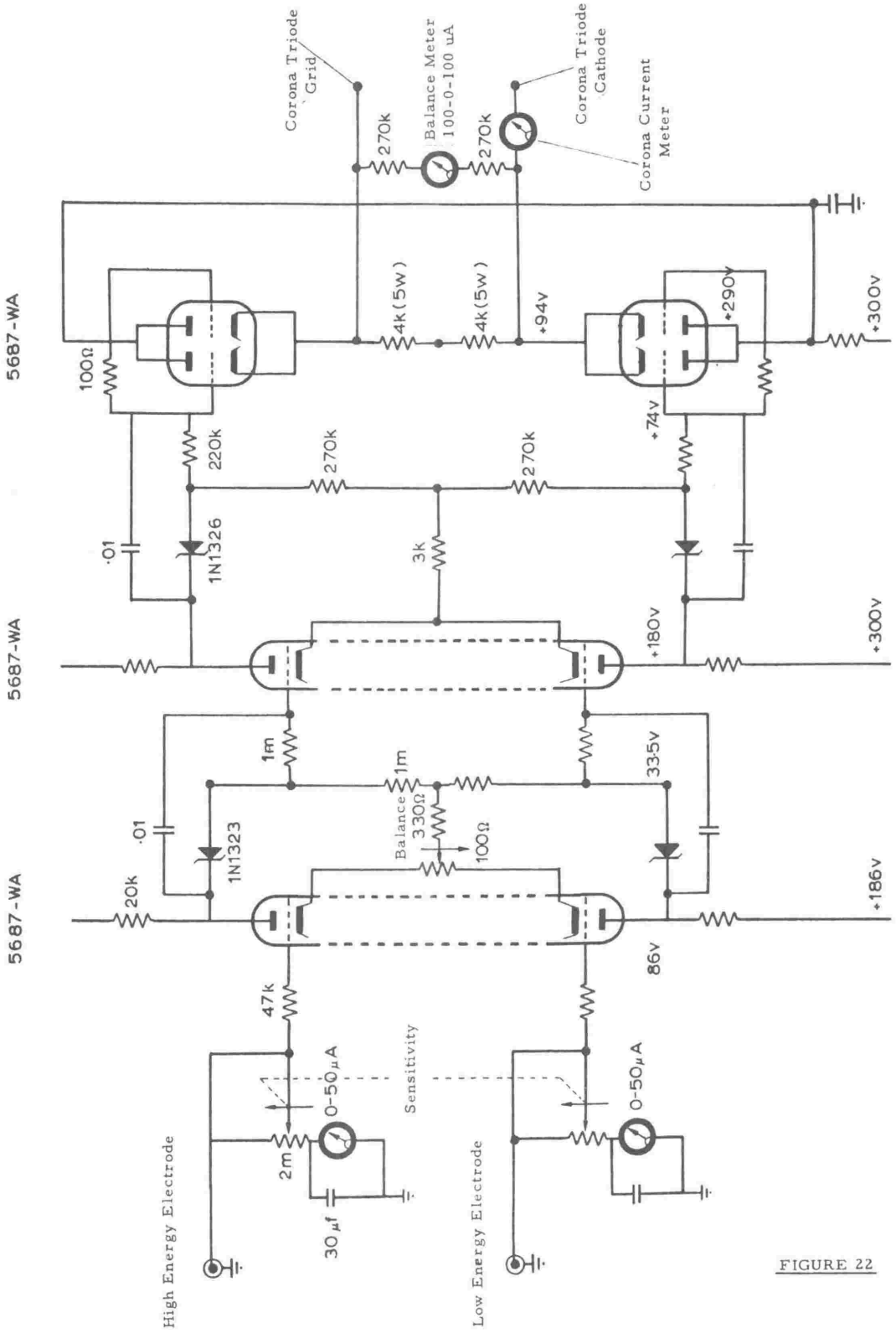

FIGURE 22

STABILIZING AMPLIFIER POWER SUPPLY CIRCUIT

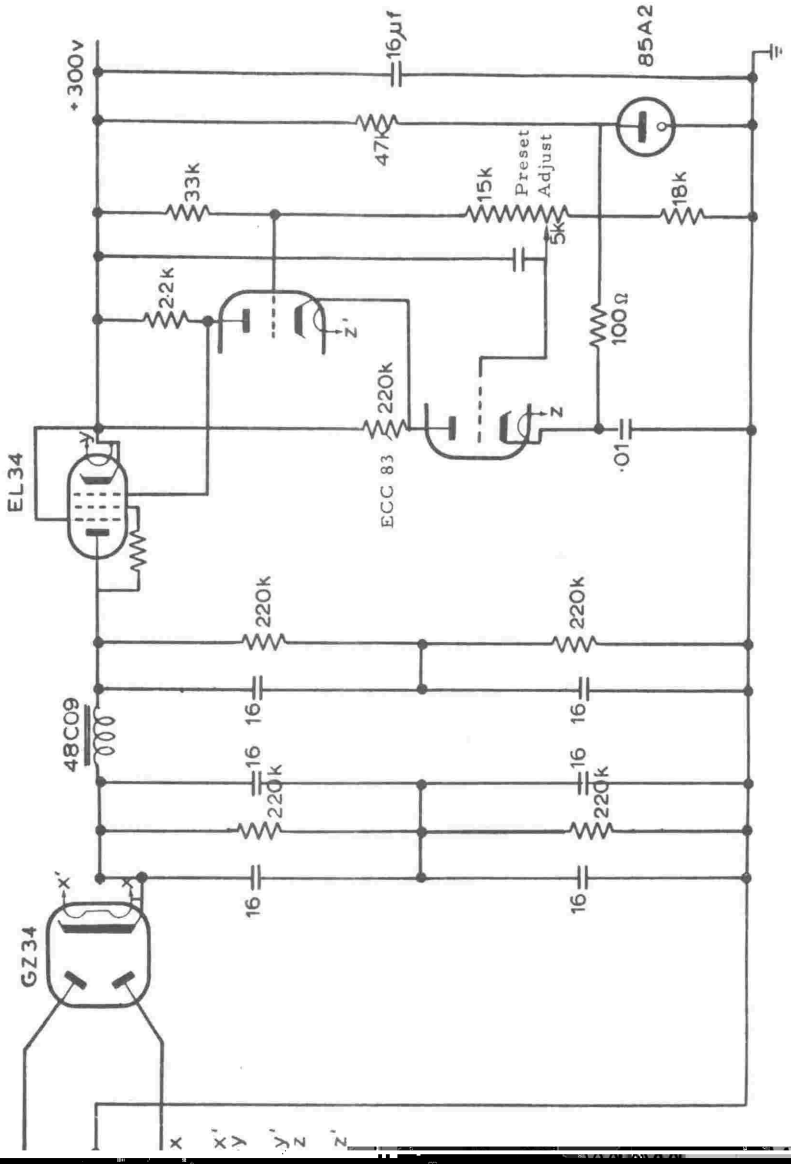

When the two channels of the stabilizing amplifier are correctly balanced the voltage signal appearing between grid and cathode of the corona triode represents the amplified difference in voltage between the two energy defining electrodes. If the ion beam is symmetrically placed with respect to the image slit no energy correction voltage is produced by the amplifier irrespective of the magnitude of the ion current striking the electrodes. (i.e. the stabilizing amplifier operates as a dc differential amplifier).

2.3.3.2. PERFORMANCE

The insulation resistance between each electrode and ground is approximately 100 megohms (at 500 volts) when air cooling of the image slit defining cylinders is used, and approximately 200 kilohms when water cooling is employed. This resistance appears in parallel with the sensitivity potentiometer resistance.

The components used in the construction of the amplifier have been selected in order to balance the circuit voltages and gain of the two channels. The power supply and stabilizing amplifier then reach the following specifications. The power supply regulation is better than 0.2% for supply voltage and load changes of less than 20%. The ripple on the power supply output is less than 7 mv. (rms).

The voltage gain of each channel of the stabilizing amplifier is continuously variable from 0 to 80 (approximately 0 to 160 for double ended output). The maximum output voltage swing of 164 volts corresponds to values of $\pm$ 82 volts for the corona triode grid bias. The output ripple measured between the grid and cathode of the corona triode with the inputs of the stabilizing amplifier shorted, is then less than 10 mv. (rms). The frequency response of the amplifier is such that the output voltage does not drop below 50% of the dc output level for signal frequencies less than 80 kc/second.

2.3.4. THE STABILITY OF THE FEEDBACK SYSTEM:

The stability of the feedback system is determined by the relative time constants associated with the components forming the feedback loop. The time taken for a charged particle to travel from the ion source to the image plane of the magnetic analyzer is typically less than a microsecond. The energy error signal is therefore formed within one microsecond of the change occurring in the high voltage terminal potential.

The time taken for the high voltage terminal potential to respond to a change in the corona triode grid bias is determined by the velocity of propagation of ionization through the insulating gas. This velocity is not accurately known for high pressure insulating gases[22]. If the growth of ionization through the insulating gas is caused solely by electrons drifting under the influence of the electric field between the terminal and points, then propagation times will be long. Recently, however, Kritzinger[32] has found that the velocity of propagation of ionization through an insulating gas at atmospheric pressure, is appreciably increased by the presence of oxygen, even in concentrations as small as 10 parts per million. The propagation of ionization through the gas is effected, in this case, by photons produced in the corona discharge causing furtherproduction of photoelectrons by ionization of oxygen molecules. The velocity of photons through the gas is much faster than the electron drift velocity and as a consequence the ionization growth is rapid.

The existence of this mechanism of ionization growth in the high pressure gases used in accelerator insulation, has yet to be confirmed. Recent investigations by Fenald and Baker[22] however have confirmed that the time of transit of ionization between the corona points and terminal is less than one millisecond.

In the present work the maximum stability required of the high voltage terminal potential is 2 parts in 1000 (see for example chapter 3). This means that the small amplitude ($\sim$ 0.1%) high frequency excursions in terminal potential can be tolerated.

The addition into the feedback loop of an overiding time constant can then be used to ensure unconditional stability of the feedback system.

This has been done by filtering high frequency components of the energy error signal ($\gtrsim$ 1 kc/sec) to ground through a capacity of approximately 1000 pf placed across the sensitivity potentiometer resistances. In practice it has proved convenient to locate the stabilizing amplifier in the accelerator control console, and use the capacity of the connecting signal cables as the filtering capacities.

2.3.5. INSTRUMENTATION OF THE STABILIZATION SYSTEM

2.3.5.1. ACCELERATOR CURRENTS

The four accelerator currents, namely the belt charge current, column current, corona current and beam current are monitored in the following way. The belt charge current meter (0 - 250 μA) measures the current drain from the belt charge power supply, the column current meter (0 - 50 μA) measures the current passing down through the column resistor chain to earth, and the corona current meter (0 - 100 μA), located in the cathode circuit of the corona triode (figure 22), measures the corona triode anode current.

The total ion beam current striking the object slit*, or the ion current striking any one of the four component electrodes forming the object slit, can be displayed on the 0 to 50 μA object slit-box meter. The beam current striking the magnet beam tube (composed almost entirely of the higher mass ion components in the ion beam) is continuously displayed on a 0 to 100 μA meter.

The stabilizing amplifier includes two 0 to 50 μA meters for indicating the current striking each energy defining electrode. The current striking each of the two remaining electrodes forming the image slit, (or the total current striking these two) can be displayed on the 0 to 50 μA image slit-box meter.

In addition to indicating the target current, the 0 to 25 μA target current meter can be used to display the out of focus ion current striking the focus electrode. (This electrode is a metal disc, having in the centre a circular aperture, through which the ion beam passes. It is usually located immediately in front of the target.) The current meters mentioned above are located in the accelerator control console (plate 4).

2.3.5.2. THE NUCLEAR MAGNETIC RESONANCE (NMR) GAUSSMETER:

The magnetic field strength in the pole gap of the analyzing magnet is measured using a nuclear magnetic resonance gaussmeter. (A discussion of magnetic field strength measurement using nuclear magnetic resonance absorption, is given in references (60 and 61). A novel feature of this particular gaussmeter is that it is operated remotely from a control unit in the accelerator console.

The physical locations of the NMR gaussmeter and control unit are shown in figure (18). Figure (24) shows the circuit of the NMR gaussmeter head unit. This unit consists of the field sensing probe, transistorized megacycle marginal oscillator, and a detector and audiofrequency amplifier. Figure (25) shows the circuit of the gaussmeter control and display unit.

The dc magnetic field in the region of the sample is modulated, through a range of approximately plus and minus 10 gauss, by a 50 cycle/second ac current flowing in coils wound

* The loss of secondary electrons emitted from a metal electrode under ion bombardment, can in practice cause a discrepancy between the observed and actual value of the ion current striking the electrode.

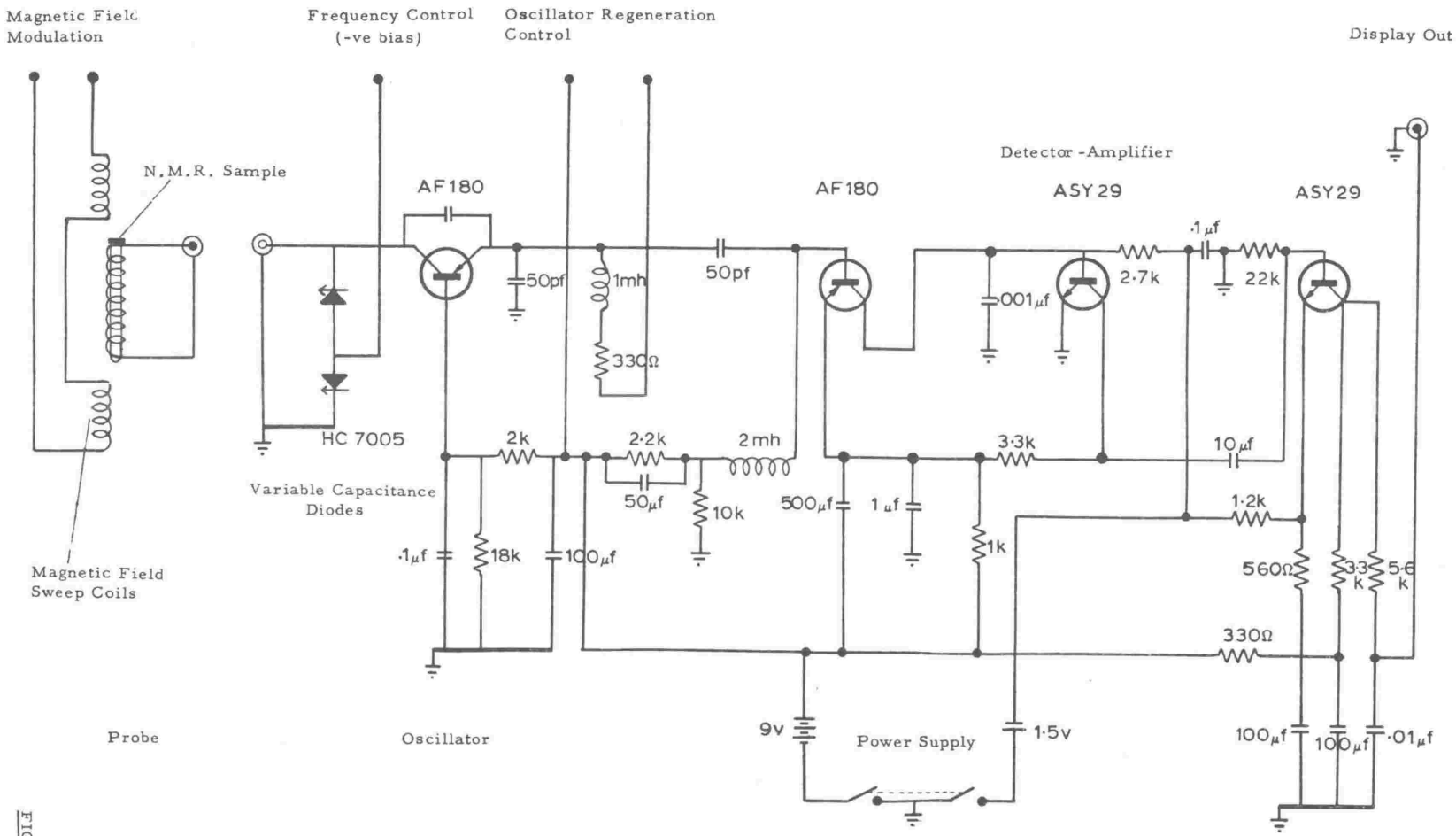

FIGURE 24

N.M.R. GAUSSMETER HEAD UNIT

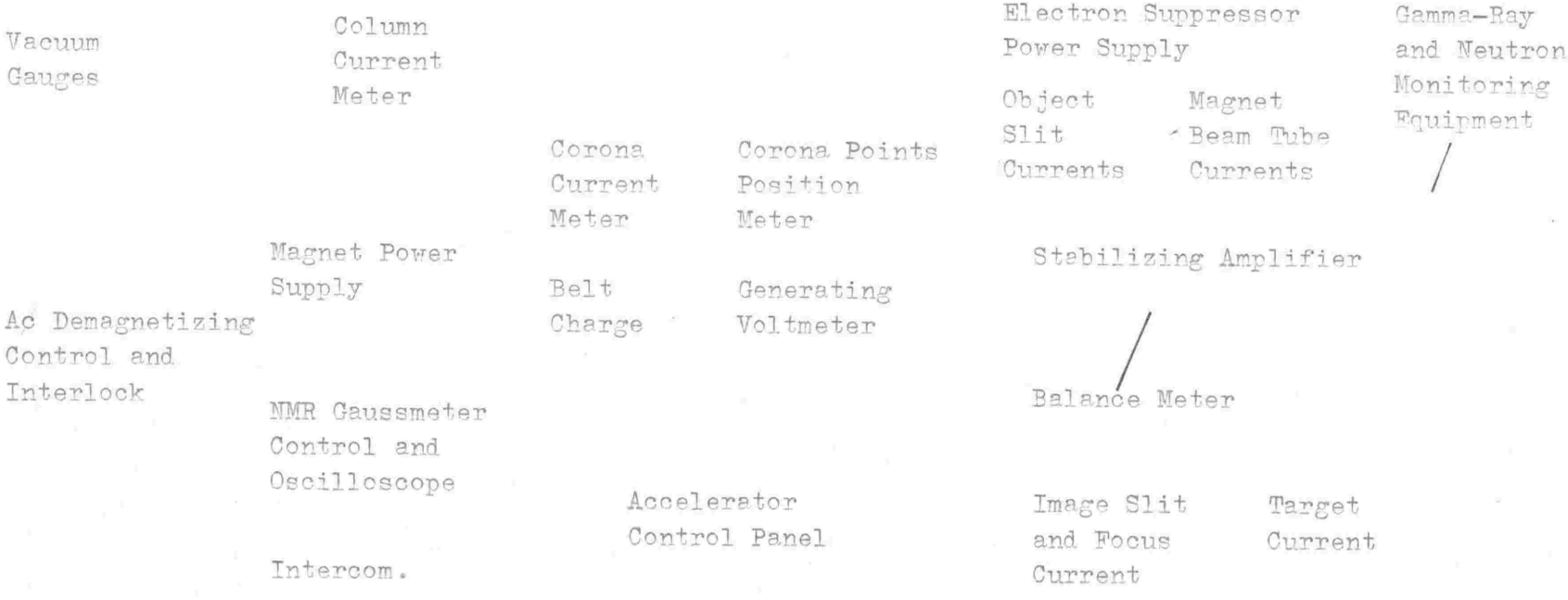

PLATE 4 ACCELERATOR CONTROL CONSOLE

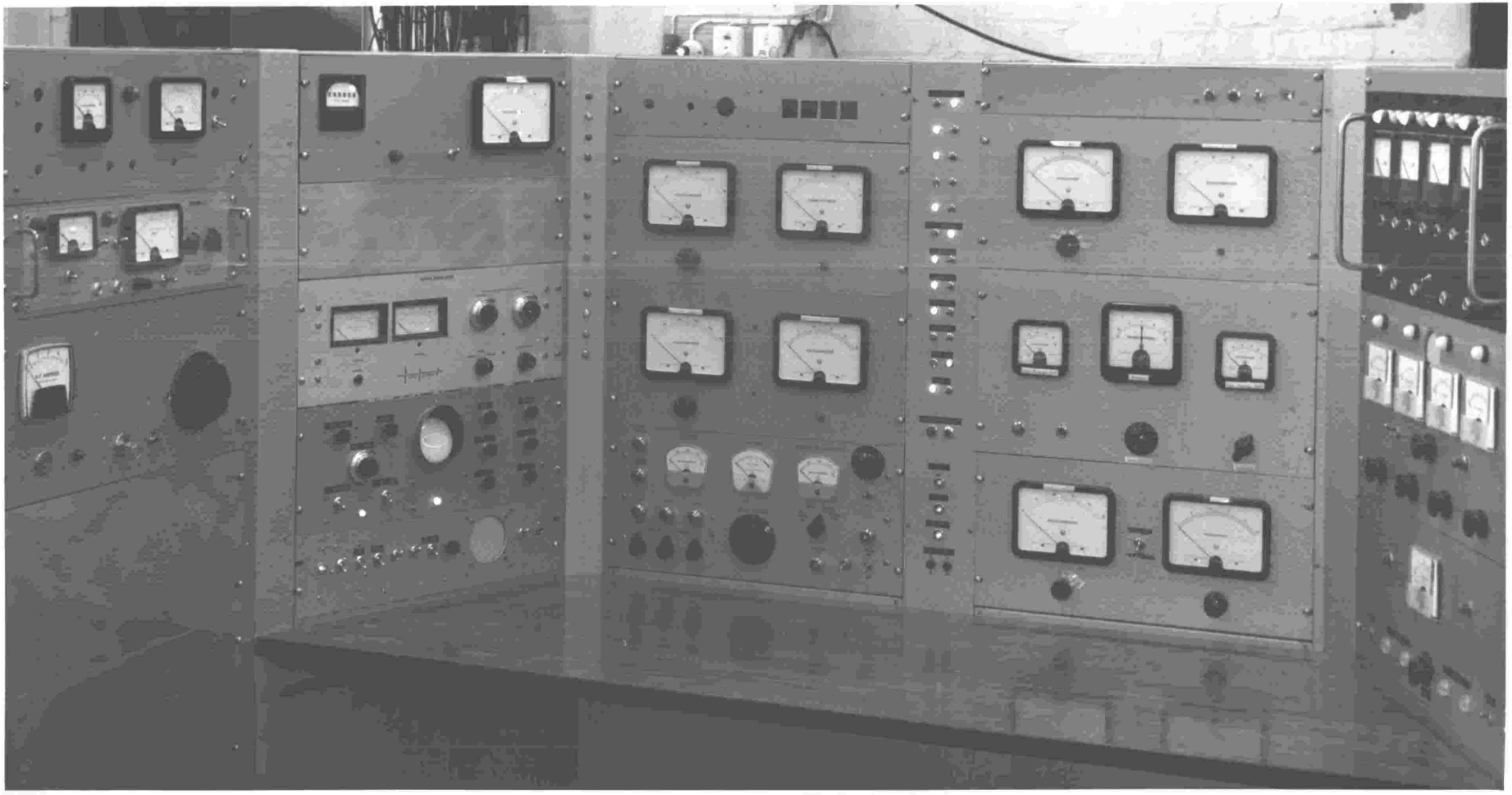

on the sample holder above and below the sample. The rf current from the marginal oscillator causes a weak oscillatory magnetic field in a direction at right angles to the modulated dc field. For a given dc magnetic field strength there is a corresponding frequency of this rf field for which nuclear magnetic resonance of the protons in the sample (distilled water containing a small quantity of ferric nitrate) will occur[60]. The relation between the marginal oscillator frequency at resonance, and the dc magnetic field strength can be found in terms of two fundamental atomic constants, the gyromagnetic ratio and the ratio of cyclotron to spin resonance frequency of the proton[25]. If the magnetic field strength B is measured in kilogauss, and oscillator frequency f in megacycles/second then[61]

$$f = 4.2577\ B \qquad (49)$$

In practice the accuracy with which B can be determined is limited only by the accuracy with which the oscillator frequency at resonance, can be measured.

At resonance, power is absorbed from the oscillating rf field, and the effective resistance of the rf coil surrounding the sample increases as a result of the rf losses. As the current supplied by the oscillator is approximately constant, the voltage across the coil increases. This voltage increase at resonance is detected, amplified, and displayed as a resonance 'dip' on the oscilloscope in the control unit. Provided the frequency of the marginal oscillator corresponds to a magnetic field strength in the range swept out during a modulation cycle, two resonance absorption dips will occur per modulation cycle (one as the magnetic field strength increases through the resonance value and the other for decreasing magnetic field at resonance). The frequency corresponding to the dc magnetic field strength in the magnet is that frequency for which the 'dips' corresponding to resonance absorption occur just as the modulation current passes through zero. In practice oscillator frequency is adjusted until the two absorption dips on the oscilloscope display coincide.

The oscillator frequency is controlled by the dc voltage applied to a pair of variable capacitance diodes (type HC,7005) in parallel with the rf sample coil. (The dependence of oscillator frequency on applied bias follows approximately a $V^{\frac{1}{2}}$ law). This method of oscillator tuning enables the oscillator frequency to be controlled remotely, and has the advantage of obviating the inevitable microphonics associated with adjustment of a mechanical tuning capacitor. The output current of the oscillator is controlled by the oscillator regeneration control. The amplitude of the resonance dip is greatest when there is only just sufficient regeneration to cause oscillation (i.e. marginal oscillation) although the signal to noise ratio is not necessarily optimum for this setting.

The control unit, shown in figure (25), consists of a regulated, continuously variable dc voltage supply (the frequency control), a variable ac current supply (the magnetic field modulation control), and the display oscilloscope. The voltage applied to the X plates of the cathode ray tube (type 3AP1) is an ac signal in phase with the sinusoidal field modulation signal. The output signal from the detector - amplifier in the gaussmeter head unit, is amplified and applied to the Y plates.

With the present variable capacitance diodes the frequency range of the gaussmeter oscillator is 6 to 9, 15 to 21, or 25 to 35 megacycles/second, depending on which of three probe assemblies is used (these probes differ only in the inductance of the rf coil surrounding the sample). In the present work frequencies not included in these ranges are obtained by placing additional capacitance in parallel with the probe. Diodes having a greater capacity range (0 to 1000 pf) have subsequently become available and will extend the frequency ranges to give complete coverage for magnetic fields between 800 and 8000 gauss using the existing three probes.

DISPLAY UNIT

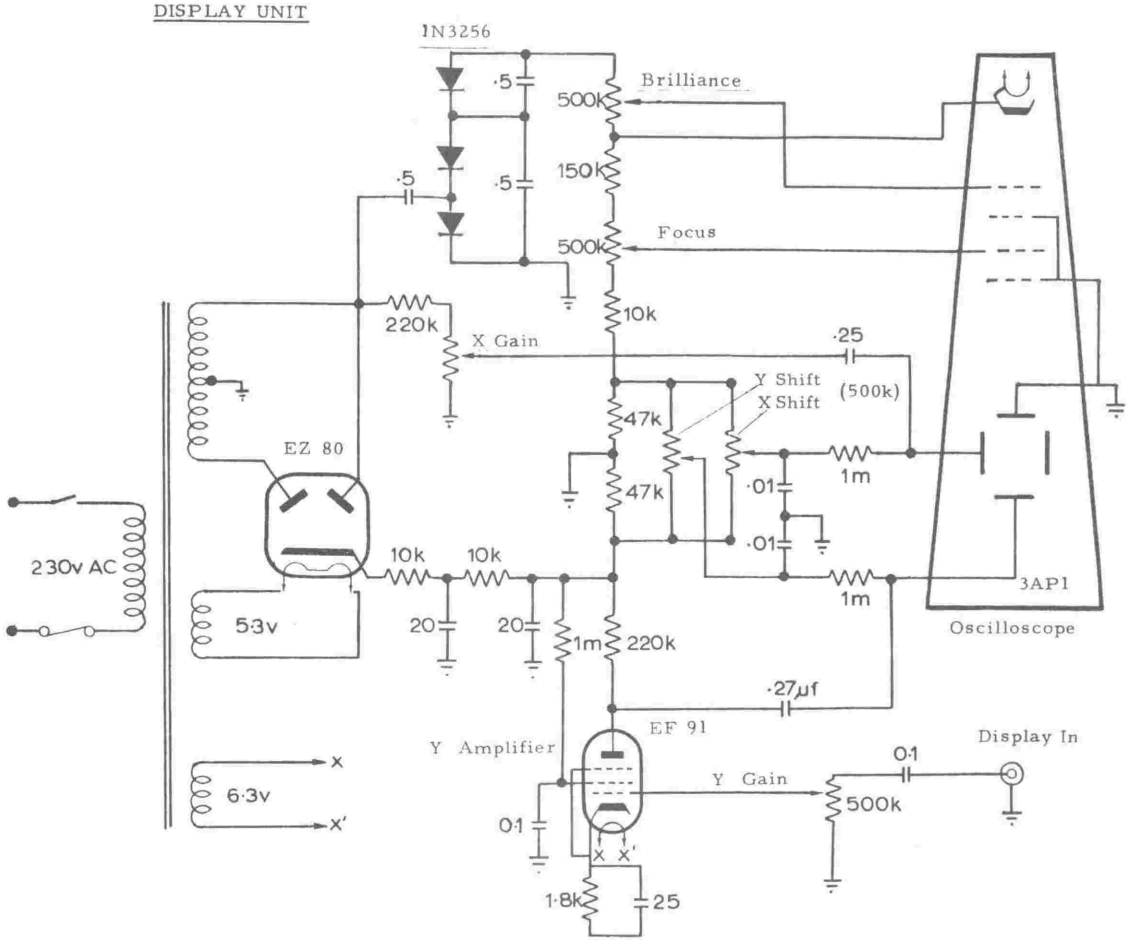

CONTROL UNIT

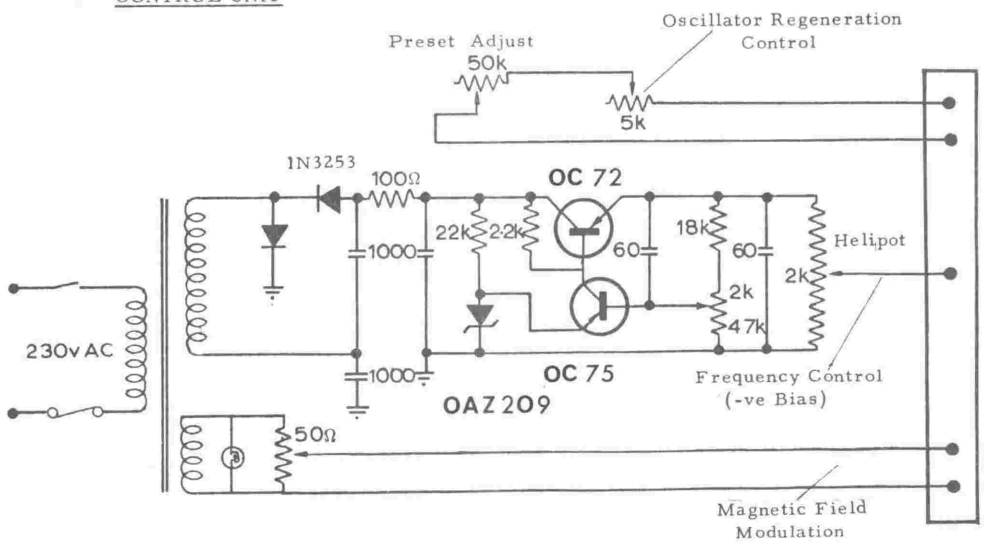

FIGURE 25

The stability of the oscillator frequency is determined by the constancy of the temperature of the variable capacitance diodes. The long term stability of 4 parts in 10^4, and better than 1 part in 10^4 for short periods (about 5 minutes) have proved adequate and no special efforts to reduce the fluctuations in diode temperature have been necessary.

The frequency of the oscillator at resonance is measured to an accuracy of 5 parts in 10^4 by beating the oscillator output against the output voltage from a crystal calibrated signal generator. (Marconi: TF-144H). The beat (difference frequency) voltage is displayed on the oscilloscope at the same time as the resonance pattern. This method has the advantage that the accuracy with which the magnetic field can be determined is relatively independent of drifts in the gaussmeter frequency, provided only that the frequency is sufficiently stable to enable a steady oscilloscope pattern to be obtained.

CHAPTER 3: THE PERFORMANCE AND CALIBRATION OF THE STABILIZATION SYSTEM

3.1 EQUIPMENT PERFORMANCE:

3.1.1. THE MAGNET COILS

Each coil was wound with approximately 900 turns of double cotton insulated copper wire (British S.W.G No. 12). Initial tests showed an excessively low leakage resistance existed between the coil windings and the copper coil former. This was attributed to dampness in the cotton insulation covering the wire. The higher insulation resistance of the second coil, wound after baking the wire for some days at 150°C, confirmed this view. The moisture in each coil was 'baked' out by passing an 8 amp current through the coil for a period of three days. The temperature in the interior of the coil (monitored by means of a copper-constantin thermocouple wound as apermanent part of the coil, during construction) at no time exceeded 80°C even though water cooling of the coil formers was not employed. During this 'bakeout' period the leakage resistance, after an initial decrease, increased to a uniform steady value. At this point the coils were sealed from the atmosphere by winding two layers of insulating paper sealed with air dry varnish over the outer surface of the coil. A layer of plastic insulating tape was used to provide a moisture impervious outer coating to the coil (see plate 5). The insulation resistance of both coils has remained constant at 1.2 megohms (measured at 500 volts) since this time. The total resistance of the two coils connected in series is 7.1 ohms measured at 18°C.

3.1.2. UNIFORMITY, STABILITY, AND REPRODUCIBILITY OF THE MAGNETIC FIELD:

The magnetic field strength at the normal site of the NMR Gaussmeter probe within the magnet pole gap (the position shown in figure 16) was found to be approximately 1.25 kilogauss

Magnet Yoke

Water Cooling Pipes

Magnet Coil Former

Mechanical Support

Water Impervious
Outer Coating

Beam Tube

Magnet Coil Former

PLATE (5 MAGNET COIL CONSTRUCTION

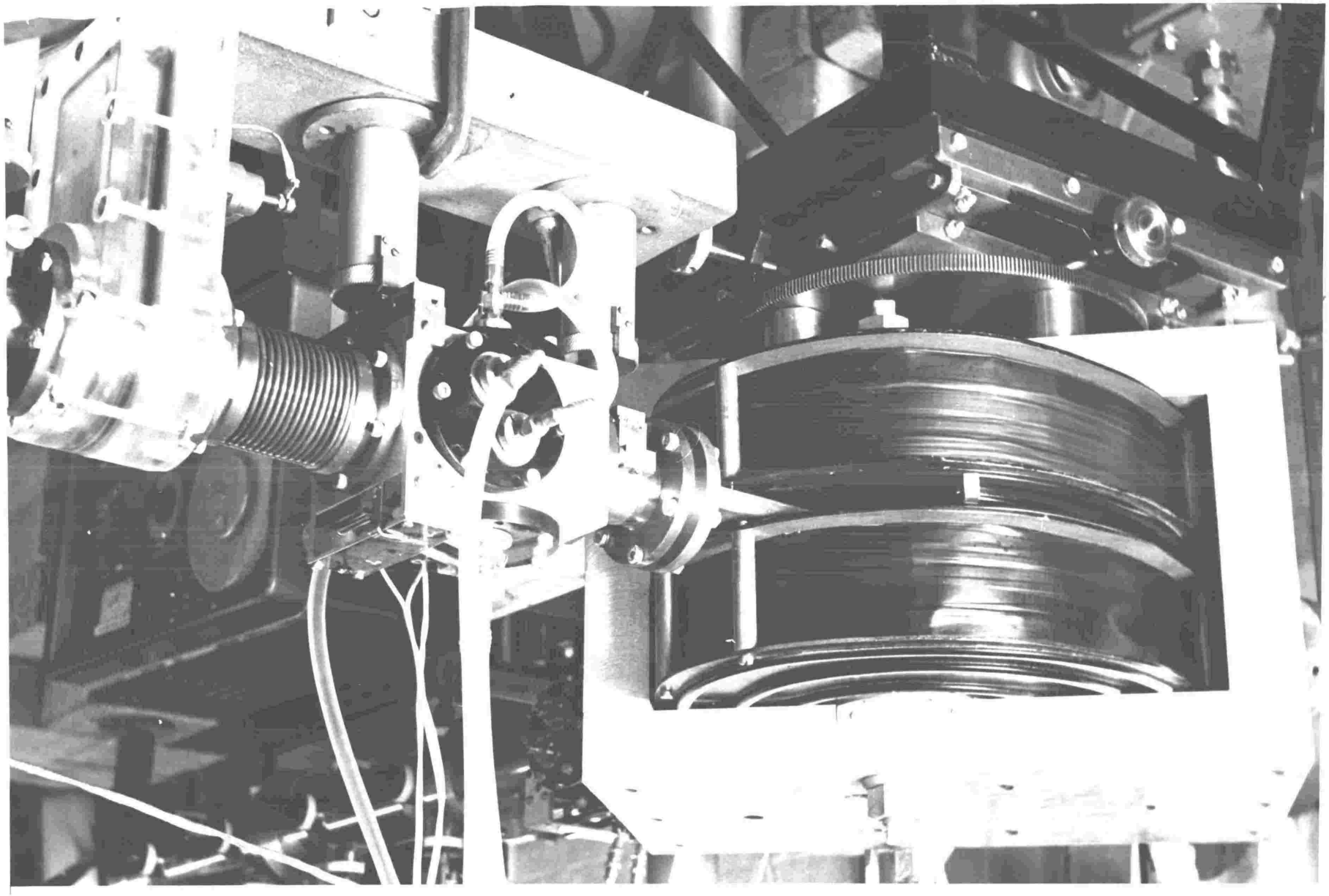

per ampere of magnet coil current, for currents of up to 6 amps. (figure 26 a). The magnetic field strength at points along the ion beam trajectory (shown in figure 10) and at points along a line at right angles to the ion path, was found to be uniform to within 5 parts in 10^4, with the exception of the field strength at the points in close proximity to the pole piece boundaries (points a,e, 5 and 5') and the two points 4 and 4'. The field strengths at points a and e were respectively 4 and 15 parts per thousand below the uniform field strength value. The fall-off in field strength in the region of points 5 and 5' is discussed in a later section (3.2.4) and is shown in figure 26 (b).

The non-uniformity of the magnetic field at the interfaces between the rotating pole sections and the pole pieces (the points labelled 4 and 4') was reduced from an initial value of 2% to less than 0.2% by reseating the rotating cylinders so as the discontinuity in surface level across the interface was less than 5 ten-thousandths of an inch. The outside surface of the rotating cylinders and the inside surface of the cylindrical bores, as well as the magnet yoke and pole pieces, were cadmium plated in order to inhibit rust formation. This resulted in no noticeable change in the field distribution in the neighbourhood of the rotating pole segments.

The stability of the magnetic field in the magnet pole gap for a constant current in the magnet coils was investigated in the following way. The gaussmeter, used with a mechanical tuning capacitor, was checked against a crystal controlled oscillator and was found to be stable to within one part in 10^5. An oscilloscope with stable triggering facilities (Tektronix, type 551) was triggered from the resonance absorption dip corresponding to the modulated dc magnetic field increasing through the resonance value (2.3.5). The second resonance absorption dip of the modulation cycle was then displayed on the oscilloscope screen. The horizontal position of this second dip was accurately calibrated in terms of small changes in magnetic field strength. (A change in magnetic field strength of 1 gauss resulted in a displacement of approximately 1 mm in the position of the dip).

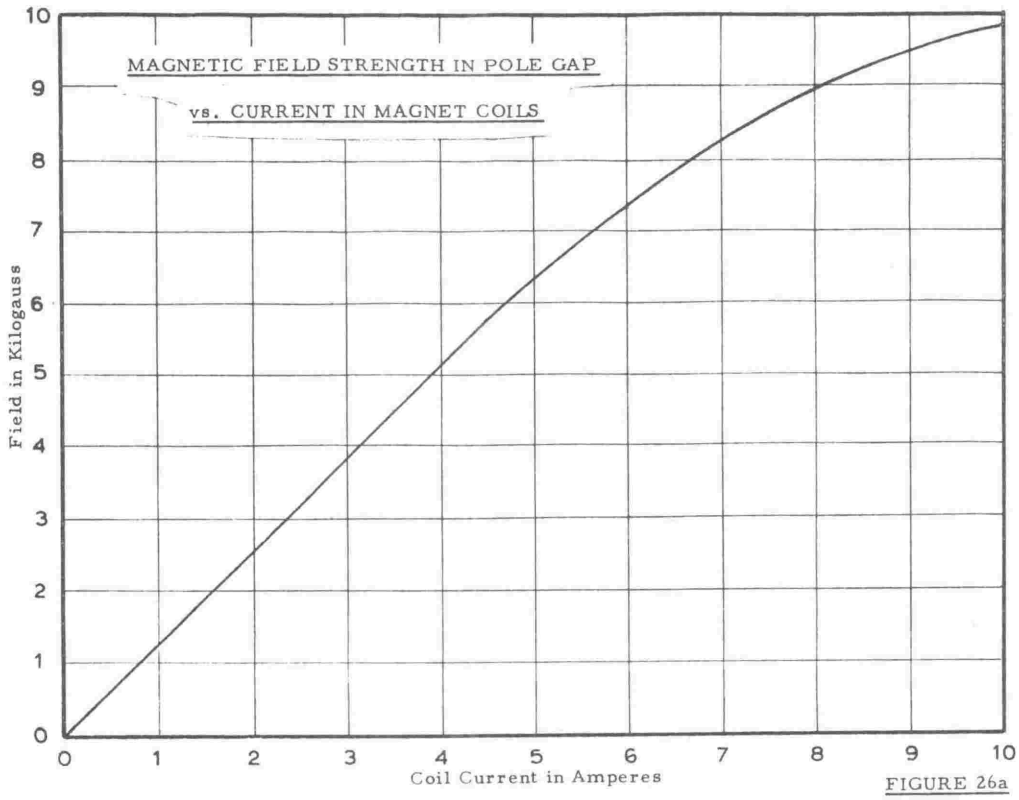
MAGNETIC FIELD STRENGTH IN POLE GAP
vs. CURRENT IN MAGNET COILS
Field in Kilogauss
Coil Current in Amperes
0
1
2
3
4
5
6
7
8
9
10

FIGURE 26a

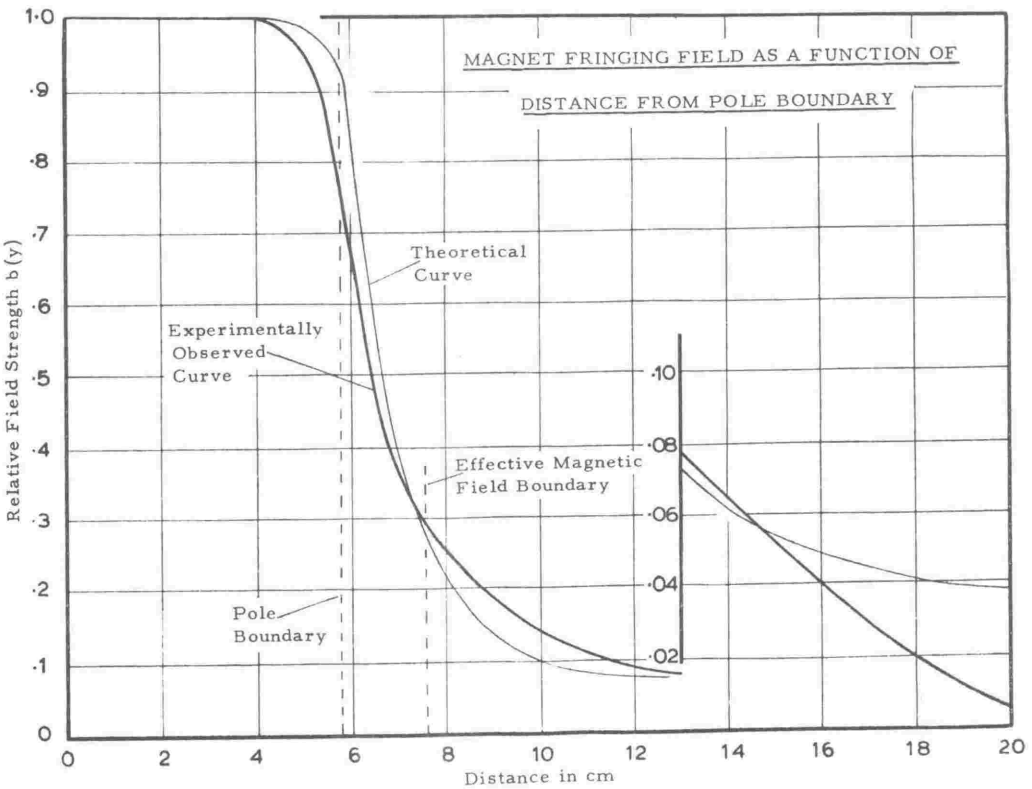
MAGNET FRINGING FIELD AS A FUNCTION OF
DISTANCE FROM POLE BOUNDARY
Relative Field Strength b(y)
Distance in cm
Theoretical Curve
Experimentally Observed Curve
Effective Magnetic Field Boundary
Pole Boundary
1·0
·9
·8
·7
·6
·5
·4
·3
·2
·1
0
·10
·08
·06
·04
·02
0
2
4
6
8
10
12
14
16
18
20

For a magnetic field strength of 8,600 gauss in the magnet pole gap, and with water cooling of the coil formers, the drift in magnetic field strength over an eight hour period at no time exceeded 2 parts in 10^4 after an initial warm up period of one hour. Without water cooling of the magnet coil formers, this figure deteriorated to 1 part in 10^3. The stability of the magnetic field was observed to be higher at lower values of the field strength in the magnet pole gap, and was considered to be in all cases adequate (see section 2.2) for the present work.

Because of differential hysteresis[58] effects occurring in the magnet iron, the integrated field traversed by the charged particles need not necessarily be strictly proportional to the magnetic field strength at the site of the field measuring probe. For this reason the reproducibility of the magnetic field distribution was investigated. The magnetic field strength at the point 3' was measured for a given field strength B, at the normal position of the gaussmeter probe (the point labelled b). In order to simulate the most extreme experimental case, the magnet coil current was cycled several times from zero to maximum current, between each pair of readings. The values of the magnetic field strength at these two locations agreed to with in 1 part in 10^3, for values of B ranging from 1000 to 8000 gauss. If the magnet iron was initially demagnetised (by the method described below) and the magnetic field was increased to the value B by folowing a virgin magnetisation curve, the magnetic field strength at the point labelled 3' was found to be reproducible to within 2 parts in 10^4.

3.1.3. THE DEMAGNETISATION OF THE MAGNET YOKE:

Conventional ac demagnetisation[53] of the magnet yoke using mains supply frequency (50 cycles per second) power fed onto the magnet field coils is only partially satisfactory. The skin thickness [62] (that depth into the magnet yoke at which the magnetising force has fallen to 1/e of its value at the surface)

is of the order of 1 mm for an alternating magnetising force of this frequency. The following method of demagnetising the magnet yoke and pole pieces has proved satisfactory.

An alternating current, having a frequency of 50 cycles per second (supplied from the 0 to 270 volt variac shown in plate 4) is passed through the magnet field coils. The current is increased to a maximum of 5 amps (rms) and then reduced to zero. At this point a remanent field of a few hundred gauss remains in the pole gap due to the failure of the ac demagnetising field to completely penetrate the magnet yoke and pole piece interior. The small remanent field is removed manually by cycling the magnet slowly through a small number of complete B - H loops of decreasing maximum amplitude. The field remaining in the gap after demagnetisation of the magnet yoke and pole pieces in this way is sufficiently small to allow a 60 kev proton beam to be centred on the straight through port of the magnet beam tube.

The magnet ac demagnetisation and dc power supply controls are fully interlocked to prevent ac power from being applied to the magnet field coils while the dc power supply is still connected. DC power can only be supplied to the magnet field coils when the ac demagnetising variac is in the zero current position, and the variac is isolated from the magnet circuit. In the event of a failure in the main power supplied to the dc magnet power supply, the high voltage induced in the magnet field coils by the collapsing dc magnetic field, is discharged by a catching diode placed across the power supply output. (The diode polarity is such that it is normally non-conducting).

3,1,4, THE VACUUM SYSTEM:

The position of the three main diffusion pumps is shown in figure (18). (The target assembly is pumped with a 2" oil diffusion pump which is not shown). Each diffusion pump is backed with a separate mechanical rotary pump, and is equipped with a liquid nitrogen cold trap as an integral part of the pump.

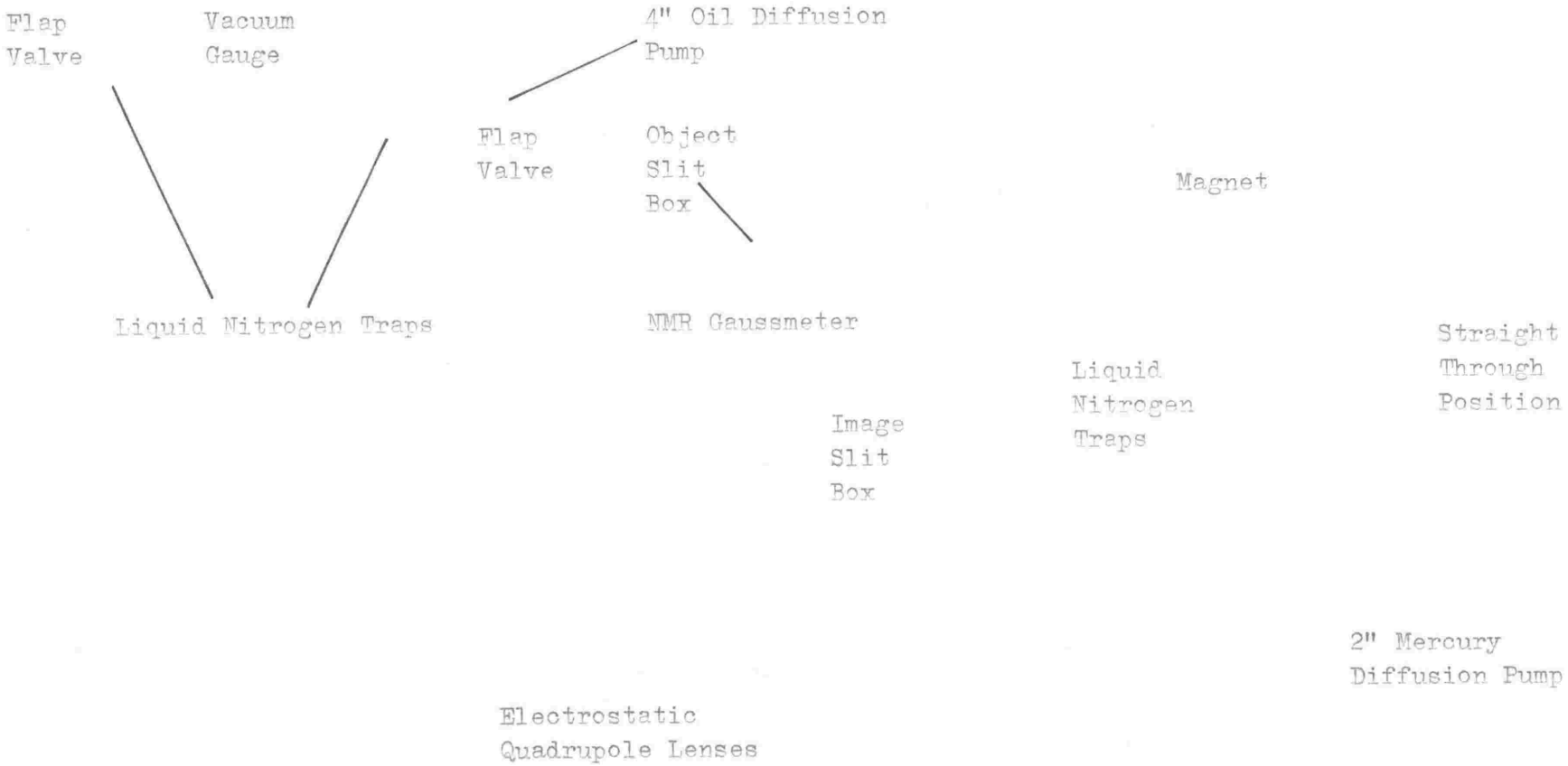

PLATE 6 LAYOUT OF VACUUM EQUIPMENT

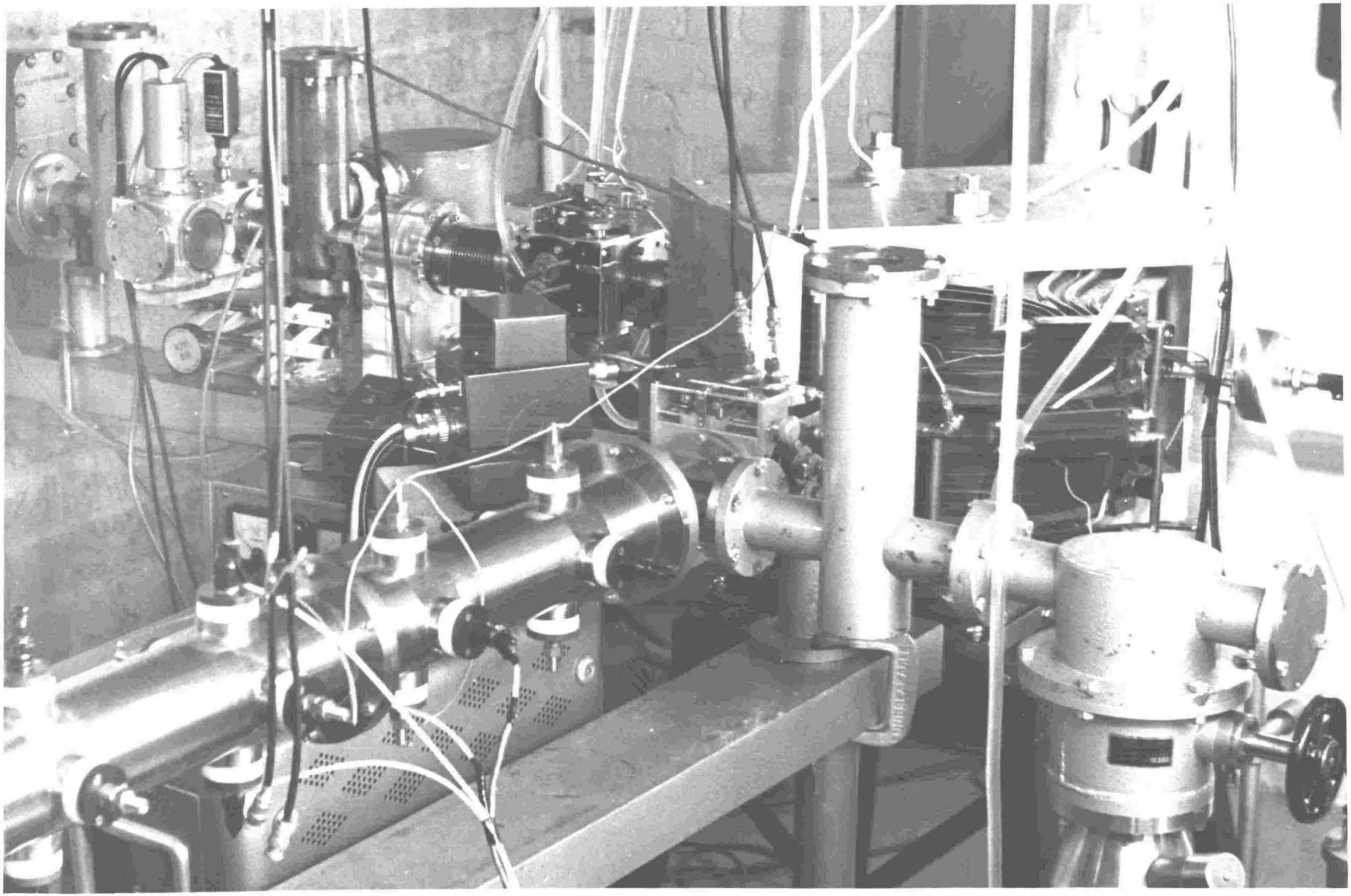

When the accelerator is not in use, the ion source glass envelope and accelerator beam tube up to a flap valve located at the dividing wall, is maintained under a vacuum corresponding to a pressure of 1 x 10^{-5} mm of mercury, by a 2" oil diffusion pump which is run continuously. The remainder of the beam tube is maintained at a pressure of approximately 15 microns, using two mechanical rotary pumps.

Before the accelerator is operated the entire beam tube is evacuated to a pressure of 1 x 10^{-5} mm of mercury, using the additional 2" and 4" oil diffusion pumps. The average pressure in the beam tube is decreased to about 3 x 10^{-6} mm of mercury on filling four liquid nitrogen cold traps situated at intervals along the beam tube. When an ion beam is produced by the accelerator, the additional gas entering the vacuum system (due to gas pumped from the ion source and outgassing of beam tube components heated by the ion beam) causes the average pressure in the beam tube to rise to a steady value between 5 x 10^{-6} and 1 x 10^{-5} mm of mercury.

3.1.5. MAGNET FOCUSSING PROPERTIES

The paths of charged particles in the horizontal and vertical planes of the image space of the analyzing magnet have been calculated using equations (7) and (14), section (2.2.1.2) respectively. Figure (27) shows the paths taken by particles in the horizontal and vertical planes for the magnet configuration $E_o = E = 26^o\ 34'$; $y_o = y_d = 2$. (The diagrammatic representation used is the direct analogy of a ray diagram for image formation by a thick lens in the equivalent optical case). The beam profile, assuming a square object, is shown for a number of distances from exit magnetic field boundary. This focussing configuration exhibits a cross-over in the image space which is smaller than the image itself. Image formation for a second double focussing case $E_o = 20^o$; $E = 43^o 26'$; $y_o = \infty$: $y_d = 0.556$; is shown for comparison. This configuration can be used to provide a point

ION TRAJECTORIES IN THE HORIZONTAL AND VERTICAL

PLANES OF THE ANALYZING MAGNET

(a) FOR THE DOUBLE FOCUSSING CONFIGURATION

$E_o = E = 26^o34'$; $y_o = y_d = 2$

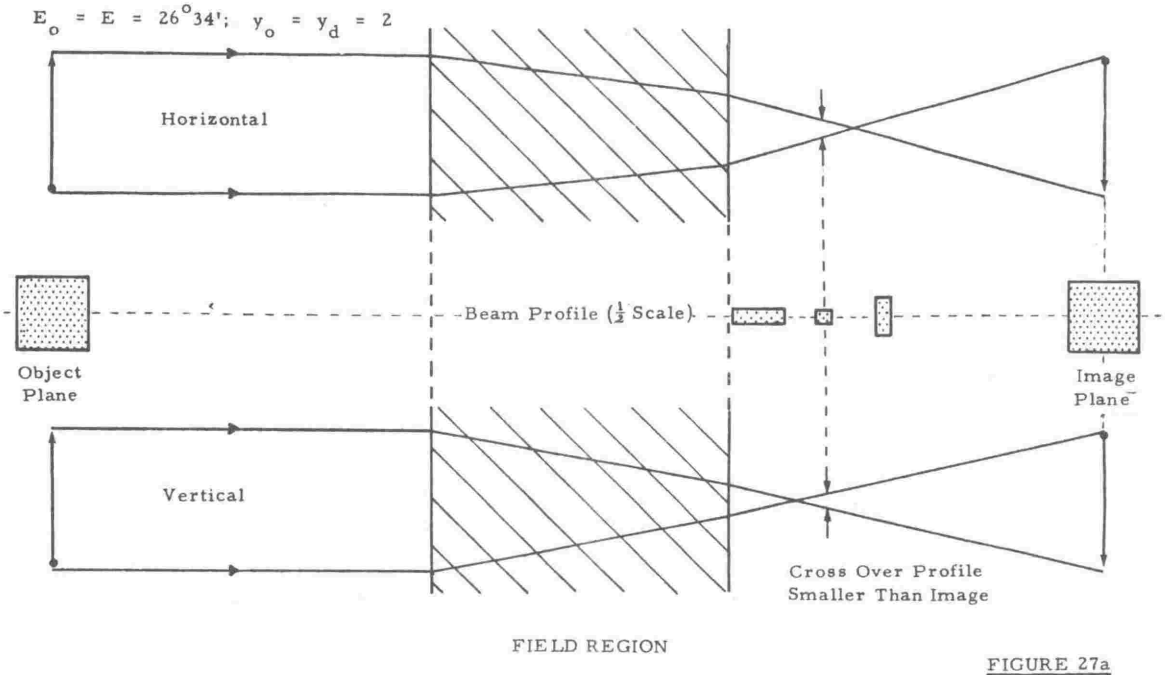

FIGURE 27a

(b) FOR THE DOUBLE FOCUSSING CONFIGURATION

$E_o = 20^o$, $E = 43^o26'$; y_o $y_d = 0.556$

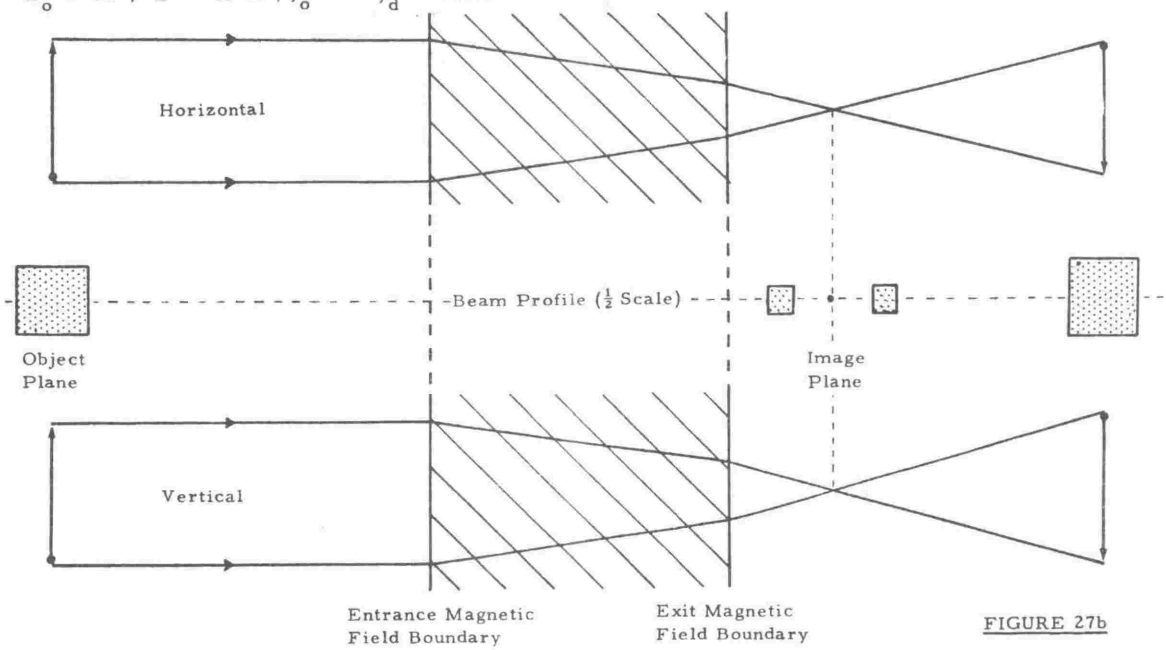

FIGURE 27b

object in the analyzer image space for a quadrupole lens following the analyzing magnet.

The focussing properties of the analyzing magnet were investigated in the following way. The magnet and magnet beam tube were positioned approximately, using a template designed on the basis of the predicted magnet deflection properties (figure 10). The image slit box was replaced by a perspex flange onto which was cemented a quartz disc covered with a fine mesh grid of tungsten wire. The ion current striking the quartz disc was collected on this discharge grid and read on the target current meter in the accelerator control console. The beam was maintained on the quartz disc by manual control of the ion beam energy (see appendix 5). The fluorescence of the quartz disc in the area bombarded by the ion beam, enabled the profile of the emergent ion beam to be directly observed. Fine adjustments were made to the magnet alignment in order to centralise the emergent ion beam accurately on the 90° magnet beam tube port. It was found that a comparison between the observed beam profile and the predicted beam profile calculated from figure (27) provided a useful guide in aligning the magnet.

The image formed by the analyzing magnet of the uniformly illuminated rectangular object slit, is a rectangle with straight sides. This indicates that aberrations in image formation introduced by field non-uniformities in the magnet pole gap, and through neglceting second order terms in A, B and x_o, in the magnet design (equation 7, section 2.2.1.2) are negligible. The vertical height of the image is found to bear a linear relation to the height of the object slit, up to the maximum object slit opening of 1 cm. The conclusion is that the beam size is not restricted by the vertical aperture of the magnet beam tube and that the transmission of a particular ion group (see section 3.4) through the magnet is virtually 100%.

The image has both a slow lateral drift, and a low amplitude, rapid, random horizontal jitter which can just be followed by eye. The slow changes in image position, which have a typical periodicity of several seconds, correspond to changes in the generator terminal potential of approximately $\pm$ 4%. This figure is calculated from the observed amplitude of the image displacements and the known dispersion of the analyzing magnet (figure 19). The rapid image displacements correspond to terminal potential fluctuations of amplitude less than 1% of the terminal potential. The frequency of these fluctuations is typically between 2 and 20 cycles per second.

The estimated geometrical image width (i.e. the width of the image in the absence of the fluctuations in the ion beam energy discussed above) is in good agreement with the value expected from figure (27), for the particular distance of the quartz disc from the magnetic field boundary. When the ion beam is focussed on the object slit, the beam profile observed in the image plane of the analyzing magnet is, in the first order, identical with the beam profile in the plane of the object slit. As expected the focussing properties of the analyzing magnet show no significant variation with the energy or the charge to mass ratio of the ions in the analyzed beam.

3.1.6. THE STABILIZATION SYSTEM:

In order to investigate the performance of the stabilization system the image slit box was mounted on the 90° magnet beam tube port. The analyzed ion beam passing through the image slit was viewed on a quartz disc which was mounted, in the manner described above, on the exit port of the image slit box. The analyzed beam position was observed as a function of the gain of the stabilization feedback loop, with the following results. (A detailed description of the operation of the accelerator in conjunction with the stabilization system is given in appendix (5)).

THE ENERGY STABILIZED ACCELERATOR

PLATE 7

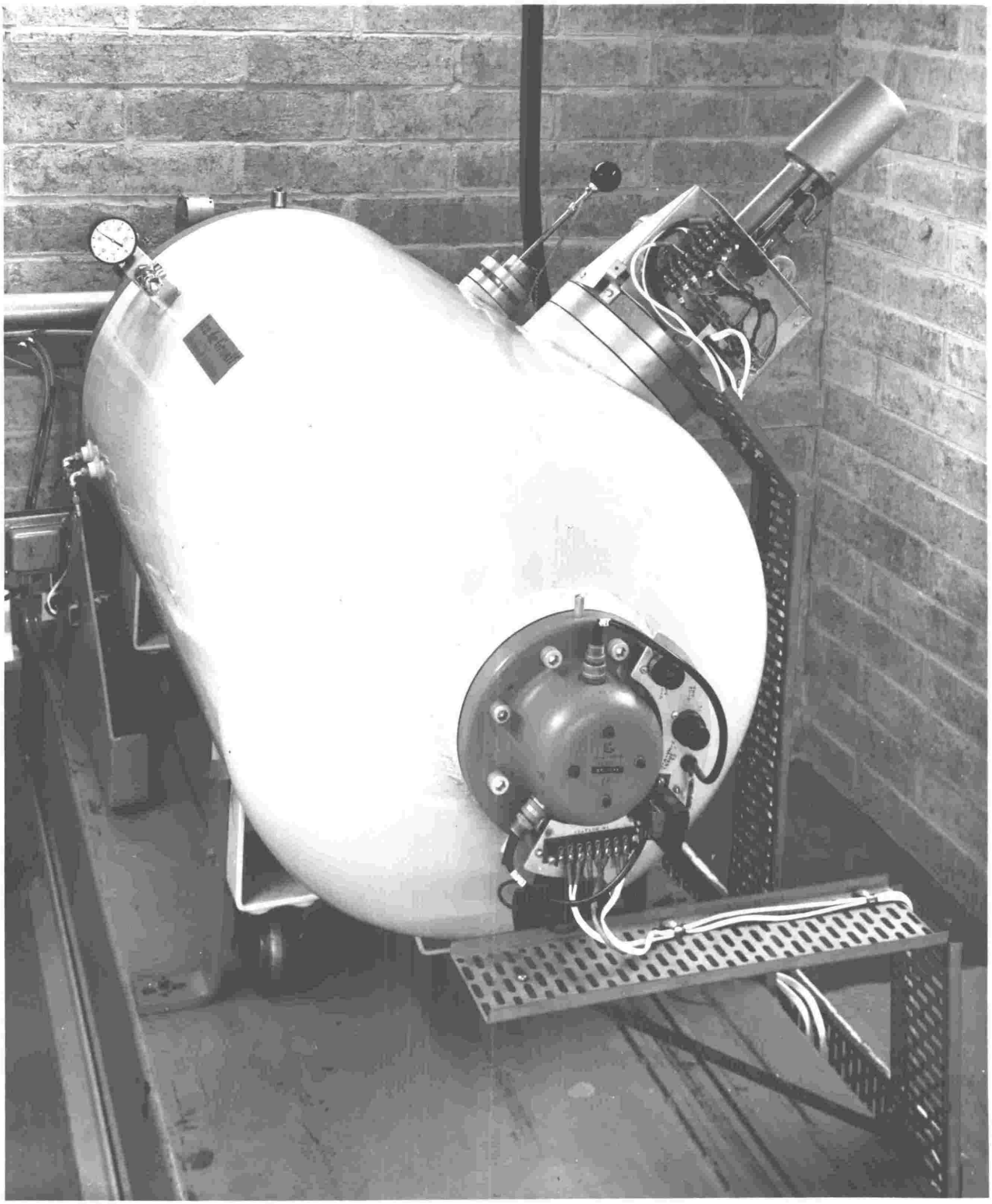

With the stabilizing amplifier gain at zero, terminal potential fluctuations cause the analyzed ion beam position to fluctuate in the manner already described (in section 3.1.5). Only the slowest of these changes can be corrected by manual control of the accelerator terminal potential. As the stabilizing amplifier gain is increased the analyzed ion beam is constrained between the energy defining electrodes by the action of the stabilizing system. At low loop gains the current striking the energy defining electrodes is an appreciable fraction ($\sim 50\%$) of the total analyzed beam current. Increases in amplifier gain cause the ion current striking each electrode to decrease.

For stable, balanced operation of the stabilizing amplifier (as described in appendix 5) the current striking each electrode is found to be typically between 5 and 10% of the total analyzed ion current passing through the image slit. This figure does not depend greatly on the image slit width (provided the object slit width is kept equal) or on the total intensity of the analyzed ion beam. It is concluded from these observations that the fluctuations in terminal potential observed in the absence of stabilization, are considerably reduced by the action of the stabilization system.

The response of the stabilization system to large amplitude changes made in the accelerator operating conditions, depends of course, on the initial settings of the accelerator and stabilization controls, and on the magnitude of the analysed ion current. For example, for typical values of the analyzed ion currents (10 to 20 μA) a current of approximately 1 μA strikes each energy defining electrode, when the stabilized accelerator is operated under the optimum settings outlined in appendix (5). Under these conditions the belt charge current can be altered over a range of at least 50 μA. without any change being observed in the accelerator terminal potential. (The range of belt charge current change which can be compensated for by the stabilization system is determined in practice by the operating current range

of the corona triode). Furthermore, the accelerator terminal potential can be swung over a range of 100 kv or so, solely by changes made in the magnet current. (The limit here, is set by the drop in analyzed ion current resulting from defocussing of the primary ion beam caused by the change in terminal potential).

From a practical point of view, the stabilization system should remain 'locked' onto the analyzed ion beam, while fine adjustments are made to the accelerator controls. This has proved to be the case, although the demands made on operator skill increase when the analyzed ion current is below 1 or 2 μA and high settings of loop gain are used. Most difficulties are obviated if adjustments are made in the rotational sequence described in appendix (5). No serious difficulties have been experienced in operating the energy stabilized accelerator over the range of analyzed ion currents ($\sim\frac{1}{2}$ μA to 40 μA) and energies (60 to 500 kev) used to date. A measurement of the spread in energy of the analyzed ion beam, and a more detailed analysis of the performance of the stabilization system is given in section 3.3.

3.2. ENERGY CALIBRATION OF THE MAGNET:

3.2.1. INTRODUCTION

The energy of the ion beam is determined by using the analyzing magnet as a precision momentum spectrometer. Two methods are available for calibrating the energy of the analyzed ion beam in terms of the magnetic field strength at the site of the field measuring probe.

In the first, the magnetic field strength along the particle trajectory between the object and image slits is accurately measured for a given value of the magnetic field strength B_o, at the normal site of the gaussmeter probe. The integrated effect on the particle trajectories, of the non-uniform magnetic field regions, is then allowed for by evaluation of the integral in equation (8), appendix (6). In this way, the real magnetic field distribution can be replaced for the purposes of calculation, by an equivalent uniform magnetic field of strength

B_o, located between effective magnetic field boundaries situated outside the real pole boundaries. The value of the radius of curvature required to give 90^o deflection of the ion beam can then be calculated, and the analyzed ion beam energy related to the value of B_o through equation (40) (2.2.1.7.). The advantage of this method of energy calibration is that the charged particle energy is related to the magnetic field strength in terms of the fundamental physical quantities of charge and mass.

In practice, however, this method has a number of disadvantages. In general the precise ion trajectory within the magnetic field is not known, and if the evaluation of the integral in equation (8), appendix (6) is not to become subject to appreciable error, special techniques for determining the exact ion trajectory in the magnetic field region must be employed. Included in these techniques, for example, are such methods as employing a light flexible current carrying wire stretched between the object and image slit to duplicate the particle trajectories when the field is applied[63]; closely defining the ion beam path within the field region with a series of narrow apertures placed along the beam path[25]; and tracing the ion path through the field region using a trial and correction procedure such as that described by Bainbridge[51]. (In this latter method the field is measured in the first instance, along the estimated ion path. The equations developed in appendix (6) then enable a more accurate estimate of the ion path to be made, over which the field is remeasured. The actual ion path through the magnetic field region is determined by successive application of this iterative procedure). In general these techniques are difficult to apply. With the type of magnet yoke configuration used in the present analyzer, there is the added technical difficulty of positioning the field measuring probe with sufficient accuracy, within the narrow confines of the magnet pole gap. For these reasons a second method of energy calibration, which obviates the above field integration problem, is used in this work.

In this method, the magnetic analyzer is calibrated by measuring the analyzed ion beam energy directly in terms of the resonance energy of nuclear reactions induced in suitable target materials. These resonance energies are accurately known from previous absolute measurements in which either a magnetic analyzer and a calibration technique similar to that described above[25,70], or an electrostatic analyzer[30,31] (to which the above disadvantages do not apply) has been used.

To be suitable for calibration purposes, reactions in addition to having a precisely known resonance energy, should have a narrow resonance width[64], a high reaction cross section at resonance, and an easily detected reaction product. The following table lists four reactions chosen as being suitable for calibration purposes in the low energy region of interest, ($E < 500$ kev.)

TABLE 1

	Reaction	Resonance Energy (kev)	Full Width (kev)	Reference	Cross Section (mb.)	Reference
	$B^{11}(p,\gamma)\ C^{12}$	163.1 ± 0.4	7.0 ± 1 6.3 ± 1	66 65	0.16	67 68
*	$F^{19}(p,\alpha\gamma)\ O^{16}$	340.5 ± 0.2	3.3 ± 0.2 2.4 ± 0.3	25,70 30	160	69
	$Li^{7}(p,\gamma)\ Be^{8}$	441.2 ± 0.3	12.0 ± 1 12.2 ± 0.5	25,70 65	6.0	71 72
*	$F^{19}(p,\alpha\gamma)\ O^{16}$	483.6 ± 0.3	0.9 ± 0.1 1.5 ± 0.2	30 31	> 32	69

The two fluorine $(p,\alpha\gamma)$ reactions marked with an asterisk are particularly suitable as calibration reactions, because of their relatively narrow resonance width and large cross-section.

3.2.2. EXPERIMENTAL:

3.2.2.1 TARGET PREPARATION:

The targets used for calibration purposes were in all cases thick targets, i.e. the energy lost by a proton (having an energy close to the resonance energy of the reaction under study) in traversing the target, was large compared with the reaction resonance width. Targets were prepared by evaporating from a hot filament in vacuum, a thin film of target material onto the polished surface of a 1mm. thick copper disc. Compounds were chosen which evaporated at a lower temperature than the temperature at which they decomposed. The compounds used were sodium tetraborate (boron target), calcium fluoride (fluorine target), and lithium fluoride (lithium target).

One of the difficulties encountered in bombarding a target with a beam of charged particles is the buildup of a surface layer of carbon due to the decomposition on the surface of the target of organic vapours from the vacuum system[30]. This effect was reduced by isolating the target from the rest of the vacuum system with a liquid nitrogen cold trap placed immediately in front of the target. A further reduction in the rate of carbon buildup was achieved by maintaining the target temperature[64] above the temperature of the surrounding beam tube. Even so, appreciable carbonisation (a layer having an equivalent thickness of 0.5 kev for a 400 kev proton) had formed on targets that had received more than 10^4 micro-coulombs of protons. For this reason fresh targets were inserted immediately prior to the precise calibration runs.

In the first experiments the front face of the target was covered with a tungsten mesh discharge grid, to prevent error from charge accumulation on the non-conducting target surface. This precaution was subsequently found to be unnecessary as no displacement of the resonance peaks was observed on removing the grid.

3.2.2.2 EXPERIMENTAL PROCEDURE:

The high energy gamma-rays produced in the target were detected with a scintillation detector placed in close proximity to the target. The scintillation detector comprised a NaI (T1) scintillator ($1\frac{1}{4}$ inches in diameter by $1\frac{1}{8}$ inches deep) optically coupled to a 6810-A photomultiplier tube. The pulses from the photomultiplier were amplified and fed into an integral pulse height discriminator, the output of which was recorded on a ratemeter, or in the case of the boron resonance reaction, on a scaler. Because of the low cross-section of this reaction at resonance, it proved necessary to shield the scintillation detector with lead, in order to reduce the background count rate in the photomultiplier channel. The photomultiplier was operated at a reduced EHT voltage and a high discriminator threshold bias voltage was used. The pulses recorded then corresponded to an energy release of 2 Mev or more in the scintillator, and the contribution from the background count rate to the total count rate at resonance was less than 3%.

The target was mounted on a liquid nitrogen trap placed at the exit of the image slit box. The horizontal object and image slit widths were each set a 1 mm (corresponding to a total fractional energy spread of 5 parts in 10^3 in the analyzed proton beam). The stabilization system was used to hold the analyzed proton beam centred on the image slit. Low target currents (typically about 2 uA) were used so as to avoid excessive local heating of the thin target film.

The bombarding energy of the protons was increased stepwise through the resonance value of the reaction under study, by altering the magnetic field in the magnet pole gap. The gamma-ray count rate, target current, and NMR gaussmeter frequency were accurately measured at each point. The gamma-ray yield per micro-coulomb of proton beam striking the target was calculated for each point and a thick target resonance step plotted (as in figure 28) for each of the four reactions listed in table 1.

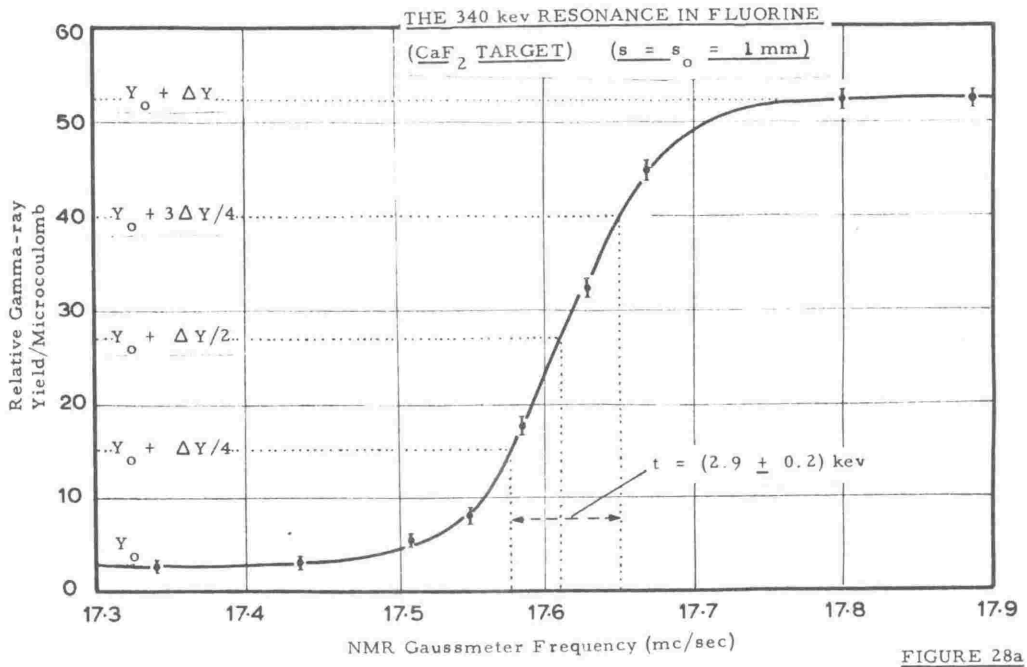

FIGURE 28a

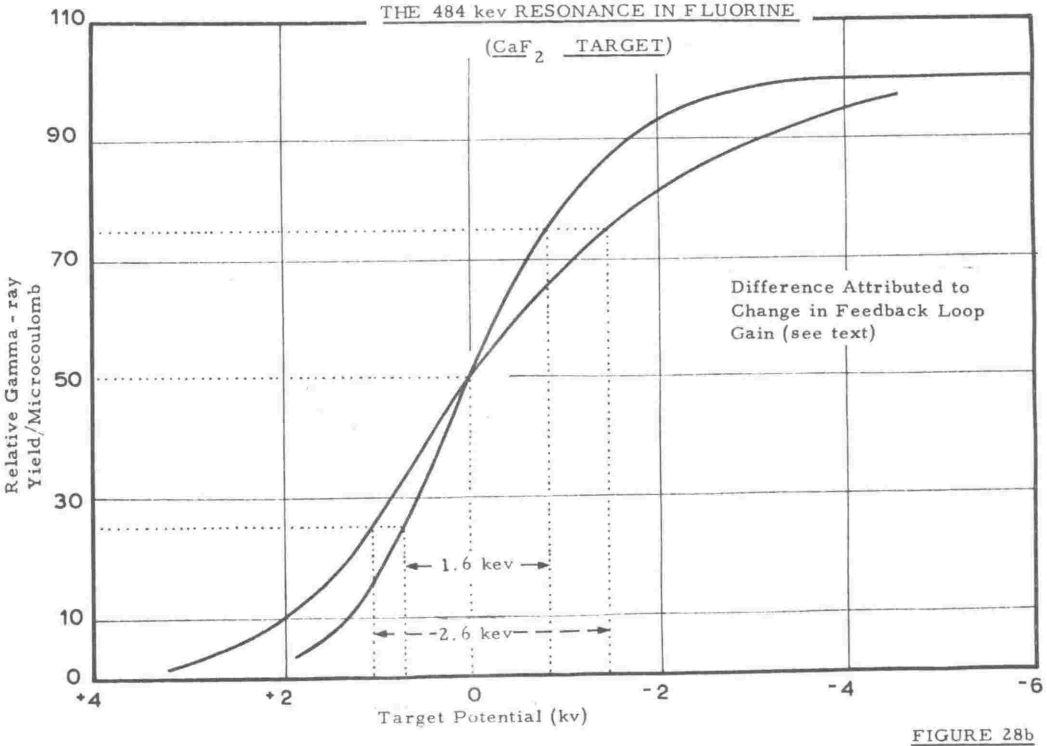

FIGURE 28b

3.2.3. ANALYSIS OF RESULTS:

The experimental points are fitted with an approximate least squares fit (see figure 28). The resonant energy is the energy at which the increase in yield is one half the maximum increase in yield of the thick target step[64]. If the background (off resonance) gamma-ray yield is Y_o and the increase in yield of the thick target step is ΔY, then the resonant energy corresponds to the yield $Y_o + \frac{1}{2}\Delta Y$. The NMR gaussmeter frequency corresponding to this value of the yield is the frequency corresponding to the reaction resonance energy. The values obtained in this way are summarised in table 2.

TABLE 2

TARGET NUCLIDE	PROTON ENERGY (KEV)	GAUSSMETER FREQUENCY (MEGACYCLES / SEC.)
Boron	163.1	12.18 ± .02
Fluorine	340.5	17.61 ± .01
Lithium	441.2	20.10 ± .03
Fluorine	483.6	21.04 ± .02

SOURCES OF ERROR:

The magnetic field measurement is subject to two possible errors; the first a setting error of ± .01 mc/sec. in determining the gaussmeter frequency (largely eliminated by the method of data analysis); the second caused by errors in reproducing accurately the gaussmeter probe position within the magnet pole gap. This error is found to be negligible (3.1.2.).

In the course of setting up the stabilization system a large number of $(p,\alpha\gamma)$ reaction resonance measurements have been made under different conditions of focussing, intensity and total

energy spread of the analyzed proton beam. The gaussmeter frequencies corresponding to the midpoint rises in yield for the 340 kev fluorine resonance agree to within $\pm$ .01 mc/sec. in all cases in which a fresh target had been used. The shift in the observed resonance energy [65] caused by carbon deposits and charge accumulation on the non-conducting target surface is therefore estimated as being less than 0.2 kev.

The main experimental error occurs in the determination of the gamma-ray count rate per microcoulomb of protons delivered onto the target. The error bars shown in figure (28) represent the fractional standard deviation[74] in ratemeter reading together with the error introduced through uncertainties in target current. The error in the gaussmeter frequency at resonance, quoted in table 2, arises mainly through the uncertainty in the precise position of the thick target step introduced by these two sources of error.

The values assumed for the resonance energies of the first three reactions listed in table 1, follow the values recommended by Marion[73] in a review article dealing with accelerator calibration. The value used for the 484 kev fluorine resonance is the value obtained by Bondelid and Kennedy[30]. Using the same electrostatic analyzer and calibration technique these workers obtained the value quoted in table 1 for the 340 kev fluorine resonance. The four values quoted in table 1 should therefore be mutually consistent and the relative resonance energies should lie within the quoted error. The absolute accuracy of the quoted resonance energies is, however, in some doubt. (For example, in recent determinations Hunt et al[31] have obtained higher absolute values (340.9 and 484.3 kev) for both fluorine resonance energies).

ENERGY CALIBRATION:

For non-relativistic velocities, the proton energy E_p is related to the measured NMR gaussmeter frequency f by the equation

$$E_p = k_p f^2 \qquad \text{----------(1)}$$

where k_p depends on certain physical constants of the proton (compare, for example, equations (40) and (49), chapter 2) and on the effective radius of the analyzer. (The effect of relativistic corrections, for proton energies less than 500 kev, amount to a change in k of less than one part in 2,000). Substituting the experimental values obtained (table 2) into equation (1) gives the value of k corresponding to each calibration point.

TABLE 3

f in mc/sec	E_p in kev	k_p
12.18 $\pm$ .02	163.1 $\pm$ .4	1.099 $\pm$ .006
17.61 $\pm$ .01	340.5 $\pm$ .2	1.098 $\pm$ .002
20.10 $\pm$ .03	441.2 $\pm$ .3	1.091 $\pm$ .004
21.04 $\pm$ .02	483.6 $\pm$ .3	1.092 $\pm$ .003

The error quoted in k is calculated from the possible experimental error in f, and the possible error in the absolute value of E_p, and therefore represents the possible error in the absolute value of k. The relative values of k should be consistent to within half the quoted absolute error. The value of k exhibits, within the relative error, a systematic decrease with increasing proton energy. This variation of k with energy is attributed to the variation of the effective analyzer radius with the magnetic field strength in the analyzing magnet pole gap (see section 3.2.4.)

The energy calibration can be extended to ions having a different charge, e, and mass, m , by use of the following relation derived from equations (40) and (49) chapter 2,

$$\frac{k}{k_p} = \frac{e}{m} \cdot \frac{m_p}{e_p} \cdot \frac{R^2}{R_p^2} \qquad \text{----------} \qquad (2)$$

where R is the effective analyzer radius. For a given value of frequency, R is equal to R_p and the value of k corresponding to the known value of k_p at this frequency can be calculated from equation (2). The following are the primary calibration points expressed in terms of deuteron energy.

TABLE 4

f in mc/sec	E_d in kev	k_d
12.18	81.5	$0.5496 \pm .0030$
17.61	170.2	$0.5491 \pm .0010$
20.10	220.5	$0.5456 \pm .0020$
21.04	241.7	$0.5461 \pm .0015$

The energy calibration for the three main ion species found in a hydrogen beam is shown in figure 29(a). Figure 29(b) gives the similar curves for ion species in a deuterium beam. These curves have been plotted from data calculated from the primary proton calibration points using equation (2).

3.2.4. THE EFFECTIVE ANALYZER RADIUS:

The decrease in k with increasing proton energy is attributed to the following effects. As the magnetic flux density within the magnet yoke is increased the permeability of the magnet iron increases over the range of flux densities of interest (figure 9) The resulting decrease in the magnetic reluctance of the magnet yoke and pole pieces, in relation to the parallel leakage flux paths in air, increases the tendency of the magnetic flux to be constrained within the magnet iron. The field strength at a point in the median plane of the magnet fringing field then becomes a lesser fraction of the uniform magnetic field strength in the magnet pole gap. Furthermore, the concentration of magnetic flux in the region

MAGNET ENERGY CALIBRATION

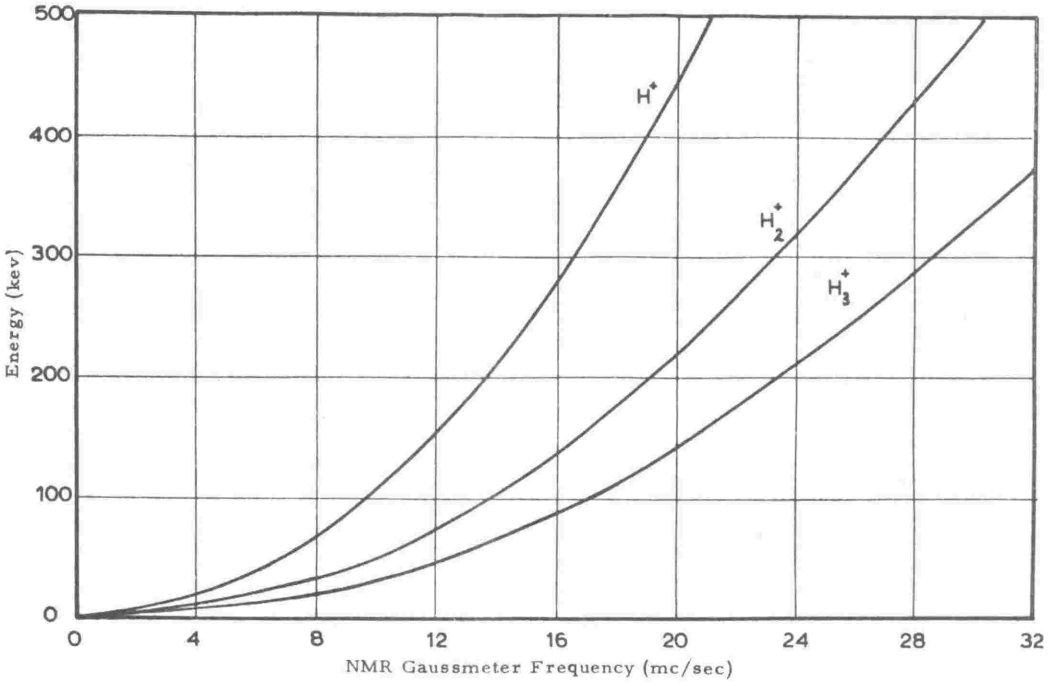

FIGURE 29b

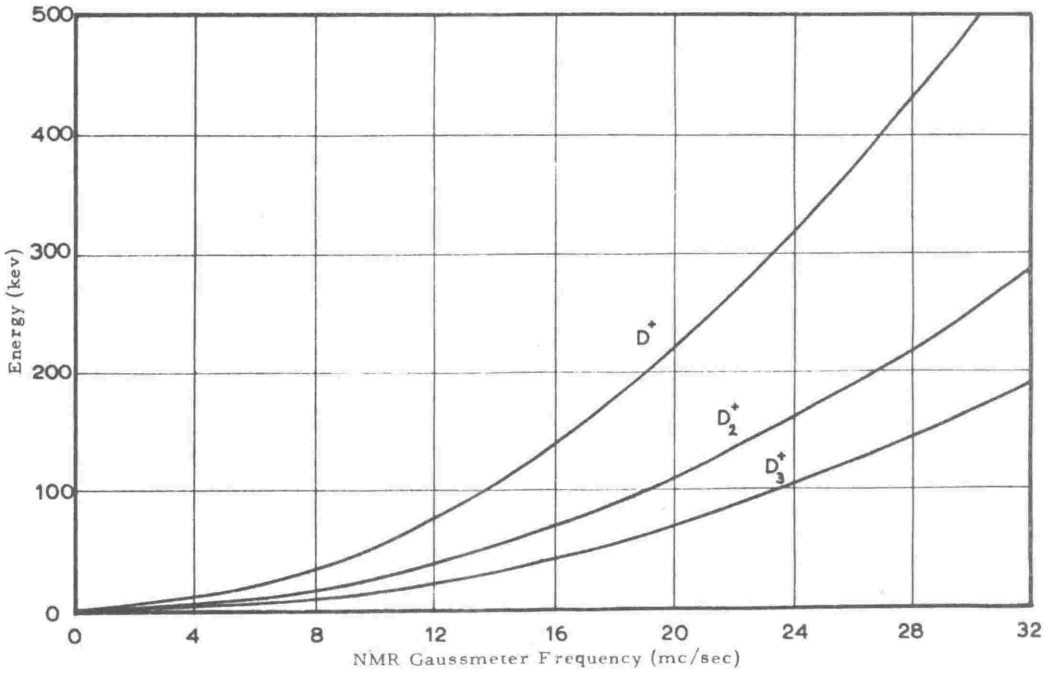

FIGURE 29a

of the sharp pole edges, at the positions where the particles enter and leave the magnetic field, causes the magnet iron in this vicinity to saturate even at very low fields. As the field is increased the area of local saturation increases and causes a relative decrease in the magnetic field strength near the pole piece boundaries. These two effects result in a decrease in the size of the effective magnetic field region at higher fields. The effective analyzer radius and consequently, the value of k, therefore, decrease with increasing magnetic field strength in the magnet pole gap.

In a practical magnet, inhomogeneities in the permeability of the magnet iron, together with discontinuities and local saturation effects occurring in the magnet yoke and pole pieces cause unpredictable perturbations of the magnetic flux distribution within the median plane of the magnet pole gap. It is not possible therefore to predict on theoretical grounds the variation of k with magnetic field strength in the pole gap, or to assess the relative contributions of the two effects discussed above to the variation of k.

Magnetic measurements made on an analyzing magnet[75, 76] made of a similar low carbon steel to the present analyzer, indicate that corner saturation effects would contribute only a few parts per thousand to the variation in k even at fields as high as 15,000 gauss in the magnet pole gap. For this reason, and in view of the relatively low permeability and high saturation flux density of the steel used in the present analyzer construction, the changes occurring in the reluctance of the magnet yoke are thought to be the predominant cause of the variations in k.

THE STRENGTH OF THE MAGNET FRINGING FIELD:

In order to confirm the existence of a decrease in effective analyzer radius with increased magnetic field strength, the strength of the magnet fringing field was measured as a function of distance from the magnet pole boundaries for two values of flux density in the magnet pole gap (corresponding to NMR gaussmeter frequencies of 12.18 mc/sec. and 21.04 mc/sec respectively) The strength of the strongly non-uniform fringing field was measured

in the following way.

The emf generated in a Hall magnetic field measuring probe[77] was calibrated directly in terms of the NMR gaussmeter frequency, with both field probes located in the same uniform magnetic field. The calibration of the Hall voltage in terms of magnetic field was found to be reproducible to within the limits of accuracy with which the emf could be determined (2 parts in 10^4). The accuracy of field measurement using a Hall probe calibrated in this way was better than 5 parts in 10^4 for fields greater than 1000 gauss, and approximately 1% for fields in the region of 100 gauss. The use of a special jig which was a neat fit within the magnet beam tube enabled the sensitive area of the Hall probe (1 square mm) to be positioned with an accuracy of 0.1 mm with respect to a datum line marked on the magnet beam tube.

Measurements of field strength were taken at 1 cm intervals along the ion beam trajectory over a range extending from the image slit to the uniform field region within the magnet pole gap. Two values were obtained for the field strength at each point, the first when measuring the field moving stepwise away from the magnet, the second moving towards the magnet. These two values agreed to within 0.15% in all cases.

The field strength corresponding to the average of the two readings at each point is shown in figure (26b) as a function of the distance from the arbitrary datum line for the case f = 21.04 mc/sec. The field strength is expressed in terms of the uniform magnetic field strength at the site of the NMR gaussmeter probe. For comparison the theoretical curve[51] based on the assumption of semi-infinite pole pieces of infinite permeability, is also included.

The separation of the effective magnetic field boundary from the real pole boundary was found from the equation obtained by substituting the experimental value of y' (=2.75 cm) in equation (8), appendix (6) i.e.

$$d = \int_{-y_d}^{2.75} b(y)\, dy - 2.75 \qquad \text{----------} \qquad (3)$$

The integral in equation (3) was evaluated using numerical integration to find the area under the curve b(y) versus y, between the stated limits of y. The values obtained for d (measured along the ion path direction) were

$$d_1 = (1.95 \pm .01) \text{ cm} \quad \text{for} \quad f = 12.18 \text{ mc/sec}$$

$$d_2 = (1.88 \pm .01) \text{ cm} \quad \text{for} \quad f = 21.04 \text{ mc/sec}$$

The absolute value of d calculated in this way is subject to large errors introduced by the factors discussed in section 3.2.1., and by the large uncertainty in y' caused by experimental difficulties in determining the precise distance of the real pole boundary from the reference datum line. The relative value of d_2 with respect to d_1 is largely independent of errors from these sources, as such systematic errors do not affect the difference $(d_2 - d_1)$. The error quoted above for d_1 and d_2 includes only those errors affecting the relative value of d_1 and d_2, namely the error introduced into the evaluation of the integral by experimental errors in the measurement of magnetic field strength and the value of y relative to the chosen datum line.

The decrease in effective analyzer radius ΔR corresponding to the increase in magnetic field strength is simply $(d_2 - d_1)$. The resulting fractional change in the analyzer calibration factor k, found from differentiation of equation (2) is

$$\frac{\Delta k}{k} = \frac{2\Delta R}{R} = (7 \pm 2) \text{ parts per 1000.}$$

This value is in good agreement with that obtained on the basis of (p, γ) reaction resonance energies.

3.2.5 DISCUSSION:

The energy of the momentum analyzed ions is related to the NMR gaussmeter frequency through the analyzer calibration factor k (equation 1), where the value of k depends on the charge to mass ratio of the ions (equation 2) and to a limited extent on the magnetic field strength in the magnet pole gap. The error introduced through inaccuracies in measurement of gaussmeter frequency can be made negligible compared with other experimental errors, and hence the accuracy of the energy calibration at a given ion energy depends on the accuracy with which k may be determined for the corresponding value of the magnetic field strength.

For proton energies in the range 0 to 500 kev (and deuteron energies 0 to 250 kev) the value of k can be determined with an accurancy of $2\frac{1}{2}$* parts per 1000, by taking an average, weighted according to frequency, of the two values of k corresponding to the two fluorine resonance reactions. For the highest accuracy the value of k, for deuteron energies greater than 250 kev, should be obtained by comparing the measured fringing field distribution with the distribution at a magnetic field strength for which the value of k is accurately known, (for example, at the magnetic field strength corresponding to the 340 kev fluorine resonance). Changes in k of less than 2 parts per 1000 can be detected by such a comparative method. The individual errors in k are independent and so the total error in k is given by the square root of the sum of the squares of the individual errors. For deuteron energies greater than 250 kev, k can therefore be determined with an accuracy of better than 3 parts per 1000.

* This figure is determined in the main by uncertainties existing in the absolute values of the (p, γ) reaction resonance energies

A second experimental method can be used to determine k in this range of magnetic field strengths. Two additional calibration points can be determined for magnetic fields corresponding to gaussmeter frequencies of approximately 24.4 mc/sec. and 36.5 mc/sec., by studying the boron (p,γ) resonance using an H_2^+ ion beam (of $\sim$326 kev) and an H_3^+ ion beam (of $\sim$489 kev) respectively. The accuracy of this method is severely limited however, by the large fractional error in the absolute value of the boron resonance energy (table 1), and by the experimental inaccuracies introduced because of the low cross-section and relatively large resonance width of the boron reaction. For this reason, the first method is to be preferred and is used in this work.

3.3. THE ENERGY RESOLUTION OF THE ENERGY STABILIZATION SYSTEM:

The total energy spread in the analyzed ion beam depends only on the horizontal object and image slit widths (equation 39, section 2.2.1.6). The energy spread (full width at half maximum; abbreviated in the following to (fwhm)) can be calculated from the total energy spread, only by assuming a particular form for the energy distribution (i.e. the number of particles having a given energy as a function of energy) within the analyzed ion beam. It has been shown (section 2.3.1.2) that for a uniform distribution of energies at the entrance slit of the analyzer, the output beam profile (number of particles plotted as a function of distance across the image plane) is an isosceles triangle centred around the path of a particle having the mean ion beam energy. Most authors [78,79,80], e.g., then assume without further elaboration, that the energy distribution of the ion beam in the image plane of the analyzer also takes the form of an isosceles triangle. The reason for this assumption is not apparent.

In practice the energy distribution in the incident ion beam is not uniform but depends on the amplitude and frequency of the fluctuations occurring in the potential of the Van de Graaff accelerator high voltage terminal, and therefore on the gain and frequency response of the energy stabilizing feedback loop. If the terminal potential is assumed to have a normal * distribution[81] about a mean potential, then the energy distribution in the ion beam (averaged over a time interval that is long compared with the typical period of the terminal potential fluctuations) is a normal distribution centred about a mean energy. This mean energy is the energy corresponding to the mean line central orbit through the analyzing magnetic field. As particles neither gain nor lose energy during deflection in the magnetic field, the energy distribution of the ion beam in the image plane of the analyzer, is a normal distribution. The energy distribution of the section of the ion beam passing through the image slit is determined by the ratio of the image slit width (measured as the fractional change in energy required to displace the ion beam through one slit width in the image plane) to the width (fwhm) of the normal energy distribution of the ion beam in the image plane.

According to the theory of servomechanisms[82,83] an error in the potential of the high voltage terminal is decreased by a factor $1/(1 + G)$ where G is the loop amplification. In practice G is a function of frequency, and the degree of cancellation of an error in the terminal potential, depends on the rapidity with which the terminal error voltage develops. For a given frequency response of the stabilization feedback loop, the energy spread in the analyzed ion beam depends on the relative amplitude of the frequency components in the fluctuations of the generator terminal potential.

* or Gaussian

The action then of the stabilizing system is to decrease the full width at half maximum of the analyzed ion beam energy distribution, in relation to the total energy spread which is determined solely by the object and image slit widths. In the ideal case, the normal energy distribution can be approximated by an isosceles triangle of base width equal to the total energy spread. The full width at half maximum of this energy distribution is then equal to half the total energy spread given by equation (39), section 2.2.1.6.

If the loop gain is decreased, the energy spread (fwhm) in the analyzed ion beam willincrease to a steady value equal to the total energy spread. Further decreases in loop gain are accompanied by decreases in the intensity of the analyzed ion beam as a smaller proportion of ions satisfy the energy requirements for transmission through the analyzer image slit. At a certain point the loop gain becomes insufficient to 'hold' the ion beam centred on the image slit and the stabilizing action ceases. At the other end of the scale, if the loop gain is increased beyond a certain value the feedback system becomes unstable and oscillations will occur unless special techniques[82,83] are employed to compensate the system.

The spread in the energy of the analysed ion beam, T_1 (fwhm) provides a measure of the effectiveness of the energy stabilization system. Experimentally T_1 can be determined by analyzing the shape of the step in the thick target yield (3.2.3) from a reaction of accurately known resonance width T_2 (fwhm). At resonance, the shape of the thick target yield curve depends on the uniformity of target composition, the reaction resonance width, and the spread in energy in the incident charged particle beam. (The Doppler broadening[64] introduced by the thermal motion of the target nuclei adds a small contribution[30] ($\sim$ 80 ev) to the effective energy spread in the incident particle beam. This contribution is negligible compared with the reaction resonance widths shown in table 1, and has been neglected in the following).

The experimentally observed resonance width, t,(fwhm) may be taken as the energy separating the one quarter and three quarter increase in yield points on the thick target step[64] (the interquartile width of figure 28). T_1, may be calculated from the experimental data using the equation relating energy widths viz:-

$$T_1^2 = t^2 - T_2^2 \qquad \text{----------} \qquad (4)$$

Figure (28a) illustrates a typical thick target yield step, obtained for the 340 kev (p,γ) fluorine resonance reaction, using the method described in section 3.2.2.2. Here small increments in proton energy are made by altering the magnetic field strength in the magnet pole gap. (For the accurate measurement of resonance widths this method has the disadvantage of disturbing the beam position within the image slit). The observed interquartile width t is (2.9 ± 0.2) kev. The large uncertainty in the resonance width T_2 (the published values cover a range from 2.4 to 3.3. kev) precludes the possibility of obtaining an accurate value for T_1 by taking the difference of squares as in equation 4. The total energy spread in the analyzed beam , calculated by substituting the known slit widths $s_o = s = 1$ mm into equation 39, Chapter 2, is 1.7 kev. This gives a value for T_1 of approximately 0.8 kev, in the ideal case of a triangular energy distribution in the analyzed proton beam. (For a value of T_1 in the range 0.8 to 1.7 kev, the observed resonance width t = 2.9 kev is consistent with the reaction resonance width T_2 being in the range 2.4 to 2.8 kev. This range is extended further by the possible experimental error in t).

Figure (28)(b) illustrates similar measurements made on the 480 kev (p,γ) fluorine resonance. In this case small changes in proton energy are made by altering the potential of the target with respect to the Van de Graaff generator earth. The magnetic field strength remains constant throughout the experiment

at a value corresponding to the mid-point of the thick target step. The measurement has been made using two settings of the feedback loop gain. The observed resonance width t, at high gain (1.6 ± 0.2 kev) is considerably smaller than the value (2.6 ± 0.2 kev) obtained with a loop gain that is only just sufficient to maintain stabilization.

The published values (table 1) of the 480 kev fluorine resonance do not agree within the quoted experimental errors. An average of the two most accurate values, as indicated by the quoted experimental errors, is used in this work, namely $T_2 = (1.2 \pm 0.2)$ kev. The energy spread in the analyzed beam calculated from equation (4) for low and high loop gains, are 2.3 kev and 1.1 kev respectively. These values are in good agreement with those predicted (2.4 and 1.2 kev) on the basis of the calculated total energy spread, and the calculated energy spread (fwhm), on the assumption of a triangular distribution of energies in the analyzed beam.

It should be emphasised that the values obtained for T_1 in this way are subject to considerable error because of the large error inherent in the difference of squares of two numbers of comparable magnitude each subject to an appreciable error, and because of the large uncertainty existing in the published values of the 480 kev fluorine reaction resonance width. However the observed decrease in the experimental width of the thick target yield step, on increasing the loop gain indicates that the frequency response of the feedback loop is adequate to effect appreciable cancellation of the higher amplitude frequency components in the potential fluctuations of the generator terminal. The actual energy spread (fwhm) in the analyzed ion beam will therefore in general be less than the total energy spread calculated using equation (39), chapter 2.

3.4 ION SPECIES IN THE PRIMARY BEAM:

3.4.1. EXPERIMENTAL

In addition to atomic and molecular ions, higher mass ions are formed when hydrogen or deuterium gas is ionized in an rf ion source. The primary ion beam from the accelerator then consists of a mixture of component ions, some of which provide sufficient analyzed ion current to operate the stabilization system. During initial tests on the stabilization system it was found that some care was necessary to ensure the stabilization of the correct mass ions. For this reason, the relative intensities of the main ion components in the primary ion beam have been investigated.

The image slit box was removed from the 90^{o} port on the magnet beam tube and replaced with a perspex flange onto the surface of which a quartz disc had been cemented. The ion current striking the disc was collected on a fine tungsten mesh placed over the disc surface. The output of the stabilizing amplifier was disconnected from the corona triode, and the input to one channel was connected to the tungsten grid. A deflection of one microampere on the stabilizing amplifier balance meter corresponded to an ion current of 10^{-2} μA striking the quartz disc.

The accelerator was maintained manually at a fixed terminal potential and the magnetic field strength in the magnet pole gap was adjusted to bring each ion group in turn into the centre of the quartz disc. The gaussmeter frequency and ion current collected on the tungsten grid were noted for each ion group. The relative analyzed ion current as a function of gaussmeter frequency is shown in figure 30 (a) for the case where hydrogen gas was supplied to the rf ion source and in figure 30 (b) for deuterium gas. Because of the large range of observed ion

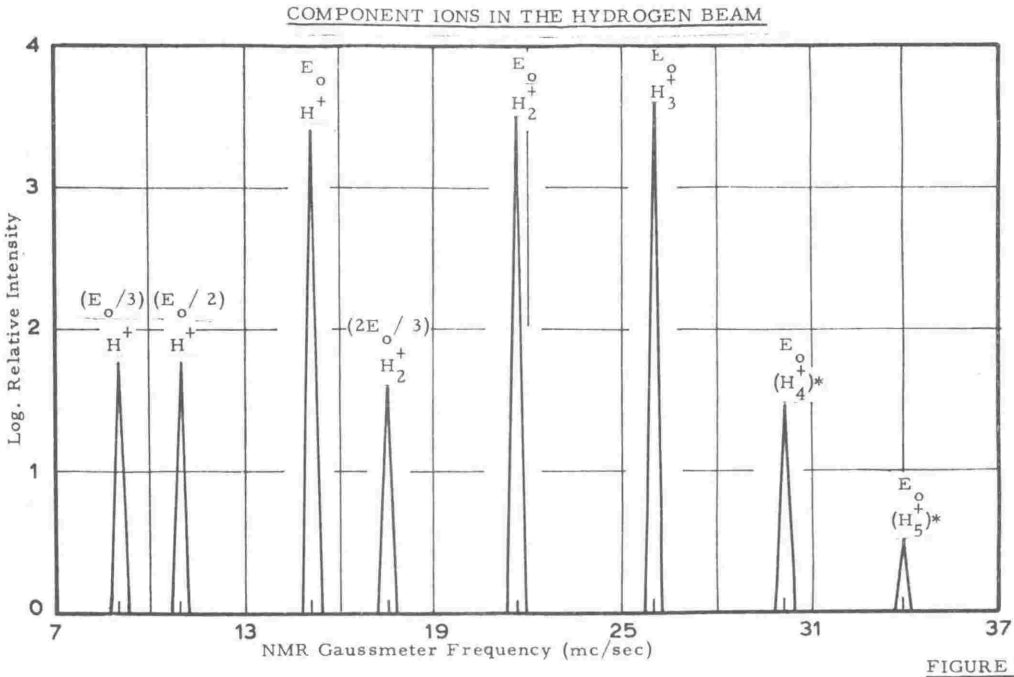

FIGURE 30a

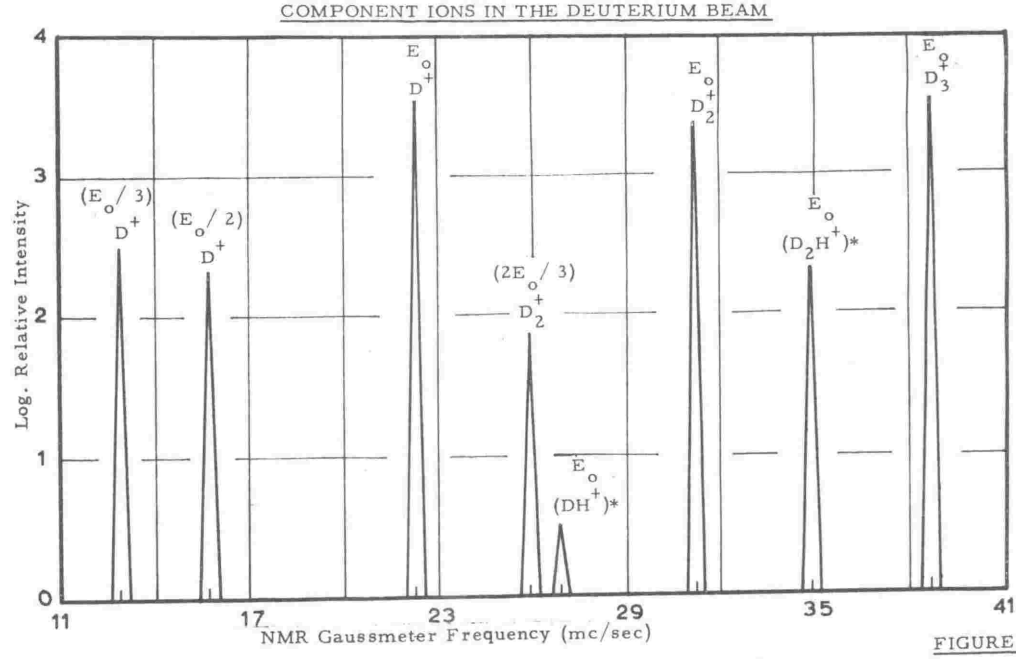

FIGURE 30b

currents the relative ion current intensity has been plotted using a logarithmic scale. No corrections have been made to the observed ion current readings, to allow for secondary electrons lost from the target[64].

3.4.2. ANALYSIS OF RESULTS:

The generating voltmeter calibration (in terms of (p, γ) reaction resonance energies) enables the terminal potential to be determined with an accuracy of $\pm$ 2%. The terminal potential and hence accelerating voltage can be kept constant to within $\pm$ 10 kv. of the chosen value, using manual accelerator control. For the accelerating voltage used (248 $\pm$ 10 kv.) the atomic (H^+) and molecular (H_2^+) hydrogen ions, would be expected, on the basis of the magnet energy calibration (figure (29)), to be observed at gaussmeter frequencies of 15.1 and 21.3 mc/sec. respectively. A treble mass, singly charged H_3^+ ion[65] having this energy is expected at a frequency of approximately 26.2 mc/sec. The three ions H^+, H_2^+, and H_3^+ therefore account for the three main peaks observed at frequencies of 15.05, 21.60 and 26.0 mc/sec. respectively, in the hydrogen spectrum.

The weaker intensity, subsidiary peaks have been identified in the following way. For a given magnetic field strength in the analyzing magnet, the energy divided by the charge to mass ratio of the analyzed ions is determined uniquely (see for example equation (40), section 2.2.1.7). If the energy of the three main ion groups listed above is denoted by E (where, in this case E is approximately 248 kev), then the two peaks occurring at frequencies of 8.8 and 10.95 mc/sec. are consistent with atomic hydrogen (H^+) ions having energies of E/3 and E/2 respectively. These two peaks are attributed to protons formed by the dissociation[84] of H_3^+ and H_2^+ ions which have been accelerated to the full energy E.

$$H_3^+ \longrightarrow H^+ + H_2^o$$

$$H_2^+ \longrightarrow H^+ + H^o$$

The alternative dissociation mode of an H_3^+ ion, namely

$$H_3^+ \longrightarrow H^o + H_2^+$$

gives rise to an H_2^+ ion having an energy of (2/3) E. The peak corresponding to a frequency of 17.45 mc/sec is attributed to H_2^+ ions formed in this way.

The existence of ion groups having an energy lower than the energy E corresponding to the full accelerating voltage (for a singly charged ion), has been confirmed by deflecting the primary ion beam in an electrostatic analyzer. Five main groups are observed on a quartz disc placed in the image plane of the electrostatic deflector. The observed groups, listed in order of increasing deflection in the electric field, are attributed to (1) undeflected neutral ions, (2) those ions having an energy E, (3) H_2^+ ions of energy (2/3) E, (4) protons of energy E/2 and (5) protons of energy E/3. The measured deflections are consistent with the energies tentatively ascribed on the basis of magnetic deflection.

The peaks occurring at frequencies of 30.1 and 34.0 mc/sec. are attributed to singly charged mass 4, and mass 5 ions respectively. These are thought to be ions of the type H_4^+ and H_5^+, which have the full energy E. An attempt to observe the dissociation products of these ions was not successful because of the much higher background contributed by the more abundant ions scattering onto the quartz disc from the walls of the magnet beam tube. The other main* possibility is that these ions are D_2^+ and D_2^+ H ions, formed from deuterium gas occluded on the interior surface of the rf ion source glass envelope. If this is so the intensity of the peaks would be expected to decrease with time. No such decrease has been observed and so the first possibility is regarded as the more probable.

* The other possibilities are multiply charged, higher mass ions such as C^{+++} produced by the ionization of contaminants in the ion source.

The main features of the deuterium spectrum (figure (30b)) are similar to the hydrogen spectrum. In the case of deuterium, a slightly higher accelerating voltage was used, (265 kv.). The three main peaks, at frequencies of 22.30, 31.20 and 38.8 mc/sec. correspond to D^+, D_2^+, and D_3^+ ions respectively. The peaks at 12.9 and 15.75 mc/sec. correspond to D^+ ions having an energy of E/3 and E/2 respectively, while the peak at 25.90 mc/sec. corresponds to a D_2^+ ion having an energy of (2/3) E. These ions are thought to originate in a similar way to their hydrogen counterparts, namely as the dissociation products of D_3^+ and D_2^+ ions of energy E. i.e.

$$D_3^+ \longrightarrow D_2^+ + D^o$$

$$D_3^+ \longrightarrow D_2^o + D^+$$

$$D_2^+ \longrightarrow D^o + D^+$$

The two additional peaks occurring at frequencies of 26.90 and 34.90 mc/sec are attributed to singly charged, mass three (DH^+) and mass five ($D_2 H^+$) ions respectively, the hydrogen consitituent being supplied by hydrogen gas occluded onto the interior wall of the rf ion source glass envelope.

THE DISSOCIATION MECHANISM:

The fraction of ions dissociated in collisions with residual gas molecules in the evacuated beam tube is $n\sigma l$,[84] where n is the number density of the residual gas molecules, σ is the total cross-section for dissociation, and l is the distance travelled by the ion beam. The number density of residual gas molecules averaged over the 3 metre ion path is approximately 4×10^{11} / cm^3. The total cross-section[85] for dissociation of H_2^+ ions on O_2 and N_2 molecules is approximately 2×10^{-16} cm^2 for ion energies in the range of interest. This cross-section includes the contribution due to $H_2^+ \longrightarrow 2H^+$,

$H_2^+ \rightarrow 2H^o$, and $H_2^+ \rightarrow H_2^o$ which together have about the same probability as $H_2^+ \rightarrow H^+ + H^o$. The dissociated fraction of H_2^+ ions which give rise to an H^+ ion, is from these values, approximately 1.2%. Wind[84] has estimated the angular spread of the dissociation products from the dissociation of a 270 kev H_2^+ ion to be .007 radians. In the present case, the object slit of the analyzing magnet subtends an angle of .006 radians at the ion source, and consequently the probability that both dissociation products pass through the object slit is high. The experimentally observed dissociated fraction (1.5%) is therefore in good agreement with the fraction expected from collision with residual gas molecules.

The electric field dissociation of ions[84] while in the accelerating electric field, or during deflection in the analyzing magnetic field (which is equivalent to an electric field of approximately 10^4 volts /cm) evidently does not contribute appreciably to the total dissociated fraction, for in this case a continuum of energies would be observed in the dissociation products. This view is substantiated by the magnitude of the electric field dissociation probabilities as published by Wind[84].

CONCLUSION:

The practical effect of the multiplicity of ions in the primary ion beam is that for a given field in the analyzing magnet, stable operation of the energy stabilization system will occur for a number of different high voltage terminal potentials. The production of an analyzed ion beam comprising ions having the desired charge to mass ratio and energy, can be ensured by selecting the correct high voltage terminal potential before increasing the stabilization feedback loop gain (appendix 5). The generating voltmeter, calibrated in terms of (p, γ) reaction resonance energies, provides a sufficiently accurate ($\sim$2%) indication of the terminal potential for this purpose, as the main ion components are separated by relatively large momentum intervals.

A second effect is that a sudden perturbation of the accelerator potential or of the analyzing magnetic field strength (originating in practice through a momentary interruption or surge in the mains supply voltage) can cause the stabilization system to 'lock' onto a nearby ion group. In the present work only the high intensity H^+ and D^+ ion groups are used, and consequently the above effect is immediately evidenced by a sudden decrease in the analyzed ion current. For this reason, this effect presents no problem in practice.

CHAPTER 4

THE ABSOLUTE CROSS SECTIONS OF THE $K^{39}(n,p)A^{39}$ AND $K^{39}(n,\alpha)Cl^{36}$ REACTIONS FOR 2.46 - MEV NEUTRONS

4.1 INTRODUCTION:

A convenient method of studying the nuclear reactions $K^{39}(n,p)A^{39}$ and $K^{39}(n,\alpha)Cl^{36}$, is to bombard a KI(Tl) scintillation crystal with monoenergetic fast neutrons and observe the scintillations produced by the charged particle reaction products. This method described originally by Scott and Segel[86], obviates the problem of low yields which necessarily result from targets sufficiently thin to allow low energy charged particles to emerge.

The Q value of the $K^{39}(n,p)A^{39}$ reaction is + 0.22 Mev and that of the $K^{39}(n,\alpha)Cl^{36}$ reaction + 1.35 Mev, for the case where the reactions proceed to the ground states of the respective final nuclei. Consequently both these reactions should be relatively prominent for neutron energies around 2.5 Mev. Reactions proceeding to the first excited levels in A^{39} (1.27 Mev) and Cl^{36} (0.78 Mev) are also energetically possible.

In addition to K^{39} (isotopic abundance 93.1%), a KI(Tl) scintillation crystal contains K^{40} ($\sim$.01%), K^{41} (6.9%), I^{127}, and a small quantity of thallium. For neutron energies around 2.4 Mev, neutron induced reactions in I^{127} and Tl^{205} should not be observed because of the high Coulomb barrier presented to the outgoing charged particles. Reactions in K^{40} and K^{41} should not be prominent because of their relatively low isotopic abundance. In Table 5)[89] the reactions expected for a neutron energy E_n = 2.46 Mev are shown, together with the maximum and minimum energies which the emitted particle can assume in the laboratory system.

TABLE 5

Maximum and minimum energy of emitted particle in laboratory system for E_n = 2.46 Mev

Reaction	Q (Mev)	E_{min} (Mev)	E_{max} (Mev)	
$K^{39}(n, p)A^{39}$	0.20	2.41	2.66	
$K^{39}(n, p)A^{39*}$	-1.04	1.24	1.42	
$K^{41}(n, p)A^{41}$	-1.80	0.53	0.65	
$K^{39}(n, \alpha)Cl^{36}$	1.36	3.10	3.67	
$K^{39}(n, \alpha)Cl^{36*}$	0.58	2.43	2.94	
$K^{41}(n, \alpha)Cl^{38}$	-0.09	1.88	2.31	

The asterisk denotes that the final nucleus is left in the first excited state.

Following the work of Scott and Segel, Kienle and Segel[87], investigated the possible application of the $K^{39}(n,p)A^{39}$ reaction to neutron spectrometry, and more recently Lindstrom and Neuert[88], and Dixon and Aitken[89] measured the absolute cross sections of the $K^{39}(n, p)A^{39}$ and $K^{39}(n, \alpha)Cl^{36}$ reactions using the associated particle technique in conjunction with the D - D reaction. These workers obtained the following results:

Lindstrom and Neuert: $E_n = (2.59 \pm 0.05)$ Mev

$\sigma(n, \alpha) = (36 \pm 4)$ mb

$\sigma(n, p) = (45 \pm 5)$ mb

Dixon and Aitken: $E_n = (2.46 \pm 0.10)$ Mev

$\sigma(n, \alpha) = 6$ mb

$\sigma(n, p) = (96 \pm 6)$ mb

The discrepancy between these results is too large to be explained by either experimental errors or by resonance structure in the K^{39} neutron cross-sections. For this reason a further absolute measurement of the neutron cross section of K^{39} at this neutron energy was considered worthwhile.

The above absolute cross sections can be compared with the less accurate relative cross section values obtained by Bass et al[90]. These workers obtained the following results:

Bass et al: $E_n = (2.45 \pm 0.05)$ Mev

$\sigma(n, \alpha) = (4.8 \pm 1)$ mb

$\sigma(n, p) = (80 \pm 16)$ mb

In this case the neutron flux entering the KI (Tl) scintillator was measured in terms of the response of a long counter calibrated with a Pu – α – Be neutron source of known strength. These results tend to substantiate those of Dixon and Aitken although the agreement is poor. An excitation curve measured by Bass et al using improved neutron energy resolution (less than 10 kev), exhibits pronounced resonance structure in the $K(n,p)\ A^{39}$ reaction in the neutron energy range of interest. This is discussed further in section 4.4.

4.2. THE n - He^3 COINCIDENCE SYSTEM:

4.2.1. EQUIPMENT:

The main features of the reaction chamber are shown in figure 31. An electrostatic quadrupole lens*, placed between the image slit box (figure 18) and the reaction chamber allowed a 100 kev D^+ ion beam to be focussed onto a reaction zone of approximately 5 mm diameter on a 0.005 inch thick, water cooled gold target. The "drive-in" deuterium concentration in the target was sufficient after about 30 minutes to give a yield, from the D - D reaction, of 10^5 neutrons per second (into a 4π solid angle) with a target current of 20 μA.

The He^3 recoil detector placed at an angle of 74° from the incident beam direction defined a cone of associated neutrons at an angle of 90°. This neutron direction was chosen for the following reason. When all D - D reactions in the target take place at the full incident deuteron energy (i.e. the target is ideally thin) the neutron energy is determined solely by the angle of emission of the neutron. If, however, a thick target is used the D - D reactions take place within the target, over a distance equal to the range of the incident deuterons in the target material and consequently the reacting deuterons have a continuous spectrum of energies below the incident deuteron energy. The neutrons emitted at a particular angle are then no longer monoenergetic but have a spread in energy. This spread in energy is minimized for neutrons emitted at angles in the region of 90° to 100°, for in this region the neutron energy has the least dependence on the reacting deuteron energy (figure 2).

* On loan from the N.Z. Institute of Nuclear Sciences, Gracefield, Lower Hutt.

At this neutron angle, the angular divergence of the cone of tagged neutrons depends on both the solid angle subtended by the recoil counter and on the spread in reacting deuteron energies introduced by the thick target. The position of the KI(Tl) scintillator, shown in figure 31, was such as to completely encompass the tagged neutron beam defined by the recoil particle detector. In this regard allowance has been made for the finite area of the reaction zone on the target.

The focus ring served as a collimator on the incident deuteron beam and prevented large excursions in the position of the deuteron beam on the target. An electron suppressor prevented secondary electrons from the target forming appreciable current densities in the neighbourhood of the recoil counter. Such currents have been found to impair the operation of the solid state detector despite the use of protective foils.

4.2.2. ELECTRONICS:

A schematic diagram of the electronics used is shown in figure 31. An Ortec 101-201 amplifier system* was used in the He^3 channel with a solid state detector, the equivalent noise figure of the system being 6.8 kev (fwhm) for an input capacitance of 40 pf. A conventional single channel pulse height selector (Dynatron Radio Ltd. type N.101) was used to determine a pulse height window on the He^3 peak. This pulse height selector provided a standard output pulse of amplitude 20 volts and width 0.7 μseconds, whenever the input pulse amplitude lay between the preset limits.

The neutron channel was designed to handle high count rates since the neutron detector will respond not only to reactions produced by tagged neutrons but will also be subject to target room background - scattered neutrons and gamma rays. The non-overloading double delay line amplifier used required fast rising

* Manufactured by Oak Ridge Technical Enterprises Corporation

TARGET CHAMBER ARRANGEMENT

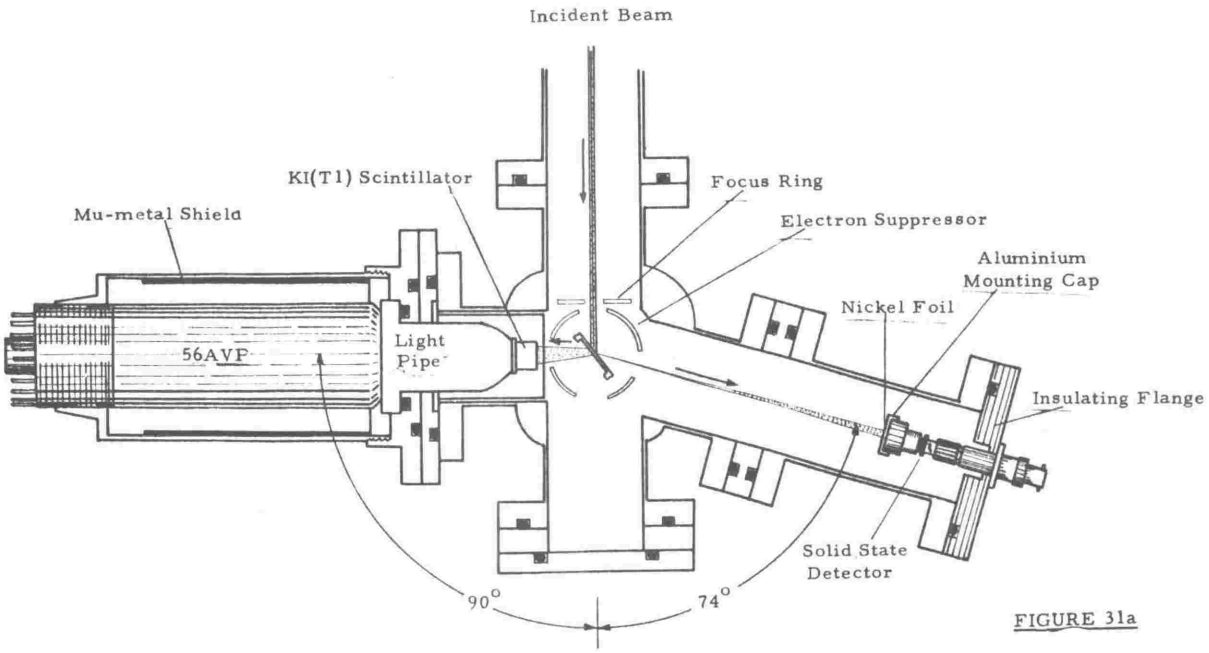

FIGURE 31a

SCHEMATIC DIAGRAM OF THE ELECTRONICS

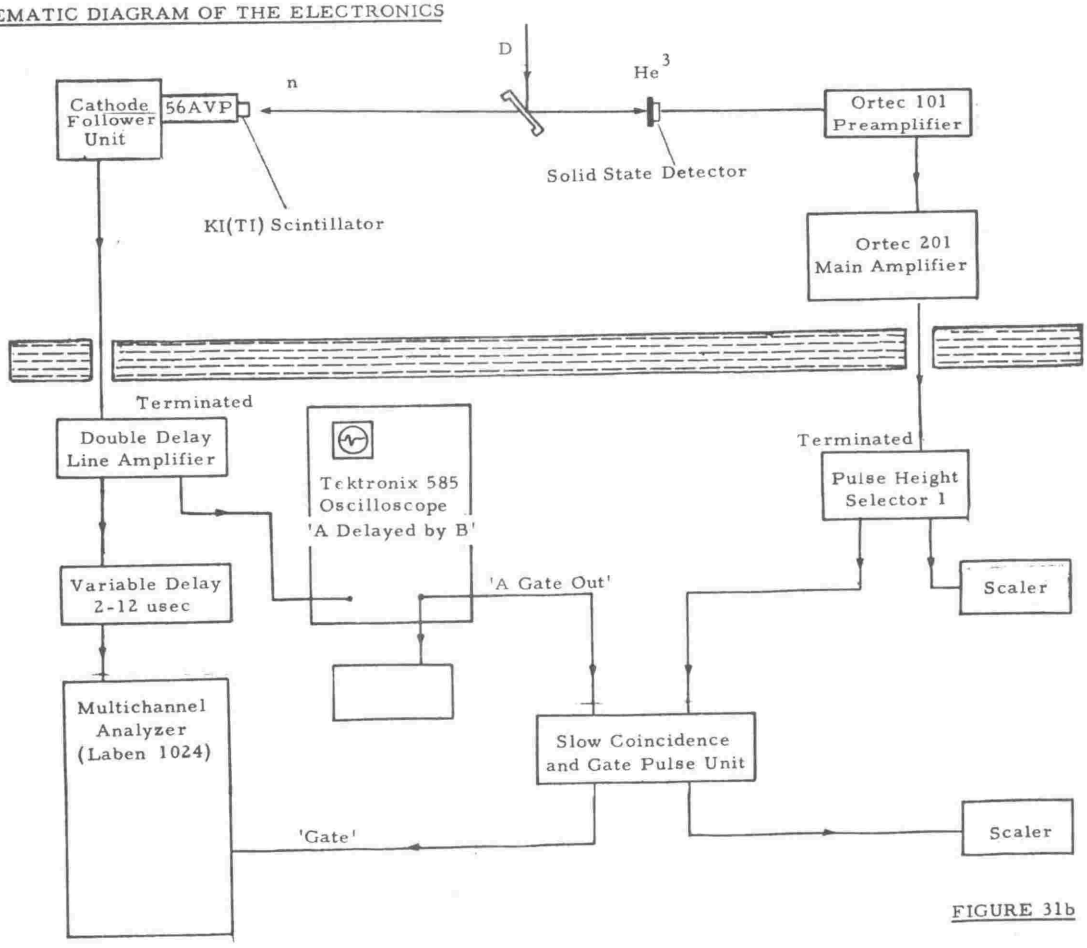

FIGURE 31b

input pulses with a relatively slow decay time. This slow decay was obtained by taking the photomultiplier pulses from a dynode having a 1 MΩ load resistance. A non-shaping, fast rise cathode follower driving a terminated 75 Ω line ensured that the pulse shape was preserved at the input to the double-delay line amplifier.

Neutron induced events in the KI(Tl) scintillator give rise to a continuous spectrum of pulse heights and thus a conventional pulse height selector cannot be used in this channel without introducing a prohibitively large time spread. This time spread arises because of the relatively high triggering level of the discriminator. This problem was overcome by using a Tektronix type 585 oscilloscope as a low trigger level discriminator. In the "A delayed by B" mode, the release of the main (A) sweep can be delayed by a continuously variable amount by altering the B time base setting. The duration of the "A Gate" pulse can be varied continuously over a wide range by adjusting the A sweep speed. In this way the oscilloscope is used as a low trigger level, variable delay, variable pulse width, standard pulse generator. The oscilloscope triggers equally well on positive, negative, or as in this case, bipolar pulses. (The uses of an oscilloscope in nuclear instrumentation are discussed more fully in references 91, 92).

The resolving time of the slow coincidence unit was determined by the duration of the input pulses. The adjustment of the A sweep speed thus gave a continuously variable coincidence resolving time. The output of the coincidence unit was used to gate a multichannel pulse height analyzer (Laben type 1024). Random coincidences were determined by increasing the delay setting of the oscilloscope by 20 μseconds and observing the coincidence count rate as indicated by the gate pulse scaler. It should be noted that the delay can be increased in this way without altering the deadtime of the system. Three scalers were used to monitor the countrate at the points shown in figure 31. Knowledge of these count rates was required in order that the number of random coincidences occurring during an experiment could be calculated.

4.2.3. RECOIL PARTICLE DETECTION:

At low deuteron bombarding energies the cross sections for the D (d,n) He^3 and D (d,p) T reactions are approximately equal. In addition therefore, to He^3 particles, there will also be incident on the recoil particle detector tritons and protons with energies of 1 Mev and 3 Mev respectively, together with deuterons elastically scattered from the primary beam, light emitted from the target, and neutron capture gamma rays from surrounding material. For this reason unambiguous identification of the 800 kev He^3 particles is difficult. This difficulty accounts for the relatively scant attention given the associated particle technique applied to the D - D reaction, compared with that afforded the T(d,n) He^4 reaction in which the recoil alpha particle has an energy of 3.5 Mev for low incident deuteron energies.

Shapiro and Higgs[5] have used a magnetic field to deflect the He^3 particles into a windowless KI(Tl) scintillator so situated that light from the target could not enter it. This system was probably unsuitable for absolute cross section measurements because of the possibility of pulses arising from the β^- decay of the naturally occurring K^{40} in the scintillator falling within the He^3 pulse height window. The authors make no mention of this however, but do state that scattered deuterons contributed to the counts recorded in the He^3 peak. Franzen et al[7] working at a deuteron energy of 900 kev avoided scattered deuterons by using a gas target, but their He^3 detector did not discriminate against protons and tritons. Okhuysen et al[4] detected He^3 particles in an organic scintillator covered with a thin aluminium absorber, despite the small pulse size.

Lindstrom and Neuert[88] introduced the He^3 particles into a proportional counter through a thin mica window. The gas pressure in the proportional counter was adjusted so as the He^3 particles gave the largest output pulses. Dixon and Aitken[89] used a thin Cs I (Tl) scintillation crystal with a thin aluminium film ($\sim$225 ug/cm^2) evaporated onto the front face. This film stopped

light from the target but was of insufficient thickness to stop completely scattered deuterons.

In the present work the two most successful recoil He^3 particle detectors have been a thin Cs I (Tl) crystal-photomultiplier combination and a solid state detector . A typical spectrum of recoil He^3 particles obtained using a 0.5 mm thick Cs I (Tl) scintillator optically coupled to a Philips 153 - AVP photomultiplier is shown in figure 32 (a). The recoil particles were collimated by means of a 2.3 mm diameter hole in a brass cover placed in front of the crystal and over which a thin nickel foil window (225 $\mu g/cm^2$) had been mounted. This method proved more reliable than the evaporation of thin aluminium films directly onto the face of the crystal. A peak to valley ratio of 1.6:1 was consistently obtained with occasional improvement to as high as 2:1. Dixon and Aitken have obtained peak to valley ratios of 3:1. The observed variation in the peak to valley ratio for the He^3 peak in a Cs I (Tl) crystal has been attritubed to variations in the characteristics of the drive-in target.[89]

The spectrum shown in figure 32b was obtained using an Ortec, silicon surface-barrier detector of resistivity 5300 ohm - cm and an alpha energy resolution of 23.5 kev (fwhm), with an applied bias of 40 v. A 450 $\mu g/cm^2$ nickel foil mounted over a hole of diameter 4.3 mm in an aluminium covering cap, prevented scattered deuterons and light from reaching the counter. It was found necessary to electrically insulate the solid state detector earth from the beam tube in order to eliminate radiofrequency pickup by the detector. The peak noise level in the recoil detector channel was observed to be approximately 10% of the pulse height corresponding to the middle of the He^3 peak.

In view of the disadvantages (enumerated in chapter 1.2) associated with the use of a CsI (Tl) scintillator for recoil He^3 particle detection, a solid state detector has been used throughout the present work. The foils placed over the solid state detector

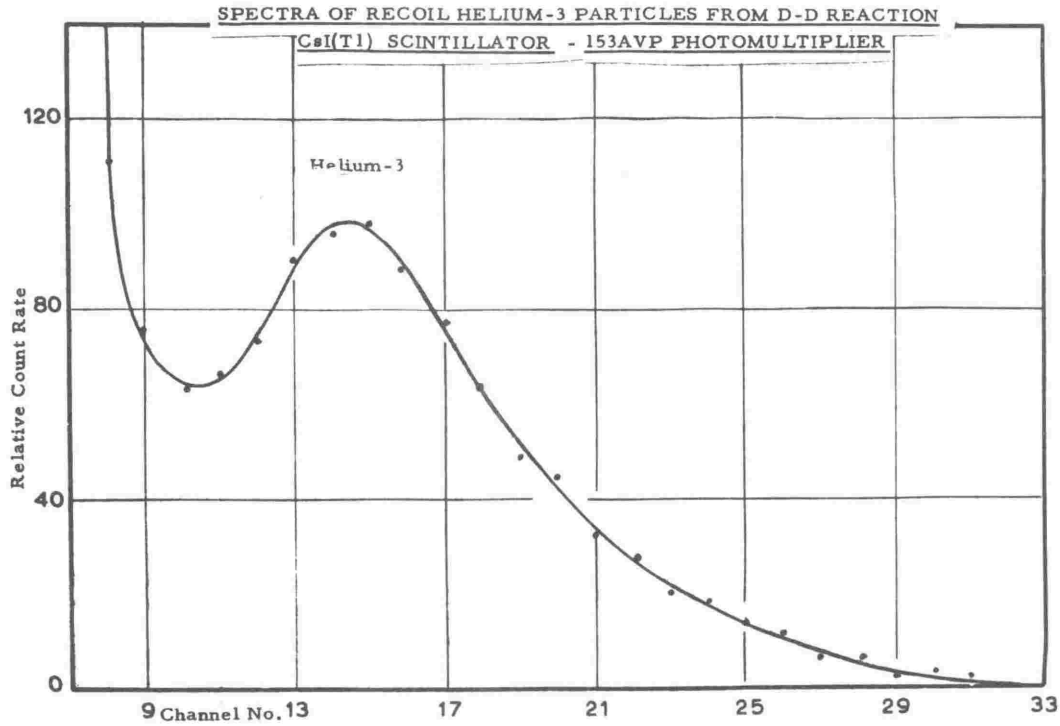

Pulses due to tritons and protons from D(d, p)T reaction are off scale to the right. FIGURE 32a

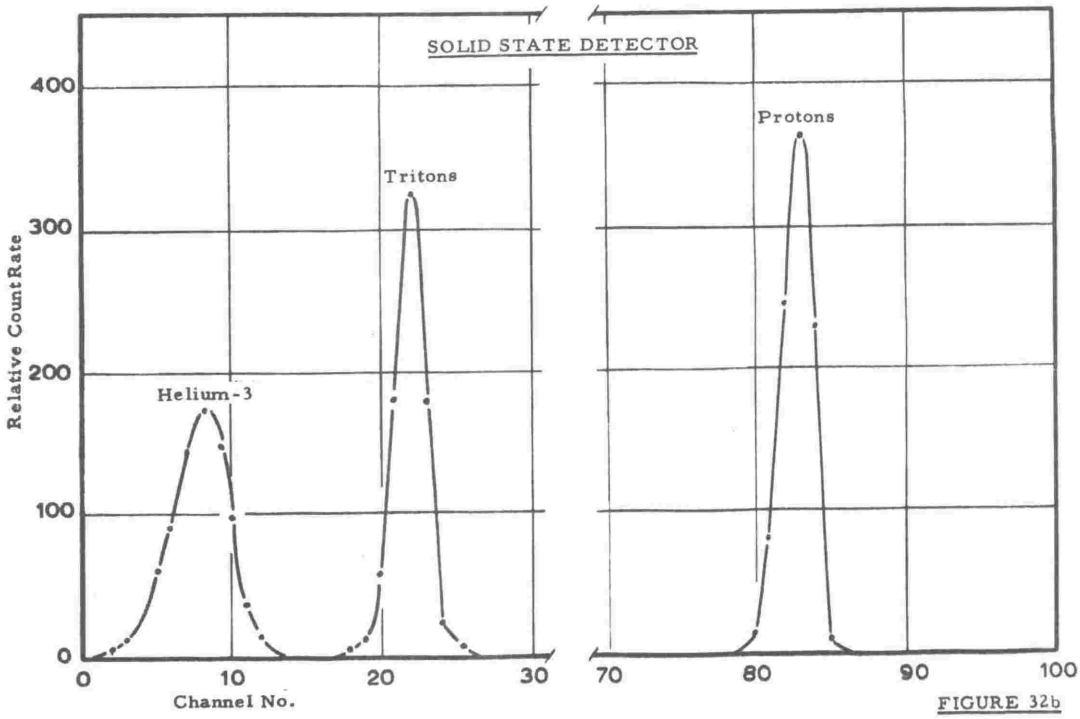

FIGURE 32b

are prepared using the method described in appendix 7. It should be noted that a low deuteron energy allows better discrimination between scattered deuterons and the He^3 recoil particles since the energy difference between them decreases at higher bombarding deuteron energies. For this reason if the deuteron energy is increased much above 100 kev the extra foil thickness required to stop the scattered deuterons results in a prohibitively large decrease in the energy of the He^3 particles.

4.2.4 THE SCINTILLATION DETECTOR:

The cylindrical (17 mm diameter, 11.12 mm deep) KI(Tl) scintillation crystal was mounted onto a lucite light-pipe (figure 31), good optical coupling between the two being ensured by a thin layer of high viscosity (10^6 centipoise) silicone oil of matched refractive index. A similar oil was used to optically couple the light pipe onto the end window of a Philips 56-AVP photomultiplier. The light-pipe used is shaped such that light leaving the scintillator at an angle to the axis of the light pipe undergoes total internal reflection at the light-pipe surface and so reaches the photocathode of the photomultiplier.

The vacuum seal onto the target chamber was made directly onto the base of the light-pipe thereby circumventing the need for a vacuum seal onto the photomultiplier glass envelope. In order to prevent light entering the scintillation detector, an aluminium window of thickness 24.2 mg/cm^2 was placed between the scintillator and the target. This thickness of aluminium is sufficient to prevent 3 Mev protons, arising from stray D-D reactions produced by scattered deuterons, from entering the scintillator.

The Philips 56-AVP photomultiplier tube is a high gain, short time resolution, 14 dynode tube, with a photocathode having an S-11 spectral response suitable for use with KI(Tl) scintillators. In the present case the focussing and accelerating electrode potentials have been adjusted for optimum energy resolution and the photomultiplier

enclosed in a mu-metal shield to minimise the effects of stray magnetic fields.

A number of different coatings* have been tried on the exterior surface of the KI(Tl) crystal in an attempt to improve the light collection from the scintillator. The best energy resolution has been obtained with an uncoated crystal treated in the following way. The plane surface of the crystal facing the photomultiplier is polished using lens tissue and a mixture of jewellers rouge and methyl alcohol (as KI(Tl) crystals are hygroscopic). Final polishing is achieved with lens tissue (held with polythene gloves) dampened with methyl alcohol. The two remaining surfaces are scuffed lightly with 400 grade carborundum paper. The matt surface obtained in this way acts as a diffuse reflecting surface.

ENERGY RESOLUTION AND CALIBRATION:

Alpha particles of energy 5.15 Mev and 5.42 Mev were obtained from a Pu^{239} and Am^{241} source respectively. The alpha particle energy was varied by means of aluminium foils placed between the source and KI(Tl) scintillator. The alpha particle energy for a given foil thickness was accurately calibrated in terms of the known linear response[93] of a solid state detector. This method of energy calibration has the advantage of not requiring an accurate knowledge of the foil thickness used.

* NOTE: A crystal coated with a white reflecting paint comprising TiO_2 pigment, chlorinated rubber base, and toluol solvent has given good resolution. However, this paint is incompatible with the silicone oil used for optical coupling and for this reason was not used. Of course water based paints cannot be used because of the hygroscopic nature of the crystal.

Protons of energy 3.05 Mev produced in the D(d,p) T reaction were used. The proton energy was varied with aluminium foils which were calibrated in terms of proton energy in the same way as above. The alpha particle and proton energy calculated from the approximate thickness and stopping power[94] of the foils used agreed in all cases within 8% of the energy measured using a solid state detector. The energies of the particles used in the energy calibration are thought to be known to an accuracy of better than 1%.

The energy resolution of the scintillation detector was found to be approximately proportional to the reciprocal of the alpha particle energy. The resolution for the 5.42 Mev alpha particles from Am^{241} was 9.6%. The energy resolution extrapolated to an alpha particle energy of 6 Mev was approximately 8.8%. This figure compares favourably with that obtained by Lindstrom and Neuert (8.8%) using a larger (25 mm x 20 mm) KI(Tl) crystal. Dixon and Aitken make no mention of the alpha particle energy resolution of their detector.

The energy resolution for 2.79 Mev protons was 11.3%. Interpolation gives the energy resolution at 2.1 Mev proton energy as 12.8%. This figure compares unfavourably with that obtained by Lindstrom and Neuert (11%). Dixon and Aitken obtained a resolution of 11 to 12% for a proton energy of 2.65 Mev. This figure is comparable to the resolution (11.4%) obtained with the present scintillation detector for protons of this energy.

Typical energy spectra obtained with this detector for alpha particles and protons are shown in figure 33. The β^- (1.32 Mev) spectrum arising from the decay of naturally occurring K^{40} contained in the crystal gives rise to a background counting rate of approximately 75 counts per second up to an equivalent proton energy of 900 kev (i.e. an alpha particle energy of 1.5 Mev).

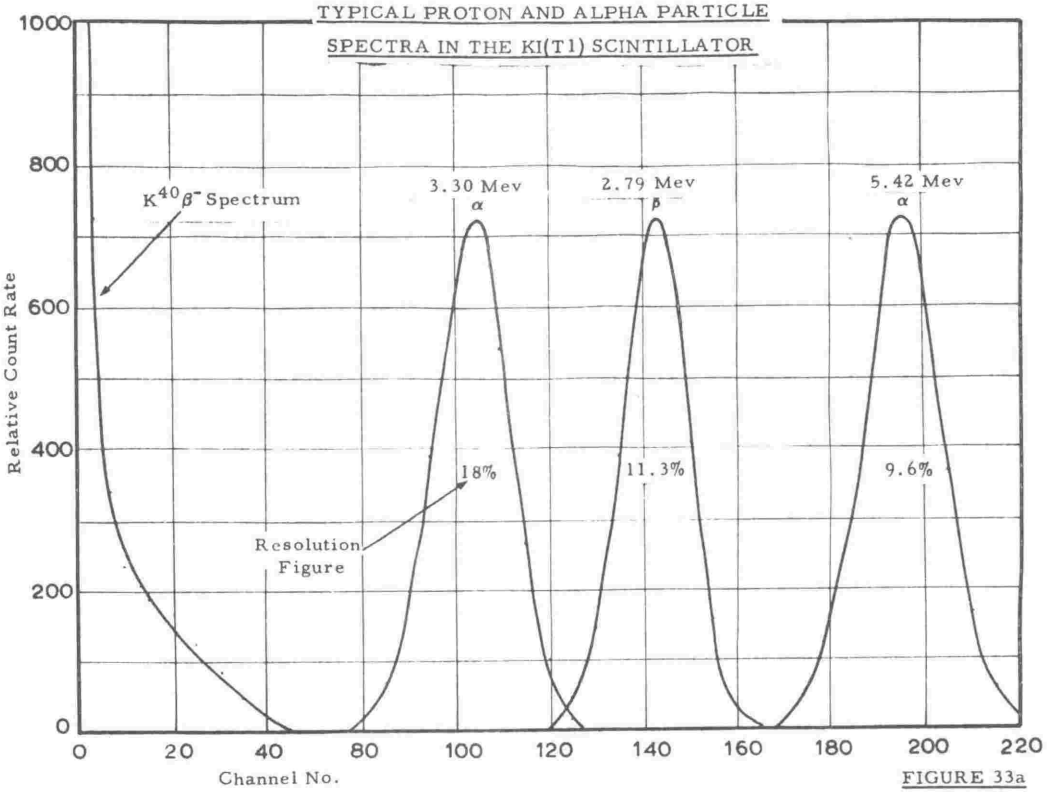

FIGURE 33a

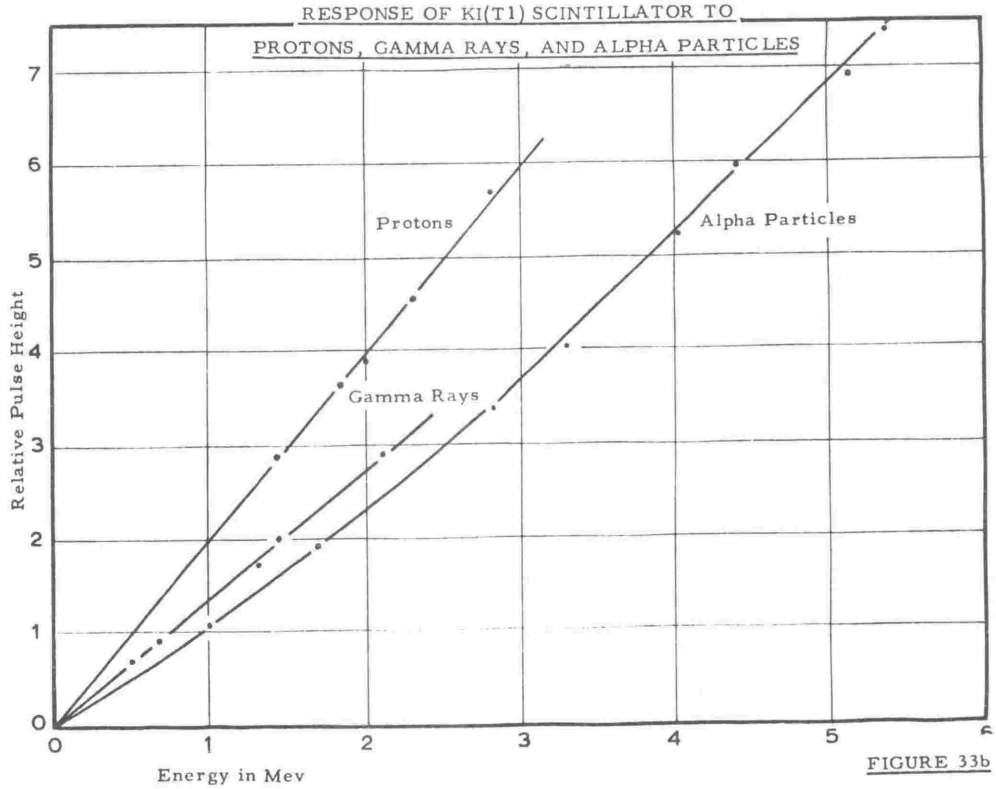

FIGURE 33b

The energy calibration of the scintillation detector for alpha particles, gamma rays and protons is shown in figure 33 (b). The gamma ray sources used were Cs^{137}, Na^{22}, Co^{60}, and Th^{228}. The end point of the K^{40} β^- spectrum provided a further calibration point on the gamma ray scale. The response is essentially linear for protons and gamma rays but non-linear for alpha particles over the energy region studied.

The response of KI(Tl) scintillation crystals has been the subject of a number of previous investigations [88,89,95-99]. These studies do not agree in detail. Dixon and Aitken attributed differences to variations in thallium concentration and other details of crystal manufacture, and found that crystals obtained from two different companies gave different relative response to protons, electrons and alpha particles. In the course of this work, three different KI(Tl) crystals obtained from the Harshaw chemical company have been used. The slight differences in the observed response have been attributed to differences in the light reflectivity from the matt crystal surface.

4.3 NEUTRON CROSS SECTION MEASUREMENT:

The spectrum of pulses from the scintillation detector in coincidence with pulses from the associated He^3 particle detector is shown in figure 34. For this experiment the accelerating voltage was 95 kv and the average deuteron current striking the target 25 μA. The data shown in figure 34 is a composite spectrum obtained after 15 runs each of 4,000 seconds duration. After each group of 3 coincidence runs, random coincidences were observed for a period of 1,000 seconds with a 20 μsecond delay placed in the scintillation detector channel.

The mean neutron energy in this experiment was 2.46 Mev. The total spread in energy of neutrons in the tagged neutron beam was $\pm$ 40 kev. This estimate is based on the known angle subtended by the recoil counter at the target ($\sim 3^\circ$), the finite area of the reaction zone on the target, and the spread in the reacting deuteron energies in the drive in target. The neutron energy spread (fwhm) is estimated as $\pm$ 25 kev.

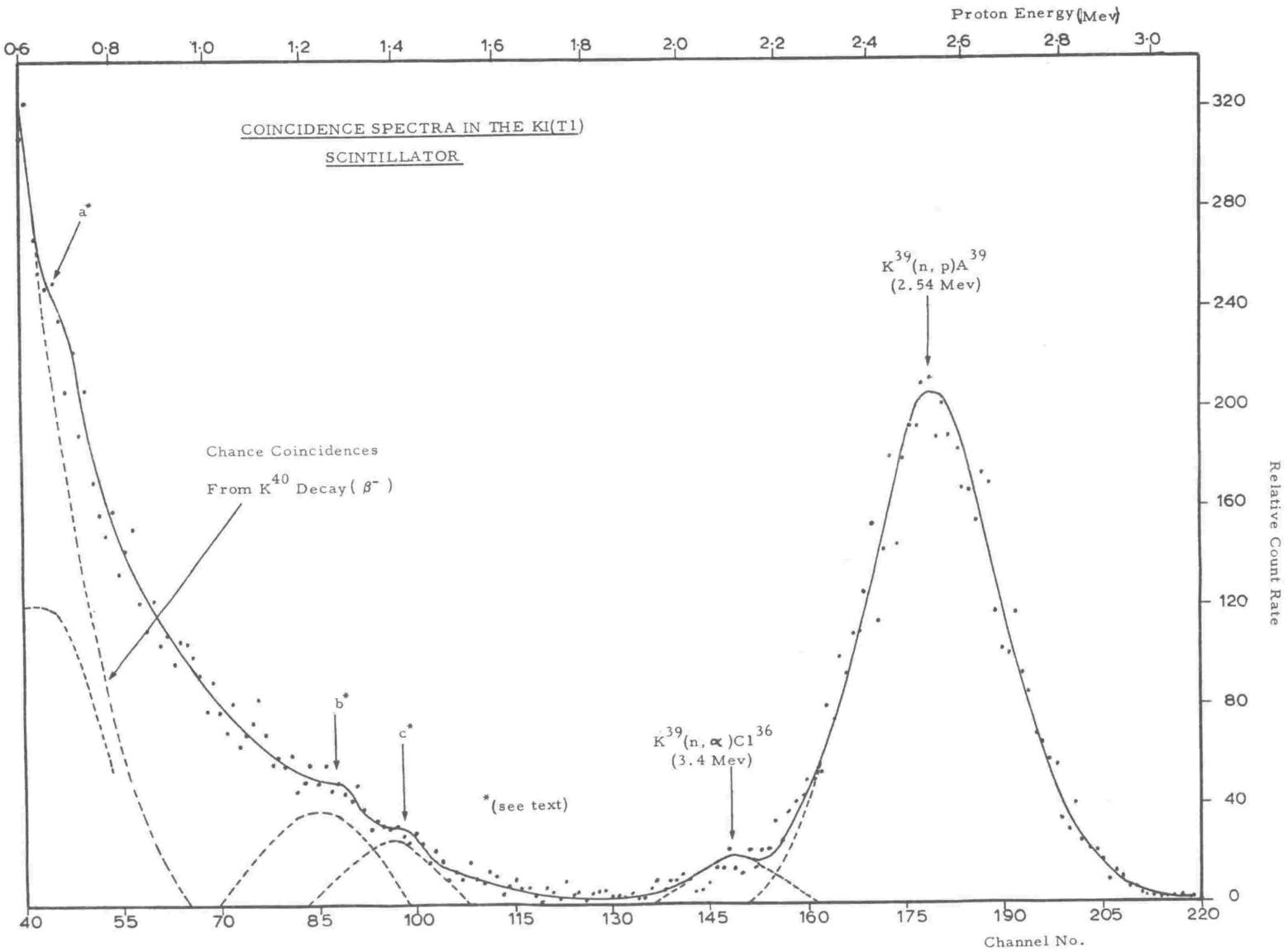
Proton Energy (Mev)
0·6
0·8
1·0
1·2
1·4
1·6
1·8
2·0
2·2
2·4
2·6
2·8
3·0
COINCIDENCE SPECTRA IN THE KI(T1) SCINTILLATOR
a*
b*
c*
Chance Coincidences
From K40 Decay (β-)
K39(n, p)A39
(2.54 Mev)
K39(n, ∝)Cl36
(3.4 Mev)
*(see text)
320
280
240
200
160
120
80
40
0
Relative Count Rate
40
55
70
85
100
115
130
145
160
175
190
205
220
Channel No.

FIGURE 34

The main peak shown in figure 34 occurs at a proton energy of (2.54 ± 0.05) Mev and is therefore attributed to the K^{39} (n,p) A^{39} reaction (see table 5). A secondary peak of much weaker intensity occurs at an alpha energy of (3.4 ± 0.1) Mev and is attributed to the K^{39} (n,α) Cl^{36} reaction. Both the line shape and resolution (12.4%) of the main proton peak are in good agreement with those expected for protons of this energy. The main features of this spectrum are in agreement with the spectrum obtained by Dixon and Aitken but differ markedly from those found by Lindstrom and Neuert. These latter workers interpreted their spectrum as showing alpha and proton peaks of nearly equal intensity.

The absolute neutron cross sections for the above reactions can be calculated from the relation,
(Number of true coincidences) = (Number of He^3 particles counted)x (Number of K^{39} atoms /cm^2 of scintillator) x (cross section), provided only that all tagged neutrons pass through the scintillator.

A total number of 5,442 coincidences was obtained in the main proton peak. Random coincidences gave rise to a total of (390 ± 25) counts under this peak at an average count rate of 0.4 counts per minute. The proton peak therefore contained (5,052 ± 100) true coincidence counts. The corresponding number of counts registered by the He^3 particle scaler was 4,586,290.

The number of K^{39} atoms/cm^2 of scintillator was calculated from the following data:

Density of KI(Tl) crystal	= 3.13 gm/cc	(94)
Molecular weight of KI	= 166 amu	(94)
1 amu	= 1.662×10^{-24} gm	(74)
Isotopic Abundance of K^{39}	= 93.1%	(55)
Length of KI(Tl) crystal	= 11.12 mm.	

The figure obtained, 1.175×10^{22} atoms/cm^2 is approximately 2.2% higher than the figure (1.150×10^{22}) deduced from the value quoted by Dixon and Aitken (1.31×10^{22} K^{39} atoms/ cm^2 for a crystal 12.7 mm in length). It is unlikely that this difference can be explained by differences in the thallium concentration (typically 0.2%).

On the basis of the above figures the absolute cross section of the $K^{39}(n,p)A^{39}$ reaction is:-

$$\sigma(n,p) = (94 \pm 2) \text{ mb}$$

The quoted error includes a counting error of $\pm$ one standard deviation, together with an estimate of the possible error in assessing the area under the proton peak.

The following is a summary of the corrections that must be made to the measured cross section to allow for attenuation and scattering of the tagged neutron beam. The attenuation of the tagged neutron beam in traversing a thickness x (cm) of material of density ρ (gm/cc), total neutron cross section σ (barns), and atomic weight A, is given by,

$$60 \frac{\rho x \sigma}{A} \quad \%$$

provided x is small compared with the neutron mean free path. The values of the total neutron cross sections used in these corrections are those given by Hughes and Schwartz.[100] The attenuation of the tagged neutron beam in the gold target backing (equivalent thickness .032 cm) is approximately 1.3%. This includes a small correction for neutrons which although scattered, still pass through the KI(Tl) scintillator. The attenuation of the neutron beam in the aluminium scintillator cover (24 mg/cm^2) amounts to only 0.1%.

The effect of inelastic scattering within the KI(Tl) crystal can be allowed for as follows. The incident neutron energy of 2.46 Mev (2.40 Mev in the centre of mass system) is not sufficient to cause excitation of the first excited state in

K^{39} (which occurs at an energy of 2.53 Mev). It is only necessary therefore to consider inelastic scattering from I^{127}. For a KI(Tl) crystal of this size the attenuation of the beam resulting from this cause is approximately 2.6%. Since many neutrons travel an appreciable path in the crystal before inelastic collision the actual flux reduction in the crystal due to inelastic scattering is approximately half the above figure, namely 1.3%. It should be noted that a neutron producing the $K^{39}(n,p)A^{39}$ reaction having first undergone inelastic scattering from an I^{127} nucleus, is unlikely to contribute to the proton peak since the energy available to the proton is in this case less.

The effect of elastic neutron scattering within the crystal is more difficult to assess. For a crystal of this size approximately 10% of the incident neutron flux will undergo elastic scattering within the crystal. However the distance travelled by a neutron in the crystal is not appreciably altered by elastic collision, and since the energy lost by a neutron through elastic collision is small, the probability that the neutron will subsequently produce a nuclear reaction is substantially unaltered. A more detailed analysis following a method described, for example, by Bell[101] shows that the increased neutron path length resulting from elastic scattering, dominates the reduction in neutron flux caused by the scattering of neutrons out of the crystal. The relevant correction amounts to an effective enhancement of the neutron flux in the crystal by approximately 1%. A second effect resulting in a correction in the same sense as this correction is the increased average neutron path length in the crystal, ($\sim$ 0.5%) resulting from the angular divergence of the tagged neutron beam.

Hydrogen, carbon, and oxygen are the main constituent atoms of the light pipe assembly on which the KI(Tl) crystal is mounted. The maximum energy of a neutron which is backscattered from the light pipe assembly into the crystal occurs when the scattering takes place from the heaviest of these, namely an oxygen nucleus. The energy of a neutron elastically back-scattered from an oxygen nucleus is 1.92 Mev (1.80 Mev for a

carbon nucleus) and correspondingly less if inelastically scattered. A neutron of energy 1.92 Mev producing the K^{39} (n,p) A^{39} reaction in the scintillator gives rise to a proton having a maximum energy in the laboratory system of 2.12 Mev. This energy is insufficient to give rise to a pulse entering the main proton peak. Furthermore the cross section for scattering from oxygen is extremely low ($\lesssim$ 200 mb) for neutron energies in the region of 2.46 Mev. For these reasons no correction is made for the backscattering of neutrons from the light pipe into the crystal.

The scattering of neutrons into the crystal by material located outside the tagged neutron cone can only contribute to the random coincidence rate since the associated He^3 particles do not enter the recoil particle detector.

A number of effects associated with the detection of the recoil He^3 particles can alter the observed cross section. Effects arising from the elastic scattering of He^3 particles by the target material can be neglected since in the worst case He^3 particles travel only a short distance (equivalent to the range of a 100 kev deuteron in the target material) before emerging from the target. If deuterons or tritons give rise to pulses that can enter the He^3 pulse height window the observed cross section will be too small. It can be seen from the recoil particle detector spectrum, figure 32 (b), that the probability of particles other than genuine He^3 particles giving rise to counts in the He^3 scaler is negligible. The resolving time losses in the He^3 scaler at the count rates used ($\sim$130 counts per second maximum) are also small.

To summarise, a correction of + 2.7% is made to the observed cross section to allow for attenuation of the tagged neutron beam due to scattering in the target backing and scintillator cover and due to inelastic scattering in the crystal itself. A correction of -1.5% is made to allow for the increase in neutron path length resulting from elastic scattering within the crystal and the angular divergence of the tagged neutron beam.

The corrected value of the cross section is

$$\sigma(n,p) = (95 \pm 4) \text{ mb}$$

The increase in the quoted error arises from uncertainties in the calculation of the effect of elastic neutron scattering within the crystal.

The weaker intensity peak (figure 34) is attributed to the $K^{39}(n,\alpha)Cl^{36}$ reaction. For a neutron energy of 2.46 Mev the Cl^{36} nucleus recoils with an energy of approximately 700 kev. The light output from KI(Tl) for such heavy charged particles is not accurately known. The very much lower light output for alpha particles than for protons of the same energy (figure 33 b) suggests that the light output for heavy recoil nuclei should be negligible. However there is some evidence that the light output for heavy charged particles is greater than expected[102,103]. The subsidiary peak in figure 34 corresponds to an alpha energy of (3.4 ± 0.1) Mev if the light output for the recoil Cl^{36} nucleus is assumed negligible.

The area under the alpha peak has been estimated by fitting the experimental data with a curve based on the known spectrum shape of the scintillation detector for an alpha particle of this energy. By fitting the curve to the relatively well defined low energy side of the alpha peak an estimate of the area obscured by the proton peak has been made. The number of true coincidence counts obtained in the alpha peak is (325 ± 50). The large quoted error arises through the large uncertainty in assessing the area under the alpha peak and to a lesser extent through the poor statistical accuracy of the experimental data. A value of

$$\sigma(n,\alpha) = (6.2 \pm 1.0) \text{ mb}$$

for the absolute cross section of the $K^{39}(n,\alpha)Cl^{36}$ reaction is obtained.

The values obtained here, $\sigma(n,p) = (95 \pm 4)$ mb and $\sigma(n,\alpha) = (6.2 \pm 1)$ mb are in excellent agreement with those found by Dixon and Aitken, namely (96 ± 6) mb and

approximately 6 mb respectively. Two minor differences exist. In the present work the overall correction tended to raise the observed cross section by approximately 1.2% implying factors tending to attenuate the tagged neutron beam predominated. In the case of Dixon and Aitken the applied correction lowered the observed cross section by 1.5% implying factors tending to enhance the effective neutron flux predominated. No correction was made by these workers for attenuation of the neutron beam in the material between the deuterium target and the scintillator. Unfortunately it is not possible to estimate the magnitude of this correction as the relevant details of their experimental arrangement are not described. A second difference arises from the value taken for the number density of K^{39} atoms in a KI(Tl) scintillator. If the value quoted by Dixon and Aitken is used in evaluating the present results the absolute cross sections are raised by approximately 2%.

The present results are quite different to those obtained by Lindstrom and Neuert a slightly higher incident neutron energy, $E_n = (2.59 \pm 0.05)$ Mev. In an attempt to observe the much more prominent alpha peak obtained by these workers, the ungated spectrum from the scintillation counter has been examined at two further neutron energies. Figure 35 shows the ungated spectra obtained with the scintillation detector located at angles of 0°, 74° and 90° with respect to the incident deuteron beam direction. The neutron energies corresponding to these angles of observation are 2.85 Mev, 2.56 Mev, and 2.46 Mev respectively. The gated spectrum of neutron induced events in the scintillator is shown for comparison at a neutron energy of 2.45 Mev.

The increased width of the peak in the ungated spectrum is attributed to the large spread in energy of the neutrons scattered into the crystal from surrounding material. In the gated spectrum pulses arising from this source are rejected since the He^3 particle associated with the scattered neutron does not enter the recoil particle detector. The lower average

UNGATED NEUTRON INDUCED EVENTS IN THE KI(T1) SCINTILLATOR

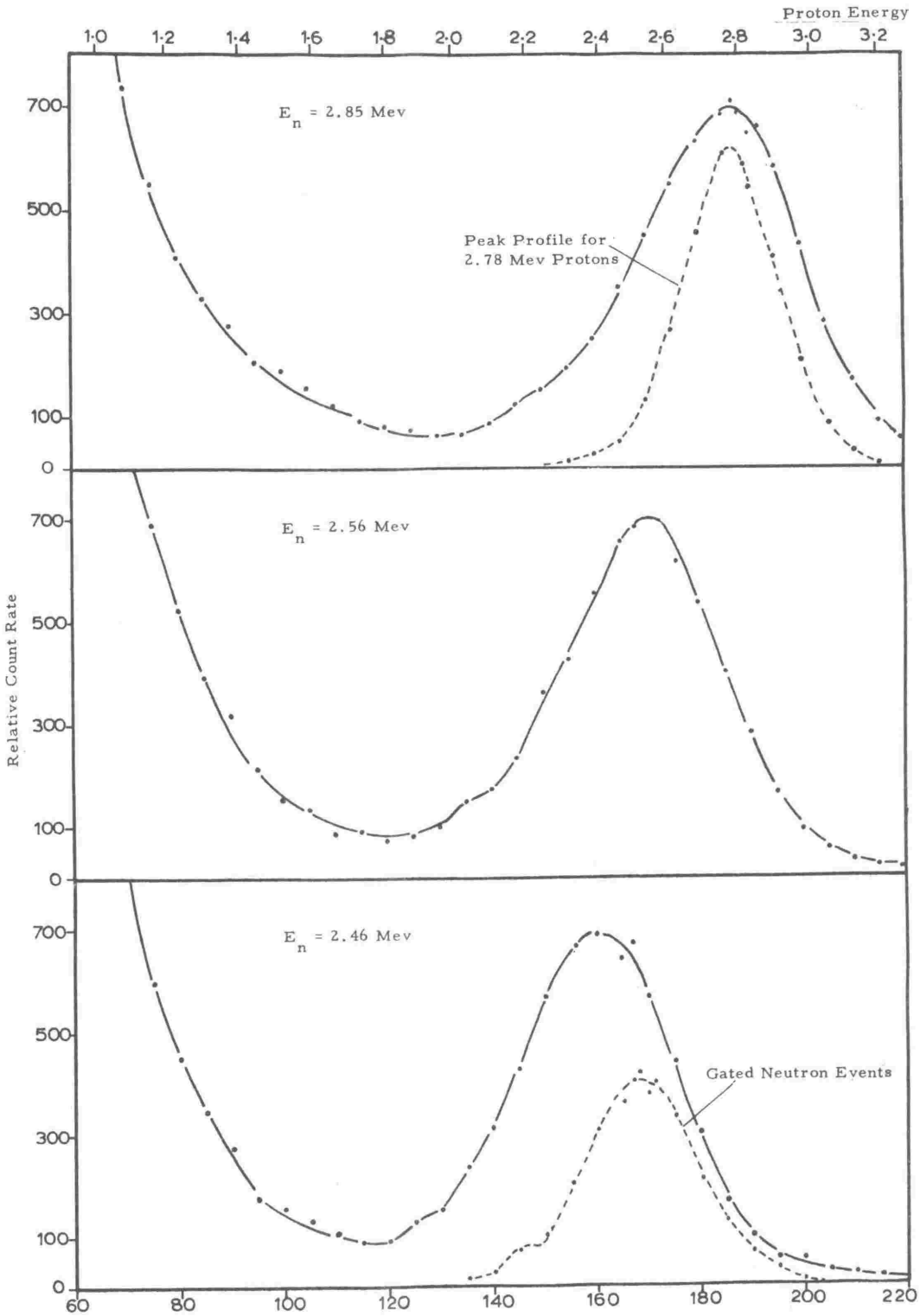

FIGURE 35

energy of the inelastically scattered neutrons causes the peak in the ungated spectrum to appear at a slightly lower energy than in the gated spectrum. The energy of neutrons elastically scattered into the crystal depends primarily on the original angle of emission of the neutron from the target. This energy can he higher or lower than the neutron energy corresponding to the angle of observation of the scintillation counter and consequently elastically scattered neutrons result in a broadening of the ungated peak.

The width of the peak in the ungated spectrum increases with increasing neutron energy. This is probably due, at least in part, to the greater dependence of the neutron energy on

Some features of the low energy end of the gated spectrum (figure 34) are of interest. A discontinuity (labelled a*) occurs at a proton energy of 0.58 Mev. There is no known excited level in A^{39} that would give rise to a proton of this energy from an (n,p) reaction induced in K^{39}. On the basis of the Q value alone this peak could be attributed to the K^{41} (n,p) A^{41} reaction. However for this reaction to give rise to a discontinuity of this size in the presence of the chance coincidence background from the β^- decay of K^{40} and background gamma radiation, it would require a cross section of the order of 10 to 15 times that of the K^{39} (n,p)A^{39} reaction. This seems unlikely. In view of the low cross section for K^{39} (n,α) reactions leading to the ground and first excited states in Cl^{36}, it is equally unlikely that this peak results from an (n,α) reaction proceeding to a higher excited state in Cl^{36}.

For these reasons it is thought that this discontinuity (which is much more pronounced when plotted on a graph having a horizontal scale extended in the lower energy direction) is probably due to a gamma ray having an energy of approximately (0.90 $\pm$ 0.15) Mev. Gamma rays of this energy occur when neutrons are inelastically scattered from the 0.94 Mev or 1.01 Mev level in I^{127}. Evidently the cross section for inelastic neutron scattering from these levels in the neutron energy range of interest, has not been measured. An order of magnitude assessment based on the present results i.e. 100 to 200 mb would seem reasonable. It should be possible to substantiate this identification by observing the gated neutron induced spectrum in a NaI(Tl) or CsI(Tl) scintillator.

The peak labelled b* comes at a proton energy of 1.30 Mev and is almost certainly due, at least in part, to the K^{39} (n,p) A^{39*} reaction (see table 5). There is slight evidence of a small peak at an alpha particle energy of 2.5 Mev (the point labelled c*). This may indicate a small contribution to the spectrum from the K^{39} (n,α) Cl^{36*} reaction. On the basis of this spectrum it would

seem that the absolute cross sections of the K^{39} (n,p) A^{39*} and K^{39} (n, α) Cl^{36*} reactions are less than 15 mb and 6 mb respectively.

4.4. THEORETICAL ANALYSIS OF RESULTS:

According to the Bohr assumption[104], the cross section for a nuclear reaction of the type K^{39} (n, x) Y is given by the product of the cross section $\sigma'(n)$ for the formation of the K^{40} compound nucleus, and the probability P (x) that the compound nucleus, once formed, decays by the emission of a particle x with a residual nucleus Y, i.e.

$$\sigma (n, x) = \sigma'(n) \quad P(x) \qquad \text{----------} \qquad (1)$$

The compound nucleus, in general, can decay through a number of competing exit reaction channels.* The channel wave number k and channel wavelength λ , are related to the channel energy E in the centre of mass system of coordinates, and the reduced mass[105] M in the reaction channel, by

$$k = \frac{1}{\lambda} = \frac{(2\,ME)^{\frac{1}{2}}}{\hbar} \qquad \text{----------} \qquad (2)$$

It can be shown from the reciprocity theorem for nuclear reactions[105] that the probability of the compound nucleus decaying by emission of a particle x is, in terms of the above notation,

$$P(x) = \frac{k_x^2\, \sigma'(x)}{\sum_z k_z^2\, \sigma'(z)} \qquad \text{----------} \qquad (3)$$

where $\sigma'(x)$ is the cross section for the formation of the compound nucleus by the inverse reaction (i.e. a target nucleus Y bombarded by an incident particle x) with a similar notation for $\sigma'(z)$. The sum in the denominator is evaluated over all 'open' exit channels for the decay of the compound nucleus.

* The word channel, as used in this context, is defined in ref.[105]

The first excited state of K^{39} has an excitation energy of 2.53 Mev. Inelastic excitation of this state is not possible at incident neutron energies below about 2.6 Mev in the laboratory system of coordinates. The only decay mode of the compound nucleus therefore, in addition to charged particle emission, is re-emission of the neutron in the entrance channel. Furthermore, the probability of decay of the compound nucleus by neutron emission in the entrance channel, is very much larger than for proton or other charged particle emission, since the latter must penetrate the Coulomb potential barrier. The sum of cross sections in the denominator of equation (3) reduces then to

$$\Sigma_z \; k_z^2 \; \sigma'(z) = k_n^2 \; \sigma'(n) \qquad \text{----------} \qquad (4)$$

and

$$\sigma(n,x) = \frac{k_x^2 \; \sigma'(x)}{k_n^2} \qquad \text{----------} \qquad (5)$$

The K^{40} compound nucleus formed by the absorption of an incident 2.40 Mev neutron, has an excitation energy of 10.2 Mev above the K^{40} ground state. For excitation energies in this region the average level spacing in the K^{40} nucleus, predicted on the basis of the Fermi gas model[106,107], is of the order of 1 kev. Experimentally, Bass et al[90] deduced an average level spacing of approximately 20 kev, from observed resonances in the proton yield from the K^{39} (n,p) A^{39} reaction. In view of the finite ($\sim$5 to 10 kev) spread in neutron energy in this experiment, it is almost certain that some overlapping or unresolved resonances were obscured. Consequently the average level spacing in K^{40} is probably somewhat less than 20 kev. In the present work the total spread in neutron energy ($\pm$ 40 kev) results in the observed cross section being an average over some 6 or more resonances. For this reason, the region of excitation in the compound nucleus can be regarded as an energy continuum, and the value of $\sigma'(x)$ found from continuum[105] theory.

On the basis of this theory the cross section for formation of the compound nucleus does not depend on the quantum

state or any other special property of the target nucleus, but depends only on the type of incident particle x (e.g. proton or alpha particle), on the channel energy E, and on the charge and radius of the target nucleus. In this case[105]

$$\sigma'(x) = \pi \lambda_x^2 \sum (2l + 1)\, T_l(x) \qquad (6)$$

where $T_l(x)$ is the transmission coefficient through the open exit channel x, for a particle having an angular momentum l relative to the residual nucleus. A comparison of equations (5) and (6) shows

$$\sigma(n,x) = \pi \lambda_n^2 \sum_l (2l + 1)\, T_l(x) \qquad (7)$$

If p and α are substituted for x, then

$$\sigma(n,p) = \pi \lambda_n^2 \sum_l (2l + 1)\, T_l(p) \qquad (8)$$

$$\sigma(n,\alpha) = \pi \lambda_n^2 \sum_l (2l + 1)\, T_l(\alpha) \qquad (9)$$

The transmission coefficients represent the probability of a particle penetrating through the Coulomb and centrifugal barriers as well as through the potential discontinuity at the nuclear surface. On the basis of continuum theory[105], T_l is given by

$$T_l = \frac{4\,KRS_l}{\Delta_l^2 + (S_l + KR)^2} \qquad (10)$$

where K is the wave number of the nucleon inside the nuclear surface, and Δ_l and S_l are functions depending on the wave number k of the nucleon outside the nuclear surface, the radius of the residual nucleus R, the angular momentum l, the channel energy E, and the height of the Coulomb potential barrier. The values of Δ_l and S_l can be calculated in terms of R using the W.K.B.[105] approximation method. This has been done, for example by Lindstrom and Neuert.[88] The resulting values for T_l (p) are shown in table (6).

TABLE 6

Radius R (A^{39})	$T_o(p)$	$T_1(p)$	$T_2(p)$	$T_3(p)$	$\sigma(n,p)$ (mbarn)
4.0×10^{-13} cm	1.02 (1)	3.51 (2)	4.32 (3)	2.33 (4)	60.5
5.0×10^{-13} cm	1.80 (1)	8.11 (2)	1.51 (2)	1.29 (3)	133
6.0×10^{-13} cm	2.61 (1)	1.48 (1)	3.82 (2)	4.81 (3)	244

The numbers in brackets in the body of the table denote negative powers of 10. (For example 1.02 (1) denotes 1.02×10^{-1}). The cross section $\sigma(n,p)$ corresponding to a given value of R, has been calculated by substituting the values for $T_1(p)$ into equation 8. Table 7 shows the relation between $\sigma(n,\alpha)$ and the radius R of the residual Cl^{36} nucleus.

TABLE 7

Radius R of Cl^{36}	$\sigma(n,\alpha)$ mbarns
5.5×10^{-13} cm	1.81
7.5×10^{-13} cm	50.5
8.5×10^{-13} cm	212.0

The experimentally determined cross sections found in this work, namely $\sigma(n,p) = 95$ mb and $\sigma(n,\alpha) = 6$ mb correspond to the following effective radii for the respective residual nuclei:

$$R\ (A^{39}) = 4.55 \times 10^{-13} \text{ cm}$$

$$R\ (Cl^{36}) = 5.75 \times 10^{-13} \text{ cm}$$

These values have been found from a graphical interpolation of the values given in tables (6) and (7).

On the basis of the usual formula relating the effective radius of a nucleus to its mass number A, namely $R = r_o A^{1/3}$ the value of r_o given by the measured value of the (n,p) cross section is

$$r_o = 1.34 \times 10^{-13} \text{cm} \qquad (\text{for } A^{39}).$$

In the case of the (n, α) reaction, the effective channel radius R is related to r_o by

$$R = r_o A^{1/3} + \rho$$

where ρ is the effective radius of the alpha particle. The radius of the alpha particle according to Bashkin et al[108] is 2.3×10^{-13}cm. Blatt and Weisskopf[105] adopt a smaller value, $\rho = 1.2 \times 10^{-13}$cm, on the grounds that the repulsive Coulomb force continues to act on the alpha particle even when the alpha particle is partially immersed in the target nucleus. It is this latter value that is used here. The radius R of the residual Cl^{36} nucleus is then 4.55×10^{-13}cm and the corresponding value of r_o is:

$$r_o = 1.36 \times 10^{-13} \text{cm}.$$

Both the values obtained here for r_o are in good agreement with the usual statement[105], $r_o = 1.3$ to 1.5×10^{-13}cm, considering the approximation inherent in the continuum theory, and the inaccuracy of the W.K.B. method for predicting barrier penetrabilities.

CHAPTER 5: CONCLUSION

5.1. THE ENERGY STABILIZED ACCELERATOR:

Three parameters associated with the analyzed ion beam from an energy stabilized Van de Graaff accelerator are of particular interest.

(1) The mean ion energy
(2) The spread in ion energy
(3) The analyzed ion current

The last two parameters are not independent and will be discussed under the same heading.

5.1.1. THE MEAN ION ENERGY:

The mean ion energy is determined by the magnetic field strength in the pole gap of the analyzing magnet. Tests indicate that the stability of this magnetic field is better than .02%. This corresponds to a possible variation of .04% in the energy of a particle following the mean line orbit through the analyzing magnetic field.

The stability of the mean ion energy has been checked directly by observing the thick target yield from the 340 kev fluorine $(p,\alpha\gamma)$ resonance at a magnetic field strength corresponding to the mid-point rise in yield. The gamma-ray count rate for a given target current remains constant within the statistical limits of accuracy for periods in excess of 30 minutes. The yield is then observed to slowly decrease. This effect is attributed to the build up on the target surface of a carbonaceous contaminant film. The thickness of this film has been estimated by observing the displacement of the thick target yield step between fresh and used targets. The thickness obtained (approximately 0.5 kev at 340 kev proton energy, for 10^4 microcoulombs of protons delivered onto the target) is of the correct magnitude to explain the observed decrease in yield with time. The long term stability as indicated

by this method is at least as good as 0.1%.

Energy calibration techniques have been described which enable the mean energy of the analyzed ion beam to be determined with an accuracy of 0.3% for atomic ions in the energy range below 500 kev. A substantial increase in the accuracy of this calibration is precluded by the large uncertainty existing in the published values of the (p, γ) reaction resonance energies below 500 kev. The magnetic field strength corresponding to the mid-point rise in gamma-ray yield from the 340 kev fluorine resonance, is reproducible to within .05% in all cases in which a fresh target is used. The energy calibration is therefore reproducible to within 0.1%.

5.1.2. ION CURRENT AND SPREAD IN ION ENERGY:

Due to the finite object and image slit widths, the spread in the energy of the analyzed ion beam is not entirely eliminated. The predicted total fractional spread in energy based on the calculated performance of the magnetic analyzer has been verified experimentally down to a total energy spread of 0.5%, (i.e. 0.25% fwhm). For the object and image slit widths ($s = s_o = 1$mm) corresponding to this value of the energy spread, analyzed ion currents of 6 μA have been delivered onto a target located after the image slit. The contribution to the total fractional energy spread in the analyzed ion beam, resulting from modulation of the magnetic field by ripple on the magnet field coils, and instabilities in the magnetic field itself, is in all cases less than .05%.

At present efficient use of the ion beam from the accelerator is prevented by two effects associated with focussing the ion beam on the object slit. Firstly the minimum attainable cross-sectional area of the ion beam in the plane of the object slit is considerably larger than at points closer to the accelerator, and secondly, the beam position in the plane of the object exhibits an energy dependent lateral shift of up to 3 mm. This latter effect has not been eliminated either by careful beam tube alignment or by realignment of the ion source extractor and focus electrodes.

It is not possible to appreciably decrease the long ion path ($\sim$ 2.3 metres) between the ion source and the object slit owing to the exigencies of the physical layout of the target room. For this reason, it is intended to overcome the inadequacies of the accelerator focussing with an electrostatic quadrupole lens[109] (at present under construction) placed between the accelerator and the object slit. In addition to enabling fine focussing of the ion beam such a lens can be used to provide fine control over the beam position. This is accomplished by using the opposite pairs of electrodes comprising the lens, in the same way as the deflection plates in an electrostatic deflector. The action of the lens then is to both focus and centralise the ion beam on the object slit of the analyzing magnet. With the addition of this facility it should be possible to deliver an atomic ion current of at least 25 μA through an object slit having a horizontal width of 1 mm.

The question arises as to what proportion of the atomic ion current passing through the object slit will pass through the image slit. Assuming the ions have no spread in energy and the image slit width is equal to the object slit width, the magnet focussing properties are adequate to provide virtually 100% transmission through the image slit. The increase in the horizontal width of the image caused by the spread in energy of the atomic ion beam causes some fraction of the analyzed ion current to strike the energy defining electrodes forming the image slit. The fraction of the analyzed ion current that strikes these electrodes depends, of course, on the settings of the accelerator and stabilization controls. Under typical operating conditions, over a wide range of analyzed ion currents and energies, it has been found that 10 to 20% of the analyzed ion current strikes the energy defining electrodes. This implies that 80% or more of the atomic ion current passing through the object slit, is transmitted through the image slit. Any substantial increase in analyzed ion current must, therefore, come from improved performance of either, or both, the rf ion source or the beam transport system prior to the object slit. In this

regard, a recent overhaul of the ion source has resulted in a much improved percentage yield of atomic ions, and analyzed atomic ion currents in excess of 60 μA have been delivered onto a target placed after the image slit.

In addition to the neutron cross section measurements described here, the energy stabilized accelerator has been used in the development (M. Bartle, M.Sc. thesis in preparation) of a magnetic deflector for the separation of He^3 particles produced in the DD reaction from deuterons elastically scattered from the drive-in target. For these experiments it has proved convenient to set the image and object slit widths at about 5 mm. For deuteron energies around 100 kev, and the above slit settings, steady deuteron target currents in the range from 25 to 40 μA have proved to be easily attained. After initial adjustments have been completed, the accelerator and stabilization system have been found to require only occasional readjustment during the course of the subsequent experiment. Since the addition of the stabilization facility, the accelerator has been operated for over 130 hours, under experimental conditions, and during this time no serious faults have developed.

5.2. THE TAGGED NEUTRON BEAM:

A solid state detector protected from the scattered deuteron flux by a thin nickel foil, has been found to give considerable improvement over a scintillation detector in the ability to discriminate against unwanted counts in the He^3 channel. The complete resolution of the He^3 peak and consequent improved neutron flux determination is especially suited to accurate neutron cross section measurement using the associated particle technique.

The incident deuteron energy is at present limited to energies below approximately 110 kev, since at higher energies the thickness of foil required to stop the scattered deuterons stops the He^3 particles as well. For incident deuteron energies in this range the tagged neutron energy can be varied from approximately 2.3 to

2.6 Mev by altering the angle at which the neutron are observed.

The spread in energy of the tagged neutron beam is at present determined by the spread in reacting deuteron energy caused by the thickness of the drive-in target. In the cross section measurements described here it was possible to minimize this effect by observing the tagged neutron cone at 90^{o} to the incident deuteron beam. At this angle the neutron energy is relatively independent of the reacting deuteron energy. At other angles of observation it is intended to use thin deuterium loaded targets to reduce the spread in reacting deuteron energy.

5.3. THE K^{39} NEUTRON CROSS SECTIONS:

The absolute cross section for the K^{39} (n,p) A^{39} reaction at a neutron energy of 2.46 Mev has been measured to be (95 $\pm$ 4) mb, while the K^{39} (n,α) Cl^{36} cross section at the same neutron energy is (6 $\pm$ 1) mb. These values are in good agreement with those found by Dixon and Aitken but do not agree with the results of Lindstrom and Neuert who worked at a slightly higher neutron energy (2.59) Mev.

The K^{39} (n,p) and (n,α) reaction cross sections calculated on the basis of the optical model of the nucleus, are approximately 100 mb and 5 mb respectively. These estimates are subject to relatively large uncertainties arising both from the continuum theory approximation on which the calculations are based and from the W.K.B.[105] approximation method used for calculating the barrier transmission coefficients. Even considering these inaccuracies it is doubtful whether the results of Lindstrom and Neuert are compatible with this theory.

It is interesting to compare the present absolute measurements with the relative cross sections obtained by Bass et al[90]. The neutron flux entering their KI(Tl) scintillator was measured by means of a calibrated long counter placed behind the scintillation detector. The results obtained (84 $\pm$ 17) mb and (5.0 $\pm$ 1.0) mb are compatible with the present results within the quoted limits of accuracy, but

the agreement is not good. On the basis of the present results the flux determination of Bass et al should be decreased by approximately 12%.

APPENDIX I

THE KINEMATICS OF THE D(d,n) He^3 REACTION (NON-RELATIVISTIC)

This reaction can be written as

$$D + d \longrightarrow n + He^3 + Q \text{ Mev.}$$

and represented in the Laboratory system of co-ordinates by the diagram:-

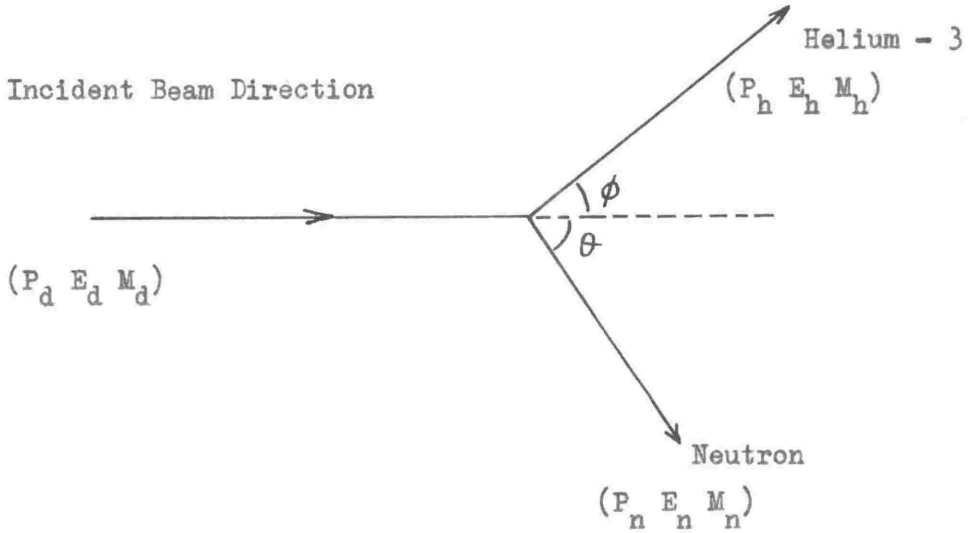

where $(P_d\ E_d\ M_d)$ are respectively the momentum, energy and mass of the incident deuteron with a similar notation for the reaction products.

Conservation of Energy requires that:-

$$E_d + Q = E_n + E_h \qquad \text{---------- (1)}$$

Conservation of Momentum along the incident beam direction requires that

$$P_n \text{ Cos } \theta + P_h \text{ Cos } \phi = P_d \qquad \text{---------- (2)}$$

while conservation of momentum along a line perpendicular to the beam direction gives

$$P_n \text{ Sin } \theta = P_h \text{ Sin } \phi \qquad \text{---------- (3)}$$

The energy E_d is related to the momentum P_d by the equation

$$E_d = \frac{P_d^2}{2M_d} \qquad \text{---------- (4)}$$

with similar relations for the pairs of energy and momentum (P_n, E_n) and (P_d, M_d).

Substituting these values of E_d, E_n and E_h in equation (1) gives

$$\frac{P_d^2}{2M_d} + Q = \frac{P_n^2}{2M_n} + \frac{P_h^2}{2M_n} \quad \text{---------} \quad (5)$$

Values for masses and Q are [9]:-

M_d	= Deuteron mass	= 2.01474	amu.
M_n	= Neutron mass	= 1.00899	amu.
M_h	= Helium -3 mass	= 3.01699	amu.
Q for the D(d,n) He^3 reaction		= 3.2685	Mev.

Using equations (2) (3) and (5) three of the five variables may be determined by letting the remaining two variables assume known values. For example P_n, ϕ and P_h may be uniquely determined for any given assumed combination of E_d and θ. Bell[10] has compiled from computor data a table of values of E_n, E_h and ϕ for 5° increments in θ_n (for θ_n between 0° and 180°) and 10 kev increments in E_d for incident deuteron energies below 500 kev. Data presented in this table has been summarised in figures 1 and 2.

APPENDIX 2:

THE RELATION BETWEEN IMAGE AND OBJECT DISTANCES FOR HORIZONTAL FOCUSSING IN A UNIFORM SECTOR - MAGNETIC FIELD

Using the notation of the associated figure, and applying the law of sines to triangles I and II one obtains

$$\frac{l}{\sin(H-E_o)} = \frac{r+r'}{\sin W} \qquad (1)$$

and

$$\frac{r'}{\sin E_o} = \frac{r}{\sin(H-E_o)} \qquad (2)$$

Eliminating r' and rearranging gives

$$l = \frac{r}{\sin W}\left(\sin(H-E_o) + \sin E_o\right) \qquad (3)$$

From symmetry, the equation for K is

$$k = \frac{r}{\sin W}\left(\sin(H-E) + \sin E\right) \qquad (4)$$

Equations (3) and (4) have been calculated for the central ray STUV. Similar reasoning applied ray ST'U'V gives

$$l + n = \frac{r}{\sin W}\left(\sin(H + A - E_o) + \sin(A_o+E_o)\right) \qquad (5)$$

and

$$k + m = \frac{r}{\sin W}\left(\sin(H+A_o-E) + \sin(A+E)\right) \qquad (6)$$

Subtracting equations (5) and (3) gives

$$m = \frac{r}{\sin W}\left(\sin(H+A_o-E)-\sin(H-E)+\sin(A+E) - \ldots\sin E\right) \qquad (7)$$

which on using the expression for the difference of two sines as a product gives

$$m = \frac{r}{\sin W}\left(2\cos(H-E+\tfrac{1}{2}A_o)\sin(\tfrac{1}{2}A_o)+ 2\cos(E+\tfrac{1}{2}A)\sin(\tfrac{1}{2}A)\right) \qquad (8)$$

As A_o and A are small (implying small angular divergence of the beam) they may be neglected in a cosineterm. Writing $(\tfrac{1}{2}A_o)$ for $\sin(\tfrac{1}{2}A_o)$ in equation (8) then gives:

PARTICLE TRAJECTORIES IN THE HORIZONTAL PLANE
OF A SECTOR-SHAPED UNIFORM MAGNETIC FIELD

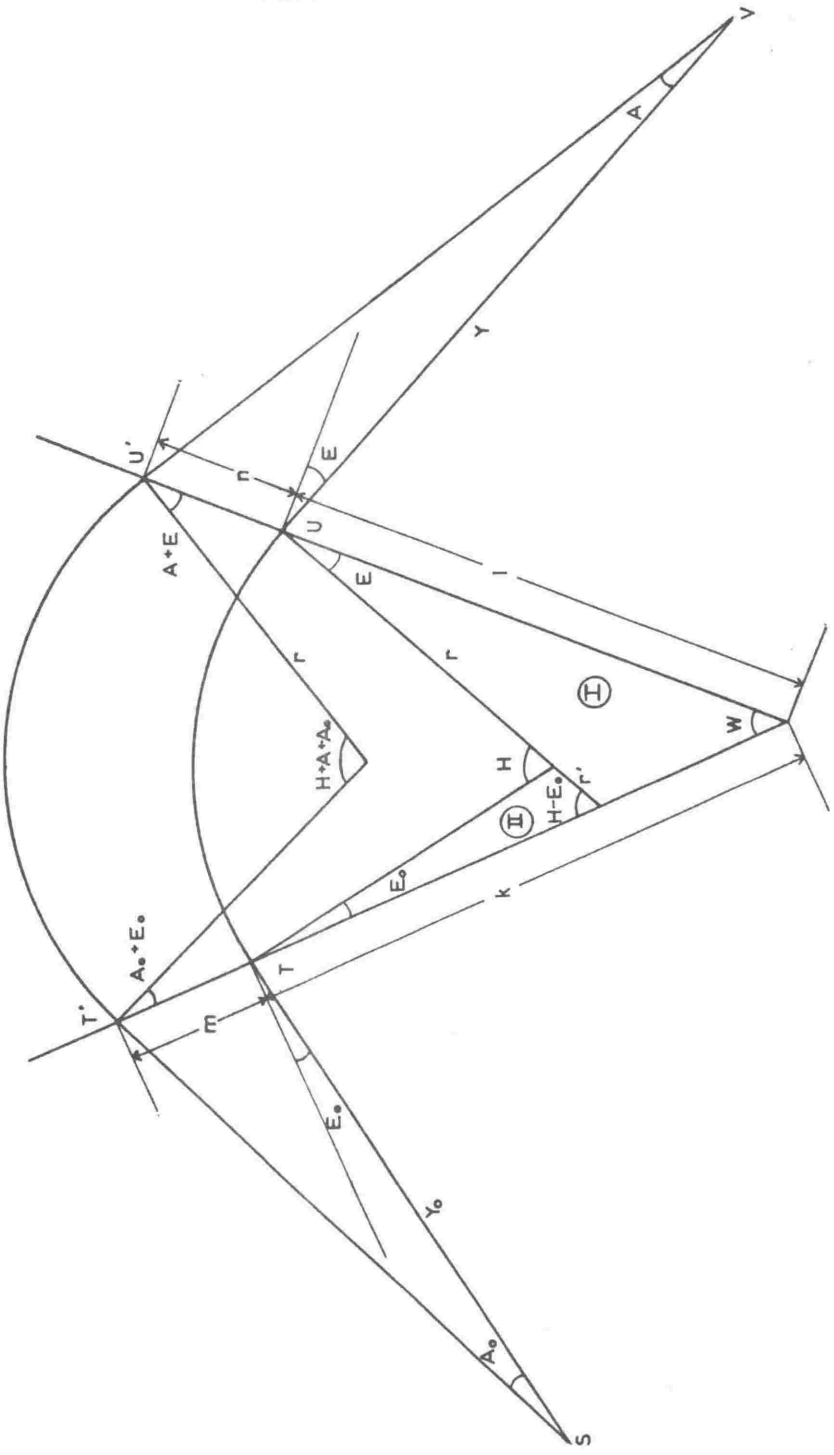

APPENDIX 2

$$m = \frac{r}{\sin W}(A_o \cos (H-E) + A \cos E) \qquad (9)$$

From symmetry subtracting equation (6) and (4) will give,

$$h = \frac{r}{\sin W}(A \cos (H-E_o) + A_o \cos E_o) \qquad (10)$$

From the figure it can be seen that

$$n \cos (A + E) \doteq n \cos E \doteq y \tan A \doteq yA \qquad (11)$$

$$n \cos E \doteq yA \qquad (12)$$

$$m \cos E_o \doteq y_o A_o \qquad (13)$$

Substituting these values for m and n in equation (5) and (6) and solving for A/A_o gives

$$A/A_o = \frac{Y_o \sin W - r \cos E_o \cos (H - E)}{r \cos E_o \cos E} \qquad (14)$$

$$A/A_o = \frac{r \cos E \cos E_o}{y \sin W - r \cos E \cos (H-E_o)} \qquad (15)$$

The conditions for horizontal focussing in the uniform sector field are obtained by equating the right hand sides of equations (14) and (15) i.e.

$$\frac{y \sin W - r \cos E \cos (H-E_o)}{r \cos E_o \cos E} = \frac{r \cos E_o \cos E}{y_o \sin W - r \cos (H-E) \cos E_o} \qquad (16)$$

Equation (16) may be solved explicitly for the image distance y (by substituting $W = H - (E_o + E)$ and expanding the cosine of the differences of angles) to give

$$y = \frac{r \cos E (y_o \cos (H-E_o) + r \sin H \cos E_o)}{y_o \sin W - r \cos E_o \cos (H-E))} \qquad (17)$$

This equation may be written in the symmetrical form by solving for tan H:-

$$\tan H = \frac{(\tan E_o + r/y_o) + (\tan E + r/y)}{1 - (\tan E_o + r/y_o)(\tan E + r/y)} \qquad (18)$$

$$= \tan (P + Q)$$

The focussing condition becomes simply $H = P + Q$

where $\tan P = \tan E_o + r/y_o$ (19)

and $\tan Q = \tan E + r/y$ ---------- (20)

Writing a_o for $\tan E_o$ and a for $\tan E$, and measuring y in units of r one obtains

$$\tan P = a_o + 1/y_o \quad \text{----------} \quad (21)$$

$$\tan Q = a + 1/y \quad \text{----------} \quad (22)$$

This gives the focussing condition in the form most suited for computing purposes.

Equation (18) may also be written in the form

$$\tan H = \frac{(a_o + 1/y_o) + (a + 1/y)}{1 - (a_o + 1/y_o)(a + 1/y)} \quad \text{----------} \quad (23)$$

APPENDIX 3

THE RELATION BETWEEN IMAGE AND OBJECT DISTANCES FOR VERTICAL FOCUSSING IN THE FRINGING FIELD OF A UNIFORM SECTOR-MAGNETIC FIELD

In 2.2.1.2. it has been shown that deflection of a charged particle beam in the Z direction occurs in the fringing field unless the beam enters and leaves the magnetic field along lines perpendicular to the field boundaries. The relation between object and image distances may be found by solving the equivalent optical problem where Z deflection occurs in thin lenses of focal lengths $r/\tan E_o$ and $r/\tan E$, placed at the points of entrance and exit respectively. If the object distance is y_o then the distance V to the image formed by the first thin lens can be found by application of the thin lens formula

$$\frac{1}{y_o} + \frac{1}{V} = \frac{\tan E_o}{r}$$

writing a_o for $\tan E_o$ and solving for V gives

$$V = \frac{r y_o}{a_o y_o - r}$$

The separation of the two thin lenses is rH where H is the angle through which the ion beam is deflected, and r is the radius of curvature of the ion beam, both measured in the median plane. The image from the first lens acts as an object for the second lens at an object distance of $(rH - V)$

$$= \frac{rH\,(a_o y_o - r) - r y_o}{a_o y_o - r}$$

Applying the thin lens formula to the second lens gives

$$\frac{a_o y_o - r}{rH(a_o y_o - r) - ry_o} + \frac{1}{y_v} = \frac{a}{r}$$

where y_v is the vertical focussing image distance measured from the exit pole boundary (figure 3). Rearranging gives

$$\frac{a_o y_o - r}{rH(a_o y_o - r) - ry_o} = \frac{ay_v - r}{y_v r}$$

$$\therefore\ y_v r(a_o y_o - r) + ry_o(ay_v - r) = rH(ay_v - r)(a_o y_o - r)$$

which yields

$$\frac{1}{(a - \frac{r}{y_v})} + \frac{1}{(a_o - \frac{r}{y_o})} = H$$

This form of the equation relating y_o and y_v has been used by Braams[47] and by Camac[45]. If all lengths are measured in units of the radius of curvature r, then this equation becomes

$$\frac{1}{(a - \frac{1}{y_v})} + \frac{1}{(a_o - \frac{1}{y_o})} = H$$

It should be noted that this derivation requires that the region over which vertical (z) deflection takes place be small compared with the path length in the uniform field region.

APPENDIX 4

NOTES ON THE TRIGNOMETRICAL MANIPULATION OF THE FOCUSSING EQUATIONS

Note 1: Equation (17) (2.2.1.2)

The horizontal angular focussing condition is from equation (16) given by $pq = 1$, which on substituting for p and q gives

$$\frac{\left[y_o \sin N - \cos E_o \cos (H - E)\right]\left[y \sin N - \cos E \cos (H - E_o)\right]}{\cos^2 E_o \qquad\qquad \cos^2 E} = 1$$

or

$$\left[y_o \sin N - \cos E_o \cos (H-E)\right]\left[y \sin N - \cos E \cos (H-E_o)\right] = \cos^2 E_o \cos^2 E$$

solving for the image distance y gives

$$y = \frac{\cos^2 E_o \cos E + \cos E \cos (H-E_o)\left[y_o \sin N - \cos E_o \cos (H-E)\right]}{\sin N \left[y_o \sin N - \cos E_o \cos (H - E)\right]}$$

$$= \left[\frac{\cos E}{(y_o \sin N/\cos E_o) - \cos (H-E)}\right]\left[\frac{\cos E_o \cos E - \cos (H-E_o)\cos(H-E)}{\sin N} + \frac{y_o \cos(H-E_o)}{\cos E_o}\right]$$

The first term in the last bracket may be simplified by putting $N = H - (E_o + E)$ (Equation 13) and expanding cosines and sines using formula of the type

$$\sin(A + B) = \sin A \cos B + \cos A \sin B$$

$$\cos(A + B) = \cos A \cos B - \sin A \sin B$$

where A is put equal to H and B equal E, E_o and $(E_o + E)$ in succession, this term is then found to be Sin H and

$$\therefore y = \frac{\cos E \,(\sin H + y_o \cos (H-E_o)/\cos E_o)}{y_o \sin N/\cos E_o - \cos (H - E)}$$

which on multiplying through by $\cos E_o$ gives equation (17)

Note 2: Equations (19) to (24) (2.2.1.2)

Equation (17), on dividing the top and bottom lines of the right hand side by $y_o \cos H \cos E \cos E_o$ inverting, and writing

$H - E_o - E$ for N, becomes

$$\frac{1}{y} = \frac{(\sin (H-E_o-E)/\cos H \cos E_o \cos E)-(\cos (H-E)/y_o \cos H \cos E)}{(\sin H/y_o \cos H) + (\cos (H - E_o) \cos E_o \cos H)}$$

Expanding sines and cosines as before:

$$\frac{1}{y} = \frac{\tan H - \tan E_o - \tan E - \tan H \tan E_o \tan E - (1/y_o) - (\tan H \tan E/y_o)}{(\tan H/y_o) + 1 + \tan E \tan H}$$

$$= \tan H - \frac{((1/y_o) + \tan E_o) - \tan E (1 + \tan H ((1/y_o) + \tan E_o))}{1 + \tan H ((1/y_o) + \tan E_o)}$$

Writing $\tan P = (1/y_o) + \tan E_o$

gives equation (21) viz:-

$$\frac{1}{y} = \tan (H - P) - \tan E$$

In a similar manner from equation 18:

$$\frac{1}{y_v} = \frac{(\tan E_o - (1/y_o)) + \tan E - H \tan E (\tan E_o - (1/y_o))}{1 - H (\tan E_o - (1/y_o))}$$

writing $\tan Q = \tan E_o - (1/y_o)$

gives

$$\frac{1}{y_v} = \frac{\tan Q}{1 - H \tan Q} + \tan E$$

$$\frac{1}{y_v} = \tan E - \frac{1}{H - \cot Q}$$

---

which is equation (22). Equation (23) is the result of eliminating $(1/y_d)$ from equations (21) and (22), while equation (24) is the result of eliminating tan E from equations (22) and (23).

Note 3: An expression for the resolution factor D_o (2.2.1.5)

In section 2.2.1.5. it is shown that the resolution factor D_o may be written in terms of the coefficients in equation (7) viz.,

$$D_o = \frac{V}{W} = \frac{\text{coefficient of the momentum dispersion, B.}}{\text{coefficient of } x_o \text{ (i.e. the magnification)}}$$

On substituting the values of v and w from equations (9) and (10),

$$D_o = \frac{2 \cos E_o \sin (\frac{1}{2}H) \left(\cos (E_o - \frac{1}{2}H) + q \cos (E - \frac{1}{2}H)\right)}{\sin N \quad q}$$

If D_o is measured at the point of horizontal focus then pq = 1, and p is given by equation (11). The above equation becomes

$$D_o = \frac{2 \cos E_o \sin \frac{1}{2}H}{\sin N} \left[\cos (E - \frac{1}{2}H) + \frac{\cos (E_o - \frac{1}{2}H)}{\cos^2 E_o}\right]\left[y_o \sin N - \cos E_o \cos (H - E)\right]$$

The term involving y_o may be written as

$$= \frac{2 \cos E_o \sin (\frac{1}{2}H) . \cos (E_o - \frac{1}{2}H)\, y_o \sin N}{\sin N \quad . \cos^2 E_o}$$

$$= y_o (2 \sin (\tfrac{1}{2}H) \cos E_o \cos (\tfrac{1}{2}H) + 2 \sin (\tfrac{1}{2}H) \sin E_o \sin (\tfrac{1}{2}H)) / \cos E_o$$

$$= y_o (\cos E_o \sin H + (1 - \cos H) \sin E_o) / \cos E_o$$

$$= y_o (\sin H + \tan E_o (1 - \cos H))$$

The coefficient of tan E_o above, differs by a factor of 2 from that given by Cross [46] but is in agreement with that quoted by Braams and Smith.[26] This discrepancy is attributed to a typographical error in Cross's paper. The term not involving y_o simplifies to (1 - cos H) on putting N = H- (E_o + E) and expanding sines and cosines as before.

$$\therefore \quad D_o = y_o (\sin H + \tan E_o (1 - \cos H)) + 1 - \cos H$$

and from symmetry

$$D = y (\sin H + \tan E (1 - \cos H)) + 1 - \cos H.$$

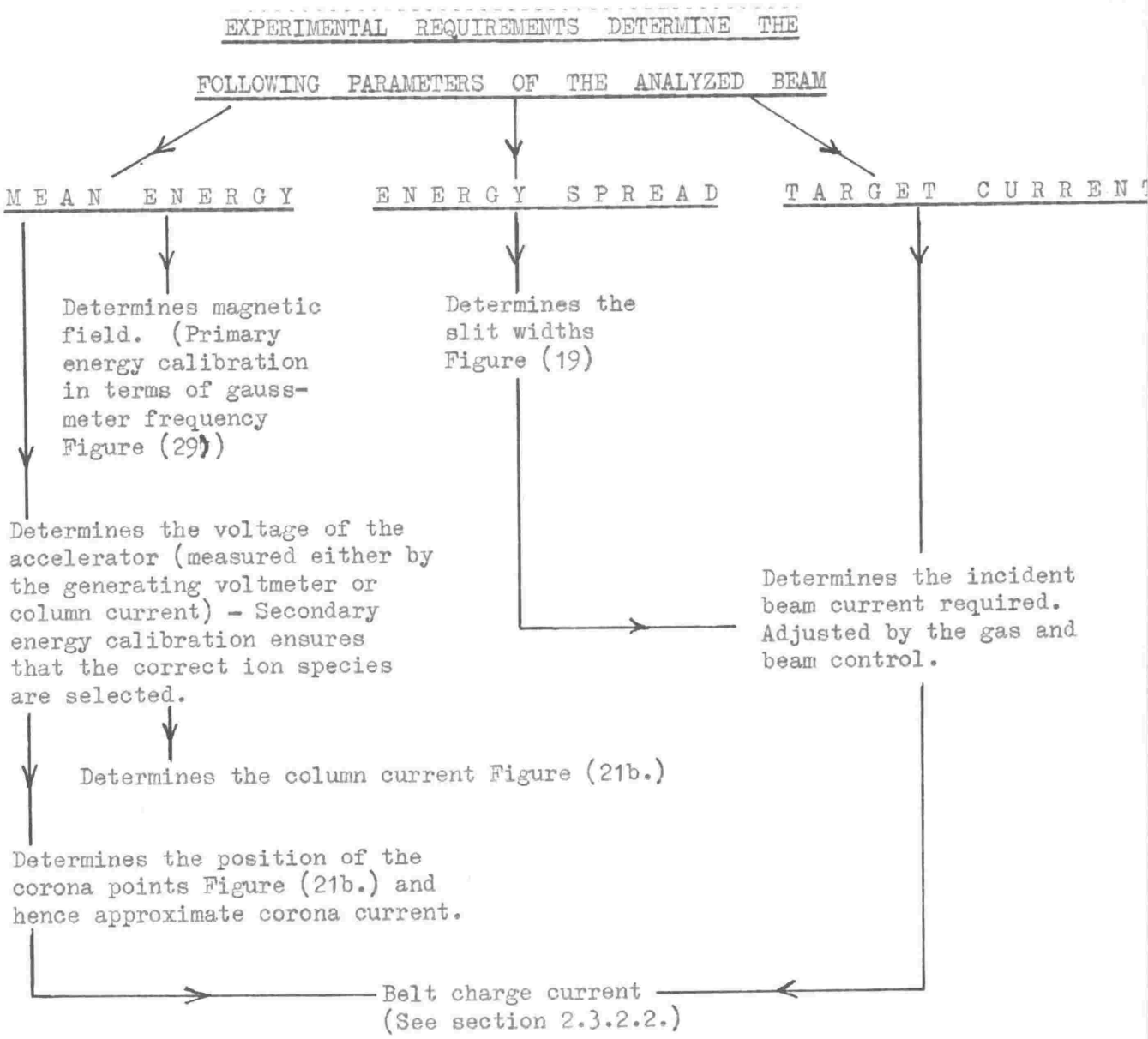

The requirements on the analyzed ion beam, (e.g. the ion species, mean energy, maximum permissible energy spread, and ion current delivered onto the target) are determined by the requirements of the particular experiment. The above scheme shows how these factors determine approximately the settings of the accelerator controls.

It has proved convenient to set the following controls, before activating the accelerator belt drivemotor. The object and image slit widths are set at the value (figure 19) required to give the desired total energy spread in the analyzed beam. The magnetic field strength

in the magnet pole gap is set at the correct value to select the required energy for the particular ion species. This is achieved by setting the gaussmeter frequency at the appropriate value given by figure (29) and adjusting the magnet coil current (figure 26) until a magnetic resonance absorbtion dip is observed on the N.M.R gaussmeter display oscilloscope. The corona points are positioned (figure 21b) so that the corona current drain at the chosen operating potential of the Van de Graaff generator, is within the operating range of the corona triode - stabilizing amplifier combination (~50 μA. drain is satisfactory). The stabilizing amplifier gain is set at zero.

Power is supplied to components in the high voltage terminal approximately half a minute (determined by the closing of a thermal delay switch) after activating the belt drivemotor. The belt charge current is adjusted to give a generator terminal potential of approximately 80 to 100 kv. (as indicated by the column current meter, figure 21b) while the rf discharge is initiated in the ion source. This is accomplished by cycling the gas pressure in the ion source (using the gas control)with the beam extraction potential at zero, (i.e. the beam control in the minimum position). Confirmation of the presence of an rf discharge in the ion source may be obtained by increasing the beam control. If ionization is occurring in the ion source a decrease in the potential of the high voltage terminal will occur as a result of the increased current drain from the terminal caused by the removal of ions from the rf discharge. Once the ion source has 'struck', the high voltage terminal potential is increased (by increasing the belt charge) to the potential corresponding to the desired energy of the ion beam. For this combination of terminal potential (the secondary energy calibration) and magnetic field strength (primary energy calibration) only ions having the desired charge to mass ratio satisfy the conditions necessary for transmission through the analyzing magnet (see section 3.4).

The gas, beam, and focus controls are adjusted to give a current of about 10 μA. passing through the object slit. Slight adjustments are made to the terminal potential in order to centralise the correct analyzed ion species on the image slit and the gain of the

stabilizing amplifier is increased to 'lock' the stabilization system onto the analyzed ion beam. At this point the gas, beam, and focus controls are optimized to give the required target current. The stabilizing amplifier gain, the position of the corona points, and the accelerator belt charge current are adjusted in rotation, to obtain stable, balanced operation of the stabilizing amplifier, (instabilities are indicated by the degree of fluctuation of the stabilizing amplifier balance meter, section 2.3.3.1). The most stable operation is usually achieved with a corona current between 50 and 90 μA., (see figures (20) and (21)). The fraction of the analysed ion current striking the energy defining electrodes is typically 5 to 10%.

Correct operation of the stabilization system can be checked in the following way. A change in the belt charge current should give rise to an error signal (indicated by a deflection of the stabilizing amplifier balance meter) and to a corresponding change in the corona current drawn from the high voltage terminal. The stabilizing action should hold the high voltage terminal potential, as indicated by the generating voltmeter, constant throughout this change. A change in magnet current should change the terminal potential (over a range of at least 100 kilovolts or so) as the error signal simulated by changing the deflection of the ion beam, causes a change in the corona current.

APPENDIX 6:

THE EFFECT OF MAGNET FRINGING FIELDS ON ION TRAJECTORIES IN THE XY PLANE

The fringing fields extending beyond the pole gap boundaries of an analyzing magnet exert significant forces on moving ions in the region between the object (and image) slit and the uniform magnetic field region. The effect on particle trajectories in the Z plane has been discussed in 2.2.1.1. For motion in the horizontal plane (the XY plane of figure 4), equation (1), (2.2.1.1.) gives

$$\frac{d^2x}{dt^2} = \frac{e}{m} B_z \frac{dy}{dt} \qquad \text{---------- (1)}$$

Similarly

$$\frac{d^2y}{dt^2} = \frac{e}{m} B_z \frac{dx}{dt} \qquad \text{---------- (2)}$$

where B_z is the vertical component of the magnetic field and is a function of y alone (assuming for simplicity that $E_o = E = 0$), i.e. B_z may be written as B(y). Integration of equation (1) above gives

$$\frac{dx}{dt} = \frac{e}{m} \int B(y)dy \qquad \text{---------- (3)}$$

where the constant of integration equals zero as the ions initially have no component of velocity in the x direction. If b(y) is defined by the relation $b(y) = B(y)/B_o$ where B_o is the magnetic field strength in the uniform field region then equation (3) becomes

$$\frac{dx}{dt} = \frac{v_o}{r} \int b(y)dy \qquad \text{---------- (4)}$$

where v_o and r are the ion velocity and radius of curvature of the ions in the uniform field region respectively. The velocity in the Y direction is given by

$$\frac{dy}{dt} = v_o - \left(\frac{dx}{dt}\right)^2 \qquad \text{---------- (5)}$$

and hence

$$\frac{dx}{dy} = \frac{\int b(y)dy}{\left[r^2 - \left(\int b(y)dy\right)^2\right]^{\frac{1}{2}}} \qquad (6)$$

If the integral is evaluated for values of y ranging from the object (or image) distance to the uniform field region then dx/dy represents the tangent of the angle made by the ion beam path with the Y axis, and for a given r, depends solely on the value of the integral $\int b(y).dy$. The effect of the fringing field can be allowed for by assuming the uniform field, B_o extends a distance d beyond the pole gap boundary, and there falls abruptly to zero. Then by definition

$$B_o\, d = \int B(y)dy$$

and

$$d = \int b(y)dy \qquad (7)$$

In practice the field non uniformity extends some distance y' inside the real pole boundary and

$$y' + d = \int_{-y_o}^{y'} b(y)dy \qquad (8)$$

where y_o is the object or image slit distance.

The above discussion is still applicable in the case where E_o and E take non-zero values except that the integral must be evaluated along the incident ion beam direction and equation (8) then gives values of y' and d along this line. The lateral (or X) displacement of the beam at the entrance to the uniform field region is obtained by integration of equation (6).

APPENDIX 7: THE FOIL WINDOW IN FRONT OF THE HELIUM - 3 DETECTOR

The foil window placed over the solid state detector is prepared in the following way. The 10^{-5} inch thick nickel foil manufactured by the Chromium Corporation of America comes mounted on a thick copper backing. A small square of nickel plus copper backing is glued over the hole in the aluminium cap covering the solid state detector. The copper backing is etched off the area of foil immediately in front of the hole using a saturated chromic acid solution containing a small quantity of sulphuric acid. After approximately 10 minutes the etch solution is removed by rinsing carefully in water. A second foil of identical thickness is mounted over the first foil and etched in a similar manner.

The time for which this etching process is carried out is critical. If the etching time is too long scattered deuterons will penetrate the foil window at incident deuteron energies below 100 kev. On the other hand, if etching times are too short the foil thickness becomes sufficient to degrade the He^3 pulse height to a level comparable with the noise level in the detector channel. It has been found that with an etching time of 10 minutes, one completed foil window in three will be satisfactory at an incident deuteron energy of 100 kev. The difference between foil windows etched in an identical way is attributed to slight variations in the thickness of the nickel foil used.

Observations made under experimental conditions indicate that a solid state detector subjected to a scattered deuteron flux of more than approximately 10^{-4} microcoulombs will probably have suffered permanent damage. For this reason it is essential that the foil window covering the detector does not exhibit fatigue effects. Preliminary results indicate that provided adequate heat conduction away from the foil window is provided (ensured in this case by the heavy aluminium mounting cap) a foil window made in this way has an infinite lifetime under accelerator conditions, mechanical shocks excepted.

ACKNOWLEDGMENTS

The author wishes to express his appreciation to the following for the invaluable assistance they gave.

Professor D. Walker and Dr. N.G. Chapman for helpful discussions on this work, suggesting the topic studied, and continued support throughout this thesis.

Physics Department staff and research students for showing constant interest.

Dr. N.G. Chapman, Mr. J.E. Callaghan and Mr. M. Bartle, the present members of the accelerator group, who shared with the author a common goal.

Mr. R.A.I. Bell, a past member of the accelerator group, for helpful discussions.

Mr. M. Owen, Mr. E. Millington, and the workshop staff for their careful construction of the magnet and other apparatus associated with this thesis.

Mr. B.E. Goodger and Mr. C.L. Kayes of the technical staff for their advice and willing assistance.

The New Zealand University Grants Committee and University Physics Department for financial assistance.

REFERENCES

1. A.O. Hanson:
"Fast Neutron Physics" J.B. Marion and J.L. Fowler (Ed.) Volume IV Part 1 Chapter 1A. (Interscience Publishers, Inc., New York) (1963)

2. W.R. Dixon & J.H. Aitken:
Nuc. Phys. 24 (1961) 456.

3. G. Lindstrom and H. Neuert, Zeit. f. Naturforsch 13a (1958) 826

4. P.L. Okhuysen, E.W. Bennett, J.B. Ashe, and W.E. Millett
Rev. Sci. Instr., 29 (1958) 982

5. P. Shapiro and R.W. Higgs Phys. Rev. 108 (1957) 710.

6. W. Franzen, P. Huber and L. Schellenberg, Zeit. f. Naturforsch., 10 a (1955) 820

7. W. Franzen, P. Huber and L. Schellenberg, Helv. Phys. Acta, 28 (1955) 328

8. B.D. Kern and W.E. Kreger, Phys. Rev. 112, (1958) 926

9. I Fowler and Brolley, Rev. Mod. Phys. 28 (1956) 103

10. R.A.I. Bell,
"Kinematics and Cross Sections of the Reactions D(d,n) He^3 and D(d,p) T"
Victoria University of Wellington Physics Department Report No. NP2 (1965) (Unpublished)

11. T.W. Bonner,
A private communication quoted in Reference (2)

12. R.G. Herb,
"Handbuch der Physik", Vol. XLIV pp. 64-104.
Springer, Berlin, (1959).

13. R.J. Van de Graaff, J.G. Trump, W.W. Buechner
Repts. Progr. in Phys. 11 (1948) 1 - 18

REFERENCES

14. M.H. Blewett
"The Electrostatic (Van de Graaff) Accelerator"
an article in "Methods of Experimental Physics"
L.C.L. Yuan and C.S. Wu. (Ed) Volume 5, Part B,
(1963) 584 (Academic Press, New York and London).

15. Recent References may be obtained from
"The Proceedings of the third Accelerator Conference"
Boston, Massachusetts, U.S.A.
Nucl. Instr. and Methods 28 No. 1 (1964).

16. M.S. Livingston and J.P. Blewett
"Particle Accelerators" McGraw-Hill, New York (1962)

17. R.J. Van de Graaff
Phys. Rev. 38 (1931) 1919A

18. A.J. Gale
Nucl. Instr and Methods. 28 (1964) No. 1 p. 1

19. J.C. Tiemeyer,
Nucl. Instr. and Methods 8 (1960) No. 1 p. 1

20. K.J. Bjostrom, T. Huus and R. Tanger,
Phys. Rev. 71 (1947) 1661

21. Subject of a research program at H.V.E.C. as outlined by
A.J. Gale, Nucl. Instr. and Methods 28 (1964) No. 1. p. 7

22. B. Jennings
I.R.E. Proc. 38 (1950) 1126

23. D.R. Chick and D.P.R. Petrie,
I.E.E. Proc Part B. 103 (1956) 137

24. J.L.W. Churchill and B. Millar
A.E.I. Research Rpt. No. A229 (1952)

25. F. Bumiller, H.H. Staub and H.E. Weaver,
Helv. Phys. Acta 29 (1956) 83

REFERENCES

26. C.M. Braams and P.B. Smith,
Nucl. Instr. and Methods 8 (1960) 27

27. C.P. Brown, J.A. Galey, J.R. Erskine and K.L. Warsh
Phys. Rev. 120 (1960) 905

28. E.J. Rogers and C.M. Turner,
Rev. Sci. Instr. 24 (1953) 805

29. R.G. Herb, S.C. Snowden, and O. Sala
Phys. Rev. 75 (1949) 246

30. R.O. Bondelid and C.A. Kennedy,
Phys. Rev. 115 (1959) 1601

31. S.E. Hunt, R.A. Pope, D.V. Freck, and W.W. Evans
Phys. Rev. 120 (1960) 1740

32. J.J. Kritzinger
Nature 197 (1963) 1165

33. N.F. Barber,
Proc. Leeds Phil. Soc. 2 (1933) 427

34. W.E. Stephens and A.L. Hughes,
Phys. Rev. 45, (1934) 123A

35. W.E. Stephens
Phys. Rev. 45, (1934) 513

36. E. Brueche and O. Scherzer,
Geometrische Elektronenoptik Julius Springer, Berlin, 1934

37. R. Herzog
Z. Physik 89 (1934) 447

38. L. Cartan,
J. Phys. et radium. 8 (1937) 453

39. M. Cotte,
Ann. Phys. 10 (1938) 333

REFERENCES

40. N. Svartholm and K. Siegbahn,
Arkiv. Mat. Astron. Fysik 33a, No. 21 (1946)
and N. Svartholm and K. Siegbahn
Arkiv. Mat. Astron. Fysik 33a, No. 24 (1946)

41. F.B. Shull and D.M. Dennison,
Phys. Rev. 71 (1947) 681
Phys. Rev. 72 (1947) 256

42. D.L. Judd
Rev. Sci. Instr. 21 (1950) 213

43. N. Svartholm
Arkiv. Fysik 2 (1950) 115

44. E.S. Rosenblum
Rev. Sci. Instr. 21 (1950) 586

45. M. Camac
Rev. Sci. Instr. 22 (1951) 197

46. W.G. Cross
Rev. Sci. Instr. 22 (1951) 717

47. C.M. Braams
Thesis, Utrecht, (1956)
See also Reference (26)

48. K.T. Bainbridge
Phys. Rev. 75 (1949) 216

49. W. Ploch and W. Walcher
z. Physik 127 (1950) 274

50. N.D. Coggeshall
J. Appl. Phys., 18 (1947) 855

51. K.T. Bainbridge
in "Experimental Nuclear Physics"
Vol. I E. Segre (Ed) Part V, 582 (1953)
(John Wiley and Sons) New York)

52. In the first instance, see reference 18, pp's 2 to 5.

REFERENCES

53. L.F. Bates
"Modern Magnetism" 4th edition,
Cambridge University Press, American Branch (1960)

54. N.H. Frank
"Introduction to Electricity and Optics"
2nd edition (1950) McGraw-Hill, New York

55. O.R. Frisch
"The Nuclear Handbook" (1958) George Newnes Ltd. London

56. F.J. Newlands
Thesis (1953) Auckland University Library (N.Z.) 538.1 N54.

57. "The Radio Amateurs Handbook" 26th edition (1949) 547

58. R.M. Bozorth
"Ferromagnetism" 1951 (59) D. Van Nostrand Co. Inc. U.S.A.

59. Loeb, Kip, Hudson and Bennett
Phys. Rev. 44 (1933) 883

60. K.K. Darrow
"Magnetic Resonance"; Bell Telephone System
Monograph No. 2065

61. J.A. Pople
"High Resolution Nuclear Magnetic Resonance"
McGraw-Hill, 1959

62. Ref. 58 p 771

63. D.R. Back, W.J. Childs, R.W. Hockney, P.V.C. Hough And W.C. Parkinson Rev. Sci. Instr. 27 (1956) 516

64. H.T. Richards
"Charged Particle Reactions" appearing in
"Nuclear Spectroscopy" F. Ajzenberg- Selove (Ed.)
Part A (1960) Academic Press, New York.

65. J.B. Marion and T.W. Bonner
"Neutron threshold Measurements" appearing in
"Fast Neutron Physics" Part II
J.B. Marion and J.L. Fowler (ed) Interscience Pub. (1963)

(66) F. Ajzenberg - Selove and T. Lauritsen:
Nucl. Phys. 11 (1959) 124

(67) T. Huus and R.B. Day:
Phys. Rev. 91 (1953) 599

(68) D.S. Craig, W.G. Cross, and R.G. Jarvis:
Phys. Rev. 103 (1956) 1414

(69) C.Y. Chao, A.V. Tollestrup, W.A. Fowler, and C.C. Lauritsen:
Phys. Rev. 79 (1950) 108

(70) F. Bumiller, F. Muller and H.H. Staub:
Helv. Phys. Acta 29 (1956) 234

(71) J.L. Fowler and T. Lauritsen:
Phys. Rev. 76 (1949) 314

(72) S.E. Hunt:
Proc. Phys. Soc. A65 (1952) 982

(73) J.B. Marion:
Rev. Mod. Phys. 33 (1961) 139
and 33 (1961) 623

(74) R.D. Evans:
"The Atomic Nucleus"
McGraw - Hill Book Co. Ltd. New York (1955) p. 805

(75) H.A. Enge:
Nucl. Instr. and Meth. 28 (1964) 119

(76) C.M. Braams:
Nucl. Instr. and Meth. 26 (1964) 83

(77) J.N. Shive:
"Semiconductor Devices"
D. Van Nostrand Co., New York (1959) Chapter 24.

(78) A.H. Morrish:
Phys. Rev. 76 (1949) 1651

(79) Ref. (30) p. 1603

(80) Ref. (26) p. 39

(81) Ref. (74) p. 748

(82) J. Dubois:
Trans. of the Chalmers Univ. of Tech. Gothenburg Sweden. Nr. 270 (1963)

(83) E.J. Angelo, jr.:
"Electronic Circuits"
McGraw - Hill Book Co. Ltd., Sec. Ed. (1964) 608

(84) H. Wind:
"Electric Field Dissociation of H_2^+ "
United Kingdom A.E.A., Research Group Rpt.
C.L.M. - R 46. (1965)

(85) D.R. Sweetman:
Proc. Roy. Soc. A 256 (1960) 416

(86) M.J. Scott and R.E. Segel:
Phys. Rev. 102 (1956) 1557

(87) P. Kienle and R.E. Segel:
Brookhaven Nat. Lab. Prog. Rpts.
BNL 502 and BNL 515 (1958)

(88) G. Lindstrom and H. Neuert:
Zeits. fur Naturforschung 13 (a) (1958) 826

(89) W.R. Dixon and J.H. Aitken:
Nucl. Phys. 24 (1961) 456

(90) R. Bass, H.P. Haenii, T.W. Bonner and F. Grabbard:
Nucl. Phys. 28 (1961) 478

(91) P.B. Johnson:
"Nuclear Half-Life Measurement Using a Fast Oscilloscope"
M. Sc. thesis. Victoria University of Wellington.

(92) I. Bergstrom, E. Bonacalza, A. Jech, M. Perez and P. Thieberger:
Nucl. Instr. and Methods 8 (1960) 151

(93) G. Dearnaley and D.C. Northrop:
"Semiconductor Counters for Nuclear Radiations"
E. and F.N. Spon Ltd. (1963) London

(94) G.W.C. Kaye and T.H. Laby:
"Tables of Physical and Chemical Constants"
12th ed. 1958, Longmans, Gt. Britain, p. 192.

(95) J.F. Raffle and E.J. Robbins:
Proc. Phys. Soc. 65B (1952) 320

(96) W.T. Link and D. Walker:
Proc. Phys. Soc. 66A (1953) 767

(97) W.E. Burcham:
Proc. Phys. Soc. 70A (1957) 309

(98) W. Franzen, R.W. Peelle and R. Sherr:
Phys. Rev. 79 (1950) 742

(99) P. Kienle and R.E. Segel:
Phys. Rev. 113 (1959) 909

(100) D.J. Hughes and R.B. Schwartz:
"Neutron Cross Sections"
Brookhaven National Laboratories BNL 325, 1958

(101) R.A.I. Bell:
M. Sc. Thesis; Victoria University of Wellington, 1964

(102) J.C.D. Milton and J.S. Fraser:
Phys. Rev. 96 (1954) 1508

(103) W.E. Burcham:
Proc. Phys. Soc. 70A (1957) 309

(104) N. Bohr:
Nature, 137, (1936) 344

(105) J.M. Blatt and V.F. Weisskopf:
"Theoretical Nuclear Physics"
John Wiley and Sons, 1952

(106) J.M.B. Lang and K.J. Le Couteur:
Proc. Phys. Soc. 67 (1954) 586

(107) T.D. Newton:
Can., J. Phys. 34 (1956) 804

(108) S. Bashkin, B. Petree, F.P. Mooring, and R.E. Peterson:
Phys. Rev. 76 (1949) 574

(109) N.M. King:
An article in "Progress in Nuclear Physics"
O.R. Frisch, Ed., 9 (1964) 73,
Pergamon Press.